



TECHNISCHE  
UNIVERSITÄT  
WIEN  
Vienna | Austria

## DISSERTATION

# Modeling and Simulation of Fatigue Damage in Power Semiconductors

carried out for the purpose of obtaining the degree of Doctor technicae (Dr. techn.),  
submitted at TU Wien, Faculty of Mechanical and Industrial Engineering, by

**Dipl.–Ing. Martin SPRINGER**

Mat.Nr.: 0926110

Im Winkl 17, 3743 Röschitz, Austria

under the supervision of

Assoc. Prof. Dipl.–Ing. Dr. techn. Heinz E. Pettermann

Institute of Lightweight Design and Structural Biomechanics, E317

reviewed by

Assoc. Prof. Dr. Albert Turon Travesa  
AMADE, University of Girona

Dipl.–Ing. Dr. mont. Hans–Peter Gänser  
Materials Center Leoben Forschung GmbH



# Abstract

One of the main design challenges for modern power semiconductor devices is the reduction of the device footprint while maintaining or even increasing the power density. This leads to extreme operational conditions, which have to be withstood by the utilized materials and compounds. The lifetime of a device is not limited by the first occurrence of fatigue damage onset. Instead, a certain region of material failure is necessary to impede the heat flow and lead to a critical temperature increase and potential thermal runaway. Therefore, the whole fatigue life needs to be assessed, ranging from early damage formation to damage onset and spatial damage progression. Advanced methods within the framework of the Finite Element Method are developed to describe potential fatigue damage and interface degradation of the power metallization caused by active power cycling with massive overload pulses.

A continuum damage mechanics based approach is formulated to describe fatigue damage inside the ductile power metallization. The approach utilizes a phenomenological multiaxial fatigue criterion for the description of damage onset and a strain energy density based criterion for the assessment of damage progression. Additionally, the effect of damage on the thermal conductivity is included in the model. The approach is implemented into the Finite Element Method allowing for the simulation of spatial damage evolution with respect to the number of load cycles. Furthermore, the change of the thermal field caused by damage degraded heat conduction is considered. The fatigue damage modeling approach is exemplified on simulations of microcantilever beam experiments under low cycle fatigue conditions.

A cyclic cohesive zone model is formulated for the simulation of cyclic delamination between the power metallization and the silicon chip. The model is based on an exponential–traction separation law formulated for monotonic loading conditions. An energy–based fatigue ex-

tension is introduced allowing for the prediction of delamination growth under cyclic loading conditions. The whole model formulation utilizes physically interpretable interface properties which can be directly obtained from experimental results. The model accounts for mixed-mode and variable amplitude loading conditions. The thermal conductance of the interface is coupled with the mechanical damage variable resulting in a deterioration of the thermal flux across the interface. The model is implemented into the Finite Element Method allowing for the simulation of structures under thermo-mechanical loading conditions. The mechanical constitutive response of the model is demonstrated on pure and mixed-mode delamination tests undergoing constant and variable amplitude loading.

The fatigue damage modeling approaches are exemplified on a simple, generic submodel of a DMOSFET device. Various simulations are conducted using the damage modeling approaches either independently or in combination with each other. The obtained damage characteristics, their evolution with load pulses, and their interactions are discussed and compared. The developed approaches predict reasonable results and provide a step forward towards physical lifetime models based on numerical simulation techniques for power semiconductor devices.

# Kurzfassung

Eine der Herausforderungen für die Auslegung und Konstruktion von modernen Leistungshalbleitern besteht in der Erhaltung oder sogar Erhöhung der ertragbaren Leistungsdichte bei gleichzeitiger Reduktion der Bauteilgröße. Diese Anforderung an moderne Leistungshalbleiter führt zu extremen Lastfällen und Belastungen der verwendeten Materialien und Materialverbunde im Inneren der Bauteile. Die Lebensdauer von Leistungshalbleitern wird jedoch nicht durch das erstmalige Auftreten von Materialermüdung beschränkt, sondern durch die Ausbreitung eines Ermüdungsrisse, welcher die Wärmeabfuhr in das umliegende Material verhindert. Hierdurch kommt es zu einem lokalen Temperaturanstieg welcher bis zur Überhitzung und zum Ausfall des Leistungshalbleiters führen kann. Um Aussagen über die Bauteillebensdauer treffen zu können muss somit die gesamte Ermüdungslebensdauer beginnend bei der Entstehung von Materialschädigung bis hin zur Ausbreitung von Materialversagen bewertet werden. Numerische Methoden im Bereich der Finiten Elemente Methode werden entwickelt um den Schädigungsprozess in der Metallisierung und den Grenzflächen eines Leistungshalbleiters, hervorgerufen durch zyklische Überlastbeanspruchung, beschreiben zu können.

Ein auf Kontinuums-Schädigungsmechanik basierendes Modell zur Vorhersage von Ermüdungsschädigung im inneren der duktilen Metallisierung eines Leistungshalbleiters wird in der vorliegenden Arbeit formuliert. Das Modell verwendet ein phänomenologisches Ermüdungskriterium für mehrachsige Spannungs- und Verzerrungszustände, welches den Beginn von Ermüdungsschädigung beschreibt. Ein auf der Verzerrungsenergiegedichte basierendes Evolutionsgesetz wird für die Beschreibung der Schädigungsentwicklung eingesetzt. Die Auswirkungen der Materialschädigung auf die thermische Leitfähigkeit des Materials werden im entwickelten Modell ebenfalls berücksichtigt. In Kombination mit der Finiten Ele-

mente Methode erlaubt das formulierte Schädigungsmodell die Vorhersage von Schädigungsausbreitung in Korrelation zur Anzahl der aufgebrachten Lastzyklen. Durch die Degradation der thermischen Leitfähigkeit wird der Einfluss der Materialschädigung auf das thermische Feld mitberücksichtigt. Das Modell zur Vorhersage von Ermüdungsschädigung wird durch Simulation eines Mikrotragträgers, belastet im Kurzzeit-Schwingversuch, demonstriert.

Außerdem wird ein zyklisches Kohäsivzonenmodell formuliert, welches die zyklische Delaminationsausbreitung zwischen der Metallisierung und dem Silizium-Chip des Leistungshalbleiters beschreiben kann. Das Modell basiert auf einem exponentiellen Separationsgesetz welches für monotone Belastungen formuliert wurde. Diese Modellformulierung wird mit einem Energieansatz erweitert um die Delaminationsausbreitung in der Grenzschicht des Materialverbundes für zyklische Belastungen vorhersagen zu können. Das Kohäsivzonenmodell verwendet ausschließlich physikalisch motivierte Grenzflächenparameter welche direkt mit experimentellen Versuchen bestimmt werden können. Das Modell kann für Mixed-Mode Belastungen und variable Amplitudenbelastungen gleichermaßen eingesetzt werden. Die thermische Leitfähigkeit der Grenzschicht wird mit der mechanischen Schädigungsvariable des Modelles gekoppelt. Hierdurch wird eine Verringerung des Wärmeflusses durch die Grenzschicht im geschädigten Zustand modelliert. Thermo-mechanische Struktursimulationen werden durch die Implementierung des Kohäsivzonenmodelles in die Finite Elemente Methode ermöglicht. Das mechanische Konstitutivverhalten des Modelles wird mittels numerischer Simulationen von experimentellen Delaminationsversuchen, durchgeführt für verschiedene Belastungssituationen, demonstriert.

Die entwickelten Modelle zur Vorhersage von Ermüdungsschädigung werden auf ein vereinfachtes, generisches Submodell eines DMOSFET Leistungshalbleiters angewandt. Verschiedene numerische Simulationen werden durchgeführt und die Schädigungsmodelle werden einerseits unabhängig voneinander und andererseits in Kombination miteinander angewandt. Die erhaltenen Schädigungscharakteristiken, deren Entwicklung in Abhängigkeit von der Anzahl an Lastzyklen, sowie die Interaktion zwischen den einzelnen Schädigungsmechanismen werden miteinander verglichen und diskutiert. Die entwickelten Schädigungsmodelle liefern zufriedenstellende Vorhersagen und stellen somit einen weiteren Schritt in Richtung physikalisch motivierter Lebensdauermodelle, basierend auf numerischen Simulationen, für Leistungshalbleiter dar.

# Acknowledgment

This work was carried out during my employment at the Institute of Lightweight Design and Structural Biomechanics (ILSB) at the Vienna University of Technology (TU Wien). Funding was jointly provided by the Austrian Research Promotion Agency (FFG, Project No. 846579) and the Carinthian Economic Promotion Fund (KWF, contract KWF-1521 | 26876 | 38867).

My deepest gratitude goes to my thesis adviser Prof. Heinz E. Pettermann for his support, ideas, and suggestions throughout every stage of this work. Our numerous, fruitful discussions and his valuable feedback taught me to scientifically reflect on and articulate my work. Furthermore, I am thankful to Prof. Albert Turon and Dr. Hans-Peter Gänser for acting as reviewers on my thesis.

I would like to thank all members of the ILSB for creating such a friendly and supportive work environment. My gratitude goes to the heads of the institute during my time at the ILSB, Prof. Philipp Thurner, Prof. Helmut Böhm, and em.Prof. Franz Rammerstorfer. Special thanks go to my office mates, Botond Dohnál, Jan Kaul, Tilen Ceglar, and especially my long-term office mate Martin Schwab, all who contributed many fruitful as well as work distracting discussions and kept my spirits up. I would also like to thank my predecessor Grygoriy Kravchenko for introducing me to his work, providing tremendous help at the beginning of my work. Additionally, I would like to thank Maria Steininger for all the administrative help and Gerhard Schneider for providing an outstanding computational infrastructure.

I am grateful to the members of the Kompetenzzentrum Automobil- und Industrieelektronik GmbH, Villach (KAI) for their help and support during this time. Special thanks

go to my industrial supervisor Dr. Balamurugan Karunamurthy, who introduced me to the field of microelectronics and its many challenges. In addition, the helpful discussions and valuable support from Dr. Michael Nelhiebel, Dr. Johannes Zechner, and the head of KAI, DI Josef Fugger, are greatly acknowledged.

In the course of this work, I had the great opportunity to stay for three months at the AMADE group at the University of Girona. Special thanks go to Albert Turon for hosting me and for the productive discussions during my stay. Furthermore, I would like to thank all members of the AMADE group for creating such an inviting work environment and for the wonderful time in Catalonia.

I would like to thank Caitlyn Collins for all of her help during proofreading of this work.

Finally, I would like to thank my family and friends for their support throughout my studies.



# Contents

<b>Notations</b>	<b>IX</b>
<b>1 Introduction</b>	<b>1</b>
1.1 Motivation . . . . .	1
1.2 Background . . . . .	7
1.3 Scope of the present work . . . . .	7
<b>2 Literature Review</b>	<b>9</b>
2.1 Fatigue, Fracture, and Damage Mechanics . . . . .	9
2.2 Lifetime Models for Power Semiconductors . . . . .	34
<b>3 Fatigue Damage Modeling in the Bulk Material</b>	<b>37</b>
3.1 Introduction . . . . .	38
3.2 Orthotropic Continuum Damage Model . . . . .	41
3.3 Numerical Implementation . . . . .	54
3.4 Cycle Jump Technique . . . . .	58
3.5 Demonstration Studies . . . . .	62
3.6 Application – Microcantilever Beam . . . . .	66
3.7 Summary . . . . .	74

<b>4</b>	<b>Cyclic Cohesive Zone Model for the Interface</b>	<b>77</b>
4.1	Introduction . . . . .	78
4.2	Constitutive Model . . . . .	81
4.3	Implementation Aspects . . . . .	98
4.4	Cycle Jump Technique . . . . .	101
4.5	Demonstration of the Model . . . . .	103
4.6	Summary . . . . .	116
<b>5</b>	<b>Application – DMOSFET</b>	<b>119</b>
5.1	Introduction . . . . .	119
5.2	FEM–Model . . . . .	121
5.3	Simulation Results and Discussion . . . . .	131
5.4	Summary . . . . .	143
<b>6</b>	<b>Conclusion</b>	<b>147</b>
<b>A</b>	<b>CDM – Effective Material Properties</b>	<b>151</b>
<b>B</b>	<b>CCZM – Integrals</b>	<b>157</b>
<b>C</b>	<b>CCZM – Interface Stiffness Matrix</b>	<b>159</b>
<b>D</b>	<b>CDM – Routine</b>	<b>165</b>
<b>E</b>	<b>CCZM – USERINTER</b>	<b>169</b>
	<b>Bibliography</b>	<b>175</b>
	<b>Curriculum Vitae</b>	<b>A</b>

# Notations

## Abbreviations

2D	...	Two-Dimensional
3D	...	Three-Dimensional
Al	...	Aluminum
APDL	...	ANSYS Parametric Design Language
BK	...	Benzeggagh–Kenane
CBT	...	Corrected–Beam–Theory
CCZM	...	Cyclic Cohesive Zone Model
CDM	...	Continuum Damage Mechanics
CTE	...	Coefficient of Thermal Expansion
CTOD	...	Crack Tip Opening Displacement
Cu	...	Copper
CZ	...	Cohesive Zone
CZM	...	Cohesive Zone Model
DCB	...	Double–Cantilever–Beam
DMOS	...	Double–diffused Metal–Oxide–Semiconductor
DMOSFET	...	Double–diffused Metal–Oxide–Semiconductor Field–Effect Transistor
ECM	...	Experimental Compliance Method
ELM	...	Empirical Lifetime Model
ENF	...	End–Notched–Flexure
EPFM	...	Elasto–Plastic Fracture Mechanics
$\epsilon$ -N	...	Strain–Life
FEM	...	Finite Element Method
FIP	...	Fatigue Indicator Parameter
FPZ	...	Fracture Process Zone
FS	...	Fatemi–Socie

HCF	...	High Cycle Fatigue
HRR	...	Hutchinson, Rice, and Rosengren
IGBT	...	Insulated–Gate Bipolar Transistors
LCF	...	Low Cycle Fatigue
LEFM	...	Linear–Elastic Fracture Mechanics
MCC	...	Minimum Circumscribed Circle
MDM	...	Maximum Damage Method
MMB	...	Mixed–Mode–Bending
MOSFET	...	Metal–Oxide–Semiconductor Field–Effect Transistor
LC	...	Load Cycle
PLM	...	Physical Lifetime Model
RVE	...	Reference Volume Element
SET	...	Single Element Test
Si	...	Silicon
SIF	...	Stress Intensity Factor
SWT	...	Smith–Watson–Topper
S–N	...	Stress–Life
TMF	...	Thermo–Mechanical Fatigue

### Scalars, tensors, and matrices

Throughout this thesis scalar, tensorial, vectorial quantities are addressed using the notation presented in the listing below. The individual components of such vectors or tensors may be addressed by indices. Note, that no distinction is made between physical and mathematical vectors.

#### Scalar notation

$a, b$  ... scalars

#### Tensor notation

$\mathbf{a}, \mathbf{b}$  ... vectors

$\mathbf{D}, \boldsymbol{\sigma}$  ... second–order tensor

$\mathbb{M}, \mathbb{S}$  ... fourth–order tensor

#### Voigt notation (component ordering see Appendix A)

$[\varepsilon_q], [\sigma_q]$  ... second–order tensor using vector notation

$[M_{pq}], [S_{pq}]$  ... fourth–order tensor using matrix notation

**Symbols of recurring Latin Letters**

$a$	...	crack length
$a_0$	...	initial crack length
$\Delta a$	...	crack growth increment
$dA$	...	area of surface element
$d\tilde{A}$	...	effective area of surface element
$b$	...	fatigue strength exponent or specimen width
$b_\gamma$	...	shear fatigue strength exponent
$B$	...	mode mixity
$c$	...	fatigue ductility exponent
$c_\gamma$	...	shear fatigue ductility exponent
$C$	...	specimen compliance
$C$	...	contour or Paris law exponent
$C_I, C_{II}, C_m$	...	pure mode and mixed-mode Paris law exponents
$C_1$	...	plasticity parameter for the Chaboche kinematic hardening model
$[C_{pq}]$	...	elasticity matrix
$\mathbb{C}$	...	elasticity tensor
$d_s$	...	internal state variable (CCZM)
$d_{\text{tot}}$	...	total internal state variable (CCZM)
$\mathcal{D}$	...	damage onset variable (CDM)
$\mathcal{D}^0$	...	damage onset criterion (CDM)
$D$	...	damage evolution variable (CDM & CCZM)
$D_b$	...	damage evolution variable of the bulk fatigue approach (CDM)
$D_{cz}$	...	damage evolution variable of the cyclic cohesive zone model (CCZM)
$D_s$	...	static damage variable (CCZM)
$D_f$	...	fatigue damage variable (CCZM)
$D_{\text{tot}}$	...	total damage variable (CCZM)
$\Delta D$	...	damage increment (CDM & CCZM)
$\mathbf{D}$	...	second-order damage tensor (CDM)
$\mathbf{e}_i$	...	unit normal vectors
$E_0$	...	Young's modulus of the undamaged material
$E, E_i$	...	Young's moduli
$\tilde{E}, \tilde{E}_i$	...	Young's moduli of the damaged material

$G, G_{ij}$	...	shear moduli
$\tilde{G}, \tilde{G}_{ij}$	...	shear moduli of the damaged material
$\mathcal{G}$	...	total energy release rate
$\mathcal{G}_c, \mathcal{G}_c$	...	critical energy release rate
$\mathcal{G}_M$	...	energy release rate for pure mode $M$ loading
$\mathcal{G}_{Mc}$	...	critical energy release rate for pure mode $M$ loading
$\mathcal{G}_{sh}$	...	sum of the energy release rates for shear loading
$\mathcal{G}_{th}$	...	fatigue threshold
$\mathcal{G}_{Mth}$	...	fatigue threshold for pure mode $M$ loading
$\Delta\mathcal{G}$	...	energy release rate range
$h$	...	thermal conductance
$h_{cz}$	...	thermal conductance across the cohesive zone
$h_{int}$	...	thermal conductance across the undamaged interface
$h_{cont}$	...	thermal conductance across the damaged interface during contact
$\mathbb{H}$	...	fourth-order tensor characterizing the orthotropic yield condition
$\mathbb{H}_0$	...	$\mathbb{H}$ of the undamaged material
$I$	...	second moment of area
$\mathbf{I}$	...	second-order identity tensor
$\mathbb{I}$	...	fourth-order identity tensor
$J$	...	J-Integral
$J_M$	...	mode $M$ decomposed J-Integral
$k$	...	thermal conductivity
$\tilde{k}$	...	thermal conductivity of the damaged material
$K_1, K_2$	...	damage onset material parameters Darveaux model
$K_3, K_4$	...	damage evolution material parameters Darveaux model
$K_{cont}$	...	penalty contact stiffness
$K_{sc}$	...	initial penalty contact stiffness
$K_{fc}$	...	final penalty contact stiffness
$K_M$	...	stress intensity factor for the crack opening mode $M$
$K_{Mc}$	...	fracture toughness for the crack opening mode $M$
$\mathbf{K}$	...	interface stiffness matrix
$\Delta K$	...	cyclic stress intensity factor
$\ell$	...	characteristic element length
$l$	...	specimen length
$l_{cz}$	...	length of the cohesive zone
$l_e$	...	element length

$m$	...	number of load blocks or Paris law exponent
$m_{\text{I}}, m_{\text{II}}, m_{\text{m}}$	...	pure mode and mixed-mode Paris law exponents
$M$	...	index describing the crack opening mode $M = \{\text{I}, \text{II}, \text{III}\}$
$M_{\text{I}}, M_{\text{II}}$	...	bending moments for pure mode loading
$M_1, M_2$	...	bending moments for mixed-mode loading
$M_{\text{cz}}$	...	fitting coefficient for the cohesive zone length
$\mathbb{M}$	...	fourth-order damage effect tensor
$n_{\text{cz}}$	...	fitting exponent for the cohesive zone length
$n_i$	...	number of cycles in a load block $i$
$N$	...	load cycle number
${}^{\text{S}}N$	...	stabilized load cycle number (CDM)
$N^{\text{S}}$	...	last simulated load cycle number (CCZM)
$N_{\mathcal{D}}$	...	number of cycles for microcrack nucleation
$N_{\text{F}} = N_{\text{N}} + N_{\text{P}}$		total fatigue life (number of cycles to fatigue fracture)
$N_{\text{N}} = N_{\mathcal{D}} + N_{\text{R}}$		number of cycles for fatigue crack initiation
$N_{\text{R}}$	...	number of cycles for microcrack growth causing mesoscopic fracture
$N_{\text{P}}$	...	number of cycles for fatigue crack propagation
$N_{\text{T}}$	...	transition life
$\Delta N$	...	cycle jumps
$\Delta N^{\mathcal{D}}$	...	cycle jumps associated with the damage onset criterion
$\Delta N^{\mathcal{D}}$	...	cycle jumps associated with the damage evolution criterion
$\Delta N_{\text{os}}$	...	cycle jumps overshooting the damage onset criterion
$p$	...	accumulated plastic strain
$P_{\text{I}}, P_{\text{II}}$	...	reaction forces
$\mathcal{P}$	...	fatigue indicator parameter
$q_+$	...	normal component of the thermal flux out of the interface surface $C_+$
$q_-$	...	normal component of the thermal flux out of the interface surface $C_-$
$\mathbf{q}$	...	thermal flux
$\mathbf{Q}$	...	second-order rotation tensor
$R$	...	R-ratio
$R_{\text{v}}$	...	stress triaxiality function
$\mathcal{S}$	...	parameter of the BK-criterion (CCZM)
$[S_{pq}]$	...	elastic compliance matrix
$\mathbb{S}$	...	elastic compliance tensor
$\mathbb{S}_0$	...	elastic compliance tensor of the undamaged material
$t$	...	time or specimen thickness

$T$	...	traction
$\bar{T}$	...	normalized traction
$T^o$	...	damage onset traction, cohesive strength
$T_{sh}^o$	...	shear damage onset traction
$T_i^o$	...	damage onset traction in the coordinate direction $x_i$
$T_M^o$	...	damage onset traction for the pure mode $M$ loading
$\Delta T_j$	...	junction temperature range
$u_i$	...	displacements
$U$	...	strain energy density
$\Delta w$	...	inelastic strain energy density (CDM)
$\Delta w_{mod}$	...	modified damage evolution criterion based on $\Delta w$ (CDM)
$\delta w_{i,i-1}$	...	dissipated strain energy density between two consecutive LCs
$\delta w_{i,i-1}^{th}$	...	threshold value of $\delta w_{i,i-1}$ for the acceptance of a stabilized LC
$\delta W_{i,i-1}$	...	dissipated strain energy between two consecutive LCs
$\delta W_{i,i-1}^{th}$	...	threshold value of $\delta W_{i,i-1}$ for the acceptance of a stabilized LC
$\Delta w$	...	specific work range (CCZM)
$\mathcal{W}_s$	...	dissipated energy rate due to interface opening
$\mathcal{W}_f$	...	dissipated energy rate due fatigue loading
$\mathcal{W}_d$	...	total dissipated energy rate
$x_i$	...	coordinates
$\boldsymbol{x}$	...	location of material point
$\boldsymbol{X}$	...	back-stress tensor

### Symbols of recurring Greek Letters

$\alpha$	...	coefficient in the damage evolution law
$\boldsymbol{\alpha}$	...	kinematic internal hardening variable
$\beta$	...	shape parameter of the cohesive law
$\gamma_a$	...	engineering shear strain amplitude
$\gamma_m$	...	engineering mean shear strain
$\gamma'_f$	...	shear fatigue ductility coefficient
$\gamma_1$	...	plasticity parameter for the Chaboche material model
$\Delta \gamma_{max}$	...	maximum engineering strain amplitude
$\delta_I, \delta_{II}$	...	displacement amplitudes
$\Delta$	...	interface separation



$\bar{\Delta}$	...	normalized interface separation
$\Delta^o$	...	damage onset separation
$\Delta_i$	...	interface separation in the coordinate direction $x_i$
$\Delta_c$	...	decohesion separation
$\Delta_3^{\text{fc}}$	...	interface penetration for the final penalty contact stiffness
$\Delta_t$	...	crack tip opening displacement
$\varepsilon'_f$	...	fatigue ductility coefficient
$[\varepsilon_p]$	...	total strain vector in Voigt notation
$\varepsilon$	...	total strain tensor
$\varepsilon^e$	...	elastic strain tensor
$\varepsilon^p$	...	plastic strain tensor
$\Delta\varepsilon$	...	total strain range
$\Delta\varepsilon^p$	...	plastic strain range
$\Delta\varepsilon_1$	...	maximum normal strain range
$\eta$	...	BK-exponent
$\theta$	...	azimuthal angle
$\vartheta$	...	temperature
$\kappa$	...	material property in the FS criterion
$\varkappa_1, \varkappa_2$	...	modified damage evolution law – material parameters (CDM)
$\lambda$	...	effective separation or plastic multiplier
$\lambda_{\text{tot}}$	...	total effective separation
$\nu, \nu_{ij}$	...	Poisson's ratios
$\tilde{\nu}, \tilde{\nu}_{ij}$	...	Poisson's ratios of the damaged materials
$\boldsymbol{\nu}$	...	unit normal vector
$\xi_i$	...	coordinates
$\boldsymbol{\xi}_i$	...	unit vectors
$\Xi$	...	plane
$\Pi$	...	potential energy
$\sigma_a$	...	stress amplitude
$\sigma_e$	...	fatigue limit or endurance limit
$\sigma_{\text{EQ}}$	...	von Mises equivalent stress
$\sigma'_f$	...	fatigue strength coefficient
$\sigma'_H$	...	hydrostatic stress
$\sigma_m$	...	mean stress
$\sigma_n^{\text{max}}$	...	maximum normal stress acting on the plane of $\Delta\gamma_{\text{max}}$
$\sigma_Y$	...	yield stress

$[\sigma_p]$	...	stress vector in Voigt notation
$\boldsymbol{\sigma}$	...	Cauchy stress tensor
$\tilde{\boldsymbol{\sigma}}$	...	effective stress tensor
$\Delta\sigma$	...	stress range
$\tau_f'$	...	shear fatigue strength coefficient
$\nu$	...	degradation factor for the thermal conductance during contact
$\phi$	...	mix mode ratio
$\varphi$	...	polar angle
$\omega$	...	damage parameter describing the orthotropy during damage evolution
$\Omega$	...	domain

### Symbols for Operation (following [160])

$(\cdot)$	...	scalar product, contraction* $\mathbf{u} \cdot \mathbf{v} = u_i v_i$
$(:)$	...	double contraction $\mathbf{A} : \mathbf{B} = A_{ij} B_{ij}$
$\nabla$	...	gradient of scalar field $\text{grad} f = \nabla f = (\partial f / \partial x_i) \mathbf{e}_i$
$(\dot{\phantom{a}})$	...	time derivative $\dot{a} = \partial a / \partial t$
$\det[A_{pq}]$	...	determinant of matrix
$[A_{pq}]^T$	...	transpose of matrix
$  $	...	absolute value
$[[ ]]$	...	discontinuity
$\langle \phantom{a} \rangle$	...	Macauley bracket

---

\*In the case of scalar product between a tensor and a vector, or between two tensors, the dot  $(\cdot)$  representing the scalar product is usually omitted by convention.

# Chapter 1

## Introduction

### 1.1 Motivation

Power semiconductors have become the leading technology in conversion and control of electric energy. More than 50% of the electric energy utilized worldwide is estimated to be processed by power semiconductor devices [14]. These devices are used in a wide range of commercial and industrial applications. Power semiconductor devices can be found within relatively small devices such as battery chargers for smart phones and home appliances up to large-scale devices such as wind turbines and power converters for energy transmission. This vast amount of energy controlled by power semiconductors has led to a tremendous demand for highly efficient devices. Furthermore, widespread use of highly efficient power semiconductors has been reported to significantly reduce the consumed energy and, consequently, to decrease costs and environmental pollution [31, 32].

Efficiency is not the only important aspect in the development of power semiconductors; their size is also of major importance. One of the design challenges for power semiconductor devices is the reduction of the footprint size while maintaining or even increasing the power density [142]. Development of efficient, space saving power semiconductors results in saving valuable resources by reducing the required material volume and opens up new application opportunities.

The operation of power semiconductors produces dissipation losses, mainly in form of heat energy. Consequently, high temperatures and temperature gradients are introduced into the devices. This can lead to extreme operational conditions which have to be withstood by the utilized materials. To ensure safe and fully functional operation throughout the lifetime of power semiconductors, reliability of the devices is of great concern and needs to be addressed carefully. With regards to industry applications, the required lifetime for power semiconductors is seldom below ten years and reaches demands of up to 30 years or more [142]. Such long lifetime ranges cannot be tested under field conditions, which necessitates accelerated testing procedures. Two of the most common testing procedures are active power cycling and passive temperature cycling tests [80]. Both tests are based on the findings that temperature swings are an essential stress condition for every power electronic device. The two tests can be distinguished from one another based on their respective heating sources. In passive temperature cycling [34] the heating source comes from its environment (passive) and is easier to apply and control. In contrast, in active power cycling the chip is actively heated by the energy dissipated during its operation [96, 115, 214]. Thus, the temperature distribution inside the chip package and temperature cycle times differ between these tests. Since active power cycling reproduces the actual working conditions it is considered to be the more realistic stress test for power semiconductor devices [55]. Therefore, lifetime estimations and reliability testing is usually based on active power cycling.

A schematic representation of a discrete power semiconductor chip–package is presented in Fig. 1.1. The silicon chip is directly soldered to a solid copper lead frame, which serves as a mounting surface. The contact leads are fixed by mold compound and connected by bond wires to the metallization layer on top of the silicon chip. The main failure mechanism reported for such packages are: bond wire fatigue, metallization degradation, solder fatigue, delamination at interfaces, and chip cracking [68]. Regarding the temperature swings during operation, the coefficients of thermal expansion are different for the materials within the multilayer stack of the chip package. These leads to thermally induced cyclic mechanical stresses and, consequently, to thermo–mechanical fatigue of the materials causing any one or combinations of the above–mentioned failure mechanisms. Therefore, the mismatch of the coefficients of thermal expansion of the involved materials has a major impact on

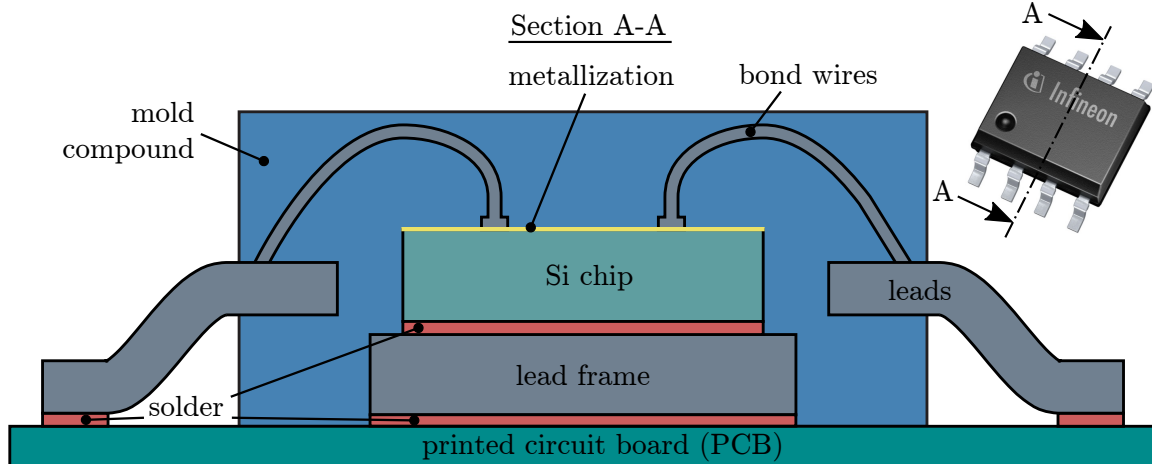


**Figure 1.1:** Schematic representation of a discrete power semiconductor chip package cross section (modified from [123]).

the reliability of the chip package [142]. Chip cracking of the brittle silicon is most often observed directly after mounting or after a few load cycles and is primarily responsible for early field failures [52]. Bond wire and solder joint fatigue have been found to be most often responsible for device failure of insulated-gate bipolar transistors (IGBT) [14]. Thus, there is an emphasis on these two failure mechanisms within the literature [105, 129, 173, 209]. In contrast, the dominant damage mechanism in metal-oxide-semiconductor field-effect transistors (MOSFET) [14] has been found to be the degradation of the power metallization [151]. Active power cycling of such devices reveals a microstructural change and material degradation in the power metallization [29, 150, 203]. Consequently, deterioration of electrical and thermal properties have been measured [163, 204] and shown to have an influence on the device lifetime [50, 69]. Additionally, thermal simulations have shown that small defects in the metallization impede heat transport and may cause local overheating in the active silicon area [164]. Such local hot-spot formation can lead to self-heating of the power semiconductor device resulting in local melt-up and catastrophic device failure [59–61, 184]. Hence, the prediction of material degradation in the power metallization has become of major interest in the reliability and lifetime assessment of power semiconductor devices.

The different mechanisms of material degradation in the metallization of a double-diffused metal-oxide semiconductor field effect transistor (DMOSFET) are shown in Fig. 1.2. The

degradation mechanisms during active power cycling with overload conditions are: fatigue crack growth, void formation, and cyclic interface delamination between the metallization and the silicon chip. Hence, degradation of the metallization is rarely due to one unique failure mechanism, but rather a combination of multiple failure mechanism. The identification and prediction of such microstructure-sensitive failure mechanisms is a complex task [153, 187, 206]. Consequently, simple lifetime models, so-called engineering approaches, are often utilized for reliability and lifetime assessment in industrial applications. These approaches can be classified as either Empirical Lifetime Models (ELMs) or Physical Lifetime Models (PLMs) [49]. ELMs are most often based on Coffin–Manson type criteria correlating device parameters, such as the temperature range [38] or dissipated electric energy [186] of an active power pulse, to an estimated number of load cycles representative of the device lifetime. The device parameters are directly obtained during active cycling tests and the applied lifetime models can be calibrated with the obtained experimental results. A disadvantage of this approach is that the measured quantities are not directly related to the damage driving forces. Therefore, no information is provided about the degradation mechanism inside the chip package. For example, altered loading conditions may trigger a different damage mechanism resulting in a loss of the predictive capability of the calibrated lifetime model [208].

PLMs utilize mechanical quantities describing the damage mechanisms inside the package. Thus, a PLM is based on physical parameters rather than empirical ones and promises to result in better lifetime predictions [114, 230]. For active cycling tests of complex devices, numerical simulations are usually necessary to obtain the required physical parameters. Such simulations present a substantial challenge, but have already been successfully applied to bond wire and solder joint fatigue [48, 67, 219]. In contrast, only little work has yet been done on the simulation of the degradation in the power metallization [66, 124, 125]. Numerical modeling and simulation of the failure mechanism inside a power semiconductor requires a sound understanding of the underlying physical phenomena as characterized in [123] and summarized in the following.

**Multiphysics:** The operation of a power semiconductor device can be characterized as a coupled electro–thermo–mechanical problem which, in turn, can be described by partial differential equations. The Finite Element Method (FEM) [244, 245] provides a standard

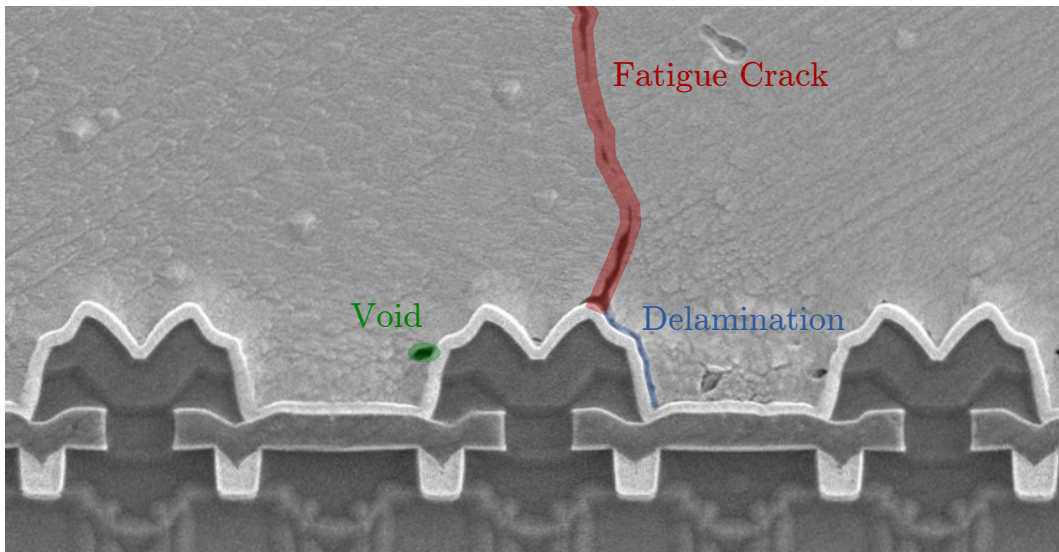


**Figure 1.2:** Scanning electron microscope image showing fatigue damage in the copper metallization of a DMOSFET formed during active power cycling with massive overload pulses. (Courtesy of KAI GmbH, Villach, published in [124, 125])

solution procedure for this kind of problem [113]. However, extensive computations are necessary to simulate the operation of a whole chip package considering the electric, thermal, and mechanical fields including their couplings. For simplification, simulations are usually split up into an electro–thermal and a thermo–mechanical analysis utilizing model reduction techniques.

**High number of load cycles:** The long lifetime and high frequency of repetitively occurring electric pulses during the operation of power semiconductor devices lead to an enormous number of load cycles, ranging from  $10^5$  to  $10^9$  and beyond. Simulations run on a cycle–by–cycle basis are therefore not feasible and cycle–jump or multiscale time domain techniques are necessary to reduce the computation time. In addition, identification and counting of load cycles are non–trivial tasks. Therefore, approaches like the rainflow cycle count method are utilized [81, 103].

**Multiple length scales and complex geometry:** Typical power semiconductor chip packages have function decisive features over multiple length scales. The dimensions of the chip package are usually within the millimeter or centimeter level. Operationally relevant features for the power semiconductors can be sized down to the sub–micrometer level. Con-

sequently, meshes resolving also small design features would be necessary and a complete device model would have dimensions ranging over at least five orders of magnitude. Producing such a high quality finite element mesh is often not feasible and computation time would exceed practical limits with today's hardware technology. Instead, numerical simulations utilize model reduction schemes such as submodelling techniques [123] or non-conforming meshes [70].

**Nonlinear material behavior:** Active power cycling induces extreme temperatures and temperature gradients into the multilayer chip package over short periods of time. Under such loading conditions, temperature and rate dependent material response is expected. Therefore, material models capable of predicting this behavior are required. Evaluation of the corresponding material properties at these high temperatures and high strain rates, especially for specimens with dimensions at the micrometer level, is a complex task and a field of ongoing research, see e.g. [108, 185].

**Microstructural evolution:** Device failure may be caused by local hot-spots occurring due to small, microscopic flaws. The nucleation and formation of microscopic flaws is strongly influenced by the microstructure of the material. The application of continuum mechanics at these length scales reaches its limits and the effect of microstructural evolution on the constitutive behavior may have a non-negligible influence. The nucleation and growth of microscopic fatigue flaws or fatigue cracks is still a topic of ongoing research and advanced methods of Fracture Mechanics or Continuum Damage Mechanics are required for a proper analysis of these phenomena [141].

As stated above, multiple limits are reached when the lifetime of a whole power semiconductor device should be predicted during operation. Simplifications and assumptions are therefore necessary to obtain a computationally feasible model. The difficulty in setting up a suitable model for the reliability assessment of a power semiconductor based on physical quantities is to keep it as simple as possible, but not simpler. In achieving this, such a model would not only be able to predict the device lifetime, but it would also help in the design of new, more reliable products. Problematic locations could be readily detected during the design process and would be eliminated before manufacture of the first prototype.



## 1.2 Background

This work is one in a series of PhD theses focused on numerical simulation of power semiconductor devices related to the automotive industry, carried out in collaboration with the Kompetenzzentrum Automobil- und Industrieelektronik GmbH, Villach (KAI).

Preceding simulation works are the thermo-elastic [121, 122] and the electro-thermal [58] analysis of power electronic devices. Simulations of multiple chip packages, both electro-thermal and thermo-elastic with non-conforming meshes, were conducted in [70].

In terms of numerical simulations related to material degradation, two preceding works have been carried out in this framework. One work has been focused on fatigue damage of solder joints, both experimentally and numerically [180]. The other work [123] has been a numerical study on the degradation of the power metallization and provided the foundation for the present thesis. In this previous thesis, fatigue damage indicators have been employed to predict fatigue crack initiation inside the metallization layer. Locations most prone for the emergence of fatigue cracks have been predicted and the initial crack growth directions have been estimated. A cyclic delamination model based on fitting parameters has been implemented accounting for progressing interface failure caused by thermo-mechanical loading. Both techniques have been applied on a DMOSFET independently. A submodeling technique has been utilized, and the necessary geometric discretization could be reduced to the size of one single DMOS cell.

## 1.3 Scope of the present work

The objective of the present work is to develop modeling strategies by means of advanced methods within the framework of the FEM. The developed models should be capable of predicting fatigue damage inside the metallization and at the interface between the metallization and the silicon chip of a power semiconductor device subjected to massive electric overload pulsing.

In Chapter 2, a literature review is provided. First, phenomenological continuum approaches, Fracture Mechanics concepts, and Continuum Damage Mechanics models are reviewed and a unified notation and nomenclature is introduced. Second, empirical and

physical lifetime models for power semiconductor devices are summarized and their advantages and disadvantages are discussed.

Chapter 3 focuses on fatigue damage modeling in the bulk material. A modeling strategy is developed which predicts fatigue damage initiation and propagation in the metallization layer. Damage nucleation is addressed by critical plane methods considering multi-axial, non-proportional loading. Total-life approaches are utilized to define a damage onset criterion. Subsequent damage evolution is modeled by a Continuum Damage Mechanics approach. The modeling strategy is applied on micrometer-sized cantilever beam tests undergoing Low Cycle Fatigue.

Chapter 4 presents the development of a cyclic cohesive zone model based on physically interpretable interface parameters. The developed model circumvents the need for parameter fitting and is capable of predicting cyclic delamination under structural thermo-mechanical, mixed-mode loading conditions. The proposed model is validated against experimental data from delamination tests conducted under constant and variable amplitude loading.

In Chapter 5, a submodel of a generic DMOSFET is utilized to demonstrate the developed fatigue damage modeling strategies. First, the two developed damage models are applied separately and the resulting damage behavior is discussed. Second, a combined modeling approach of both damage mechanisms, bulk fatigue and interface delamination, is presented, and the differences in the damage characteristics between the combined and the independent simulations are discussed.

Finally, Chapter 6 summarizes the proposed simulation methodologies and discusses their possibilities for future applications in the robustness validation of power semiconductor devices.

## Chapter 2

# Literature Review

### 2.1 Fatigue, Fracture, and Damage Mechanics

#### 2.1.1 General

Fatigue describes the changes in properties of metallic or nonmetallic materials caused by repetitive application of stresses or strains leading to damage and failure of the material.

Fatigue failures occur in many different forms [220]:

- mechanical fatigue: caused by the application of cyclic stresses or strains.
- creep fatigue: a result of cyclic loads at elevated temperatures.
- thermo-mechanical fatigue: occurs when thermal loads are applied in a repetitive way in addition to the fluctuations in mechanical loads.
- corrosion fatigue: observed when cyclic stresses or strains are applied in chemically aggressive or embrittling environments.
- contact fatigue: summarizes rolling, sliding, and fretting fatigue which occurs due to pulsating (frictional) contact between surfaces.

The above listed failure mechanisms usually take place under the influence of cyclic loads whose peak values are considerably smaller than the 'safe loads' predicted by the theory of strength.

The progression of fatigue damage in an engineering component can be broadly summarized into the following stages [220]:

- sub- and microstructural changes which cause nucleation of permanent damage.
- creation of microscopic flaws (microcracks).
- growth and coalescence of microcracks to form 'dominant' macrocracks.
- stable propagation of the dominant macrocrack.
- structural instability or complete failure.

These five stages are commonly condensed into a *fatigue crack initiation* and a *fatigue crack propagation* stage. The development of fatigue life prediction models is strongly dependent on the definition of these two stages. Dependent on the length scale of interest, material scientists may define the formation of microscopic flaws along slip bands, grain boundaries, or the roughening of fatigued surfaces as fatigue crack initiation. In contrast, practicing engineers may take the resolution of their crack detecting equipment as the size definition for an initial macrocrack susceptible to fatigue crack propagation. A clear demarcation between these two stages is therefore difficult to define and mostly dependent on the user's field of interest [220]. From a practical point of view, fatigue crack initiation can be defined as the nucleation of permanent damage, the formation, growth and coalescence of microscopic flaws resulting in mesoscopic fracture, and the formation of an initial macrocrack. This initial macrocrack defines the start of fatigue crack propagation. Any further fatigue crack growth may result in structural instability or complete fracture. Note that fatigue crack initiation differs from *crack initiation* in Fracture Mechanics, which will be discussed in Section 2.1.4.

### 2.1.2 Material response

The assessment of mechanical fatigue requires the careful examination of the cyclic stress and strain state inside the material. Ductile materials show different types of responses caused by cyclic loads. The possible responses for a ductile material under stress controlled loading are depicted in Fig. 2.1. The simplest one is a linear elastic behavior (a) obtained for stress amplitudes below the yield stress.

Increases in the stress amplitude lead to an elasto–plastic material response. Residual stresses or cyclic hardening can lead to elastic shakedown (b), which describes the vanishing of an initial elasto–plastic material response into a linear–elastic one.

A further increase in the stress amplitude may result in plastic shakedown, which is also known as reversed plasticity (c). Such a behavior is characterized by steady plastic strain amplitudes from cycle to cycle with no net accumulation of the plastic strain mean value. A stabilized cycle is characterized by a constant plastic energy dissipation in consecutive load cycles.

In contrast, ratcheting, also known as cyclic creep, is classified by a net accumulation of directional plastic strain (d). No stabilized cycle is reached and the accumulated plastic strain increases from cycle to cycle. Ratcheting accelerates the accumulation of damage caused by an increase of the cyclic plastic strain in each cycle as a result of cyclic softening and the raise of the mean strain. The treatment of this mechanism in fatigue analysis is still part of ongoing discussions. In traditional fatigue approaches no distinction is made between reversed cyclic plasticity and cyclic creep. In contrast, different studies have treated the ratcheting effect explicitly within the fatigue model. Such models are most often applied in sliding and rolling contact fatigue problems [116, 117, 198]. However, in [140] it has been stated that a separate consideration of the ratcheting effect will be redundant for fatigue loading with constant stress amplitudes and mean stresses since the mean stress consideration covers the ratcheting effect in a well–posed fatigue model. But problems may arise when the loading history is not uniform and the development of ratcheting strain is affected by the prior loading history. The counterpart of cyclic creep in stress–controlled loading is mean stress relaxation in strain–controlled loading. Here the mechanism results in a progressive reduction of the mean stress and is therefore negligible in terms of damage acceleration.

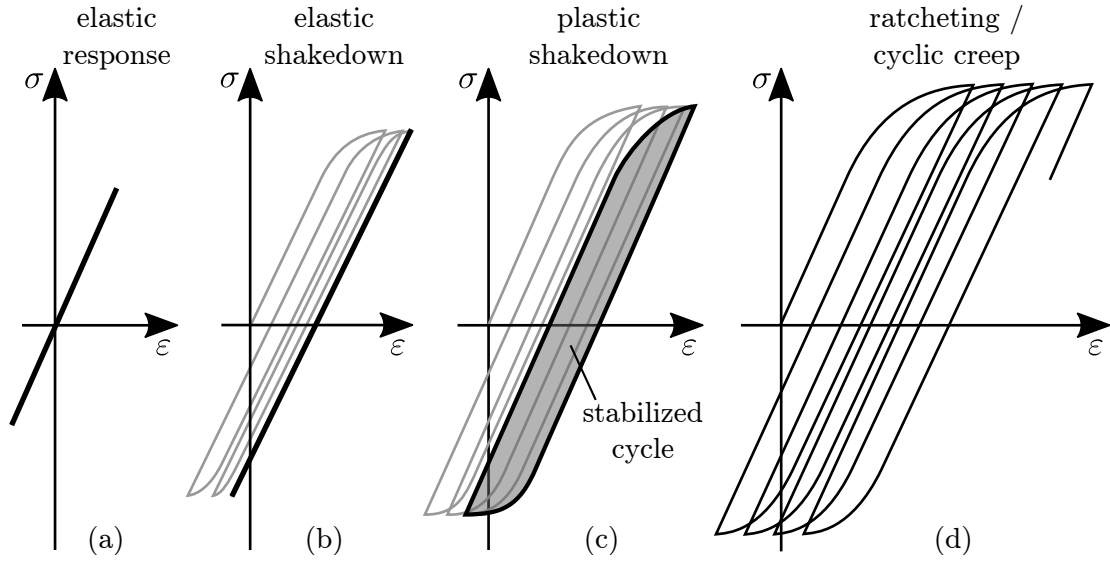


**Figure 2.1:** Summary of different types of mechanical stress–strain responses for ductile materials under cyclic loading.

### 2.1.3 Phenomenological Continuum Approaches

Classical approaches to fatigue design involve the characterization of the total fatigue life to failure in terms of the cyclic stress range (stress–life curve, S–N) or the cyclic (plastic or total) strain range (strain–life curves,  $\varepsilon$ –N) under uniaxial loads. The total fatigue life,

$$N_F = N_N + N_P \quad , \quad (2.1)$$

is the sum of the number of cycles required to induce fatigue damage into a nominally 'defect-free' material initiating a dominant fatigue flaw,  $N_N$ , and the number of cycles required to propagate this initial crack to final failure,  $N_P$ . Since fatigue crack initiation represents a major part of the total fatigue life in smooth specimens, the classical stress–based and strain–based methods represent, in many cases, design against fatigue crack initiation [220]. This assumption,  $N_F \approx N_N$ , may result in good lifetime predictions under High Cycle Fatigue (HCF) conditions, but has to be treated carefully under Low Cycle Fatigue (LCF) conditions where the fatigue crack propagation stage contributes significantly to the total fatigue life.

### Stress–Life Approach

The stress–life approach is employed in fatigue situations where the material deformation is primarily elastic. Usually, high numbers of load cycles can be withstood under such conditions and stress ranges are utilized to describe the fatigue life associated with HCF. S–N curves can be obtained from a multitude of mechanical test methods, e.g. rotating bending tests conducted on polished specimens. The total fatigue life obtained from these tests signifies the number of cycles to initiate fatigue cracks in the specimen and, additionally, the number of cycles to propagate the dominant fatigue crack to final failure as depicted in Fig. 2.2. The S–N curve for final failure is commonly described by the Basquin equation [18],

$$\frac{\Delta\sigma}{2} = \sigma'_f (2N_F)^b \quad , \quad (2.2)$$

relating the stress amplitude,  $\sigma_a = \Delta\sigma/2$ , to the stress range,  $\Delta\sigma$ , in a constant–amplitude fatigue test to the number of load reversals to failure,  $2N_F$ .  $\sigma'_f$  is the fatigue strength coefficient and  $b$  is the fatigue strength exponent. The Basquin equation does not consider any mean stress effects. Therefore, modifications of this relation have been proposed considering the influence of a mean stress,  $\sigma_m$ , e.g., [159]

$$\frac{\Delta\sigma}{2} = (\sigma'_f - \sigma_m) (2N_F)^b \quad . \quad (2.3)$$

Certain types of materials, such as mild steels or other materials which harden by strain–aging, under constant amplitude loading, exhibit a fatigue limit or endurance limit,  $\sigma_e$  (or  $\Delta\sigma_e$ ) [220]. Below this stress range the specimen may be cycled indefinitely without causing failure. Many high strength steels, aluminum alloys, or other materials which do not strain–age–harden do not, generally, show such a limit. Sometimes an endurance limit is still defined, for these materials, by the stress range safely supported by the specimen for at least  $10^7$  load cycles [220].

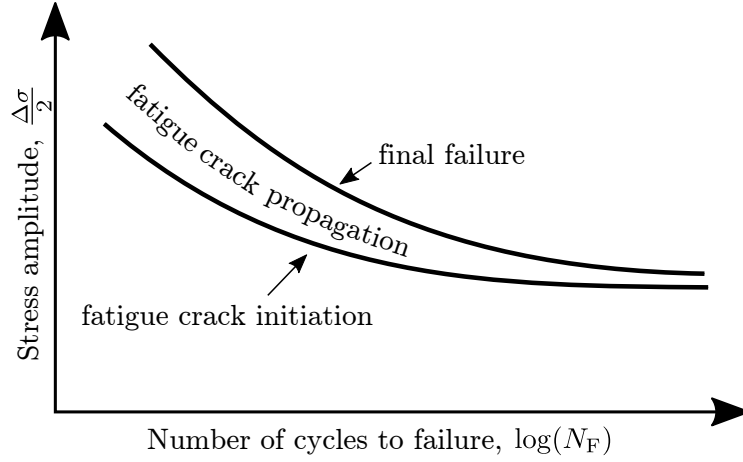


**Figure 2.2:** S–N curves indicating the fatigue crack initiation and fatigue crack propagation stages of the total fatigue life in a smooth specimen (modified from [220]).

### Strain–Life Approach

The strain–life approach is utilized when considerable plastic deformation occurs during cyclic loading. The fatigue life is therefore markedly shortened and strain based approaches are associated with LCF. Herein, the well–known Coffin–Manson relation [53, 145],

$$\frac{\Delta\varepsilon^P}{2} = \varepsilon'_f (2N_F)^c \quad , \quad (2.4)$$

correlates the plastic strain range,  $\Delta\varepsilon^P$ , to the number of load reversals to failure,  $2N_F$ .  $\varepsilon'_f$  is the fatigue ductility coefficient and  $c$  is the fatigue ductility exponent. This plastic strain–life approach can be easily combined with the stress–life approach and provides a convenient engineering expression for the characterization of the whole fatigue life,

$$\frac{\Delta\varepsilon}{2} = \frac{\sigma'_f}{E} (2N_F)^b + \varepsilon'_f (2N_F)^c \quad , \quad (2.5)$$

where  $E$  is the Young’s modulus. The total strain–life approach is depicted in Fig. 2.3 indicating the transition life,  $N_T$ , at which elastic and plastic strain amplitudes are equal. Below the transition life the fatigue life of the material is dominated by ductility (LCF), whereas above the transition life the fatigue life is dictated by the material strength (HCF).



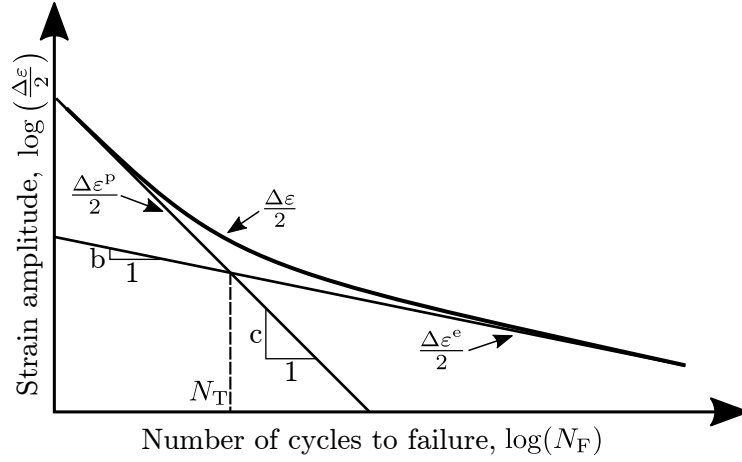


**Figure 2.3:** Relationship between the total strain amplitude and the number of cycles to fatigue failure, obtained from superposition of the Basquin and Coffin–Manson relations.

### Damage accumulation

Cumulative damage rules are necessary to evaluate the lifetime of a structure under service loading. In contrast to the constant amplitude loading scenarios for the determination of material fatigue properties, structures are subjected to varying cyclic load amplitudes. One of the simplest and most often used criteria to describe fatigue damage caused by different blocks of constant amplitude loading is the Palmgren–Miner linear damage accumulation rule [156, 175],

$$\mathcal{D} = \sum_{i=1}^m \frac{n_i}{N_{F_i}} \quad , \quad (2.6)$$

where  $n_i$  is the number of cycles in a load block  $i$  of constant stress amplitudes.  $m$  is the sequence of load blocks and  $N_{F_i}$  describes the number of cycles to failure for the different load blocks with different stress amplitudes and mean stresses obtained from the Basquin equation. The simplicity of this rule and the requirement of no further parameters, in particular, has led to widespread use in industrial applications. However, numerous studies have shown that the Palmgren–Miner rule can be highly inaccurate and may result in non-conservative lifetime predictions [190].

Therefore, modifications and extensions of the Palmgren–Miner rule have been presented and more complex damage accumulation rules have been developed. Comprehensive reviews can be found in [42, 74]. One possible extension are the so-called double linear damage

rules. They were first proposed in [86] where the damage process has been separated into two stages. This approach can be formulated as [146]

$$N_N = \alpha N_F \quad (\text{fatigue crack initiation}), \quad (2.7)$$

$$N_P = (1 - \alpha) N_F \quad (\text{fatigue crack propagation}). \quad (2.8)$$

In these formulae the coefficient  $\alpha = \langle 1 - PN_F^{-0.4} \rangle$ , where  $P$  is a material parameter describing the fatigue crack propagation stage. The Macaulay brackets, defined as

$$\langle x \rangle = \begin{cases} 0, & x < 0 \\ x, & x \geq 0 \end{cases}, \quad (2.9)$$

avoid a negative value of alpha. Fig. 2.4 illustrates the double linear damage rule plotted in terms of the remaining load cycle ratio,  $n_2/N_{F_2}$  at a second stress level,  $\sigma_{a_2}$  against the cycle ratio,  $n_1/N_{F_1}$ , applied at an initial stress level,  $\sigma_{a_1}$ . If the cycle ratio applied,  $n_1/N_{F_1}$ , is less than required to initiate a fatigue crack at this load level, then the remaining cyclic life ratio  $n_2/N_{F_2}$  is along AB. Point B corresponds to the special case, where fatigue crack initiation occurs only with  $n_1 = N_{N_1}$ , which is then followed in the propagation phase by  $n_2 = N_{P_2}$ . Beyond  $N_{N_1}/N_{F_1}$  the applied load cycle ratio, is more than required to initiate a fatigue crack and the fatigue crack propagation stage is entered. This phase is represented by the line BC. The remaining cyclic life ratio is then defined by line BC. The lines AB and BC are linear which represents the assumed linear damage accumulation in the two stages [147].

### **Multiaxial fatigue models**

Components and structures in many practical applications undergo complex multiaxial loading conditions leading to complex local stress–strain histories. In practice sometimes one stress or strain component may be dominant and a uniaxial lifetime model may be sufficient [189]. In applications where this is not the case, multiaxial fatigue models are necessary to assess the lifetime. Such models can be categorized into stress, strain, and energy based criteria. Additionally, criteria based on the critical plane methods have been

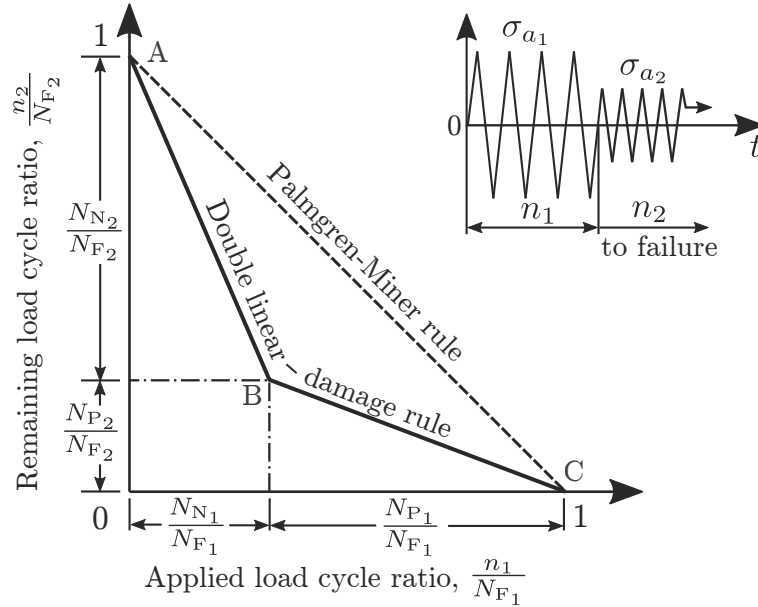


**Figure 2.4:** Fatigue damage predicted by a double linear damage accumulation rule. The damage accumulation of a two-stress-level fatigue test is illustrated (modified from [147]).

shown to provide reasonable predictions of the fatigue life and fracture plane orientations. A comprehensive review of more than thirty multiaxial failure criteria is provided in [118].

Two of the most commonly used multiaxial fatigue models based on the critical plane method are the Fatemi–Socie (FS) [73] and the Smith–Watson–Topper (SWT) [215] parameters. The first is utilized for the prediction of fatigue damage in ductile materials that predominantly fail by the nucleation and growth of shear microcracks, as depicted in Fig. 2.5(a). The latter is suitable for high-strength materials where failure is governed by the nucleation and growth of tensile cracks, indicated in Fig. 2.5(b). Multi-axial fatigue criteria can be utilized to determine not only the total fatigue life characterized by  $N_F$  but also the part of the fatigue life contributing to fatigue crack initiation. Different definitions for fatigue crack initiation, characterized by  $N_N$ , are utilized, e.g. the first observation of a surface crack of a certain length [217] or the definition of a certain load drop occurring during cycling [73]. Hence, different test procedures are often not easily comparable.

Under proportional loading, where the axis of the principal stresses and strains do not rotate during a load cycle, the orientation of the critical plane can easily be identified and

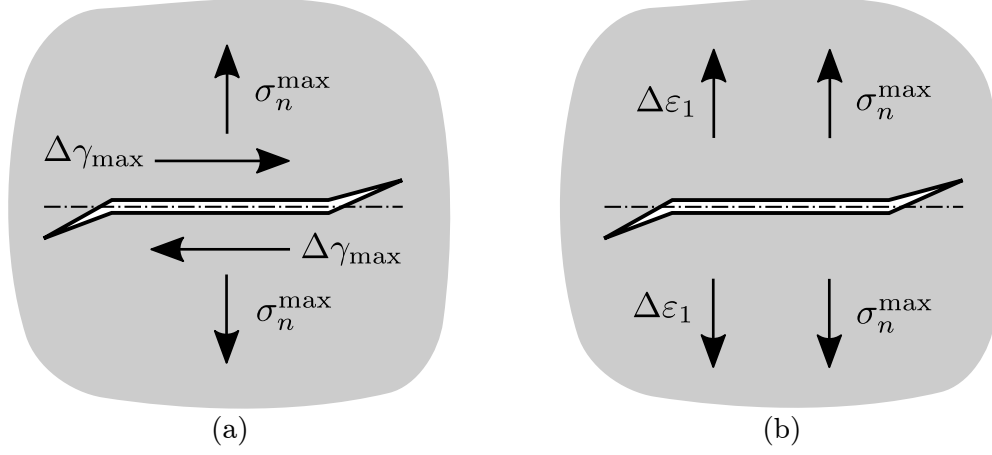


**Figure 2.5:** Fatigue crack initiation caused by the normal stress,  $\sigma_n^{\max}$ , and (a) the cyclic shear strains ( $\Delta\gamma_{\max}$ ), predicted by the FS-criterion, and (b) the cyclic tensile strains ( $\Delta\varepsilon_1$ ), predicted by the SWT-criterion.

is defined by either the maximum shear or maximum principal strain amplitude. The FS damage model is given as [216]

$$\frac{\Delta\gamma_{\max}}{2} \left( 1 + \kappa \frac{\sigma_n^{\max}}{\sigma_Y} \right) = \frac{\tau_f'}{G} (2N_N)^{b_\gamma} + \gamma_f' (2N_N)^{c_\gamma} \quad , \quad (2.10)$$

where  $\Delta\gamma_{\max}/2$  is the maximum shear strain amplitude and  $\sigma_n^{\max}$  is the maximum normal stress acting on the plane of  $\Delta\gamma_{\max}/2$ . The material properties on the left-hand side of the equation are the yield stress,  $\sigma_Y$ , and the material property,  $\kappa$ , describing the sensitivity of crack formation to the normal stress. On the right-hand side,  $G$  is the shear modulus. The fatigue life properties are summarized in Table 2.1. The SWT damage model considers the plane with the maximum normal strain amplitude,  $\Delta\varepsilon_1/2$ , as the most critical one and is given as [216]

$$\sigma_n^{\max} \frac{\Delta\varepsilon_1}{2} = \frac{(\sigma_f')^2}{E} (2N_N)^{2b} + \sigma_f' \varepsilon_f' (2N_N)^{b+c} \quad , \quad (2.11)$$

where  $E$  is the Young's modulus. The right-hand side fatigue properties are stated in Table 2.1.

Under non-proportional loading the axis of the principal stresses and strains may rotate during a load cycle. Hence, the orientation of the critical plane is also varying with time and loading path. Identification of the critical plane is therefore more complicated and various approaches have been suggested. Following [15], the critical plane is defined as the

**Table 2.1:** Material fatigue parameters obtained from fatigue tests [216].

	Axial	Shear
Fatigue strength coefficient	$\sigma'_f$	$\tau'_f \approx \sigma'_f / \sqrt{3}$
Fatigue strength exponent	$b$	$b_\gamma \approx b$
Fatigue ductility coefficient	$\varepsilon'_f$	$\gamma'_f \approx \sqrt{3}\varepsilon'_f$
Fatigue ductility exponent	$c$	$c_\gamma \approx c$

plane experiencing the maximum value of the damage parameter during a load cycle. This way, the FS model reads

$$\left\{ \frac{\Delta\gamma}{2} \left( 1 + \kappa \frac{\sigma_n^{\max}}{\sigma_Y} \right) \right\}_{\max} = \frac{\tau'_f}{G} (2N_N)^{b_\gamma} + \gamma'_f (2N_N)^{c_\gamma} \quad (2.12)$$

and the SWT parameter follows as

$$\left\{ \sigma_n^{\max} \frac{\Delta\varepsilon}{2} \right\}_{\max} = \frac{(\sigma'_f)^2}{E} (2N_N)^{2b} + \sigma'_f \varepsilon'_f (2N_N)^{b+c} \quad (2.13)$$

A detailed review and discussion on the predicted critical planes of these two models is provided in [123].

#### 2.1.4 Fracture Mechanics

In contrast to the classical approaches to fatigue design, in Fracture Mechanics [85, 126, 127] every engineering component and every real material is assumed to be inherently flawed, i.e. initial cracks, pores, inhomogeneities, delaminations, or similar are present. This principal is based on the consideration that the size of a preexisting flaw is generally determined from nondestructive detection techniques, which have physical resolution limits. Hence, a material cannot be assumed to be flawless when small defects below the resolution limit are not detectable [127]. Consequently, in Fracture Mechanics, the existence of defects is explicitly assumed and modeled as a crack of a certain size. The exploitable fatigue life is then defined as the number of load cycles to propagate this (existing or assumed) initial crack to some critical length.

The prediction of the fatigue crack propagation involves empirical fatigue crack growth laws [220]. These laws utilize Fracture Mechanics parameters originally developed for quasi-static crack growth in linear-elastic or elasto-plastic materials. Hence, a short review on these methods is provided before fatigue crack propagation is covered.

### **Linear-Elastic Fracture Mechanics**

From a macroscopic point of view, Fracture Mechanics describes the behavior of cracks in bodies in terms of continuum mechanics. In the initial state a crack has a specific size and shape. As long as the crack does not change, it is regarded as a static or stationary crack. The moment at which crack propagation starts, caused by critical loading, is called crack initiation. The crack size then increases and the crack enters an unsteady state. The following crack propagation can be either unstable if the crack keeps growing without any further increase of the external loading or stable, if an additional increase in the external loading is necessary for further crack growth. Linear-Elastic Fracture Mechanics (LEFM) analyzes crack problems in linear-elastic bodies, whose deformation behavior follows the generalized Hooke's law. Except for very brittle materials, physical or geometrical nonlinearities occur in almost all structures, particularly at notches or crack tips. The region around the crack tip is the so-called fracture process zone (FPZ). The complex microscopic fracture process inside the FPZ cannot be described by classical continuum mechanics. Hence, in LEFM the nonlinear effects occurring inside this FPZ have to be small and negligible from a macroscopic point of view. Such a small, localized FPZ around the crack tip is found especially in brittle materials, which provide the typical application field for LEFM [85, 127].

The fracture process in LEFM is either described by stress based or energy based approaches. In isotropic linear-elastic materials the asymptotic near field solution around the crack tip is always of the same mathematical form. The severity of this crack tip field is entirely determined by the stress intensity factors (SIF),  $K_M$ , where the index  $M = \{I, II, III\}$  denotes the crack opening mode. The magnitudes of these three SIFs are determined by the solution of the boundary value problem given by a body containing a sharp crack. The SIFs are dependent on the geometry of the body, the size and position of the crack, as well as the loading and boundary conditions. Furthermore, the SIFs characterize the loading

state' in a finite region around the crack tip [127]. Therefore, the SIFs provide an excellent basis for the formulation of fracture criteria,

$$K_I = K_{Ic} \quad , \quad K_{II} = K_{IIc} \quad , \quad \text{and} \quad K_{III} = K_{IIIc} \quad , \quad (2.14)$$

where  $K_{Mc}$  are the fracture toughness values representing the material resistance against crack initiation for the different opening modes.

Another possibility for the formulation of a fracture initiation criterion is the consideration of the energy balance of a body during crack propagation. This approach results in the definition of the energy release rate,

$$\mathcal{G} = -\frac{d\Pi}{dA} \quad , \quad (2.15)$$

where  $-d\Pi$  describes the available amount of potential energy supplied by external loads and the elastically stored strain energy for crack propagation corresponding to the increase of the area  $dA$ . The minus sign indicates the decrease of the potential energy and, therefore, the energy dissipation during crack propagation. Based on this consideration the energetic fracture criterion,

$$\mathcal{G} = \mathcal{G}_c \quad , \quad (2.16)$$

states that a certain fracture energy,  $\mathcal{G}_c$ , the critical energy release rate (a material property), is required to obtain material separation and formation of new crack surfaces. In the theory of linear elasticity the stress intensity factor concept by Irwin and the energy criterion by Griffith are equivalent and can be converted into each other. In the case of isotropic materials, the relation follows as [127]

$$\mathcal{G} = \mathcal{G}_I + \mathcal{G}_{II} + \mathcal{G}_{III} = \frac{1}{E'} (K_I^2 + K_{II}^2) + \frac{1+\nu}{E} K_{III}^2 \quad . \quad (2.17)$$

Herein,  $E' = E$  for plane stress, or  $E' = E/(1-\nu^2)$  for plane strain, where  $E$  is the Young's modulus and  $\nu$  the Poisson's ratio.

The J-Integral is an additional parameter based on energy considerations. In LEFM the J-Integral [193] is equivalent to the energy release rate,  $J = \mathcal{G}$ , but has outstanding importance in the analysis of fracture mechanics problems with elasto-plastic material behavior.

Consider a homogeneous, elastic (either linear or nonlinear) body containing a crack with the strain energy density  $U$ , zero body forces and, for simplicity, infinitesimal strains. Then the J-Integral is obtained as [127]

$$J = \int_C \left( U dx_3 - T_i \frac{\partial u_i}{\partial x_1} ds \right) , \quad (2.18)$$

where  $C$  defines the contour of an arbitrary chosen domain,  $\Omega$ , with the outward normal vector,  $\mathbf{n}$ , surrounding the crack tip as depicted in Fig. 2.6.  $T_i = \sigma_{ij}n_j$  are the tractions acting on  $C$  and  $\partial u_i/\partial x_1$  denotes the derivatives of the displacement field,  $u_i$ , with respect to the coordinate  $x_1$ .

The mode decomposed J-Integrals for the crack opening modes  $M$  are defined as [197]

$$J_M = \lim_{\rho \rightarrow 0} \int_C \left( U^M dx_3 - \sigma_{ij}^M n_j \frac{\partial u_i^M}{\partial x_1} ds \right) , \quad (2.19)$$

where  $C$  is a contour of vanishing radius  $\rho$ .  $\sigma_{ij}^M$  and  $u_i^M$  are the decomposed stresses and displacements, respectively, of mode  $M$ . The strain energy is given as  $U^M = \int_0^\varepsilon \sigma_{ij}^M d(\varepsilon_{ij}^M)$ . The mode decoupled stresses and strains can be found in [197]. The mode decomposition of the J-Integral can be useful for the analysis of interface cracks where the crack path

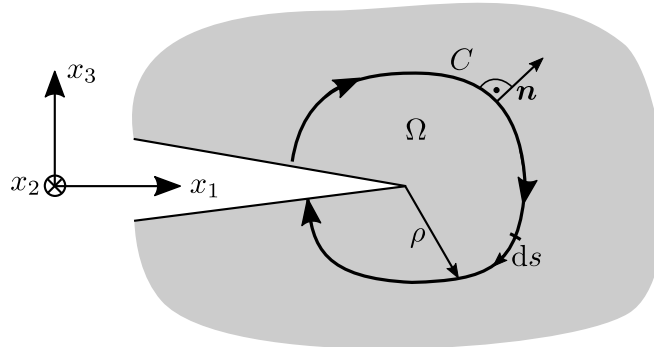


**Figure 2.6:** Crack coordinate system,  $x_1$ - $x_2$ - $x_3$ , and contour,  $C$ , for the J-Integral evaluation.



is *a priori* known. The analysis of general three-dimensional (3D) crack configurations undergoing mixed-mode loading is still a topic of ongoing research and not covered in this review, for details see [157, 212].

For elastic bodies, the J-Integral is path-independent for stress-free and straight crack faces. If the crack surfaces are loaded or curved,  $J$  is, in general, path-dependent. Under such circumstances, a 'path-independent' characterization of  $J$  is still possible if a contour of vanishing radius,  $\rho$ , is chosen.

### **Elasto-Plastic Fracture Mechanics**

The loading of components made up of an elasto-plastic material containing a crack introduces stress concentrations at the crack tip. Consequently, yielding and plastic deformation occur. An increase in the loading leads to an expansion of the plastic zone and violates the LEFM assumption of a small and negligible area of nonlinear effects. The previously mentioned concepts are therefore not applicable and different parameters are necessary to characterize the crack tip state in Elasto-Plastic Fracture Mechanics (EPFM). The most often used parameters are the J-Integral and the crack tip opening displacement (CTOD) [85].

In EPFM the magnitude of  $J$  identifies the intensity of the crack tip field in a hardening elastic-plastic material within the plastic zone around the crack tip. All stresses, strains and displacements are specified by the Hutchinson, Rice, and Rosengren solution (HRR) [106, 107, 194] and are proportional to  $J$ . Consequently, the J-Integral in the context of EPFM is comparable to the stress intensity factors utilized in LEFM.

The J-Integral concept in EPFM is based on the deformation theory of plasticity. The plastic deformation theory is incapable of capturing phenomena such as large strains, local unloading, or physical cracking mechanisms. Any redistribution of the stress state or simply unloading leads to a loss of the path independence and uniqueness of  $J$ . Therefore, the application of  $J$  in EPFM has to be restricted to stationary cracks under monotonically increasing, proportional loading [127].

In contrast, the CTOD,  $\Delta_t$ , is a measure of the displacement state of the crack tip and is motivated by experimental observations [36, 233]. In ductile materials the crack tip undergoes plastic deformations during loading, resulting in wide stretching and blunting of

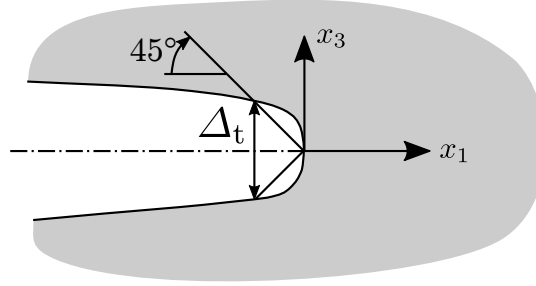


**Figure 2.7:** Definition of the crack tip opening displacement,  $\Delta_t$ .

the originally sharp crack tip as depicted in Fig. 2.7. Based on  $\Delta_t$  an elasto–plastic fracture criterion can be defined as

$$\Delta_t = \Delta_c \quad , \quad (2.20)$$

where  $\Delta_c$  describes the material specific limit against crack initiation.

Considerations in EPFM are often limited to simple rate–independent material models based on the deformation theory of plasticity. Even in these limited cases, analytic solutions are only found for certain specific configurations. Therefore, either numerical simulation tools, such as the FEM, or simplified modeling strategies are commonly used to describe crack initiation and growth in elasto–plastic materials. One of the simplest models is the Dugdale model [64], which is based on the observation of a strip–like plastic zone in front of the crack tip under Mode I loading, as depicted in Fig. 2.8. Herein, the plastic zone is modeled by a fictitious crack of length  $d$  whose crack surfaces are subjected to the yield stress,  $\sigma_Y$ . Thus, the elasto–plastic model is reduced to a purely elastic one. The opening of the fictitious crack at the end of the plastic zone is equal to  $\Delta_t$ , enabling the application of the fracture criterion defined in Eq. (2.20).

Advanced versions of the Dugdale model are provided by Cohesive Zone Models (CZM), capable of modeling fracture in a variety of materials. This concept has been first introduced in [16], where the material failure process during fracture is assumed to take place in a limited region in front of the crack tip, the so–called cohesive zone. Damage primarily occurs inside the cohesive zone and the rest of the body obeys the common constitutive law. The complex damage process inside the cohesive zone is substituted by a CZM of vanishing thickness, which describes the interaction of the crack surfaces by a traction–separation

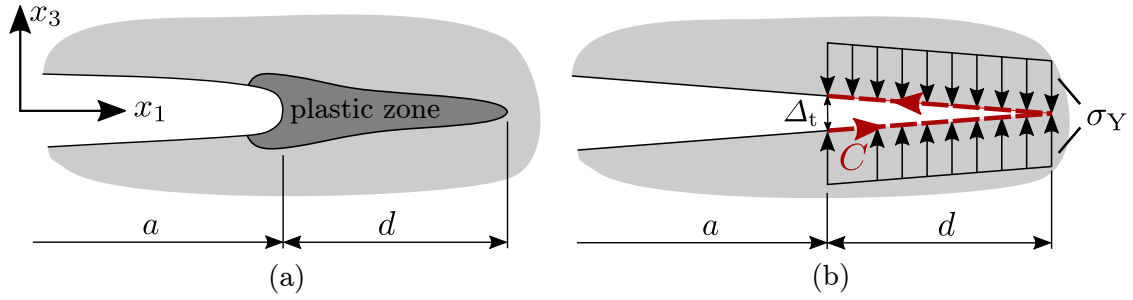


**Figure 2.8:** Dugdale model for a strip-like plastic zone. (a) physical plastic zone in front of crack tip, (b) modeling approach employing a fictitious crack of length  $d$  subjected to the yield stress,  $\sigma_Y$ .

law. A schematic representation of the cohesive zone in front of the crack tip is depicted in Fig. 2.9(a). A traction–separation law  $T(\Delta)$ , where  $T$  denotes the traction and  $\Delta$  the separation, is sketched in Fig. 2.9(b). The law describes the local constitutive behavior. The cohesive strength of the material is given by  $T^\circ$ , and complete material separation is indicated by the critical decohesion,  $\Delta_c$ . Integration of the traction–separation law leads, by definition, to the critical energy release rate,

$$\mathcal{G}_c = \int_0^{\Delta_c} T(\Delta) \, d\Delta \quad . \quad (2.21)$$

Crack initiation and growth is obtained when the provided energy release rate of the system,  $\mathcal{G}$ , equals the critical energy release rate,  $\mathcal{G}_c$ , of the material, Eq. (2.16). The energy release

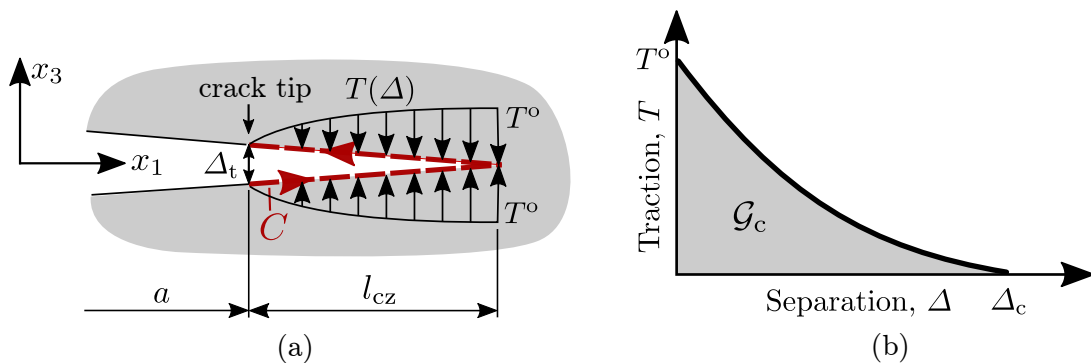


**Figure 2.9:** Cohesive Zone modeling approach. (a) cohesive zone in front of the crack tip, subjected to the cohesive traction  $T(\Delta)$ , (b) physical traction–separation law.

rate can be obtained by calculating the J-Integral directly along the boundary of the cohesive zone. The integration path,  $C$ , along the boundary of the cohesive zone is depicted in Fig. 2.9(a). The choice of the integration path leads to a vanishing of the first term in Eq. (2.18),  $\int U dx_3 = 0$ . Additionally, only pure Mode I loading is assumed in the following consideration. Hence, no shear deformation occurs and only the cohesive traction normal to the crack plane,  $T_3 = T(\Delta)$ , must be considered. The opening displacement of the upper,  $u_3^+$ , and lower,  $u_3^-$ , crack faces can be substituted by the separation,  $\Delta = u_3^+ - u_3^-$ , where  $u_3^+ = -u_3^-$ . This way, the J-Integral is obtained as [193]

$$J = \int_C \left( -T_3 \frac{\partial u_3}{\partial x_1} \right) ds = - \int_0^{l_{cz}} T(\Delta) \frac{d\Delta}{dx_1} dx_1 = \int_0^{\Delta_t} T(\Delta) d\Delta \quad , \quad (2.22)$$

where  $l_{cz}$  defines the length of the cohesive zone. For steady-state crack growth with a fully developed cohesive zone, the crack tip separation equals the decohesion separation. Hence, for crack extension  $\Delta_t = \Delta_c$  in Eq. (2.22) and in accordance with Eq. (2.21) the J-integral equals the critical energy release rate,  $J = \mathcal{G}_c$ . This equivalence holds true as long as the assumptions for LEFM are fulfilled. In EPFM, the critical separation energy can be approximated by the physical initiation value, i.e.  $\mathcal{G}_c \approx J_i$ , provided that the J-integral is sufficiently path independent [127].

CZMs can be easily implemented into the Finite Element Method. In the pioneering work described in [99] the CZM has been implemented directly through corresponding forces at the relevant nodes for crack propagation. A more commonly used approach is based on special-purpose interface elements which follow the required traction-separation law but do not have any other constitutive properties. These elements are meshed between the boundaries of continuum elements, which means that the crack path has to be *a priori* known. Hence, CZMs are often used to describe interface cracks in bi-material compounds or delaminations in laminated composites where the crack paths are constrained to occur between the individual plies [88].

### Fatigue Crack Growth

Cracks experiencing cyclic loading may propagate although the fracture parameter characterizing crack initiation is far below the static fracture toughness. This phenomenon of sub-critical cyclic crack growth is called fatigue crack growth. During fatigue nucleation small cracks may be formed which are strongly influenced by the surrounding microstructure and advanced methods in terms of Fracture Mechanics are necessary to assess them [141, 239]. Application of the previously listed Fracture Mechanics methods requires an initial macroscopic crack with a length of approximately 10 times the grain diameter [127]. Only then, the assumptions of the classical Fracture Mechanics theory will be valid.

In Fracture Mechanics, fatigue crack growth is characterized by the fatigue crack propagation rate,  $da/dN$ , where  $a$  is the crack length and  $N$  the number of load cycles. If the requirements for LEFM are fulfilled, i.e. a negligibly small plastic zone at the crack tip, the fatigue crack growth rate can be described by the stress intensity factor concept in the form of a cyclic stress intensity factor,

$$\Delta K = K_{\max} - K_{\min} \quad , \quad (2.23)$$

where  $K_{\max}$  and  $K_{\min}$  are the stress intensity factors for the maximum and minimum loading, respectively, during a load cycle. Depicting the experimentally obtained fatigue crack growth rate as a function of the cyclic stress intensity factor in a double logarithmic plot yields in Fig. 2.10. The plotted curve is divided into regions I, II and III. In Region I the lower limit of the curve is identified by the threshold  $\Delta K_{\text{th}}$ . Below this value, no fatigue crack propagation is detected. This region is influenced by microstructural effects whereas in Region II the influence of the loading dominates. Region II is described by the well-known Paris law [177],

$$\frac{da}{dN} = C(\Delta K)^m \quad , \quad (2.24)$$

where the exponent,  $m$ , and coefficient,  $C$ , are dependent on the material, temperature, mean stress, and environment. The upper end of the plotted curve, Region III, marks the transition to quasi-static crack growth, indicated by  $\Delta K_c$ .

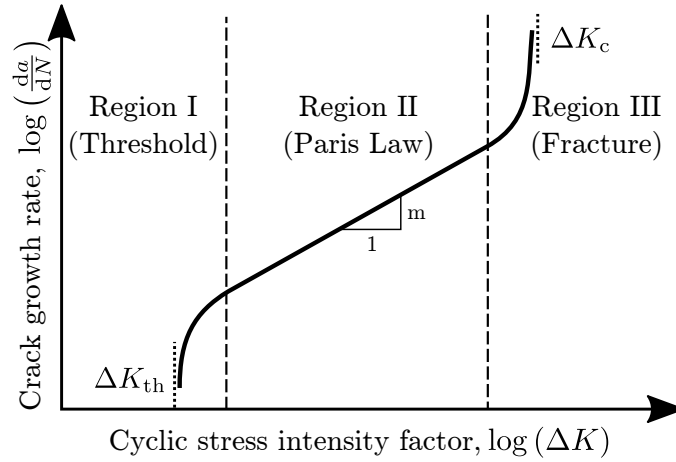


**Figure 2.10:** Crack growth rate,  $da/dN$ , as a function of the cyclic stress intensity factor,  $\Delta K$ .

Another approach for EPFM, analogous to the Paris law, utilizes the CTOD to characterize fatigue crack growth [62]. Herein, a cyclic CTOD parameter,  $\Delta\Delta_t = \Delta_t^{\max} - \Delta_t^{\min}$ , is related to the fatigue crack growth rate,

$$\frac{da}{dN} = C_t(\Delta\Delta_t)^{m_t} \quad , \quad (2.25)$$

with the material constants  $C_t$  and  $m_t$ . A large number of further fatigue crack growth laws are available and some of them are summarized in [168].

In engineering components, loads of constant amplitudes are rarely found. Structures and components undergo more complex time-varying loading conditions. In contrast to constant amplitude loading, fatigue crack propagation at variable amplitude loading depends not only on  $\Delta K$  and the load ratio,  $R = \sigma_{\min}/\sigma_{\max}$ , but is also determined by the whole loading history. This so-called sequence effect can lead to both (i) accelerated and (ii) decelerated fatigue crack growth and influences the component's lifetime. Three different loading situations are presented in Fig. 2.11 and the resulting fatigue crack growth rate is depicted. Different models have been formulated to account for this sequence effect. These models range from simple accumulation rules towards more advanced concepts, e.g. strip yield models [167]. All of these models require a detailed knowledge of the whole service load history to obtain an accurate lifetime estimation.

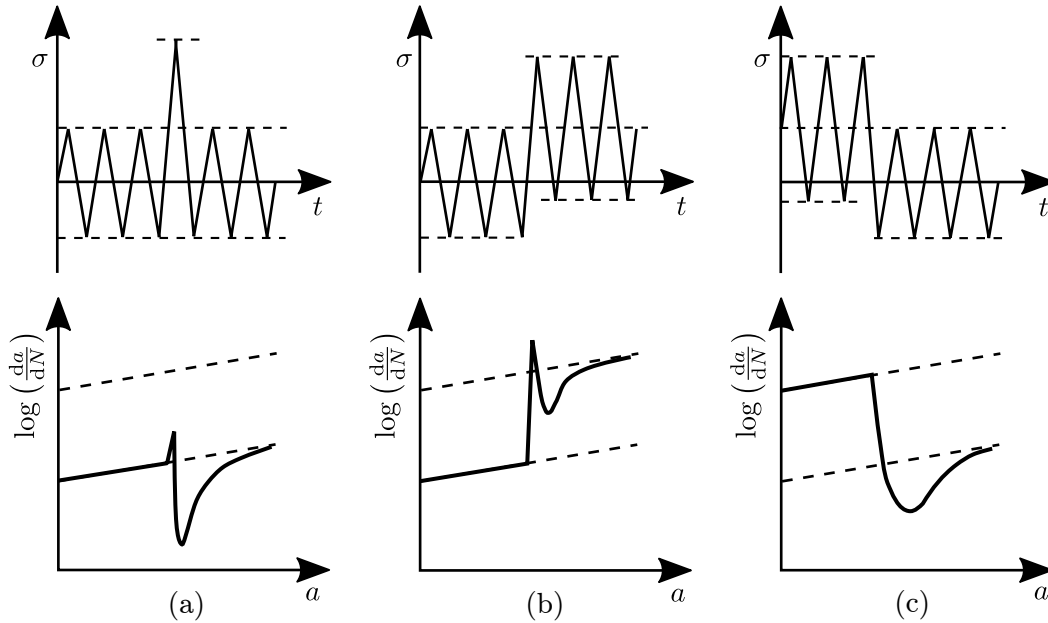


**Figure 2.11:** Illustration of the sequence effect depicted for (a) a single overload cycle, (b) a low–high block sequence, and (c) a high–low block sequence [127].

### 2.1.5 Continuum Damage Mechanics

Continuum Damage Mechanics (CDM) describes the damage and fracture process from a continuum mechanics point of view. A real material is assumed to possess small continuously distributed defects, i.e. microcracks, microvoids, or microscopic cavities. During deformation these micro-defects can form, grow, and coalesce to influence the macroscopic material properties. This process is called damage and leads, in its final stage, to complete material separation. Material damage can be classified into brittle, ductile, creep, and fatigue damage [161]. The dominating mechanism for brittle damage is nucleation and growth of microcracks. In contrast, ductile and creep damage are dominated by the formation, growth, and coalescence of voids. During fatigue damage, microplastic cyclic deformations lead to the nucleation of microcracks, which start to propagate and coalesce [85].

To model microscopic discontinuities in materials by means of continuum mechanics, a homogenization of the microstructure is necessary. The obtained macroscopic stresses and strains are therefore averaged over some Reference Volume Element (RVE). The homoge-

nized material behavior is described by constitutive laws utilizing damage variables. The damage progression is characterized by damage evolution laws. This way, CDM provides a local description of the deformation and damage state of the material points inside a structure. The constitutive laws in combination with the evolution laws allow for the prediction of the whole damage process, from a pristine material to local material failure (comparable to an initial macrocrack). Thus, CDM established a link between classical continuum mechanics and fracture mechanics.

The development of micro-defects reduces the stiffness of the material during loading. One way to characterize the damage state is by using the degradation in the elastic modulus [43, 135]. The corresponding damage variable is obtained as

$$D = 1 - \frac{E(D)}{E_0} \quad , \quad (2.26)$$

where  $E_0$  denotes the Young's modulus in the initial undamaged state and  $E(D)$  in the damaged state. Modeling of the damage state by means of the Young's modulus can be utilized for the formulation of both elasto-damage and elasto-plasto-damage constitutive laws, as depicted in Fig. 2.12.

In the case of randomly distributed micro-defects, the damage state is usually taken as isotropic. Therefore, the application of one scalar damage variable is suitable. If the micro-defects have an oriented geometry, e.g. aligned micro-cracks or a non-uniform distribution,

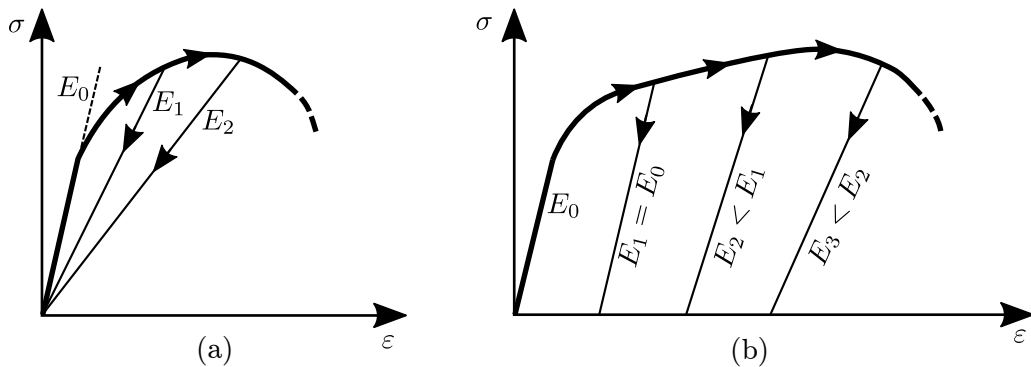


**Figure 2.12:** Damage evolution for (a) an elasto-damage and (b) an elasto-plasto-damage material behavior (modified from [85]).



the assumption of isotropic damage may not be accurate enough. Hence, more complex theories capturing anisotropic 3D damage have been developed [160].

### Fatigue Damage

Following [160], fatigue damage in the framework of CDM distinguishes between HCF and LCF. In HCF, so-called two-scale damage models are utilized. Plastic strains occurring under HCF are very small and the elastic-plastic-damage theory cannot be applied directly. Hence, in [134] a microscopic volume element inside an RVE has been postulated in which the development of elastic-plastic damage is allowed. Based on this assumption, a damage evolution law is derived and a damage onset criterion is defined. Thus, resulting in the prediction of the number of cycles to fatigue crack initiation,

$$N_N = N_D + N_R \quad , \quad (2.27)$$

which is the sum of the number of cycles for microcrack nucleation,  $N_D$ , and the number of cycles for microcrack growth causing mesoscopic fracture,  $N_R$ . Furthermore, the elaborated two-scale damage model [137–139] is capable of assessing variable amplitude loading and predicts a cumulative damage behavior that is comparable to the double linear damage rule depicted in Fig. 2.4.

In contrast to HCF in CDM, LCF is caused by the accumulation of plastic damage and, as such, the elastic-plastic-damage theory [133] can be directly applied. The damage evolution follows as [63, 160],

$$\dot{D} = \frac{\sigma_{EQ}^2 R_v}{2ES(1-D)^2} \dot{p} H(p - p_N) \quad , \quad (2.28)$$

where  $\sigma_{EQ}$  is the von Mises equivalent stress,  $p$  is the accumulated plastic strain, and  $p_N$  is the corresponding threshold value indicating damage onset.  $E$  and  $S$  represent the material properties and  $H(\cdot)$  denotes the Heaviside function.  $R_v$  is the stress triaxiality function,

$$R_v = \frac{2}{3}(1 + \nu) + 3(1 - 2\nu) \left( \frac{\sigma_H}{\sigma_{EQ}} \right)^2 \quad , \quad (2.29)$$

where  $\nu$  is the Poisson ratio and  $\sigma_H$  the hydrostatic stress.

Numerical methods are typically utilized to properly describe the elasto–plastic material response under multiaxial cyclic loading and to integrate the damage evolution law in Eq. (2.28). To obtain an analytic solution a simple uniaxial tension–compression load history is assumed, where  $\sigma_{EQ} = \sigma$ ,  $\dot{p} = |\dot{\varepsilon}^P|$ , and  $R_v = 1$ . Then the number of cycles correlated to microcrack nucleation is described as

$$N_{\mathcal{D}} = \frac{p_N}{2\Delta\varepsilon^P} \quad , \quad (2.30)$$

where  $\Delta\varepsilon^P$  is the plastic strain range. The threshold value,  $p_N$ , can be defined as the total plastic work supplied to the material during loading subtracted from the energy dissipated in the form of heat during deformation, see [160]. The number of cycles to mesoscopic fracture,

$$N_{\mathcal{R}} = \frac{4ESD_c}{K^2} (\Delta\varepsilon^P)^{-(M+2)/M} \quad , \quad (2.31)$$

is obtained by postulating a cyclic stress–strain relation,  $\Delta\varepsilon^P = [\Delta\sigma/(K(1-D))]^M$  and integrating Eq. (2.28). Herein,  $E$  denotes the Young’s modulus,  $K$ ,  $M$ , and  $S$  are material constants, and  $D_c$  is the critical damage value indicating material failure. In the particular case of  $p_N = 0$  the number of cycles for microcrack nucleation becomes  $N_{\mathcal{D}} = 0$  and the number of load cycles to fatigue crack initiation simplifies to  $N_N = N_{\mathcal{R}}$ . In this case Eq. (2.31) represents a power relation between  $\Delta\varepsilon^P$  and  $N_N$  and is equivalent to the Coffin–Manson law, Eq. (2.4).

### 2.1.6 Comments on thermo–mechanical fatigue

Thermo–mechanical fatigue (TMF) is caused by a cyclic variation of the thermal and mechanical stress and strain fields. In TMF, mechanical fatigue, creep fatigue, and corrosion fatigue mechanisms may interact or compete with each other resulting in material damage. The complexity of TMF has resulted in a variety of models trying to describe these mechanisms. Reviews on models considering interactions of these damage mechanisms can be found in [77, 78, 243]. In [79], a classification of different TMF approaches is provided. The lifetime models are characterized into three classes, (i) phenomenological models relying on mechanical quantities only, without explicit consideration of the different damage mechanisms, (ii) damage accumulation models explicitly accounting for the different damage

mechanisms, and (iii) fracture mechanics based crack growth models utilizing the inelastic strain at the crack tip.

TMF shows similarities to LCF, mostly due to the (high) plastic strains occurring during cyclic loading. This leads to the application of lifetime models developed for LCF under TMF conditions. These models rely on mechanical quantities only and do not explicitly consider environmental or creep effects. Such models take the influence of the temperature indirectly into account by means of temperature dependent material parameters. Therefore, strain or energy based approaches such as the total strain–life, the FS, or SWT models are commonly used to approximate the fatigue life under TMF conditions. Major advantages of these models are their simplicity and their limited number of required material parameters.

In contrast, damage accumulation models treat the effects of fatigue, oxidation, and creep separately and propose a cumulative damage rule enabling lifetime estimations. Approaches of this category are the strain range partitioning [87], the Neu–Sehitoglu [165, 166], and the Lemaitre–Chaboche [136] TMF damage models. Drawbacks of these models include their complexity, the high number of required material parameters and the requirement for substantial computational power.

The experimentally motivated fracture mechanics approaches focus on the crack tip deformation. Lifetime predictions are carried out by defining crack growth laws, which may also account for crack closure effects as proposed in [196, 211]. Such concepts are mostly suitable for brittle materials [79].

In conclusion, a well–accepted framework for the prediction of TMF does not exist yet and the choice of the lifetime model is often related to the available experimental data, the application, and the loading conditions [79]. Hence, the above–mentioned models, even the most complex ones, have no general validity and their application is limited by a number of restrictions. One simple and promising parameter for the formulation of a TMF lifetime model is the (inelastic) strain energy. In [102], LCF and TMF tests of stainless steel have been conducted and compared to a multiaxial energy–based damage model showing good results in the predictive capability of the parameter. In [234], the Neu–Sehitoglu model has been compared to an energy criterion on TMF tests of an aluminum alloy. The Neu–Sehitoglu model showed good agreement with the experimental data, but also required

a large set of input parameters. The energy criterion, with a much smaller set of input parameters, yielded a lifetime prediction just as reasonable as the Neu–Sehitoglu model. In [79], the plastic strain energy per cycle has been utilized and conditioned by parameters accounting for high temperature damage and mean stress effects. The model has been compared to classical approaches, i.e. Coffin–Manson, total strain–life, SWT, and the plastic dissipated energy, and has shown good predictive capabilities.

## 2.2 Lifetime Models for Power Semiconductors

### Empirical Lifetime Models

In the following, a short summary of Empirical Lifetime Models (ELMs) employed for power semiconductors is provided. These approaches utilize parameters such as the junction temperature range, mean temperature, frequency, and wire bond current to estimate the device lifetime.

The simplest model builds upon a *Coffin–Manson* like law and utilizes the junction temperature range,  $\Delta T_j$ , for the estimation of the number of load cycles to failure,

$$N_F = \alpha (\Delta T_j)^{-n} \quad . \quad (2.32)$$

Herein,  $\alpha$  and  $n$  are fitting parameters obtained from experiments.

The *Coffin–Manson–Arrhenius* [94, 95] model is obtained by including an additional mean temperature value,  $T_m$ , and is given as

$$N_F = \alpha (\Delta T_j)^{-n} \exp\left(\frac{E_a}{kT_m}\right) \quad , \quad (2.33)$$

where  $k$  is the Boltzmann constant and  $E_a$  is an activation energy parameter also obtained by experiments.

The *Norris–Landzberg* [170] model additionally considers the frequency,  $f$ , of the temperature cycles and is given as

$$N_F = A f^{n_2} (\Delta T_j)^{-n_1} \exp\left(\frac{E_a}{kT_m}\right) \quad , \quad (2.34)$$

where  $n_1, n_2$ , and  $A$  need to be determined experimentally.

The *Bayerer* [19] model,

$$N_F = K (\Delta T_j)^{\beta_1} \exp\left(\frac{\beta_2}{T_{j,\max} + 273\text{K}}\right) t_{\text{on}}^{\beta_3} I^{\beta_4} V^{\beta_5} D^{\beta_6} \quad , \quad (2.35)$$

utilizes a large set of parameters, where  $T_{j,\max}$  is the maximum junction temperature,  $t_{\text{on}}$  is the heating time,  $I$  is the applied DC current,  $D$  is the diameter of the bond wires, and  $V$  is the blocking voltage. Finally,  $K$  and  $\beta_i$  are constants extracted from large data sets of reliability experiments.

Further models are available and can be found in [38, 49]. The development of more advanced models including a larger set of input parameters may result in better lifetime predictions under very specific conditions. However, the main drawback of this model type, in not considering the actual physical failure mechanisms, still remains.

### Physical Lifetime Models

In contrast to ELMs, Physical Lifetime Models (PLMs) aim to consider the actual physical failure mechanisms. Hence, PLMs are gaining more prevalence in the lifetime modeling of power semiconductor devices [230]. PLMs require the knowledge of the stress and strain fields inside the device. Electro-thermal and thermo-mechanical simulations of at least one stabilized load cycle are necessary to obtain these quantities. In a post-processing step, established models such as the Coffin-Manson law, Eq. (2.4), the total strain-life curve, Eq. (2.5), critical plane methods, Eqs. (2.10 and 2.11), or energy-based models are employed for the lifetime prediction. Reviews on these models, most often applied to solder joint or wire-bond fatigue, can be found in [132, 195]. Models for creep fatigue interactions are reviewed in [238]. A well-known model which considers both the fatigue crack initiation stage and the fatigue crack propagation stage has been proposed in [56]. Both stages are described by energy approaches as

$$N_N = K_1 \Delta w^{K_2} \quad (\text{fatigue crack initiation}), \quad (2.36)$$

$$\frac{da}{dN} = K_3 \Delta w^{K_4} \quad (\text{fatigue crack propagation}), \quad (2.37)$$

where  $N_N$  is the number of load cycles for fatigue crack initiation,  $da/dN$  is the fatigue crack propagation rate and  $\Delta w$  is the inelastic strain energy density dissipated in one cycle.  $K_i$  are the model constants obtained by parameter calibration between numerical results and experimental data. This model is extensively used for the analysis of solder joint fatigue and has been implemented in the commercial FEM software Abaqus V6(2016) (Dassault Systemes Simulia Corp., Providence, RI, USA), where a CDM extension allows for progressive damage modeling.

## Chapter 3

# Fatigue Damage Modeling in the Bulk Material

A Continuum Damage Mechanics formulation is derived focusing on material degradation caused by thermo-mechanical fatigue conditions in micrometer-sized structures. Stage I microcrack nucleation is considered to have an essential influence on the material degradation. The Fatemi-Socie critical plane method is utilized for the prediction of microcrack nucleation. Damage evolution is obtained from an empirical energy criterion based on the inelastic strain energy density. The orientation of the microcracks aligned with the predicted critical plane is employed to model anisotropic damage. Therefore, a second-order damage tensor, whose principal axes are aligned with the critical plane orientation is utilized. This way, an orthotropic progressive loss of material integrity is obtained. In combination with the Finite Element Method, the formulation enables not only the modeling of local material failure, but also the simulation of structural deterioration. The approach is implemented in Ansys APDL v16.2 (ANSYS Inc., Canonsburg, PA, USA) and exemplified on micrometer-sized cantilever beams under Low Cycle Fatigue loading conditions.

### 3.1 Introduction

Power semiconductor devices have to withstand a large number of high current and high power density pulses. These loading conditions introduce very high temperatures and temperature gradients into the multilayer structure of a power semiconductor device [163]. The mismatch between the coefficients of thermal expansion of the different materials in combination with the temperature swings leads to cyclic mechanical stresses and strains, and, therefore, to a thermo-mechanical fatigue (TMF) problem. The repetitive application of operational as well as overload pulses, caused by error conditions, results in material degradation [150, 164, 203] and the deterioration of electrical and thermal properties [204]. Further operation of the device may result in overheating and destruction of the power semiconductor [60, 184]. The assessment of sustainable load cycles is, therefore, of great importance in the design and testing of power semiconductor devices.

This chapter focuses on the modeling and simulation of fatigue damage inside the metallization layer of a power semiconductor. The metallization layer is usually made up of a ductile material, such as Aluminum (Al) or, in newer technologies, Copper (Cu), and has a thickness of a few micrometers. During overload pulsing of the device, microscopic flaws may nucleate in the metallization and result in the formation and propagation of fatigue cracks [163, 164] which impede the heat flow and may lead to local overheating and possible destruction of the device. Hence, the proper assessment of the whole device lifetime includes the prediction of fatigue crack initiation and fatigue crack propagation.

First described in [35], fatigue crack evolution is now commonly accepted to occur in two stages [41]. In stage I, fatigue cracks nucleate along planes of maximum shear. Followed by stage II fatigue crack propagation along planes of maximum tensile loading. Hence, the assessment of microcrack nucleation requires a criterion which takes the planes of maximum shear into account. Therefore, different phenomenological criteria are available in the literature. These criteria can be divided into stress-based, strain-based, and energy-based formulations [118]. Stress-based criteria are typically used in High Cycle Fatigue (HCF), whereas strain based criteria are employed in Low Cycle Fatigue (LCF) problems. Energy-based criteria can be found in both HCF and LCF regimes. For multiaxial loading conditions critical plane methods are the most often recommended criteria providing high



accuracy in the fatigue assessment of engineering components [221]. Two of the most often utilized critical plane methods are the Fatemi–Socie model (FS) [73] for the nucleation and growth of shear microcracks and the Smith–Watson–Topper model (SWT) [215] for the nucleation and growth of tensile cracks [216]. These models have shown to provide accurate predictions about the orientation of emerging (micro)cracks as well as reasonable lifetime predictions.

In contrast to purely phenomenological criteria also Continuum Damage Mechanics (CDM) approaches have been applied successfully to model fatigue crack initiation [5, 28, 137, 160]. These models often originate from fundamental thermodynamics and describe damage as the progressive loss of material integrity. Therefore, CDM models enable not only a lifetime prediction, but also the modeling of material degradation and, consequently, structural deterioration. The progressive loss of material integrity is described by damage evolution laws, which are typically based on phenomenological approaches. Some of these formulations utilize only mathematical formulations which do not provide a better insight into the physical phenomenon, and may be even incompatible with the well–proven critical plane methods [154].

In the present work, a CDM approach is formulated based on phenomenological criteria utilizing physical quantities for the description of fatigue crack initiation. The approach is sketched in Fig. 3.1. The FS critical plane method is employed to act as a damage onset criterion to describe microcrack nucleation on planes of maximum shear loading (stage I fatigue crack growth). This way, not only the lifetime fraction for microcrack nucleation is determined but also the orientation of the emerging microcracks is predicted. Continuous loading leads to an accumulation and coalesce of microcracks and, consequently, to a loss of material integrity. Depending on the loading conditions and the material response, the emerging microcracks can be aligned in a certain direction resulting in an anisotropic damage behavior. Therefore, a damage modeling formulation accounting for an anisotropic loss of material integrity is employed in the model. The thermal influence on fatigue is indirectly taken into account by temperature dependent constitutive laws, the coefficients of thermal expansion (CTE), and the simulation of temperature gradients. Oxidation is assumed to be negligible because the power metallization is encapsulated by mold compound in a chip package and no aggressive environment is expected to be present at the power

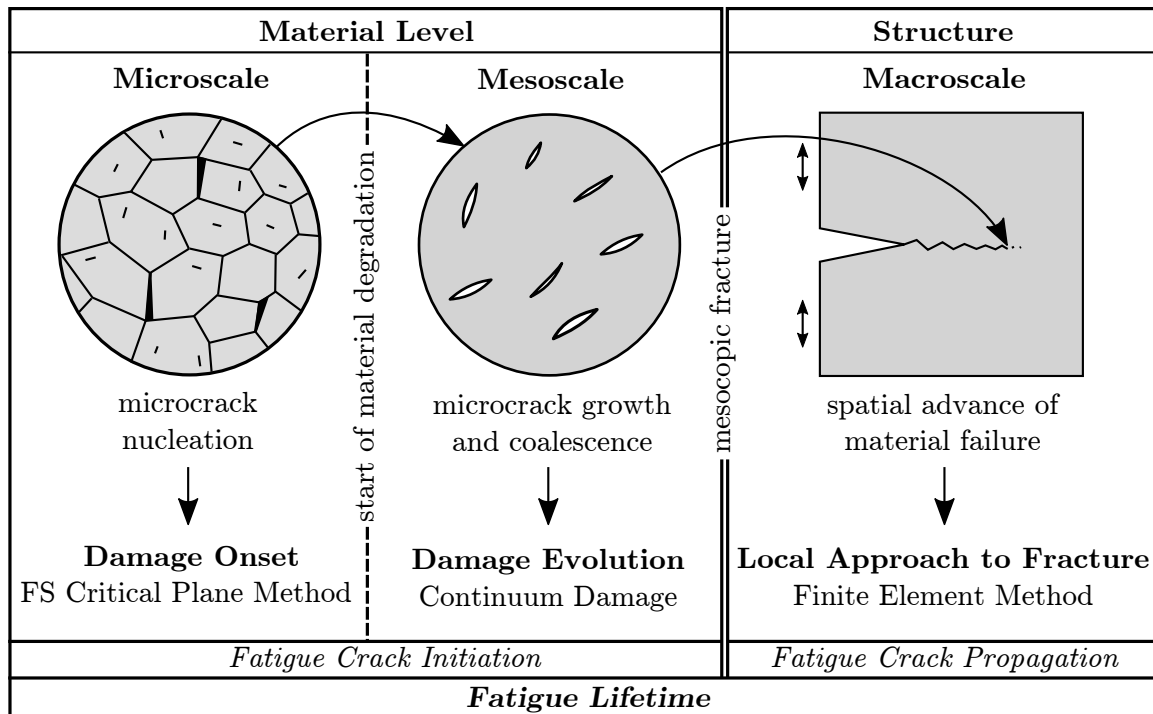


**Figure 3.1:** Overview of the fatigue damage modeling approach for bulk materials.

metal. Since the time period of a single power pulse is usually in the range of milliseconds, high-temperature creep effects and creep fatigue interactions are assumed to be small and negligible in this work. Under these assumptions, energy-based criteria have been shown to provide an efficient way to assess the fatigue lifetime, particularly for TMF, by keeping the set of required material parameters in a reasonable range [79, 102, 234]. Hence, a damage evolution law based on the inelastic strain energy is utilized in the present work. The damage evolution law describes the progressive loss of material integrity until mesoscopic fracture occurs. The mesoscale is defined as the smallest scale where the material can still be idealized as homogeneous continuum. Thus, mesoscopic fracture is equivalent to the first occurrence of an initial macrocrack which marks the transition between fatigue crack initiation and fatigue crack propagation. Fatigue crack propagation is modeled by combining the local formulation of the CDM approach with the Finite Element Method (FEM). This way, not only fatigue crack initiation is modeled, but also the simulation of the damage and fracture process up to structural failure is enabled [160]. This means that fatigue crack propagation is represented by an evolving spatial zone of material failure

causing deterioration of the structural properties without the need of an additional fatigue crack growth law.

## 3.2 Orthotropic Continuum Damage Model

Before the CDM model is derived in detail, a short summary of the utilized methods is presented here. The FS damage model is employed for the prediction of microcrack nucleation and combined with the Palmgren–Miner linear damage accumulation rule accounting for damage onset.\* The critical plane is identified as the plane experiencing maximum damage. Damage evolution is obtained from an empirical energy criterion based on the inelastic strain energy density augmented with the hydrostatic stress. A second order damage tensor is utilized to model a direction–dependent loss of material integrity. The critical plane orientation is used to define the orthotropic constitutive behavior of the damaged material. The effective elastic properties of the damaged material are predicted by the hypothesis of complementary strain energy equivalence.

### 3.2.1 Damage Onset – Multiaxial Fatigue Criteria

The original FS damage model, a multiaxial fatigue criterion based on the critical plane method [73], is given as

$$\frac{\Delta\gamma_{\max}}{2} \left( 1 + \kappa \frac{\sigma_n^{\max}}{\sigma_Y} \right) = \frac{\tau_f'}{G} (2N_F)^{b\gamma} + \gamma_f' (2N_F)^{c\gamma} \quad , \quad (3.1)$$

where,  $\Delta\gamma_{\max}$  is the maximum engineering shear strain range and  $\sigma_n^{\max}$  is the maximum normal stress acting on the plane of  $\Delta\gamma_{\max}$ . Hence, in the original formulation, the critical plane is identified as the plane experiencing  $\Delta\gamma_{\max}$ . The yield stress is denoted as  $\sigma_Y$ ,  $\kappa$  is a material property, and  $G$  is the shear modulus. Originally, this model has been developed for isothermal problems where  $\kappa$  and  $\sigma_Y$  are constant. For TMF problems these parameters are temperature dependent. Nevertheless, the FS damage model has been successfully applied

---

\*The FS damage model is employed since fatigue cracks nucleate on planes of maximum shear loading during stage I fatigue crack growth. The SWT damage model, Eq. (2.13), is additionally implemented into the numerical simulation routine (see Appendix D) but is not used in the present work.

to TMF problems by approximating the material properties as constant values resulting in reasonable lifetime predictions [71]. The parameters of the lifetime model are the number of cycles to failure,  $N_F$ , the shear fatigue strength coefficient,  $\tau'_f$ , the shear fatigue strength exponent,  $b_\gamma$ , the shear fatigue ductility coefficient,  $\gamma'_f$ , and the shear fatigue ductility exponent,  $c_\gamma$ . Often these material fatigue properties are not available and make lifetime estimation a difficult task [72]. Therefore, different approximation techniques have been proposed to estimate the required material fatigue properties [201, 216].

An additional problem arises in the definition of  $N_F$ . In the original formulation [73], a certain load drop has been defined to indicate "failure" of the specimen. This definition does not distinguish between the fatigue crack initiation and the fatigue crack propagation stages. Unfortunately, a unified definition for the transition between these two stages does not exist and is mostly dependent on the user's field of interest [220]. However, further experimental data are available, especially for multiaxial fatigue criteria, which report the number of load cycles until a fatigue crack of a certain length is detected, e.g. [217]. This data can be utilized to define a transition between the number of cycles for fatigue crack initiation,  $N_N$ , and fatigue crack propagation,  $N_P$ , resulting in the total fatigue life,

$$N_F = N_N + N_P \quad . \quad (3.2)$$

Within the framework of CDM, the number of cycles to fatigue crack initiation,

$$N_N = N_D + N_{\mathcal{R}} \quad , \quad (3.3)$$

is further divided into the number of cycles for microcrack nucleation,  $N_D$ , and the number of cycles for microcrack growth,  $N_{\mathcal{R}}$ , causing mesoscopic fracture [160]. In the proposed CDM approach the FS critical plane method will be utilized as a damage onset criterion predicting the number of cycles for microcrack nucleation,  $N_D$ .

In the following, the computation of the normal stress,  $\sigma_n$ , and the shear strain amplitude,  $\gamma_a = \Delta\gamma/2$ , acting on a plane,  $\Xi$ , is discussed. In Fig. 3.2(a), the stress and strain state of an arbitrary material point in a stabilized load cycle is given by the time varying stress tensor,  $\boldsymbol{\sigma}(t)$ , and strain tensor,  $\boldsymbol{\varepsilon}(t)$ , in the reference coordinate system  $(x_1-x_2-x_3)$ . The orientation of  $\Xi$  is defined by the unit normal vector,  $\boldsymbol{\xi}_1$ . Together with the two unit vectors

$\xi_2$  and  $\xi_3$  lying in  $\Xi$ , an orthonormal basis ( $\xi_1$ – $\xi_2$ – $\xi_3$ ) is formed. The unit vectors are given by the rotation angles  $\theta$  and  $\varphi$  in the reference coordinate system as [123]

$$\xi_1 = \begin{bmatrix} \cos \varphi \cos \theta \\ \cos \varphi \sin \theta \\ -\sin \varphi \end{bmatrix}, \quad \xi_2 = \begin{bmatrix} -\sin \theta \\ \cos \theta \\ 0 \end{bmatrix}, \quad \text{and} \quad \xi_3 = \begin{bmatrix} \sin \varphi \cos \theta \\ \sin \varphi \sin \theta \\ \cos \varphi \end{bmatrix}. \quad (3.4)$$

The computation of the normal traction component acting on  $\Xi$  is straightforward and provided by

$$\sigma_n(t) = \xi_1 \cdot \sigma(t) \xi_1. \quad (3.5)$$

In the case of non-proportional loading, the determination of  $\gamma_a$  becomes a non-trivial and computational expensive optimization problem. A review of the four most commonly used methods, the Minimum Circumscribed Circle (MCC), the Longest Chord, the Longest Projection, and the diagonal of the Maximum Rectangular Hull, can be found in [183]. The only method providing unique solutions for  $\gamma_a$  and the mean shear strain,  $\gamma_m$ , is the MCC method. Hence, the MCC method proposed in [176] is utilized in the current work. This method searches for the smallest circle containing all points of a curve,  $\Psi$ , as depicted in Fig. 3.2(b). The center of the circle is defined by  $\gamma_m$  and the radius of the circle defines  $\gamma_a$ . According to [26], the MMC method can be formulated as a min-max optimization problem of the following form,

$$\gamma_m = \min_{\gamma'} \left\{ \max_t \|\gamma(t) - \gamma'\| \right\}, \quad (3.6)$$

where  $\gamma'$  can be interpreted as an initial guess for the center of the circle with a radius,  $\max_t \|\gamma(t) - \gamma'\|$ . The radius of this circle has to be minimized. An algorithm for this problem can be found in [26]. Once the center of the circle,  $\gamma_m$ , with the minimum radius containing all points of  $\Psi$  is identified the amplitude of the engineering shear strain is obtained as,

$$\gamma_a = \max_t \|\gamma(t) - \gamma_m\|. \quad (3.7)$$

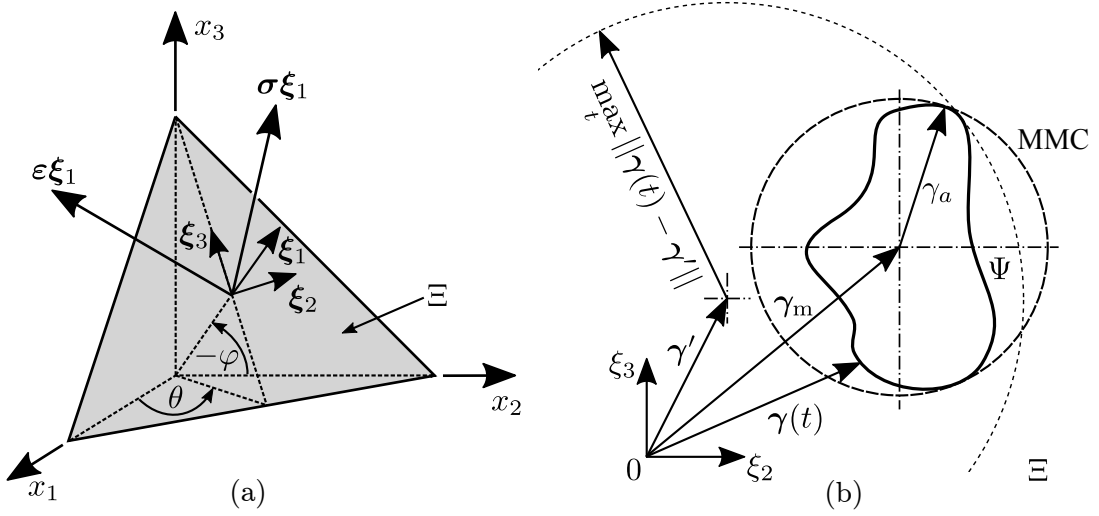


**Figure 3.2:** Evaluation of the critical plane. (a) depicts the traction and strain acting on the plane,  $\Xi$ , (b) represents the Minimum Circumscribed Circle (MMC) method for the determination of the shear strain amplitude,  $\gamma_a$ , in a stabilized cycle (modified from [123, 176]).

Numerical optimization routines are required to solve this computationally expensive problem. Parallel computing is employed to reduce the computational time. The utilized routines are based on the work of [123].

The components of the engineering shear strain vector,  $\gamma(t)$ , acting in  $\Xi$  are obtained from

$$\frac{\gamma_2(t)}{2} = \xi_2 \cdot \varepsilon(t) \xi_1 \quad , \quad (3.8)$$

$$\frac{\gamma_3(t)}{2} = \xi_3 \cdot \varepsilon(t) \xi_1 \quad . \quad (3.9)$$

Additionally, the definition of the critical plane becomes a complex task under non-proportional loading conditions [148, 232] and the orientation may be different to the critical plane predicted by the maximum shear strain amplitude, as proposed in Eq. (3.1). Different methods such as the Shear Stress– [143] or Shear Strain–Maximum Variance Method [231], the Maximum Damage Method (MDM) [15], and the Method of Weight Functions [39, 40], have been proposed to identify the critical plane of fatigue crack nucleation. As stated in [148], the MDM seems to be most closely related to the original idea of

the critical plane method and is utilized in the current work. By applying the FS criterion along with the MDM, Eq. (3.1) changes to

$$\max_j \left\{ \left[ \frac{\Delta\gamma}{2} \left( 1 + \kappa \frac{\sigma_n^{\max}}{\sigma_Y} \right) \right]_{\Xi_j} \right\} = \frac{\tau_f'}{G} (2N_{\mathcal{D}})^{b\gamma} + \gamma_f' (2N_{\mathcal{D}})^{c\gamma} \quad , \quad (3.10)$$

where  $j$  indicates the considered plane  $\Xi_j$  out of an infinite number of possible plane orientations. The critical plane,  $\Xi_c$ , is identified as the plane where the Fatigue Indicator Parameter (FIP),

$$\mathcal{P}_j^{\text{FS}} = \left[ \frac{\Delta\gamma}{2} \left( 1 + \kappa \frac{\sigma_n^{\max}}{\sigma_Y} \right) \right]_{\Xi_j} \quad , \quad (3.11)$$

reaches its maximum. For variable amplitude loading or a change in the phase angle of non-proportional loading, as depicted in Fig. 3.3, a damage accumulation rule is required to determine the critical plane experiencing maximum damage. In Fig. 3.3(a) two load blocks of constant amplitude loading,  $\sigma_{a_i}$  are depicted, where  $n_i$  is the total number of load cycles inside the  $i$ -th load block. In Fig. 3.3(b) two load cycles of different phase angles,  $\Delta\varphi_i$  are displayed, where  $N_i$  denotes the load cycle number of one load cycle inside the  $i$ -th load block. Under such loading conditions the widely used Palmgren–Miner linear damage accumulation rule [156, 175] is employed to predict damage contribution for microcrack nucleation,

$${}^{(j)}\mathcal{D} = \sum_{i=1}^m \frac{n_i}{{}^{(j)}(N_{\mathcal{D}})_i} \quad , \quad (3.12)$$

where  $i$  defines the sequence of  $m$  load blocks of both constant load amplitudes and constant phase angles.  $n_i$  is the number of load cycles corresponding to the  $i$ -th load block.  ${}^{(j)}(N_{\mathcal{D}})_i$  is associated to the number of load cycles to microcrack nucleation for the load block  $i$  and the plane  $\Xi_j$ .  $N_{\mathcal{D}}$  is obtained from the implicit Eq. (3.10) by application of an iterative solution scheme. Finally, the damage onset criterion is defined as

$$\mathcal{D}^{\mathcal{O}} = \max_j \left\{ \sum_{i=1}^m \frac{n_i}{{}^{(j)}(N_{\mathcal{D}})_i} \right\} = 1 \quad , \quad (3.13)$$

and the critical plane,  $\Xi_c = \Xi_j$ , is identified as the plane first reaching this criterion. In summary, the proper assessment of the critical plane for non-proportional, varying amplitude loading involves the application of the FS criterion along with the MDM utilizing a linear damage accumulation rule.

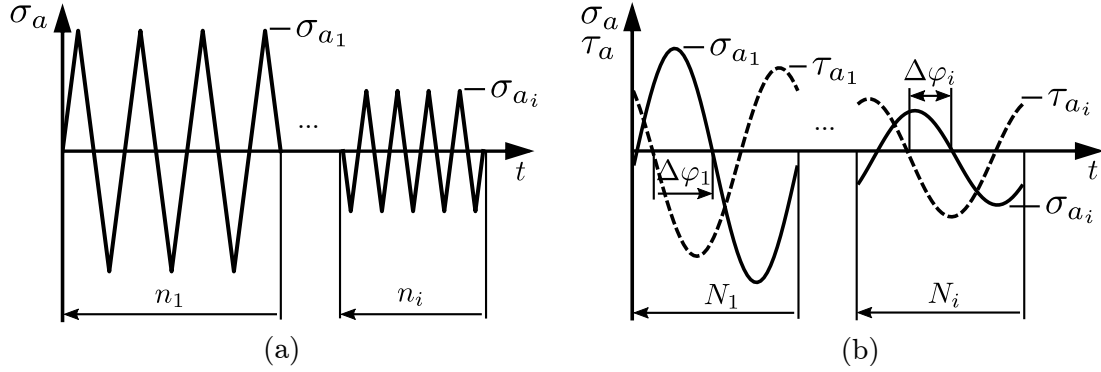


**Figure 3.3:** Variable amplitude loading conditions. (a) load blocks of constant amplitude loading,  $\sigma_{a_i}$ , (b) load cycles of constant phase angles,  $\Delta\varphi_i$ .

### 3.2.2 Damage Evolution – Inelastic Strain Energy

Once the damage onset criterion is reached the number of cycles for microcrack nucleation,  $N_{\mathcal{D}}$ , is known. Afterwards, microcrack growth and coalescence lead to material degradation and result in a loss of material integrity. This process is described by a damage variable,  $D$ , and the number of load cycles for microcrack growth,  $N_{\mathcal{R}}$ . The macroscopic material properties are affected during this stage, and the degradation of the material parameters is described by the damage variable,  $D$ . Various approaches are available in the literature defining different damage evolution laws which, in turn, describe the damage state of the material. As discussed in Section 2.1.6, approaches based on the inelastic strain energy density provide a simple and effective method for the prediction of the damage evolution under TMF loading conditions. Therefore, a damage evolution law based on the inelastic strain energy density is utilized in the subsequent model formulation.

The dissipated or inelastic strain energy parameter, first proposed in [75] for the prediction of fatigue failure, is computed for a stabilized load cycle as

$$\Delta w = \int_{1 \text{ cycle}} \boldsymbol{\sigma} : \dot{\boldsymbol{\epsilon}} dt \quad , \quad (3.14)$$

where  $\boldsymbol{\sigma}$  is the stress tensor,  $\dot{\boldsymbol{\epsilon}}$  is the rate of the strain tensors, and  $t$  is the time. A schematic representation of  $\Delta w$  for a stabilized load cycle is depicted in Fig. 3.4. Various modifications of such energy based parameters accounting for multiaxial loading or mean



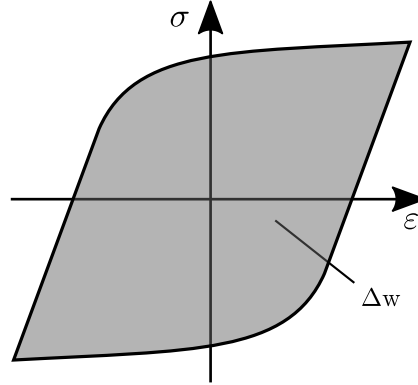


**Figure 3.4:** Inelastic strain energy density dissipated over a stabilized load cycle.

stress effects have been proposed in the literature [144, 178]. In this work, a simple criterion proposed in [2] for TMF is utilized. The modified criterion is given as

$$\Delta w_{\text{mod}} = \Delta w + \alpha \sigma_{\text{H}}^{\text{max}} \quad , \quad (3.15)$$

where  $\sigma_{\text{H}}^{\text{max}}$  denotes the maximum hydrostatic pressure which occurs during the stabilized cycle. The coefficient  $\alpha$  is obtained from experimental data and adjusts the influence of the hydrostatic stress state on the lifetime prediction.

In the commercial FE code Abaqus V6(2016) (Dassault Systemes Simulia Corp., Providence, RI, USA) the work of [56, 130] is utilized and a damage evolution law based on the inelastic strain energy density defined as

$$\frac{dD}{dN} = \frac{K_3}{\ell} \Delta w^{K_4} \quad , \quad (3.16)$$

where  $\ell$  is the characteristic length obtained from the element size in a FEM analysis.  $K_3$  and  $K_4$  are material parameters which have to be determined by comparison of numerical results with experimental data. In the current work, the modified energy parameter of Eq. (3.15) is utilized in combination with the damage evolution law of Eq. (3.16) resulting in

$$\frac{dD}{dN} = \frac{\varkappa_1}{\ell} (\Delta w_{\text{mod}})^{\varkappa_2} \quad , \quad (3.17)$$

where  $\varkappa_1$  and  $\varkappa_2$  denote the material parameters for the present model formulation.

Finally, the damage variable is obtained by integration of Eq. (3.17) and follows as

$$D = \int_{N_{\mathcal{D}}}^N \frac{\kappa_1}{\ell} (\Delta w_{\text{mod}})^{\kappa_2} dN \quad . \quad (3.18)$$

Once the damage variable reaches a value of one, a loss of material integrity is predicted and the number of cycles for microcrack growth,  $N_{\mathcal{R}} = N$  for  $D = 1$ , is obtained.

### 3.2.3 Orthotropic Damage Modeling

In CDM the physical meaning of the damage variable,  $D$ , characterizing the damage state of the material is usually interpreted as the reduction of the load carrying effective area due to void or microcrack development [111, 191]. Following [160], the three-dimensional anisotropic damage state of a continuum can be specified by effective area reduction in the principal planes of the damage tensor. Therefore, an arbitrary surface element in the current damaged configuration is considered and defined by the area  $dA$  and the unit normal vector to this area  $\boldsymbol{\nu}$ , as depicted in Fig. 3.5(a). The coordinate system (1–2–3) denotes the principal material axes. Further, a fictitious undamaged configuration is postulated which is mechanically equivalent to the damaged configuration. Herein, the corresponding surface element is denoted by the area vector,  $\tilde{\boldsymbol{\nu}}d\tilde{A}$ , as depicted in Fig. 3.5(b). The damage variable of a second order damage tensor is then defined by a linear transformation of the area vector,  $\boldsymbol{\nu}dA$ , from the current damaged configuration into a fictitious undamaged configuration,

$$\tilde{\boldsymbol{\nu}}d\tilde{A} = (\mathbf{I} - \mathbf{D}) \boldsymbol{\nu}dA \quad . \quad (3.19)$$

Herein,  $\mathbf{I}$  is the second-order identity tensor and  $\mathbf{D}$  a second-order damage tensor characterizing the damage state induced by an arbitrary distribution of voids and / or microcracks.  $\mathbf{D}$  is symmetric and can be expressed by its spectral decomposition,

$$\mathbf{D} = \sum_{i=1}^3 D_i \mathbf{n}_i \otimes \mathbf{n}_i \quad , \quad (3.20)$$

where  $D_i$  are the principal values and  $\mathbf{n}_i$  the unit normal vectors describing the principal directions. A second order damage tensor is capable of modeling the damage state up to

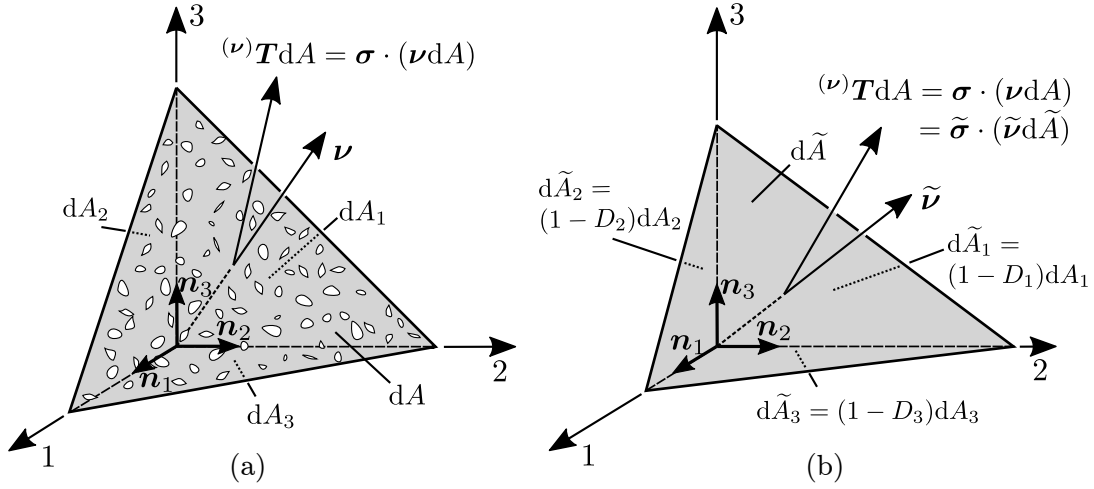


**Figure 3.5:** Effective area reduction in the principal planes of the damage tensor. (a) current damaged configuration, (b) fictitious undamaged configuration (modified from [160]).

orthotropic complexity. Higher order tensors would be necessary to treat more complex anisotropic behavior. Nevertheless, orthotropic elasticity has been shown to represent the elastic properties of a damaged material containing distributed microcracks with sufficient accuracy, even for significant crack densities [112].

For the formulated CDM approach, the critical plane orientation is postulated to characterize the anisotropic damage state. Therefore, the orientation of the critical plane described by the orthonormal basis  $\boldsymbol{\xi} = \{\boldsymbol{\xi}_1, \boldsymbol{\xi}_2, \boldsymbol{\xi}_3\}$ , is utilized as the basis for the principal directions (1–2–3) of the damage tensor. Normal to the critical plane ( $\boldsymbol{\xi}_1$ -axis) the highest loss of material integrity, caused by the nucleation and growth of aligned microcracks, is expected and the damage tensor defined as

$${}^{(\xi)}\mathbf{D} = \sum_{i=1}^3 D_i \boldsymbol{\xi}_i \otimes \boldsymbol{\xi}_i = \begin{bmatrix} D & 0 & 0 \\ 0 & \omega D & 0 \\ 0 & 0 & \omega D \end{bmatrix} . \quad (3.21)$$

Herein,  $D$  is the damage variable obtained from Eq. (3.17). Since, not all microcracks are perfectly aligned with the critical plane the parameter  $\omega \in [0, 1]$  is introduced to describe the damage influence on the transverse directions. If  $\omega = 0$  damage is only modeled along

the  $\xi_1$ -direction and the transverse directions remain undamaged. If  $\omega = 1$  an isotropic damage behavior is obtained. The diagonal form of  $\mathbf{D}$  is only obtained in its principal basis,  $\xi = \{\xi_1, \xi_2, \xi_3\}$ , which is aligned with the principal material axes (1–2–3). In the general case the damage tensor has to be expressed in the global coordinate system ( $x_1$ – $x_2$ – $x_3$ ) as

$${}^{(x)}\mathbf{D} = {}^{(x,\xi)}\mathbf{Q}^T {}^{(\xi)}\mathbf{D} {}^{(x,\xi)}\mathbf{Q} \quad (3.22)$$

where  ${}^{(x,\xi)}\mathbf{Q}$  denotes the rotation tensor from the global coordinate system ( $x$ ), defined by the orthonormal basis  $x = \{\mathbf{e}_1, \mathbf{e}_2, \mathbf{e}_3\}$ , into a rotated coordinate system, ( $\xi$ ), defined by the orthonormal basis  $\xi = \{\xi_1, \xi_2, \xi_3\}$ . The rotation tensor can be obtained from the direction cosines as

$${}^{(x,\xi)}Q_{ij} = \mathbf{e}_j \cdot \xi_i \quad . \quad (3.23)$$

In the following all operations are done in the global coordinate system. For better readability and simplicity the indication of the coordinate system ( $x$ ) is dropped.

### 3.2.4 Elastic Constitutive Equation

In CDM the constitutive equation for a damaged material is derived by the use of the effective stress and a hypothesis of mechanical equivalence. The effective stress tensor,  $\tilde{\boldsymbol{\sigma}}$ , can be defined as the stress induced in the fictitious undamaged configuration, when the surface element  $d\tilde{A}$  is subjected to the identical surface force vector  ${}^{(\nu)}\mathbf{T}dA$  as in the damaged configuration (Fig. 3.5). The effective stress tensor follows from

$${}^{(\nu)}\mathbf{T}dA = \boldsymbol{\sigma}(\boldsymbol{\nu} dA) = \tilde{\boldsymbol{\sigma}}(\tilde{\boldsymbol{\nu}} d\tilde{A}) = \tilde{\boldsymbol{\sigma}}(\mathbf{I} - \mathbf{D})(\boldsymbol{\nu} dA) \quad , \quad (3.24)$$

where  $\boldsymbol{\sigma}$  is the Cauchy stress tensor. After rearranging Eq. (3.24) the effective stress tensor follows as

$$\tilde{\boldsymbol{\sigma}} = (\mathbf{I} - \mathbf{D})^{-1} \boldsymbol{\sigma} \quad . \quad (3.25)$$

In the case of anisotropic damage, the obtained  $\tilde{\boldsymbol{\sigma}}$  is asymmetric, which makes the formulation of constitutive and evolution equations inconvenient [160]. Hence, different methods

for the symmetrization of the effective stress tensor have been proposed. In the present work, the symmetric effective stress tensor proposed by [54] is utilized and reads

$$\tilde{\boldsymbol{\sigma}} = (\mathbf{I} - \mathbf{D})^{-\frac{1}{2}} \boldsymbol{\sigma} (\mathbf{I} - \mathbf{D})^{-\frac{1}{2}} \quad . \quad (3.26)$$

The hypothesis of complementary strain energy equivalence, also suggested in [54], results in a symmetric compliance tensor and is therefore utilized. An elastic–plastic material is considered and the internal change due to plastic deformation is considered by an internal state variable,  $\boldsymbol{\alpha}$ . This way, the complementary strain energy functions of the material in the undamaged and damaged state are given as [160]

$$V_0(\boldsymbol{\sigma}, \boldsymbol{\alpha}) = \frac{1}{2} \boldsymbol{\sigma} : \mathbb{S}_0 : \boldsymbol{\sigma} - \phi(\boldsymbol{\alpha}) \quad , \quad \text{and} \quad (3.27)$$

$$V(\boldsymbol{\sigma}, \mathbf{D}, \boldsymbol{\alpha}) = \frac{1}{2} \boldsymbol{\sigma} : \mathbb{S}(\mathbf{D}) : \boldsymbol{\sigma} - \phi(\boldsymbol{\alpha}) \quad , \quad (3.28)$$

respectively.  $\mathbb{S}_0$  and  $\mathbb{S}(\mathbf{D})$  denote the fourth order elastic compliance tensors of the undamaged and the damaged material, respectively. The hypothesis,

$$V(\boldsymbol{\sigma}, \mathbf{D}, \boldsymbol{\alpha}) = V_0(\tilde{\boldsymbol{\sigma}}, \boldsymbol{\alpha}) \quad , \quad (3.29)$$

states that the complementary strain energy function of the damaged material, is given by the corresponding function,  $V_0(\tilde{\boldsymbol{\sigma}}, \boldsymbol{\alpha})$ , of the undamaged material and the effective stress tensor. The application of this hypothesis results in the elastic constitutive equation of the damaged material,

$$\boldsymbol{\varepsilon}^e = \frac{\partial V_0(\tilde{\boldsymbol{\sigma}}, \boldsymbol{\alpha})}{\partial \tilde{\boldsymbol{\sigma}}} = [\mathbb{M}^T(\mathbf{D}) : \mathbb{S}_0 : \mathbb{M}(\mathbf{D})] : \boldsymbol{\sigma} \quad , \quad (3.30)$$

and the definition of the elastic compliance tensor of the damaged material,

$$\mathbb{S}(\mathbf{D}) = \mathbb{M}^T(\mathbf{D}) : \mathbb{S}_0 : \mathbb{M}(\mathbf{D}) \quad , \quad (3.31)$$

where  $\mathbb{M}(\mathbf{D})$  denotes the fourth order damage effect tensor. The determination of the compliance tensor,  $\mathbb{S}(\mathbf{D})$ , is provided in Appendix A.

In the case of isotropic damage the material damage tensor reduces to

$$\mathbb{M}(D) = \frac{1}{(1-D)^2} \mathbb{I} \quad , \quad (3.32)$$

where  $\mathbb{I}$  is the fourth-order identity tensor and  $D$  a scalar damage variable. The elastic engineering parameter set for the damaged material simplifies to

$$\tilde{E} = (1-D)^2 E, \quad (3.33)$$

$$\tilde{\nu} = \nu \quad , \quad (3.34)$$

where  $\tilde{E}$  denotes the damaged Young's modulus and  $\tilde{\nu}$  the damaged Poisson ratio.

With respect to thermo-mechanical simulations an ad-hoc extension for the thermal conductivity is introduced. The thermal conductivity is degraded the same way as the Young's modulus and follows for the damaged material as

$$\tilde{k} = (1-D)^2 k \quad , \quad (3.35)$$

where  $k$  is the thermal conductivity of the undamaged material and  $D$  is the isotropic damage variable obtained from Eq. (3.17). This way, the heat flow through the damaged region is impeded.

### 3.2.5 Rate-Independent Plastic Constitutive Equation

The anisotropic elastic-plastic damage constitutive equation is based on the work of [51]. The small strain framework is utilized, which is justified by the application of the model to cyclic loading conditions. The main equations of a rate-independent orthotropic plastic constitutive model are summarized below considering kinematic hardening. For simplicity isothermal conditions are assumed in the model explanation below.<sup>†</sup>

---

<sup>†</sup>Note that in the conducted thermo-mechanical simulations (Chapter 5) thermal strains are accounted for in the linear elastic constitutive equation and temperature dependent properties are utilized in the plastic constitutive equation.

Under these assumptions the total strain can be written as,

$$\boldsymbol{\varepsilon} = \boldsymbol{\varepsilon}^e + \boldsymbol{\varepsilon}^p \quad , \quad (3.36)$$

the sum of the elastic,  $\boldsymbol{\varepsilon}^e$ , and plastic strain,  $\boldsymbol{\varepsilon}^p$ . Consequently, by substituting Eq. (3.36) into Eq.(3.30) and rearranging, Hooke's law of linear elasticity,

$$\boldsymbol{\sigma} = \mathbb{C}(\mathbf{D}) : (\boldsymbol{\varepsilon} - \boldsymbol{\varepsilon}^p) \quad , \quad (3.37)$$

is obtained, where  $\mathbb{C}(\mathbf{D})$  denotes the elasticity tensor of the damaged material. A kinematic hardening formulation [134] is employed and combined with the orthotropic yield criterion of Hill [98]. The yield criterion reads [46]

$$f(\tilde{\boldsymbol{\sigma}}, \mathbf{X}; \mathbf{D}) = \|\tilde{\boldsymbol{\sigma}} - \mathbf{X}\|_{\mathbb{H}} - \sigma_Y = 0 \quad , \quad (3.38)$$

where  $\mathbf{X}$  is the back-stress tensor for kinematic hardening and  $\sigma_Y$  is the yield stress. It is assumed that the damage effect on  $\mathbf{X}$  is already taken into account by the experimentally determined material flow curve [188]. The yield condition, Eq. (3.38), is defined with Hill's criterion within a quadratic norm definition as

$$\|\tilde{\boldsymbol{\sigma}}\|_{\mathbb{H}} = [\tilde{\boldsymbol{\sigma}} : \mathbb{H}_0 : \tilde{\boldsymbol{\sigma}}]^{\frac{1}{2}} = [\boldsymbol{\sigma} : \mathbb{H}(\mathbf{D}) : \boldsymbol{\sigma}]^{\frac{1}{2}} \quad , \quad (3.39)$$

where  $\mathbb{H}_0$  is a fourth order tensor characterizing the yield condition of an orthotropic undamaged material. Based on [51]  $\mathbb{H}_0$  is applied to the effective stress. This way, an initial isotropic yield condition results in an orthotropic yield condition during damage progression. Similar to the compliance tensor of the damaged material,  $\mathbb{S}(\mathbf{D})$ , the tensor describing the yield condition for the damaged material follows as [51]

$$\mathbb{H}(\mathbf{D}) = \mathbb{M}^T(\mathbf{D}) : \mathbb{H}_0 : \mathbb{M}(\mathbf{D}) \quad . \quad (3.40)$$

The matrix representation of  $\mathbb{H}(\mathbf{D})$  and the evaluation of the damaged plastic properties are provided in Appendix A.

Finally, an associated flow rule is employed and the plastic strain rate obtained as

$$\dot{\boldsymbol{\varepsilon}}^p = \dot{\lambda} \frac{\partial f}{\partial \boldsymbol{\sigma}} \quad , \quad (3.41)$$

where  $\lambda$  is the plastic multiplier and can be found in [134].

### 3.3 Numerical Implementation

The commercial software Ansys APDL v16.2 (ANSYS Inc., Canonsburg, PA, USA) is employed for the FEM analysis. The orthotropic CDM approach is implemented into Ansys Parametric Design Language (APDL). Herein, the stress and strain tensors are accessible as element or nodal values. In the present work, the element values, defined as the average of the nodal values of a finite element, are utilized for the computation of the multiaxial fatigue criteria. Hence, material points are represented in a discrete way by finite elements. Python 2.7 (Anaconda Distribution 4.1.1, Continuum Analytics, Austin, TX, USA) combined with IPython 4.2.0 [182] enabling parallelization are employed for the computation of the multiaxial fatigue criteria and the damage onset criterion, identifying the critical plane. Material degradation is realized by changing the material cards of individual elements. The analysis is set up on a cycle-by-cycle basis. Each load cycle is simulated by a single FEM run. A restart analysis is performed for subsequent load cycles. This way, the whole loading history is considered and the material properties are degraded between consecutive load cycles. Additionally, a cycle jump technique is implemented to reduce the computation time.

A flow chart of the presented approach is depicted in Fig. 3.6. The FEM analysis of a structure requires the definition of material properties in addition to boundary and loading conditions. The expected region of material damage requires an adequately fine mesh for a sufficient resolution of the stress and strain states during the whole load cycle. The first load cycle (LC) is simulated and, afterwards, a predefined stopping criterion dependent on the structure and expected failure behavior is checked. The stopping criterion can be defined as a certain load drop during the analysis, as a maximum number of load cycles or



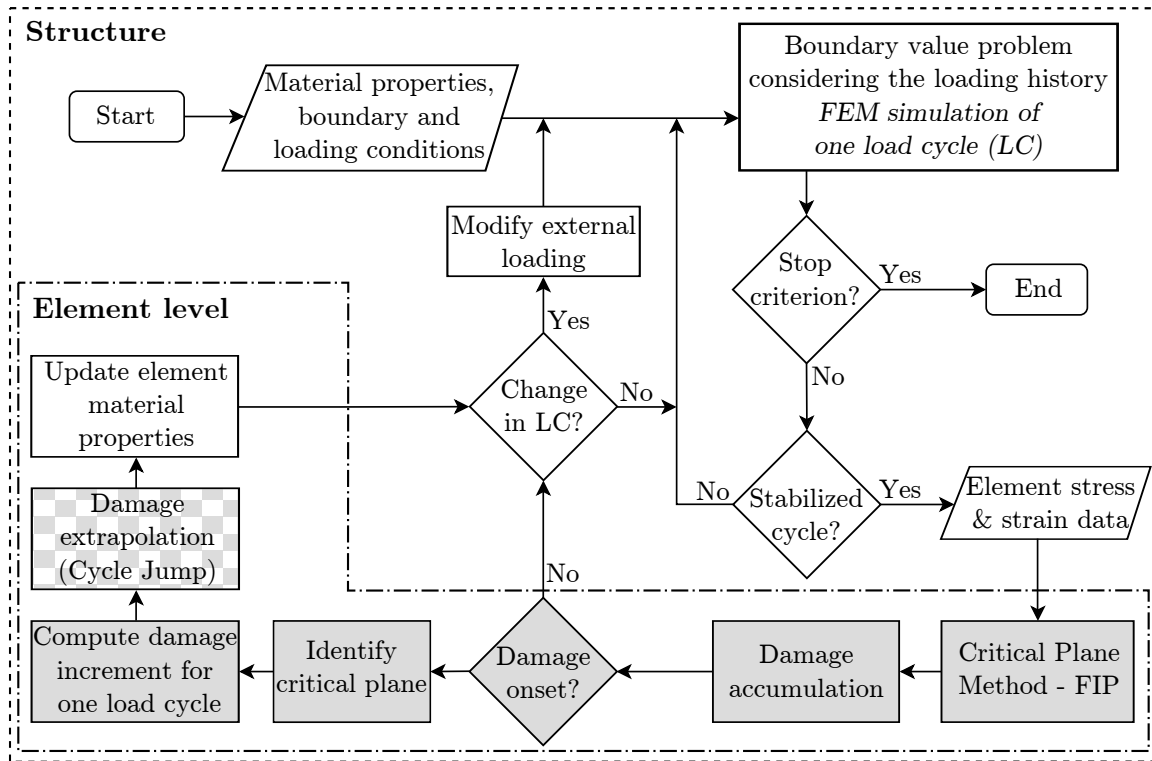


**Figure 3.6:** Flow chart representing the CDM approach for the modeling of fatigue damage in bulk materials. The operations in the white boxes are executed in APDL, whereas the computations in the grey boxes are carried out by a Python script.

as a maximum number of finite elements with reduced stiffness. If the stopping criterion is not reached, the analysis is continued.

For constant amplitude cycling, the stress and strain states for the critical plane method are typically taken from a stabilized cycle occurring after plastic shakedown. In the present work, a cycle jump technique (Section 3.4) for constant amplitude loading is introduced. The required variables required for the cycle jump technique are taken from a stabilized cycle. A stabilized cycle can be obtained only if the load spectrum can be represented by load blocks of constant loading conditions. For certain variable amplitude loading conditions, which cannot be represented by such a loading history, a simulation on a cycle-by-cycle basis is required.

Assuming that the load spectrum can be represented by load blocks of constant loading conditions, a stabilized cycle can be identified by the vanishing change of the dissipated strain energy density of two consecutive load cycles [123],

$$\delta w_{i,i-1} = \frac{\Delta w_i - \Delta w_{i-1}}{\Delta w_{i-1}} \quad , \quad (3.42)$$

where  $\Delta w_i$  and  $\Delta w_{i-1}$  denote the dissipated strain energy densities of the load cycles ( $i$ ) and ( $i - 1$ ), respectively. A stabilized cycle is accepted when the dissipated strain energy density is smaller than a predefined threshold value,  $\delta w_{i,i-1} < \delta w_{i,i-1}^{\text{th}}$ . This criterion needs to be fulfilled for all material points. In the present work, material degradation is explicitly modeled and plastic shakedown may not be reached for all material points, especially, for points close to or in the damaged region. Hence, the dissipated strain energy of the whole structure,

$$\delta W_{i,i-1} = \frac{\Delta W_i - \Delta W_{i-1}}{\Delta W_{i-1}} \quad , \quad (3.43)$$

is utilized as a criterion for identifying plastic shakedown. Herein,  $\Delta W_i$  and  $\Delta W_{i-1}$  denote the dissipated strain energy of the whole structure during the load cycles ( $i$ ) and ( $i - 1$ ), respectively. A load cycle where  $\delta W_{i,i-1} < \delta W_{i,i-1}^{\text{th}} = 0.01$  is accepted as stabilized and the multiaxial fatigue criterion, Eq. (3.10), is evaluated.

The identification of the critical plane requires the computation of the FIP, Eq. (3.11), on different planes,  $\Xi_j$ . Only a finite number of possible planes can be considered as candidates for the critical plane. Therefore, an icosahedral discretization of a hemisphere is utilized to obtain an equally distributed spacing between the individual planes. A discretization of 33 different planes provides a good compromise between accuracy and computation time.

The critical plane orientation and the start of material degradation are defined by the damage onset criterion, Eq. (3.13). The criterion is updated after each stabilized cycle, at all material points for all considered planes. After the damage onset criterion is reached, the damage evolution law, Eq. (3.17), is integrated over the number of applied load cycles defining the damage state of a material point. The damage state together with the critical plane orientation is utilized for the definition of the damage tensor, Eq. (3.21). The damage tensor, in turn, describes the orthotropic elastic properties of the material point in the damaged state, Eq. (3.31).

The change of the material properties for material points inside the damaged region is realized by changing the material cards of individual elements between two consecutive load cycles. The damage variable,  $D \in [0, 1)$ , required for the definition of the damaged compliance tensor,  $\mathbb{S}(\mathbf{D})$ , and the yield condition of the damaged material,  $\mathbb{H}(\mathbf{D})$ , is discretized by an increment of  $\Delta D = 0.01$  resulting in 101 possible damage states for each of the 33 considered plane orientations. To avoid convergence issues complete material failure is approximated as  $D = 1 \approx 0.999$ , resulting in a stiffness degradation by a factor  $10^{-6}$  and non-zero yield stress values. The elastic constitutive behavior of these damage states is of orthotropic symmetry. Ansys APDL v16.2 allows the definition of the orthotropic elastic properties in combination with the Hill plasticity only in the principal material axes. The orientation of the principal material axes towards the global coordinate system is separately defined by the element coordinate system. The definition of the elastic compliance matrix in combination with the Hill plasticity model in the global coordinate system is not allowed for in Ansys APDL v16.2. Additionally, the change of the element coordinate system between consecutive load cycles is not possible in the commercial FEM software. The orientation of the critical plane and, therefore, the orientation of the principal material axes are not known *a priori* and have to be determined during the simulation. Hence, the principal material axes cannot be predefined by the element coordinate system as required in Ansys APDL v16.2. Therefore, a user programmed material subroutine of an elastic-plastic material model would be required. The coding of such a subroutine was beyond the scope of this work. Hence, two simplification strategies are utilized to demonstrate the formulated approach. First, the orthotropic damage behavior is simplified to an isotropic damage behavior by  $\omega = 1$  in Eq. (3.21). Second, the critical planes for all material points are approximated by the most critical planes determined at the time point of first damage onset in the structure. Therefore, two simulation are required. One simulation for the evaluation of the multiaxial fatigue criterion after the first stabilized load cycle is reached. The obtained plane orientations of this simulation correspond to the plane orientations of first damage onset in the structure. These plane orientations are then utilized in the second simulation, where the principal material axes of all material points are predefined and aligned with these approximated critical planes. This way, the orthotropic damage behavior can be demonstrated. Material cards for isotropic and orthotropic damage states

are predefined in the different simulations and the card closest to the predicted damage state is utilized in the simulation.

### 3.4 Cycle Jump Technique

If the external loading conditions do not change for the subsequent load cycles, as in a block of load cycles with constant amplitude loading, a cycle jump technique is utilized to reduce the computational time. The cycle jump technique distinguishes between damage onset and damage evolution. The number of cycles for the first damage onset inside the structure is dictated by the damage onset criterion. Afterwards, a damage extrapolation technique, similar to [57], is employed to define the number of load cycles for the cycle jump. The cycle jump technique is applied after a stabilized cycle has been found. The principal idea of the technique is illustrated in Fig. 3.7.

In the following considerations  $N$  denotes the actual load cycle number. Hence, each cycle of the whole loading history is uniquely identified by a single number  $N$ . The considered loading history consists of  $m$  load blocks of constant load amplitudes and constant phase angles.  $m$  is the total number of load blocks and the index  $i$  identifies the different load blocks.  $n_i$  is the total number of load cycles in the  $i$ -th load block, whereas  $N_l^{(i)}$  identifies a load cycle,  $l$ , in the load block  $i$ . Hence,  $N_1^{(i)} = 1$  for the first load cycle of  $n_i$  and  $N_{n_i}^{(i)} = n_i$  for the last load cycle, respectively. A stabilized load cycle in a load block  $i$  is denoted by  $^S N_k^{(i)}$ , where the index  $k$  indicates the number of the stabilized cycle.

The cycle jump technique is first discussed on a single load block ( $i = 1$ ). For simplicity the index ( $i$ ) is dropped in the subsequent formulae. For the first stabilized cycle,  $^S N_1$ , the whole structure consists of undamaged material. Hence, the number of load cycles possible for the first cycle jump is dictated by the damage onset criterion as,

$$\Delta N_1 = \min_{\mathbf{x}} \left\{ {}^{(c)}(N_{\mathcal{D}}(\mathbf{x})) \right\} + \Delta N_{\text{os}} \quad , \quad (3.44)$$

where the number of cycles to microcrack nucleation,  $N_{\mathcal{D}}$ , is computed for all material points,  $\mathbf{x}$ , inside the structure.  ${}^{(c)}(N_{\mathcal{D}}(\mathbf{x}))$  is predicted by the multiaxial fatigue criterion, Eq. (3.10), utilizing the critical plane,  $\Xi_c$ . The minimum number of cycles to microcrack

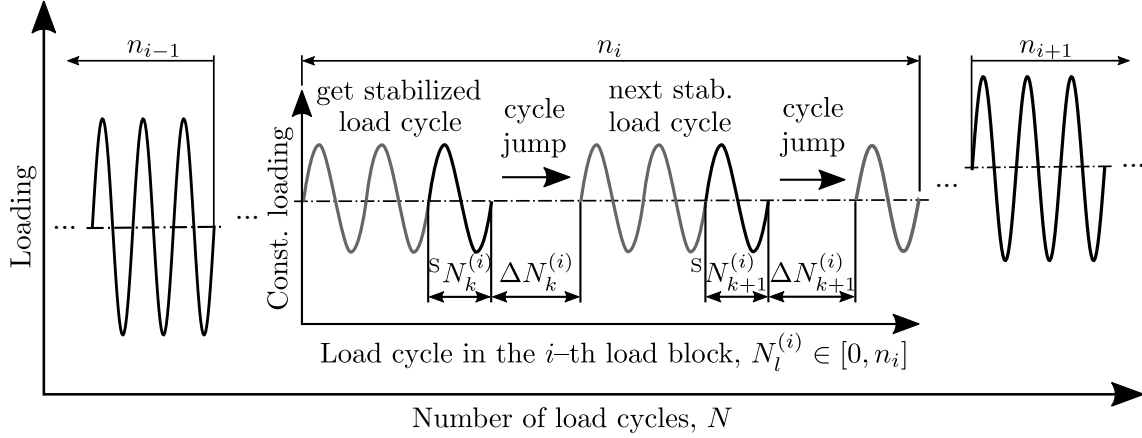


**Figure 3.7:** Illustration of the cycle jump technique. Three different load blocks are depicted and the application of the cycle jump technique is exemplified for the load block,  $n_i$ .

nucleation of all material points defines the first onset of material damage inside the structure. Continued loading results in damage progression and possibly in damage onset at other material points. The parameter,  $\Delta N_{os} \geq 1$ , is referred to as the number of load cycles overshooting the damage onset criterion. This is helpful if knowledge about the damage progression rate is already available from previous simulations. A proper definition of this parameter speeds up the subsequent adjustment of the cycle jump technique resulting in a reduced simulation time. If no information about the damage progression rate is available,  $\Delta N_{os} = 1$  is taken to overshoot the damage onset criterion and cause material damage inside the structure.

Subsequent to damage onset, damage propagation starts and the number of cycles for the cycle jump technique is dictated by the highest damage rate occurring inside the structure. A damage extrapolation technique is utilized to compute the damage increment for the cycle jump,

$$\Delta D_k(\mathbf{x}) = \Delta N_k \left( \frac{dD}{dN} \right)_k(\mathbf{x}) \quad \text{for } k \geq 2 \quad , \quad (3.45)$$

where  $\left( \frac{dD}{dN} \right)_k(\mathbf{x})$  is the damage rate in  ${}^S N_k$ , computed by Eq. (3.17) for all  $\mathbf{x}$ .  $\Delta N_k$  is the number of load cycles for the cycle jump. The damage caused in the computed load cycles to reach a stabilized cycle is approximated by the damage rate of the stabilized cycle,  $\left( \frac{dD}{dN} \right)_k$ , and considered in the number of cycle jumps,  $\Delta N_k$ . A tolerance field which defines

limits for  $\Delta D_k(\mathbf{x})$  is defined and an adaptive algorithm is employed to adjust the number of cycles for the next cycle jump based on the previous one. The procedure can be summarized as

$$\Delta N_{k+1} = \begin{cases} \left(\frac{\Delta D_{\max}}{\Delta D_k^{\max}}\right) \Delta N_k & \text{for } \Delta D_k^{\max} > \Delta D_{\max} \\ \left(\frac{\Delta D_{\min}}{\Delta D_k^{\max}}\right) \Delta N_k & \text{for } \Delta D_k^{\max} < \Delta D_{\min} \\ \Delta N_k & \text{else} \end{cases}, \quad (3.46)$$

where  $\Delta N_k$  denotes the number of load cycles of the previous cycle jump. The maximum damage increment,  $\Delta D_k^{\max} = \max_{\mathbf{x}} \{\Delta D_k(\mathbf{x})\}$ , obtained during  $\Delta N_k$ , is utilized to predict the number of load cycles for the next cycle jump,  $\Delta N_{k+1}$ . Therefore, a maximum and minimum damage tolerance,  $\Delta D_{\max}$  and  $\Delta D_{\min}$ , respectively, are prescribed for the adaptive cycle jump algorithm. Dependent on  $\Delta D_k^{\max}$ , the load cycle number can be increased, decreased, or kept constant. Due to the explicit nature of this procedure it is reasonable to define a maximum allowed number of cycles for the cycle jump, similar to Eq. (3.49). This avoids situations of substantial exceedance in the extrapolated damage increment, possibly, caused by sudden changes in the stress and strain states of certain material points.

The adaptive algorithm is first applied for  $\Delta N_2$ , where  $\Delta N_1 = \Delta N_{\text{os}}$  is defined as a start value. For subsequent load cycles further material points may reach the damage onset criterion resulting in the start of damage progression. Damage onset of material points may also happen during the cycle jump and the jump cycles need to be split up into a part contributing to the damage onset criterion and a part contributing to damage propagation. Therefore, the number of load cycles until the damage onset criterion would be reached is computed as,

$$\Delta N_{k+1}^{\mathcal{D}}(\mathbf{x}) = N_l \frac{1 - \mathcal{D}}{\mathcal{D}_i}. \quad (3.47)$$

for all material points. This way, the number of load cycles necessary to reach the damage onset criterion for each material point is obtained. The expression utilizes an extrapolation scheme of the damage onset criterion, as depicted in Fig. 3.8.  $\mathcal{D}$  defines the state of the damage onset criterion over all simulated load cycles, whereas  $\mathcal{D}_i$  indicates the contribution to the damage onset criterion of the load block  $i$ . If  $\Delta N_{k+1}^{\mathcal{D}}(\mathbf{x})$  is smaller than  $\Delta N_k$ , damage onset occurs during the cycle jump. The numbers of load cycles necessary to reach the damage onset criterion,  $\Delta N_{k+1}^{\mathcal{D}}(\mathbf{x})$ , do not contribute to the damage progression and

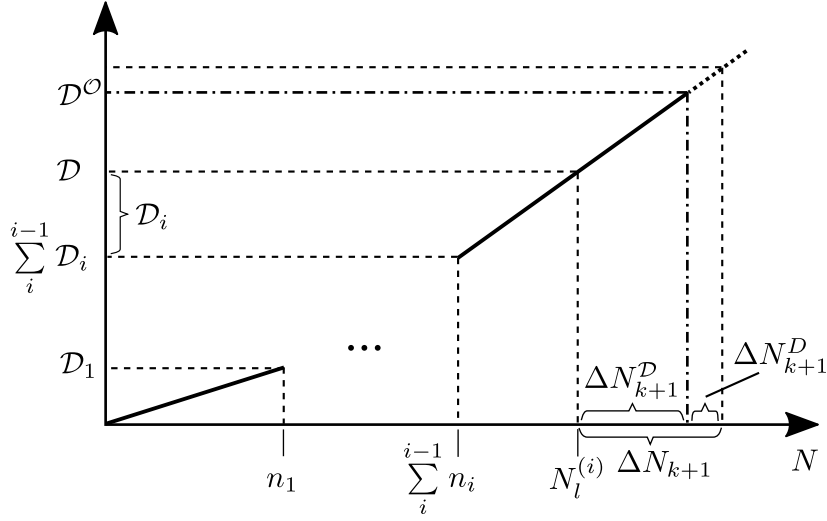


**Figure 3.8:** Damage extrapolation technique for elements reaching the damage onset criterion,  $\mathcal{D}^O(\mathbf{x})$ , during the cycle jump. The total number of jump cycles,  $\Delta N_{k+1}$ , is split up into a fraction corresponding to the damage onset criterion,  $\Delta N_{k+1}^D$  and a fraction corresponding to the damage evolution,  $\Delta N_{k+1}^D$ .

the number of cycles for the progressive damage extrapolation needs to be reduced for this material point as

$$\Delta N_{k+1}^D(\mathbf{x}) = \Delta N_{k+1} - \Delta N_{k+1}^D(\mathbf{x}) \quad . \quad (3.48)$$

For elements not reaching the damage onset criterion during the cycle jump no damage progression occurs.

The described procedure can be applied to multiple load blocks,  $m$ . Depending on if damage onset already has occurred inside the structure, the cycle jump technique of a subsequent load block starts either with Eq. (3.44) or Eq. (3.46). In the latter case the cycle jump increment for the actual load block,  $\Delta N_{k+1}^{(i+1)}$  is predicted from the cycle jump increment of the previous load block,  $\Delta N_k^{(i)}$ . This technique, is sufficient if the loading amplitude does not change drastically. If large changes are expected  $\Delta N_{os}$  is utilized instead of  $\Delta N_k^{(i)}$ .

Finally, the number of cycles possible for the cycle jump in a load block ( $i$ ) is limited by

$$\Delta N_k^{(i)} \leq n_i - N_l^{(i)} \quad , \quad (3.49)$$

where  $n_i - N_l^{(i)}$  denotes the remaining number of load cycles in the considered load block. If the predicted cycle jump number is higher than the remaining load cycles in a load block the jump cycles are set to,

$$\Delta N_k^{(i)} = n_i - N_l^{(i)} \quad . \quad (3.50)$$

### 3.5 Demonstration Studies

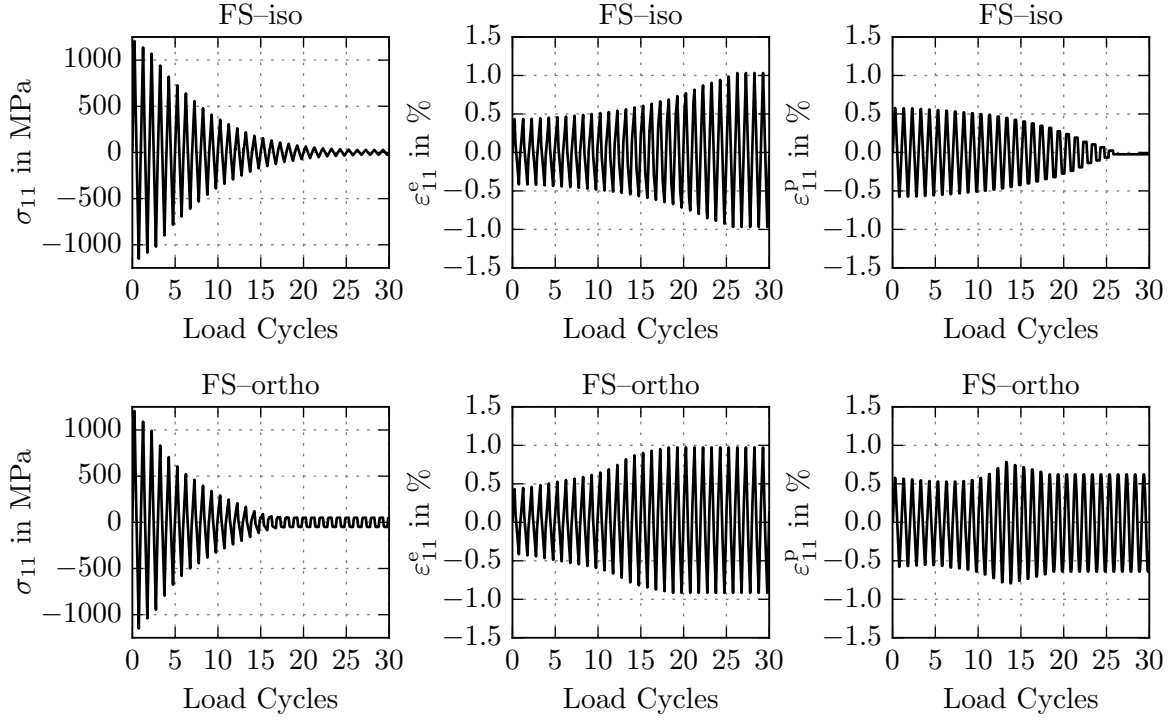
Single element tests are performed to demonstrate the orthotropic material degradation of the proposed approach. An elastic–perfectly–plastic constitutive behavior is modeled and a uni–axial strain state applied. A cyclic strain amplitude is prescribed along the  $x_1$ –direction as,  $\varepsilon_{11} = \varepsilon_0 \sin(t)$ , where  $\varepsilon_0 = 0.01$  and  $t$  indicates the time. In the transverse direction the strains  $\varepsilon_{22} = \varepsilon_{33} = 0$  are fixed by displacement boundary conditions. According to the FS multiaxial fatigue criterion an infinite number of critical planes, aligned under  $45^\circ$  towards the loading direction, exists under these loading conditions. For the demonstration purpose the plane normal to the  $x_1$ – $x_2$ –plane and oriented under  $45^\circ$  from the  $x_1$ –axis towards the  $x_2$ –axis is chosen as the critical one. The plane is *a priori* known and the orthotropic principal material axes can be predefined in the FEM analysis. In the following, a comparison between isotropic (FS–iso) and orthotropic (FS–ortho) damage modeling is provided. The damage onset criterion is manually set to be fulfilled already at the beginning of the simulation. The first load cycle is simulated and the damage variable computed. Before the second load cycle is applied, the elastic properties of the single element are degraded in accordance to the damage variable and the damage model. Isotropic damage is modeled by setting the parameter  $\omega = 1$  in Eq. (3.21), whereas for orthotropic damage  $\omega = 0$  is chosen. Subsequently, additional load cycles are applied until complete material failure ( $D = 1$ ) occurs. For the demonstration purpose, the fatigue parameters are chosen in such a way that material failure is obtained after a small number of load cycles. Therefore, the cycle jump technique is not employed. The input parameter set for the demonstration purpose is summarized in Tab. 3.1.

In Fig. 3.9 the stress and strain response, in loading direction ( $x_1$ ), is depicted of the single element. The stress component,  $\sigma_{11}$ , the elastic strain component,  $\varepsilon_{11}^e$ , and the plastic strain component,  $\varepsilon_{11}^p$ , are provided for isotropic and orthotropic damage modeling, respectively.



**Table 3.1:** Material parameters chosen for the demonstration purpose.

$E$	$\nu$	$\sigma_Y$	$\kappa_1$	$\kappa_2$	$\alpha$
100 GPa	0.35	100 MPa	$5 \cdot 10^{-5} \frac{\text{mm}}{\text{cycle}(\text{MPa})^{\kappa_2}}$	0.5	0.0

**Figure 3.9:** Comparison between the SET utilizing either isotropic (FS-iso) or orthotropic (FS-ortho) damage modeling. The stress,  $\sigma_{11}$ , elastic strain,  $\varepsilon_{11}^e$ , and plastic strain,  $\varepsilon_{11}^p$ , response in loading direction ( $x_1$ ) are depicted.

The initial response of both models is equal for the first load cycle. After the first load cycle damage modeling starts and the elastic strain component increases due to stiffness degradation. The applied displacement amplitude remains constant and, consequently, the plastic strain component decreases in the isotropic case. In the orthotropic case an almost constant plastic strain amplitude is obtained. The obtained loss of material integrity is slightly faster in the isotropic damage model compared to the orthotropic degradation. In the isotropic case the stiffness degradation is direction independent and  $\sigma_{11}$  vanishes to zero. In contrast, a minor cyclic stress amplitude remains in the orthotropic case. Herein, the stiffness degradation is direction dependent and a complete loss of material

integrity is only obtained in the normal direction to the critical plane,  $\xi_1$ . The stress and strain components normal to the critical plane orientation are depicted in Fig. 3.10 for the orthotropic damage model.  ${}^{(\xi)}\sigma_{11}$ ,  ${}^{(\xi)}\varepsilon_{11}^e$ , and  ${}^{(\xi)}\varepsilon_{11}^p$  represent the stress, elastic strain, and plastic strain response, respectively. It is clearly visible that under this orientation the stress component of the orthotropic model vanishes, as expected, to zero. The elastic strain increases as well as the plastic strain after a phase inversion in load cycle 4. In the isotropic case the rotated stress and strain components are identical to the ones depicted in Fig. 3.9. Finally, the evolution of the damage variable,  $D$ , is depicted in Fig. 3.11. The first damage increment is obtained after the first simulated load cycle. The damage evolution of both models starts nearly identical. After load cycle 4 the damage rate of the isotropic model slows down, whereas in the orthotropic case an almost linear increase in the damage variable is obtained. Hence, the isotropic model results in a longer lifetime. In the orthotropic case a damage variable of  $D = 1$  is already reached after 8 load cycles. Nevertheless, a minor residual load carrying capability in the global coordinate directions remains, whereas in the isotropic case ultimate material failure is obtained in all directions after 12 load cycles.

The evolution of the elastic parameters of the damaged material is depicted in Fig. 3.12. This parameter set is employed for the definition of the compliance matrix of the FS–ortho model during the simulation. The evaluation of the elastic parameters for the damaged material is provided in Appendix A. The Young’s modulus,  $\tilde{E}_1$ , of the damaged material

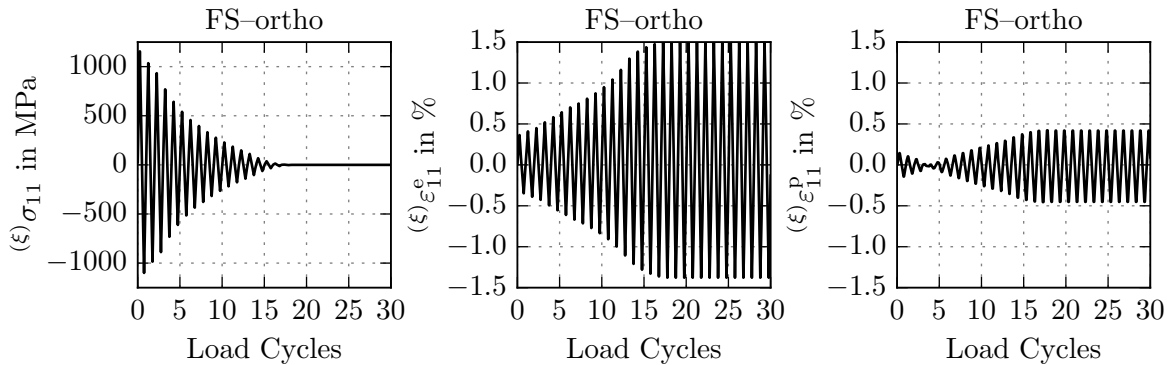


**Figure 3.10:** Constitutive response of the SET utilizing orthotropic damage modeling. The stress,  ${}^{(\xi)}\sigma_{11}$ , elastic strain,  ${}^{(\xi)}\varepsilon_{11}^e$ , and plastic strain,  ${}^{(\xi)}\varepsilon_{11}^p$ , are aligned with the coordinate axis,  $\xi_1$ , of the critical plane.

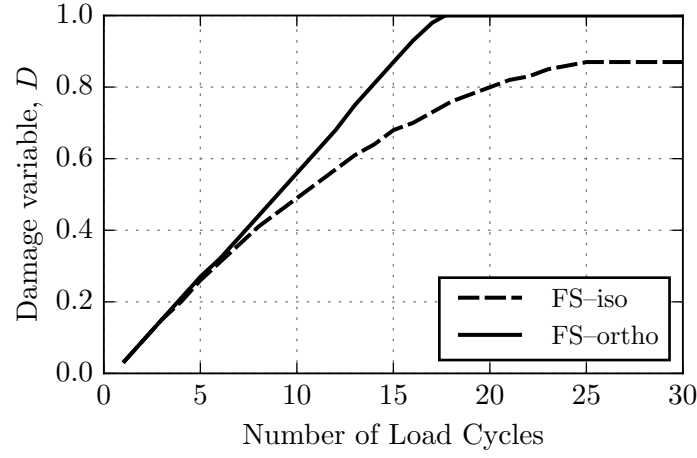


**Figure 3.11:** Comparison of the damage evolution of the SET utilizing isotropic (FS-iso) and orthotropic (FS-ortho) damage modeling.

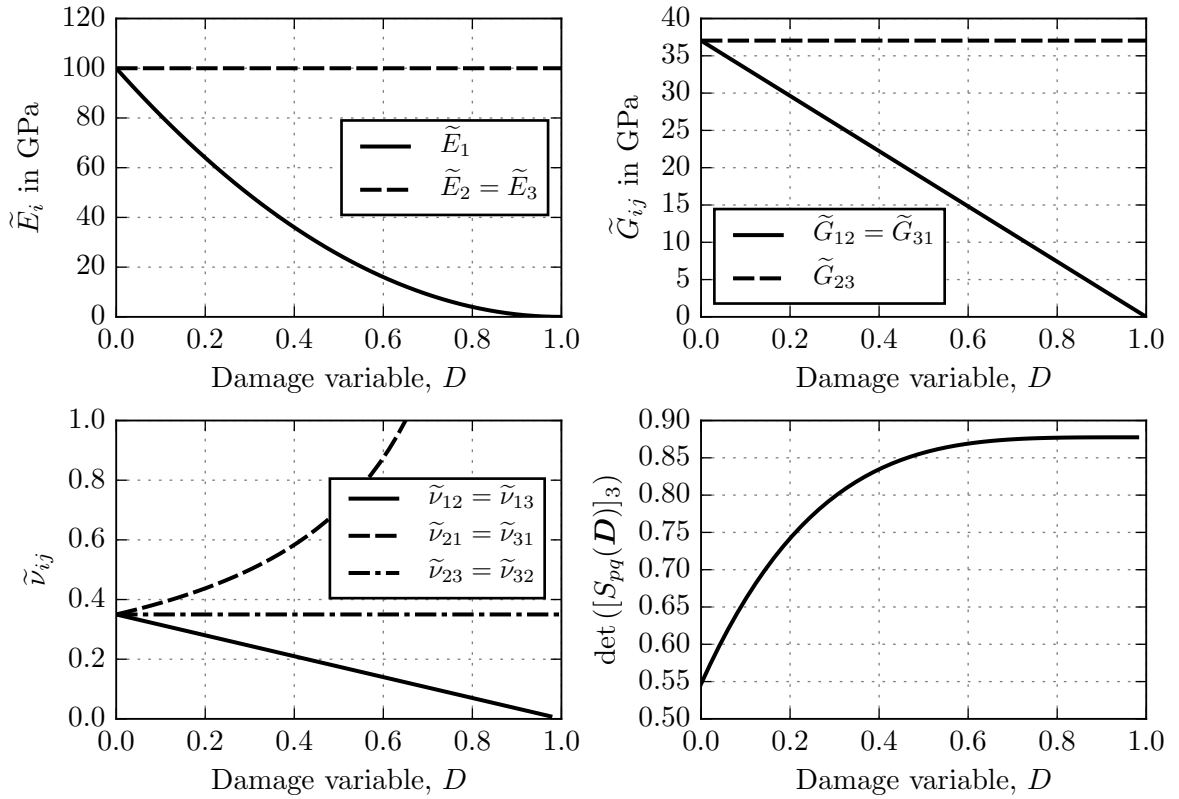


**Figure 3.12:** Degradation of the effective elastic properties according to the hypothesis of complementary strain energy equivalence for orthotropic damage modeling. The principal material axes are aligned with the critical plane coordinate system,  $\xi_1$ - $\xi_2$ - $\xi_3$ .

decays quadratically with the damage variable, whereas  $\tilde{E}_2$ , and  $\tilde{E}_3$  remain unchanged. The shear moduli,  $\tilde{G}_{12}$  and  $\tilde{G}_{31}$ , follow a linear slope, whereas  $\tilde{G}_{23}$  remains constant. The Poisson ratio's,  $\tilde{\nu}_{ij}$  are depicted in the third figure and follow similar trends. The orthotropic compliance matrix of the damaged material,  $[S_{pq}(\mathbf{D})]$ , has to be positive-definite [1],

$$\det ([S_{pq}(\mathbf{D})]_3) = 1 - \tilde{\nu}_{12}^2 \frac{\tilde{E}_1}{\tilde{E}_2} - \tilde{\nu}_{23}^2 \frac{\tilde{E}_2}{\tilde{E}_3} - \tilde{\nu}_{13}^2 \frac{\tilde{E}_1}{\tilde{E}_3} - 2\tilde{\nu}_{12}\tilde{\nu}_{23}\tilde{\nu}_{13} \frac{\tilde{E}_1}{\tilde{E}_3} > 0 \quad , \quad (3.51)$$

which is governed by the hypothesis of complementary strain energy equivalence and is fulfilled for the stated problem.

### 3.6 Application – Microcantilever Beam

Before the orthotropic CDM approach is employed for power semiconductors, the approach is exemplified under purely mechanical loading conditions. Cyclic bending experiments on freestanding polycrystalline Copper (Cu) micron lines have been conducted in [236]. The micron lines, comparable to micrometer-sized cantilever beams, have been produced by a photolithographic process. The microcantilever beams have been used as bending samples in LCF experiments at constant temperature. One of the tested specimens is simulated by a 3D-FEM analysis with boundary conditions reflecting the experimental test conditions. Material damage is modeled by the numerical analysis, resulting in structural deterioration. The predicted spatial damage distribution and structural degradation are compared to the experimental data.

The microcantilever beam, modeled for the FEM analysis, has a cross-section of  $23\mu\text{m} \times 21\mu\text{m}$  and a length of  $260\mu\text{m}$ . The average grain size of the polycrystalline Cu is  $2.7\mu\text{m}$ . The specimen is illustrated by the 3D-FEM model depicted in Fig. 3.13. Tetrahedral, fully integrated, continuum elements with quadratic interpolation functions are utilized for the discretization. The mesh is refined in the region of expected fatigue damage near the fillet. Displacement boundary conditions are used for fixation and cyclic loading which is applied at the neutral axes at the end of the beam. The LCF loading is conducted for constant displacement amplitudes,  $u_a = 19.5\mu\text{m}$ , with an R-ratio of  $R = -1$ .

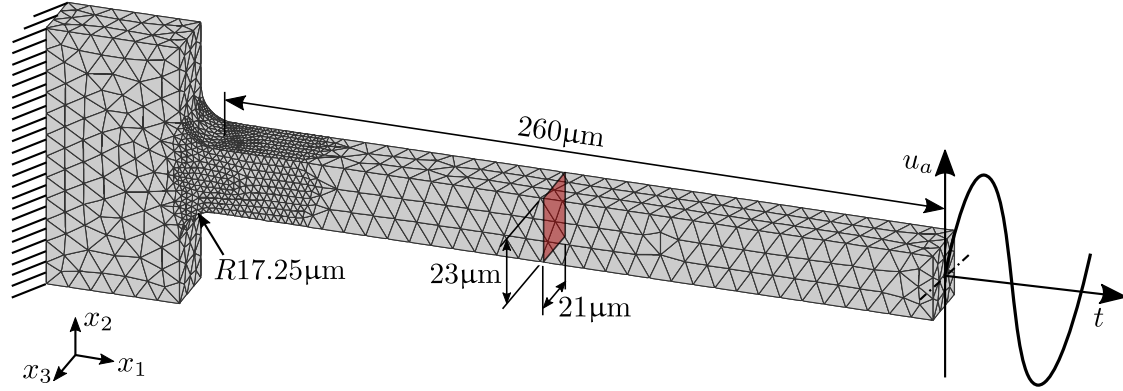


**Figure 3.13:** 3D FEM model of the micrometer-sized cantilever beam, indicating the geometry, mesh discretization, and boundary conditions.

The elasto–plastic constitutive behavior of the polycrystalline Cu is modeled as isotropic in the undamaged state. The Chaboche nonlinear kinematic hardening model [44, 45] for only one back–stress component,

$$\dot{\mathbf{X}} = \frac{2}{3}C_1\dot{\varepsilon}^{\text{pl}} - \gamma_1|\dot{\varepsilon}^{\text{pl}}|\mathbf{X} \quad , \quad (3.52)$$

is employed for the modeling of the plastic hardening behavior.  $\mathbf{X}$  is the back–stress tensor,  $\dot{\varepsilon}^{\text{pl}}$  is the plastic strain rate, and  $C_1$  and  $\gamma_1$  are material parameters. The elastic–plastic material properties are obtained from Sample A in [235], where tensile tests of the same polycrystalline Cu as utilized in [236] have been carried out. The stress–strain curve is used to identify the Young’s modulus,  $E$ , the yield stress,  $\sigma_Y$ , and the plastic parameters  $C_1$  and  $\gamma_1$ . The Poisson’s ratio,  $\nu$ , is chosen to be equal to that of bulk copper. The elasto–plastic material properties are summarized in Table 3.2.

The cyclic bending simulations are conducted in the LCF regime. Therefore, the part of the Basquin equation in the FS lifetime model is neglected. This simplifies the implicit Eq. (3.10) and, therefore,  $N_{\mathcal{D}}$  can be calculated explicitly. The factor weighing the influence of  $\sigma_n^{\text{max}}$  on fatigue microcrack nucleation in Eq. (3.1) is taken equal to unity,  $\kappa = 1$ , [123]. Additionally, the required fatigue parameter set for the onset criterion is reduced and only  $\gamma'_f$  and  $c_f$  need to be obtained. The choice of these shear fatigue material properties is based on the suggestions in [216], which are summarized in Table 2.1. For the polycrystalline Cu

**Table 3.2:** Elastic–plastic material properties of polycrystalline Copper with an average grain size of  $2.7\mu\text{m}$  utilizing the Chaboche nonlinear kinematic hardening model.

$E$	$\nu$	$\sigma_Y$	$C_1$	$\gamma_1$
100 GPa	0.35	125 MPa	1800 MPa	8.5

the fatigue properties  $\varepsilon'_f = 0.46$  and  $c = -0.3 \pm 0.1$  have been reported in [236]. Due to the large standard deviation of  $c$ , further sources for a comparable material were searched for. In [155], a value of  $c = -0.43$  has been reported for a similar polycrystalline Cu. Additionally, a value of  $c = -0.6$  is typically used for bulk Cu. Based on these findings, the fatigue properties are estimated as summarized in Table 3.3.

In contrast to the above properties, the parameters  $\varkappa_1$  and  $\varkappa_2$  of the damage evolution law, Eq. (3.17), cannot be obtained directly from experimental data and have to be calibrated by comparison of experimental and numerical results. In [236], only the structural degradation of a single specimen has been reported. Therefore, a proper calibration with one data set and a verification with a different data set is not possible. Hence, the same data set is utilized for calibration and demonstration of the approach. The values reported in [24] for solders are used as a starting point for the calibration. Various simulations, employing isotropic damage modeling, by different combinations of  $\varkappa_1$  and  $\varkappa_2$  have been carried out, resulting in the values given in Table 3.3. These values seem to sufficiently represent the damage evolution for the purpose of demonstration. Improved results may be obtained by application of optimization software. The coefficient  $\alpha$  in the damage evolution law, Eq. (3.17), has been reported to give good correlation with experimental data for values between 0.0055 for AlSiCu alloys [222] and 0.007 in case of austenitic stainless steels [78], subjected to LCF and TMF test conditions. Therefore, a value of  $\alpha = 0.006$ , in accordance with [123], is utilized in the present work.

The cycle jump technique is employed and the parameters are chosen as follows. An initial number of cycles overshooting the damage onset criterion is defined as  $\Delta N_{\text{os}} = 50$  in Eq. (3.44). The maximum and minimum damage tolerances in Eq. (3.46) are chosen as  $\Delta D_{\text{max}} = 0.6$  and  $\Delta D_{\text{min}} = 0.3$ . The maximum number of cycle jumps is limited by  $N_{\text{max}} =$

**Table 3.3:** Estimated fatigue and damage properties for polycrystalline Copper with an average grain size of  $2.7\mu\text{m}$ .

$\kappa$	$\gamma'_f \approx \sqrt{3}\varepsilon'_f$	$c_\gamma \approx c$	$\alpha$	$\varkappa_1$	$\varkappa_2$
1.0	0.75	-0.45	0.006	$1.9 \cdot 10^{-6} \frac{\text{mm}}{\text{cycle} (\text{MPa})^{\varkappa_2}}$	0.45

200 and the minimum number is set to  $N_{\text{max}} = 50$ . Additionally, viscous regularization is necessary to overcome convergence difficulties. Therefore, an energy–dissipation ratio of  $1 \cdot 10^{-4}$  is utilized for nonlinear stabilization. This way, the total amount of artificial energy dissipated during the simulation is less than 1% of the total strain energy and should not affect the accuracy of the results.

The cantilever beam has been simulated with two simplification strategies, (i) modeling of isotropic damage behavior, and (ii) approximation of the critical plane. In the orthotropic case no material damage is considered for in–plane direction of the critical plane by  $\omega = 0$ . The normal vectors to the approximated critical planes are depicted in Fig. 3.14. The displayed normal vectors are evaluated at first damage onset in the structure, which occurs at  $N = 682$  load cycles. The vectors are scaled by the damage onset criterion,  $\mathcal{D}$ , and depicted only for the elements on the outer surface of the beam in a side and top view.

The following contour plots are depicted for orthotropic damage modeling by approximation of the critical plane. The numerical results indicating the accumulation of the damage onset criterion,  $\mathcal{D}$ , and the evolution of the damage variable,  $D$ , are depicted in Fig. 3.15. On the left–hand side, the spatial and temporal evolution of  $\mathcal{D}$  is displayed. Three different time points indicated by the number of applied load cycles,  $N$ , are depicted. The spatial distribution of the damage onset criterion mainly evolves towards the neutral axis, whereas the elongation along the beam axis remains nearly unchanged. The corresponding state of material damage is indicated by the damage variable on the right–hand side of the figure. Material failure, modeled by a complete loss of the load carrying capability normal to the critical plane is indicated by  $D = 1$ .

Structural failure of the specimen is defined by the obtained reaction force. A decrease of 85% in the amplitude of the reaction force compared to the amplitude of the first load cycle is defined as stopping criterion. For the orthotropic material degradation this criterion

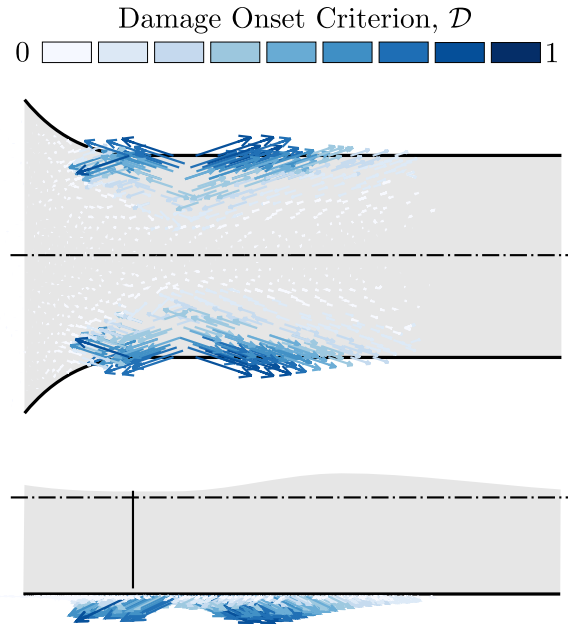


**Figure 3.14:** Vector plot of the unit normal vectors,  $\xi_1$ , scaled by the damage onset criterion, and computed for the first stabilized cycle of the simulation. The vectors are depicted only for elements on the outer beam surface in a side and top view.

corresponds to a number of load cycles of  $N = 2032$ . The predicted damage criteria are depicted in Fig. 3.16 for this number of load cycles. Additionally, Scanning Electron Microscopy (SEM) images of the simulated specimen are provided next to the numerical results. The damage state of the specimen shortly before rupture is shown on the left-hand side, whereas the failed specimen is displayed on the right-hand side. The formation of persistent slip bands in the polycrystalline Cu is clearly visible and correlates well with the region predicted by the damage onset criterion,  $\mathcal{D}$ . These slip bands lead to the formation and propagation of a dominant macrocrack resulting in fracture of the specimen. The location of the macrocrack is within the predicted region of material failure indicated by the damage variable,  $D = 1$ .

The reaction force indicating structural deterioration, for isotropic (FS-iso) and orthotropic damage modeling (FS-ortho), are displayed in Fig. 3.17. The depicted data represent an envelope curve over the load response, given by the maximum load amplitude in each load cycle. The obtained reaction force amplitude is compared to the experimental data [236].



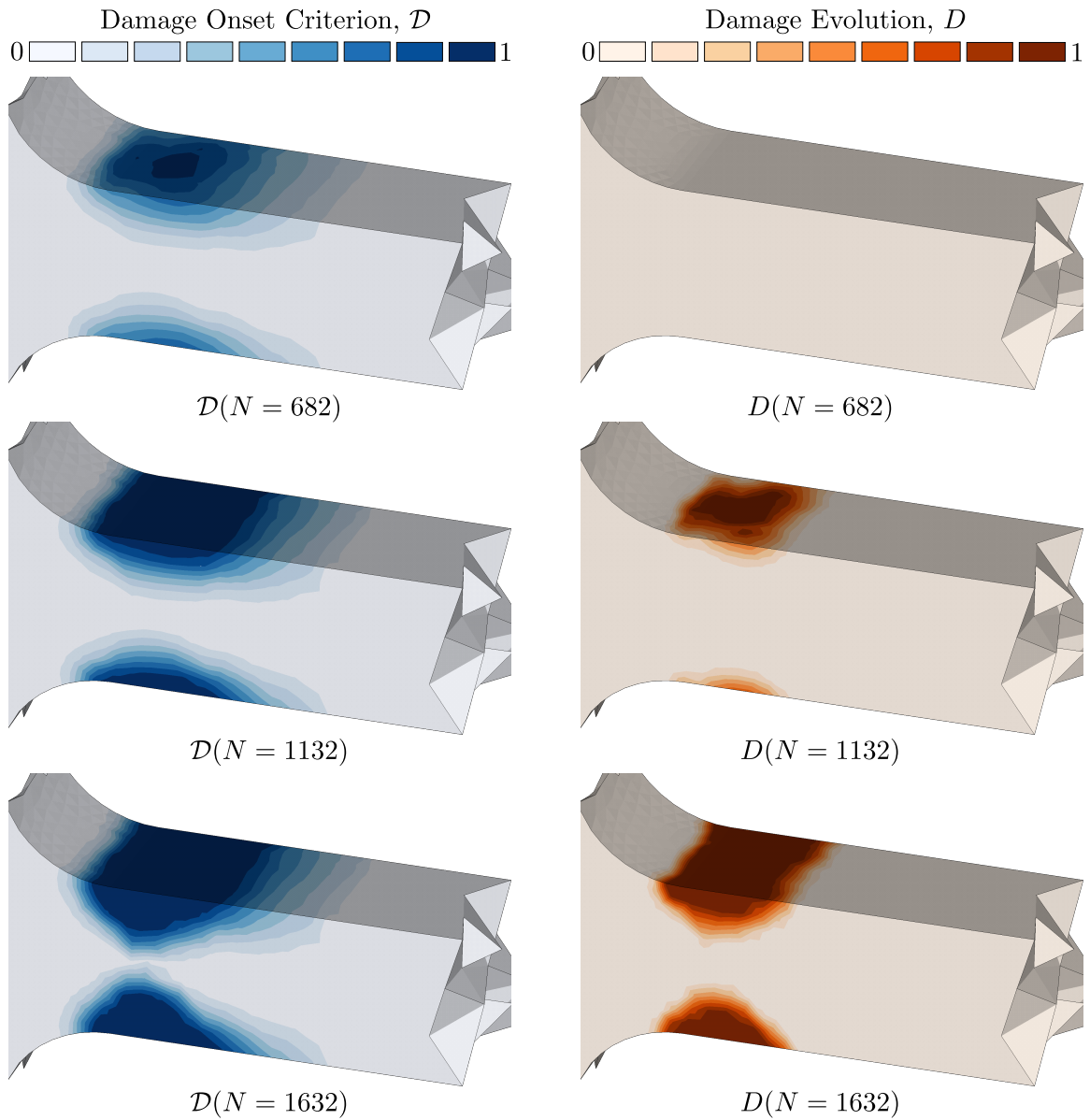


**Figure 3.15:** Contour plots of the damage onset criterion,  $\mathcal{D}$ , (left), and the damage variable,  $D$ , (right), employing the approximated orthotropic damage modeling strategy. Three different damage states are depicted and identified by the number of applied load cycles,  $N$ . Only the fine mesh region near the fillet of the microcantilever beam is displayed and the coarse elements of the surrounding region are hidden.

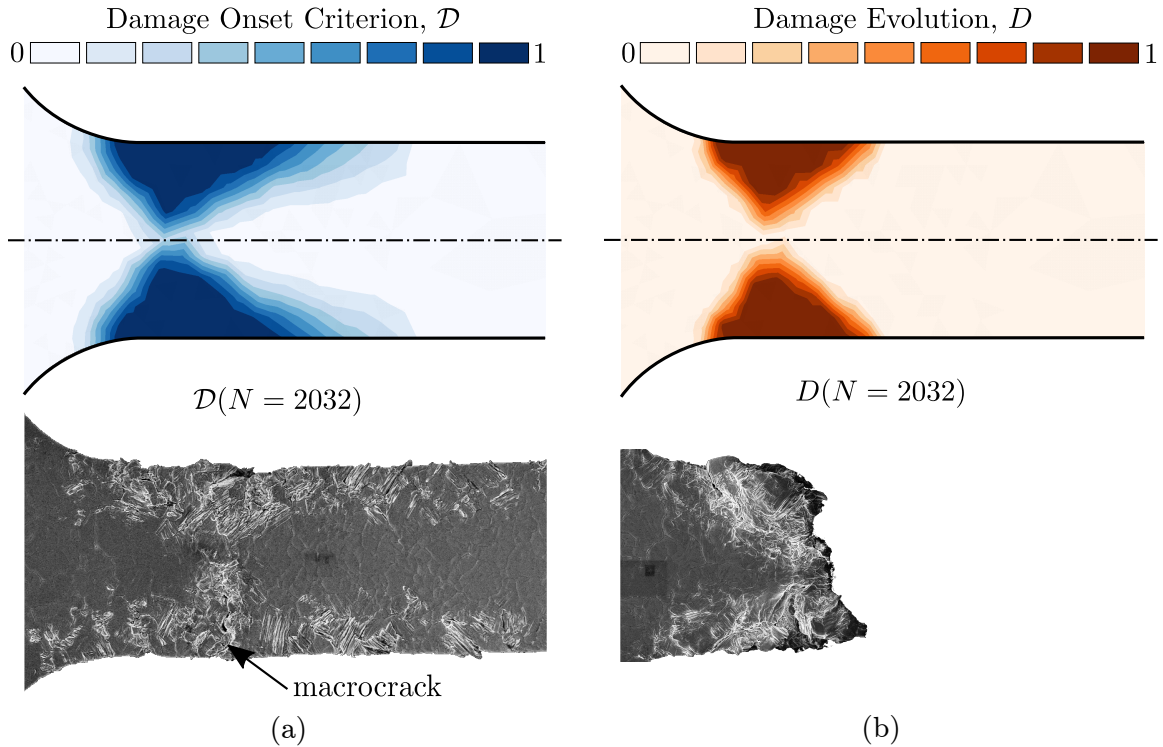


**Figure 3.16:** Contour plots of the damage onset criterion,  $\mathcal{D}$ , (left) and the damage variable,  $D$ , (right) computed for the last stabilized cycle in the simulation employing the approximated orthotropic damage modeling strategy. The fatigued specimens, a courtesy of KAI GmbH, Villach, are depicted in the second row: (a) specimen shortly before rupture, (b) failed specimen.

In contrast to the structural degradation of the test specimen, no stiffness degradation is obtained in the simulation before the damage onset criterion at  $N = 682$  is reached. Furthermore, the influence of localized material degradation on the simulated structural behavior is negligible until  $N \approx 1000$  load cycles. Afterwards, the effects of material degradation onto the structural deterioration become visible and result in a decreasing reaction force. At about  $N \approx 1600$  load cycles the rate of the structural deterioration slows down until the stopping criterion is reached. The isotropic damage model has been utilized to calibrate the material parameter  $\varkappa_1$  and  $\varkappa_2$ . This model results in a slightly conservative prediction compared to the experimental data, which is mainly influenced by these two parameters. The orthotropic damage model with approximated critical planes utilizes the same set of input parameter. This way, the difference between isotropic and orthotropic damage modeling is illustrated. In the orthotropic case stiffness degradation

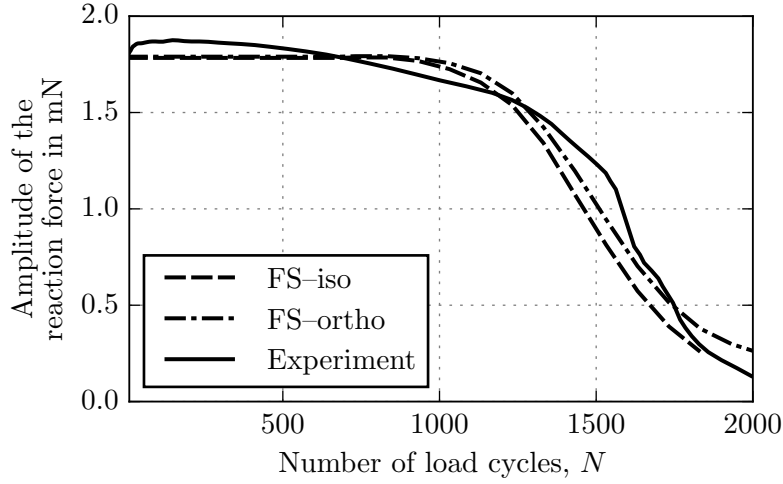


**Figure 3.17:** Amplitude of the reaction force over the number of load cycles, indicating structural deterioration of the microcantilever beam. The two simulation strategies employing the isotropic damage modeling (FS-iso), and the approximated orthotropic damage modeling (FS-ortho) are compared to experimental results.

is direction dependent resulting in a higher residual stiffness in certain load directions of the damaged elements. Hence, the obtained structural deterioration is slower than in the isotropic case.

In the orthotropic case the critical plane orientation has been approximated by the most critical plane for all material points in the first stabilized cycle. To evaluate the error made by this approximation the dot product between the approximated and the predicted, Eq. (3.13), critical plane,  $\xi_1^c \cdot \xi_1^{\text{approx}}$ , is depicted in Fig. 3.18, for elements already in the damage state ( $\mathcal{D} = 1$  or  $D > 0$ ). A value of  $\xi_1^c \cdot \xi_1^{\text{approx}} = 1$  indicates that the unit normal vectors of the approximated and the predicted critical plane are aligned. Hence, the two plane orientations are equivalent. In contrast, a value of  $\xi_1^c \cdot \xi_1^{\text{approx}} = 0$  states that the predicted critical plane is perpendicular to the approximated one. Since, the orthotropic material response also changes if different plane orientation are utilized during the simulation the predicted critical plane orientation may, again, change, if the identified critical planes are utilized instead of the approximated ones. However, this influence is assumed to be negligible, since a significant difference between the orientations of the approximated and predicted critical planes is only seen for elements near the neutral axis. These elements

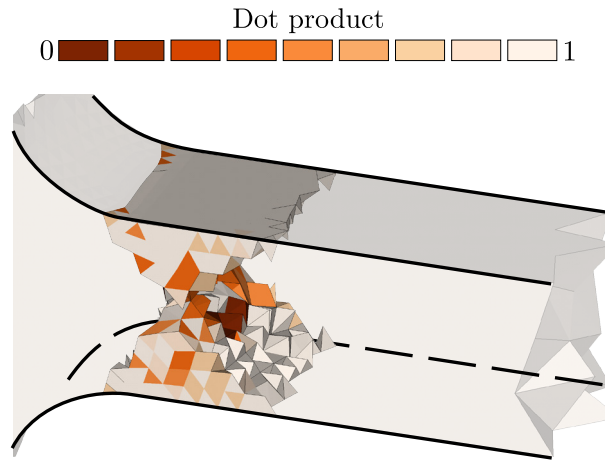


**Figure 3.18:** Dot product between the normal vectors of the approximated critical planes after the first stabilized load cycle and the predicted critical plane during the simulation, when the damage onset criterion is reached.

reach the damage onset criterion at the end of the specimen lifetime. The influence of a change in the plane orientation on the structural deterioration can, therefore, be neglected.

### 3.7 Summary

A local Continuum Damage Mechanics (CDM) approach is formulated for Thermo-Mechanical Fatigue (TMF) conditions and focuses on micrometer-sized structures. Microcrack nucleation and, especially, the resulting orientation of distributed microcracks are considered to influence the elastic properties of the damaged material. Therefore, a multiaxial fatigue criterion combined with an orthotropic CDM model is utilized to predict the fatigue lifetime by consideration of a direction dependent loss of material integrity.

The Fatemi-Socie (FS) critical plane method in combination with the Palmgren-Miner linear damage accumulation rule is employed as a damage onset criterion. The multiaxial fatigue criterion describes stage I microcrack nucleation on planes experiencing maximum shear strain. The orientation of the critical plane is identified by the Maximum Damage Method. Material degradation starts after the damage onset criterion is reached and follows a damage evolution law based on the inelastic strain energy density until material failure occurs. The elastic properties for an orthotropic loss of material integrity are described

by the hypothesis of complementary strain energy equivalence. A user subroutine would be required to correctly model the orthotropic stiffness degradation with a second order damage tensor. The coding of such a subroutine was beyond the scope of the present work. As a work around two approximation strategies are employed to demonstrate the principal behavior of the damage degradation obtained by the formulated model.

The approach is implemented into the commercial Finite Element Package Ansys APDL v16.2. The CDM formulation in combination with the Finite Element Method allows for the simulation of the whole damage process. This engineering method, also known as local approach to fracture, enables the prediction of spatial and temporal evolution of material damage, resulting in a detectable deterioration of the structural behavior.

The approach is exemplified on micrometer-sized cantilever beams under isothermal LCF conditions. The calibration of the approach and the applicability of the model on micrometer-sized structures is demonstrated. The obtained numerical results are in good agreement with the available experimental data. In Chapter 5 the approach is applied to a power semiconductor under TMF conditions.



## Chapter 4

# Cyclic Cohesive Zone Model for the Interface

A cyclic cohesive zone model is developed which is an extension of an exponential traction–separation law describing the constitutive behavior of the interface. Damage degradation under thermo–mechanical fatigue loading is accounted for using a cycle–by–cycle analysis. A Paris’ law type formulation is utilized to model fatigue damage which is based on physically interpretable interface properties, overcoming the need of any parameter fitting. Mixed–Mode loading is considered by the BK–criterion. Varying load amplitudes are captured by the model formulation. For constant amplitude loading or slowly changing load amplitudes a cycle jump technique is implemented to decrease the computational time. The effect of interface degradation onto the heat transfer across the damaged interface is modeled by linking the mechanical damage variable with the thermal conductance of the interface. The model is implemented within the framework of the Finite Element Method and includes non–local evaluation of structural parameters. Finally, the proposed model is demonstrated on Mode I, Mode II, and Mixed–Mode delamination tests.

## 4.1 Introduction

Interface failures in power semiconductor devices can occur at very different length scales and between a variety of different materials. Typically, power semiconductors are subjected to a large number of high current and high power density pulses. These loading conditions introduce very high temperatures and temperature gradients into the multilayer structure of a power semiconductor device [163]. The large mismatch between the coefficients of thermal expansion of the involved materials leads to high mechanical tractions at the interfaces and, consequently, to a risk of decohesion and delamination of the interface. The repetitive application of overload pulses may lead to cyclic delamination growth and failure of the device. Interface failures in power semiconductor devices are detected at a variety of different locations. Delaminations may occur between the die attach solder of the silicon substrate and the copper heatsink [120, 149], at the back metal [213], or between the direct-copper-bond substrate and the copper layer [97]. Furthermore, between wire bonds and the metallization [52] or the mold compound and the leadframe [65]. Finally, interface failure between the chip and the chip metallization may occur as well [21, 210]. Dependent on the location of the interface failure, different error conditions of the power semiconductor device may arise.

This chapter focuses on the modeling and simulation of cyclic delamination growth at interfaces. Cohesive Zone Models (CZM) are widely used in the framework of the Finite Element Method (FEM) to model delamination growth. These models use traction–separation laws to describe the complex damage process occurring at the interface of a bi-material compound. The implementation of traction–separation laws into FEM can be easily done and a variety of different formulations have been proposed. Reviews of CZMs which account for steady–state crack growth can be found in [20, 88].

In recent years, these formulations have been extended to account for cyclic delamination growth, which are then called Cyclic Cohesive Zone Models (CCZM). In general, these models can be categorized into two groups [11], namely hysteresis loop damage models [169, 200, 241, 242] and envelope load damage models [162, 179, 199]. Typically, hysteresis loop damage models are found in applications for the LCF regime, whereas envelope load damage models are found in HCF problems [128].



Hysteresis loop damage models [33, 202] are based on a loading–unloading formulation, which enables the consideration of varying load amplitudes during a fatigue analysis, see Fig. 4.1(a). Damage development at the interface is considered by interfacial stiffness and strength reduction during loading. This reduction is described by damage evolution laws which are often based on fitting parameters. Calibration of such models can be a difficult task and the predictive capabilities of such formulations have not been sufficiently addressed yet [11].

In contrast, for higher numbers of load cycles so-called envelope load damage models [12, 90, 131, 224] are utilized, see Fig. 4.1(b). The envelope load is ramped in an initial load increase. Subsequently, the cycle jump technique for the damage rate integration is employed and fatigue damage simulated. These models are often combined with fracture mechanics concepts, such as the Paris' law, for the description of the damage evolution under fatigue loading. This way, the formulations rely on physically interpretable interface parameters obtained from experimental tests, which provides a major advantage compared to models relying on fitting parameters. This advantage in the model calibration combined with the ability of treating effects such as mode mix, loading ratio, and delamination thresholds makes the envelope load damage models the most advanced CCZM currently available [11]. Parameter sensitivity and benchmark studies of the different formulations for HCF have been presented in [13, 109]. A drawback of envelope load damage models compared to hysteresis loop damage models is that they are often limited to constant amplitude loading. Only few models, based on this formulation, have been presented which account for varying loading conditions, e.g. [128].

Most of the above-mentioned models have been applied to two-dimensional (2D) problems only. Especially, in the case of envelope load damage models [90, 224] the extension to three-dimensional (3D) problems is a non-trivial task. This is caused by the required structural properties such as the delamination propagation direction, the energy release rates or the cohesive zone length. The determination of structural properties during the simulation requires non-local evaluation techniques. Therefore, different approaches or simplification strategies have been presented [3, 119, 229] to extend the available model formulation to account for 2D cyclic delamination growth in a 3D problem.

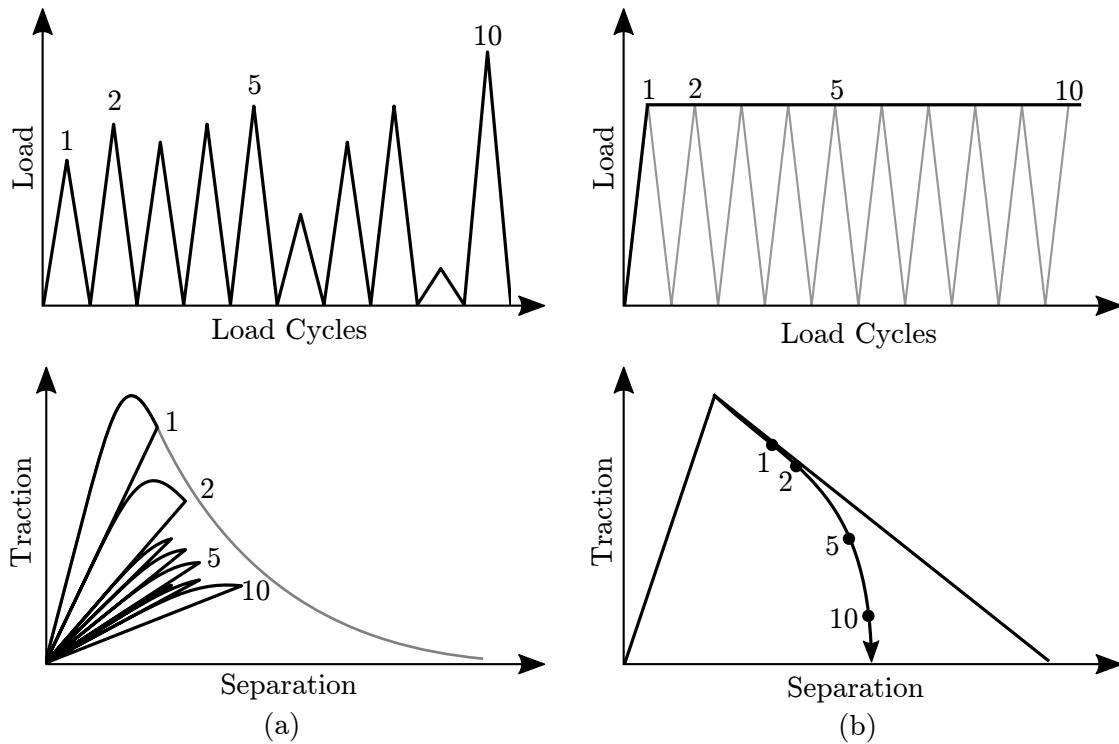


**Figure 4.1:** Schematic representation of the interface damage models. (a) hysteresis loop damage model with varying load amplitude, (b) envelope load damage model with a fixed load amplitude (modified from [11]).

In the present work, overload conditions of power semiconductors are assumed to cause cyclic delamination growth at the interface between the Si chip and the Cu power metallization. The number of overload pulses occurring during the lifetime of power semiconductors is associated with the LCF regime. Further, cyclic delamination growth between the chip and the metallization changes the local stress and strain fields. Therefore, a hysteresis loop formulation, able to account for variable loading conditions, is required for the present CCZM development. Instead of fitting parameters, a phenomenological fracture mechanics approach is employed for fatigue damage evolution. This way, the CCZM is based on physically interpretable interface properties, rather than fitting parameters.

The models utilized as foundation for the current work have been originally developed to account for fatigue loaded composite structures. In such layered components, delaminations compromise the structural integrity and lead to a loss in the load carrying capability. The CCZMs developed for this application field are the most advanced models accessible in the

literature and are, therefore, employed in the present work. These models have been focused on the mechanical degradation and do not consider effects such as thermo–mechanical fatigue or the heat flux across the interface. In order to apply such models to TMF in power semiconductor devices a thermo–mechanical extension needs to be included into the CCZM formulation.

Thermo–mechanical CZMs have been proposed in [17, 92, 110, 172, 240] and [23], where the latter work has been focused on solder joint fatigue. The present model follows the work of [93, 172], which has been applied to a CCZM in [125]. The model accounts for cyclic delamination growth under thermo–mechanical loading conditions. The thermal conductance of the interface is degraded in accordance to the damage state of the mechanical damage variable. This way, the mechanical and thermal degradation of the interface are described by one single damage variable.

The thermo–mechanical cyclic cohesive zone model is implemented into Ansys APDL v16.2 utilizing the user contact subroutine. Additionally, a cycle jump technique is employed to increase the computational efficiency and to allow for the treatment of a higher number of load cycles.

## 4.2 Constitutive Model

The proposed Cyclic Cohesive Zone Model (CCZM) is derived in this section. The CCZM is based on the formulation derived in [84] and utilizes an exponential traction–separation law to describe the constitutive interface behavior. Mixed–mode behavior is accounted for by the BK–criterion [25]. The exponential traction–separation law combined with the BK–criterion has been derived in [82] and is shortly reviewed and summarized for single–mode and mixed–mode failure in the beginning. The fatigue model extension is motivated by the CCZM formulation proposed in [83]. There, the range of the crack tip opening displacement (CTOD) has been utilized for the fatigue damage computation. The present model, in contrast, accounts for fatigue damage by a Paris’ law like approach based on the energy release rate [224]. This damage rate formulation requires the length of the cohesive zone, i.e. a structural property. Instead of approximating this cohesive zone length, as in the original formulation, the present model utilizes a non–local evaluation of the cohesive

zone length during the simulation, resulting in an increased accuracy of the approach. A nonlinear penalty contact formulation accounts for interface closure. The modeling of the degradation in the heat transfer across the interface is based on [125]. There, the thermal conductance is dependent on the mechanical damage variable, resulting in a degradation of the thermal conductance during damage progression. A simple cycle jump technique for load blocks of constant amplitudes is employed to reduce the computational time. The CCZM is implemented within the framework of the FEM, and important implementation aspects are provided at the end of this section.

### 4.2.1 Single-Mode Delamination Growth for Monotonic Loading

The CCZM builds upon an exponential traction-separation law for steady-state crack growth [84]. By considering only single-mode failure the exponential traction-separation law provides the interfacial traction as

$$T(\Delta) = T^o \bar{\Delta} \exp\left(\frac{1 - \bar{\Delta}^\beta}{\beta}\right) \quad \text{with} \quad \bar{\Delta} = \frac{\Delta}{\Delta^o} \quad . \quad (4.1)$$

Herein,  $\bar{\Delta}$  is the normalized separation and  $(\Delta^o, T^o)$  define the point of damage onset. The traction-separation law is depicted in Fig. 4.2. Interface failure is accounted for by correlating the area below the traction-separation law to the critical energy release rate as

$$\mathcal{G}_c = \int_0^\infty T(\Delta) \, d\Delta = T^o \Delta^o \psi(\beta) \quad , \quad (4.2)$$

where

$$\psi(\beta) = \beta^{\frac{2-\beta}{\beta}} \Gamma\left(\frac{2}{\beta}\right) \exp\left(\frac{1}{\beta}\right) \quad . \quad (4.3)$$

Herein,  $\beta \in \mathbb{R}^+$  is a parameter influencing the shape of the cohesive law and  $\Gamma(\bullet)$  is the Euler gamma function. The traction-separation law, as defined in Eq. (4.1), holds true only for monotonically increased loads. The work due to opening of the interface is still recoverable at closing. Hence, a damage formulation is included, and damage progression is accounted for by an elasto-damage model. An internal state variable is introduced and

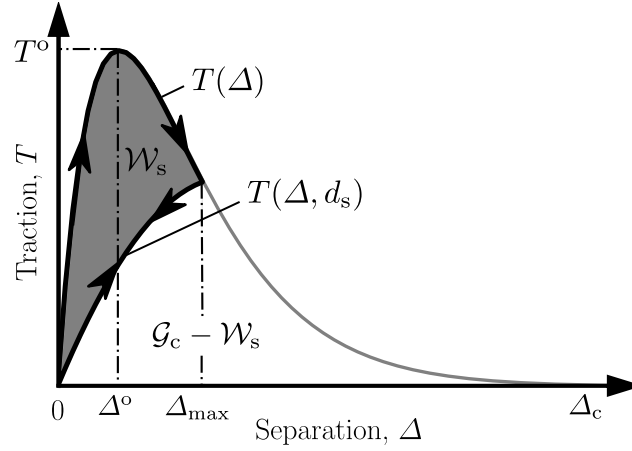


**Figure 4.2:** Traction–separation law of the steady–state delamination growth formulation. Shading indicates the amount of the dissipated energy rate,  $\mathcal{W}_s$ , during the damage process caused by interface opening.

a nonlinear unloading path back to the origin results from the formulation. The modified traction–separation law reads [84]

$$T(\Delta, d_s) = T^0 \bar{\Delta} \exp\left(\frac{2 - \bar{\Delta}^\beta/d_s - d_s}{\beta}\right), \quad (4.4)$$

where  $d_s$  is the internal state variable describing the damage state. In the undamaged case  $d_s = 1$  and for complete interface failure  $d_s \rightarrow \infty$ . Since thermodynamics requires irreversible energy dissipation associated with a damage process, the internal damage variable needs to fulfill the following restrictions

$$\dot{d}_s = \begin{cases} \dot{\bar{\Delta}}^\beta & \text{if } \bar{\Delta}^\beta \geq d_s \\ 0 & \text{if } \bar{\Delta}^\beta < d_s \end{cases}, \quad (4.5)$$

and damage onset occurs at  $(\Delta^0, T^0)$ . In a more convenient form, the evolution of  $d_s$  can be formulated as

$${}^{t+\delta t}d_s = \max(1, {}^t d_s, {}^{t+\delta t}\bar{\Delta}^\beta), \quad {}^0 d_s = 1, \quad (4.6)$$

where  $t$  is the time and  $\delta t$  the time increment. The internal state variable ranges from  $d_s \in [1, \infty)$ ; this is caused by the exponential nature of the cohesive law. In the framework of continuum damage mechanics, damage variables in the range from  $D_s \in [0, 1]$  are widely

used. Hence, in the present work an energy definition is introduced to describe the state of the static damage variable,

$$D_s(\Delta_{\max}) = \frac{\mathcal{W}_s}{\mathcal{G}_c} = \frac{1}{\mathcal{G}_c} \left[ \int_0^{\Delta_{\max}} T(\Delta) \, d\Delta - \int_0^{\Delta_{\max}} T(\Delta, d_s) \, d\Delta \right] . \quad (4.7)$$

The static damage variable,  $D_s$ , is defined by normalizing the energy dissipation rate,  $\mathcal{W}_s$ , by the critical energy release rate,  $\mathcal{G}_c$ , [224].  $\mathcal{W}_s$  is computed by calculating the area under the undamaged constitutive law,  $T(\Delta)$ , up to the maximum separation,  $\Delta_{\max}$ , and subtracting the area below the damaged constitutive law,  $T(\Delta, d_s)$ , up to the same separation  $\Delta_{\max}$ , see Fig. 4.2. Thus,  $D_s = 0$  describes the undamaged interface and, due to the exponential nature of the cohesive law,  $D_s = 0.99$  is accepted as interface failure. The computation of the integral is provided in Appendix B.

#### 4.2.2 Mixed-Mode Delamination Growth for Monotonic Loading

Mixed-mode loading is accounted for by the BK-Criterion [25]. The formulation for the BK-Criterion has been derived in [82] and is summarized below. The interfacial constitutive equations are obtained as

$$\begin{bmatrix} \bar{T}_1 \\ \bar{T}_2 \\ \bar{T}_3 \end{bmatrix} = \begin{bmatrix} \bar{\Delta}_1/\nu \\ \bar{\Delta}_2/\nu \\ \langle \bar{\Delta}_3 \rangle \end{bmatrix} \mathcal{S} \exp\left(\frac{2 - \lambda^\beta/d_s - d_s}{\beta}\right) , \quad (4.8)$$

where the indices (1,2) denote the shear directions and (3) the normal direction of the interface. The Macaulay brackets are denoted by  $\langle \bullet \rangle$  and are defined in Eq. (2.9). The term  $\mathcal{S}$  is given as

$$\mathcal{S} = 1 + (\nu - 1)B^\eta , \quad (4.9)$$

where  $\eta$  is the BK-exponent and  $\nu = \mathcal{G}_{IIc}/\mathcal{G}_{Ic} = \mathcal{G}_{IIIc}/\mathcal{G}_{Ic}$ .  $\mathcal{G}_{Mc}$  for  $M = \{I, II, III\}$  denotes the critical energy release rates for Mode I, Mode II and Mode III, respectively. The local mode mixity is given as

$$B = \left(1 - \frac{\langle \bar{\Delta}_3 \rangle^2}{\lambda^2}\right) , \quad (4.10)$$

where the effective separation is computed by the individual separations in all three coordinate directions and defined as

$$\lambda = \left( (\overline{\Delta}_1)^2 + (\overline{\Delta}_2)^2 + (\overline{\Delta}_3)^2 \right)^{\frac{1}{2}} . \quad (4.11)$$

Consequently, the evolution of the internal state variable can be defined as

$${}^{t+\delta t}d_s = \max(1, {}^t d_s, {}^{t+\delta t} \lambda^\beta) \quad \text{where} \quad {}^0 d_s = 1 . \quad (4.12)$$

The critical energy release rate under mixed-mode loading is formulated in analogy to the BK-criterion [25], but with the local mode mixity,  $B$ , as proposed in [223] and reads

$$\mathcal{G}_c = \mathcal{G}_{Ic} + (\mathcal{G}_{IIc} - \mathcal{G}_{Ic}) B^\eta . \quad (4.13)$$

An embellished calligraphic font is chosen to emphasize that the obtained mixed-mode critical energy release rate,  $\mathcal{G}_c$ , is calculated with the local mode mixity,  $B$ . In addition, a BK-like onset criterion proposed in [223] for mixed-mode loading,

$$(T^\circ)^2 = (T_I^\circ)^2 + \left( (T_{sh}^\circ)^2 - (T_I^\circ)^2 \right) B^\eta , \quad (4.14)$$

is utilized, where the shear onset traction is obtained from  $T_{sh}^\circ = \sqrt{(T_{II}^\circ)^2 + (T_{III}^\circ)^2}$ . The mixed-mode parameters  $\mathcal{G}_c$  and  $T^\circ$  together with the shape parameter,  $\beta$ , enable the definition of a mixed-mode cohesive law in dependence of the effective separation,  $\lambda$ , as depicted in Fig. 4.3. Once the effective separation reaches the critical effective separation,  $\lambda = \lambda_c$ , mixed-mode delamination growth is obtained.

Finally, the same energy definition as in the single-mode case is utilized and the internal state variable under mixed-mode loading conditions follows as

$$D_s(\lambda_{\max}) = \frac{\mathcal{W}_s}{\mathcal{G}_c} = \frac{1}{\mathcal{G}_c} \left[ \int_0^{\lambda_{\max}} T(\lambda) \, d\lambda - \int_0^{\lambda_{\max}} T(\lambda, d_s) \, d\lambda \right] . \quad (4.15)$$

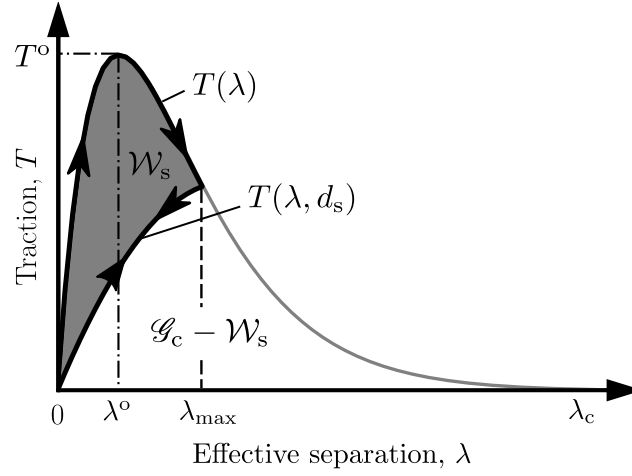


**Figure 4.3:** Cohesive law formulation accounting for mixed-mode loading conditions.

### 4.2.3 Mixed-Mode Delamination Growth for Fatigue Loading

The state of the constitutive interface behavior during steady state crack growth is depicted in Fig. 4.4. Herein, the shaded area below the traction–separation laws indicate the dissipated energy rate,  $\mathcal{W}_s$ , within and in front of the cohesive zone (CZ). In front of the CZ the constitutive behavior is purely elastic and the work done during interface opening is fully recoverable. Inside the CZ, damage progression and, consequently, energy dissipation occurs. The crack tip is defined by the end of the CZ where the delamination growth criterion,

$$\mathcal{W}_s = \mathcal{G}_c \quad , \quad (4.16)$$

is reached. The load amplitude during fatigue loading is smaller than during steady-state crack growth, and the length of the CZ,  $l_{cz}^{(fat)}$ , is shorter than during steady-state delamination growth,  $l_{cz}^{(steady)}$ , as depicted in Fig. 4.5 (top). The interface separation at the crack tip is too low to cause interface failure, i.e.  $\mathcal{W}_s = \mathcal{G}_c$ . Therefore, fatigue damage cannot be accounted for by the steady-state formulation since the unloading–reloading path of the traction–separation law, as depicted in Fig. 4.5 (middle), remains the same. Hence, no damage is accumulated or energy dissipated during cyclic loading and the stiffness and strength of the interface remains unchanged. Therefore, an additional fatigue damage formulation is necessary to account for subcritical crack growth caused by cyclic loading. The present model utilizes an energy-based approach, where, additional to the energy



dissipated by interface opening,  $\mathcal{W}_s$ , the unloading–reloading process should also cause an equivalent energy dissipation,  $\mathcal{W}_f$ , as depicted in Fig. 4.5 (bottom). This way, subcritical delamination growth can be accounted for and interface failure is reached when the sum of the dissipated energy rates equals the critical energy release rate,

$$\mathcal{W}_s + \mathcal{W}_f = \mathcal{G}_c \quad . \quad (4.17)$$

Energy dissipation caused by cyclic loading is introduced into the CZM by defining a total damage rate [224],

$$\frac{dD_{\text{tot}}}{dN} = \frac{dD_s}{dN} + \frac{dD_f}{dN} \quad , \quad (4.18)$$

where  $N$  equals the number of load cycles. The total damage rate is split up into two parts: one related to quasi–static damage,  $dD_s/dN$ , caused by overloads and one related to fatigue damage,  $dD_f/dN$ . The first term is obtained by the previously described CZM model by Eq. (4.15). For the second term, the fatigue damage rate, various formulations have been proposed and reviews can be found in [11, 226]. The present model utilizes the fatigue damage rate formulation of [224], written as [158],

$$\frac{dD_f}{dN} = \frac{1}{l_{\text{cz}}} f(\Delta w) \quad . \quad (4.19)$$

Herein,  $l_{\text{cz}}$  is the length of the cohesive zone and  $f(\Delta w)$  is a Paris’ law like function dependent on the specific work range,  $\Delta w$ , of each interface point in the cohesive interface. This Paris’ law like function defines a local delamination growth rate for each point inside the CZ. The length of the CZ is a structural property and depends on the geometry of the structure, the loading conditions, and the mode mix. In the original formulation [224] the CZ length is analytically approximated. In the present formulation this approximation is circumvented by evaluating  $l_{\text{cz}}$  during the FEM simulation. The CZ is defined as the part of the interface where the quasi–static damage variable takes a value between its two extrema,  $D_s \in (0, 1)$ . Hence, the length of the CZ is a direct result of the simulation and no assumptions have to be made.

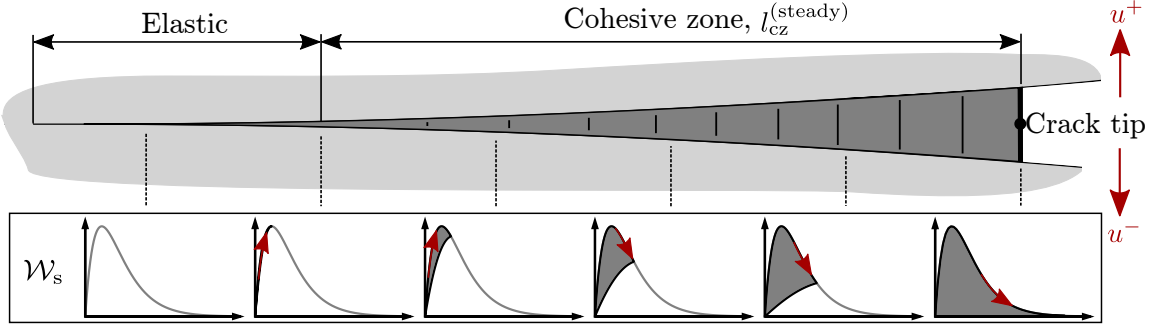


**Figure 4.4:** Steady state delamination growth obtained from monotonic interface opening. The damage state of the different points along the interface is depicted by the traction–separation laws. The dark–grey shaded areas below the traction–separation laws indicate the dissipated energy,  $\mathcal{W}_s$ , due to the interface opening.

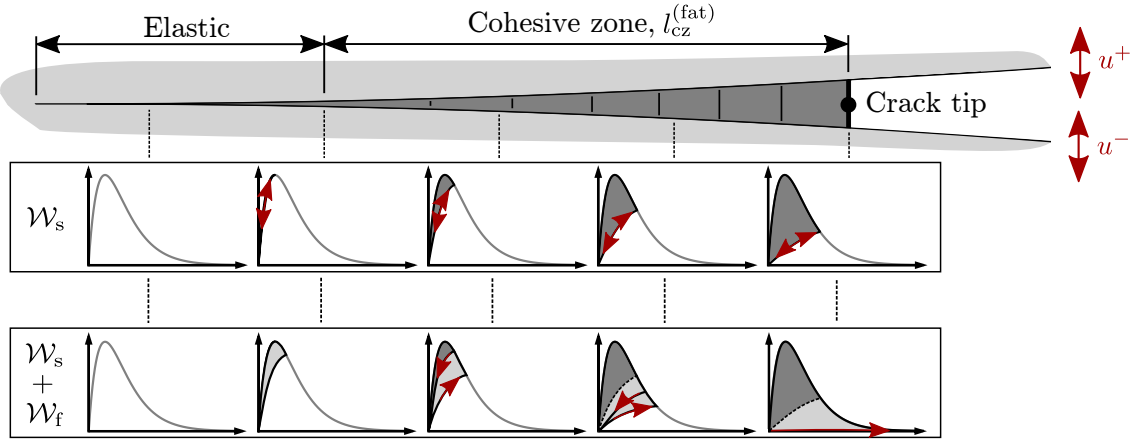


**Figure 4.5:** Subcritical delamination growth obtained from cycling loading. During fatigue loading the CZ is smaller than during steady–state crack growth. Hence, the fracture criterion is not reached by the consideration of  $\mathcal{W}_s$  (dark–grey area) alone and an additional fatigue energy  $\mathcal{W}_f$  (light–grey area) is included into the formulation.

The Paris’ law–like function in the fatigue damage rate formulation reads [224, 226]

$$f(\Delta w) = \begin{cases} C \left( \frac{\Delta w}{\mathcal{G}_c} \right)^m & \text{for } \mathcal{G}_{th} < \Delta w < \mathcal{G}_c \\ 0 & \text{for } \Delta w \leq \mathcal{G}_{th} \end{cases}, \quad (4.20)$$

where  $\mathcal{G}_c$  is the fracture toughness,  $\mathcal{G}_{th}$  is the fatigue threshold, and  $C$  and  $m$  are fatigue parameters obtained from experiments.

$\Delta w$  is the range of the specific work for each interface point and is computed by the undamaged traction–separation law as

$$\Delta w = w^{\max} - w^{\min} = \int_{\lambda_{\min}}^{\lambda_{\max}} T(\Delta) d\Delta \quad . \quad (4.21)$$

The determination of  $\Delta w$  is depicted in Fig. 4.6 and the evaluation of the integral is provided in Appendix B. The ratio between the maximum and minimum specific work can be interpreted as the R–ratio,  $R = w^{\min}/w^{\max}$ . The current fatigue model formulation is limited to cyclic loading conditions with  $R \geq 0$ .

The most straightforward approach to obtain these properties is to assume that the local development of the fatigue damage is similar to the macroscopic crack growth rate. Then, the parameters result directly from experimental  $da/dN$  curves. The typical pattern of a crack growth rate is depicted in Fig. 4.7 and divided into three regions. In region I no crack growth is observed, which means the energy release rate range,  $\Delta\mathcal{G}$ , is lower than a threshold value,  $\mathcal{G}_{\text{th}}$ . In contrast, in region III, when  $\mathcal{G}^{\max}$  reaches the value of the fracture toughness,  $\mathcal{G}_c$ , steady–state crack growth is obtained. Between these two regions the following Paris’ law variant is taken [30],

$$\frac{da}{dN} = \begin{cases} C \left( \frac{\Delta\mathcal{G}}{\mathcal{G}_c} \right)^m & \text{for } \mathcal{G}_{\text{th}} < \Delta\mathcal{G} < \mathcal{G}_c \\ 0 & \text{for } \Delta\mathcal{G} \leq \mathcal{G}_{\text{th}} \end{cases} \quad , \quad (4.22)$$

where the parameters  $C$  and  $m$  are structural properties determined by experiments. Based on the assumption that the local fatigue crack growth rate is similar to the macroscopic fatigue crack growth rate, the parameters,  $C$ ,  $m$ ,  $\mathcal{G}_{\text{th}}$ , obtained from experiments in Eq. (4.22) are identical to the parameters in the local formulation of Eq. (4.20). Hence, the fatigue input parameters for the model are directly obtained from the experimentally determined Paris law.

The mixed–mode fatigue extension of the CCZM is carried out here for 2D problems. Hence, only combinations of Mode I and Mode II loading conditions are considered in the

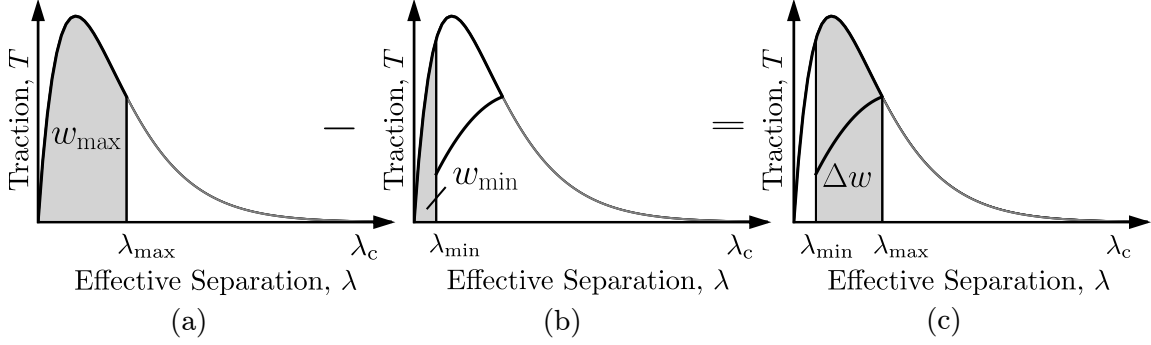


**Figure 4.6:** Illustration of the local specific work range,  $\Delta w$ , which is computed for each integration point inside the cohesive zone. (a) determination of  $w_{\max}$  at the maximum effective separation of a load cycle, (b) determination of  $w_{\min}$  at the minimum effective separation during a load cycle, and (c) illustration of  $\Delta w$ .

following. The coefficients  $C$  and  $m$  of the Paris' law for the mixed-mode loading conditions are calculated by the following formulae [30]:

$$\log(C) = \log(C_I) + \phi \log(C_m) + \phi^2 \log\left(\frac{C_{II}}{C_m C_I}\right) \quad (4.23)$$

$$m = m_I + m_m \phi + (m_{II} - m_I - m_m) \phi^2 \quad , \quad (4.24)$$

where  $C_I, C_{II}, m_I$ , and  $m_{II}$  are the pure mode parameters and  $C_m, m_m$  are mixed-mode parameters, all obtained by experiments. The mode ratio,

$$\phi = \frac{\mathcal{G}_{II}}{\mathcal{G}} = \frac{\mathcal{G}_{II}}{\mathcal{G}_I + \mathcal{G}_{II}} \quad , \quad (4.25)$$

is a structural property, where  $\mathcal{G}$  is the total energy release rate computed by the energy release rates for mode I,  $\mathcal{G}_I$ , and mode II,  $\mathcal{G}_{II}$ , respectively.

The mode ratio is computed by application of the J-Integral. In Linear Elastic Fracture Mechanics the J-Integral equals  $\mathcal{G}$  and the mode decomposition of the J-Integral [12],

$$J = J_I + J_{II} = \mathcal{G}_I + \mathcal{G}_{II} = \left( - \int_0^{l_{cz}} T_3 \frac{\partial \Delta_3}{\partial x_1} dx_1 \right) + \left( - \int_0^{l_{cz}} T_1 \frac{\partial \Delta_1}{\partial x_1} dx_1 \right) \quad , \quad (4.26)$$

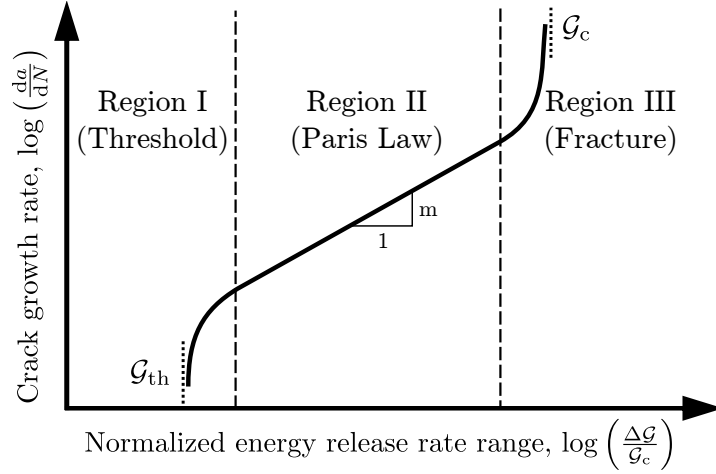


**Figure 4.7:** Typical graph of the fatigue crack growth rate as a function of the normalized energy release rate range, indicating the threshold, Paris, and fracture region.

results in the energy release rates  $\mathcal{G}_I$  and  $\mathcal{G}_{II}$ , respectively. Eq. (4.26) provides the current limitation of the present CCZM to 2D problems. The decomposition of the J-Integral for 3D simulations has been theoretically derived [104, 197], but has not been implemented into the CCZM yet.

Variable amplitude loading is accounted for in the present work, which can lead to a change of the mode ratio during a load cycle. Experimental crack growth curves are usually available for loading conditions with fixed mode ratios only. Hence, a representative time,  $t^{\max}$ , is searched for at which the critical loading conditions, i.e. the highest contribution to the damage development occurs within a load cycle,  $N$ . This time point,  $t^{\max} \in [t_N, t_{N+1})$ , is utilized for the evaluation of the mode ratio,  $\phi$ . The time point with the highest contribution to damage is identified as,

$$t^{\max} = \arg \max_{t \in [t_N, t_{N+1})} \left\{ \frac{\mathcal{G}(t)}{\mathcal{G}_c(t)} \right\} \quad , \quad (4.27)$$

where  $t_N$  denotes the time at the start of the load cycle  $N$ . The criterion relates the energy release rate,  $\mathcal{G}(t)$ , during the load cycle to a fracture criterion  $\mathcal{G}_c(t)$ . In the present work the BK fracture criterion [25] is utilized and obtained as

$$\mathcal{G}_c = \mathcal{G}_{Ic} + (\mathcal{G}_{IIc} - \mathcal{G}_{Ic}) (\phi(t))^\eta \quad , \quad (4.28)$$

where  $\mathcal{G}_c$  is the critical energy release rate computed with the structural mixed-mode ratio,  $\phi$ . Note that the local fracture criterion Eq. (4.13) and the structural fracture criterion Eq. (4.28) use different fonts for the obtained critical energy release rate. This differentiation between a local and a structural fracture criterion is necessary since the structural mode ratio,  $\phi$ , is not equal to the local mode mixity,  $B$ . The difference is illustrated in Fig. 4.8. The BK-criterion is graphically illustrated in Fig. 4.8(a) and shows the correlation between the pure mode I and mode II critical energy release rates with the predicted mixed-mode critical energy release rate. The variation of the mode mixity,  $B$ , inside the CZ for mixed-mode loading conditions with a constant mode ratio,  $\phi = 0.5$ , is depicted in Fig. 4.8(b) [207]. During mixed-mode loading the mode mixity,  $B$ , utilized in the local fracture criterion, Eq. (4.13), varies from the crack tip towards the location of damage onset, whereas the mode ratio,  $\phi$ , utilized in the structural fracture criterion, Eq. (4.28), is a single scalar value for a given loading configuration of a structural problem. Therefore, the mode ratio,  $\phi(t^{\max})$ , and not the mode mixity,  $B$ , is utilized for the determination of the mixed-mode Paris law parameters as defined in Eq. (4.24).

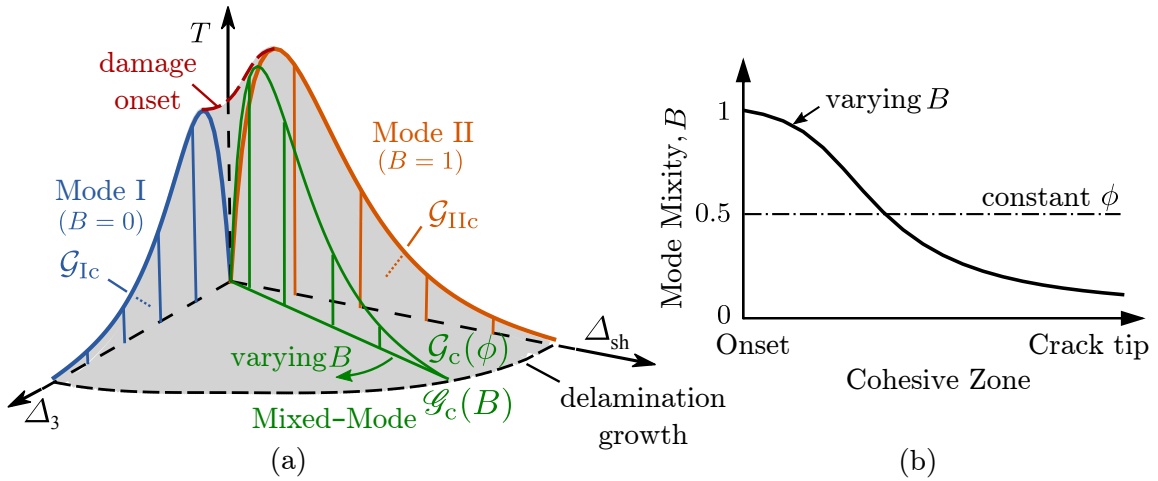


**Figure 4.8:** Local mode mixity,  $B$ , versus structural mode ratio,  $\phi$ . (a) illustration of the BK fracture criterion for evaluation of the critical energy release rate, (b) change of the predicted mode mixity,  $B$ , along the cohesive zone compared to the constant mode ratio,  $\phi$ .

The mixed-mode fatigue threshold is defined in analogy to the structural fracture criterion, Eq. (4.28), and reads

$$\mathcal{G}_{\text{th}} = \mathcal{G}_{\text{Ith}} + (\mathcal{G}_{\text{IIth}} - \mathcal{G}_{\text{Ith}}) (\phi(t^{\text{max}}))^{\eta} \quad . \quad (4.29)$$

Herein, the same mode ratio is utilized as for the calculation of the mixed-mode Paris law parameters in Eq. (4.24).

Finally, the total damage variable is obtained from the quasi-static damage variable and the fatigue damage rate as

$${}^{(N^{\text{S}})}D_{\text{tot}} = {}^{(N^{\text{S}})}D_{\text{s}} + {}^{(N^{\text{S}}-1)}D_{\text{f}} + \left. \frac{\text{d}D_{\text{f}}}{\text{d}N} \right|_{(N^{\text{S}})} \quad , \quad (4.30)$$

where  $(N^{\text{S}})$  denotes the last simulated load cycle. The static damage variable,  $D_{\text{s}}(\lambda_{\text{max}})$ , depends only on the maximum effective separation arising during the whole loading history and is, therefore, known at the end of cycle  $(N^{\text{S}})$ . The fatigue damage rate is computed for cycle  $(N^{\text{S}})$  according to Eq. (4.19) and added to the accumulated fatigue damage,  $D_{\text{f}}$ , until cycle  $(N^{\text{S}} - 1)$ .

Similar to the definition of the quasi-static damage variable, Eq. (4.7), the total damage variable is defined as

$$D_{\text{tot}} = \frac{\mathcal{W}_{\text{d}}}{\mathcal{G}_{\text{c}}} = \frac{\mathcal{W}_{\text{s}} + \mathcal{W}_{\text{f}}}{\mathcal{G}_{\text{c}}} \quad , \quad (4.31)$$

where  $\mathcal{W}_{\text{d}}$  is the total rate of the energy dissipated during the damage process.  $\mathcal{W}_{\text{s}}$  and  $\mathcal{W}_{\text{f}}$  describe the energy rates dissipated due to quasi-static and fatigue loading, respectively. The cyclic traction-separation law indicating these energy rates is depicted in Fig. 4.9. The energy based definition of  $D_{\text{tot}}$  allows for the update of the internal state variable,  $d_{\text{tot}}$ . These two variables are related in a nonlinear manner,

$$D_{\text{tot}}(d_{\text{tot}}) = \frac{1}{\mathcal{G}_{\text{c}}} \left[ \int_0^{\lambda_{\text{tot}}} T(\lambda) \text{d}\lambda - \int_0^{\lambda_{\text{tot}}} T(\lambda, d_{\text{tot}}) \text{d}\lambda \right] \quad . \quad (4.32)$$

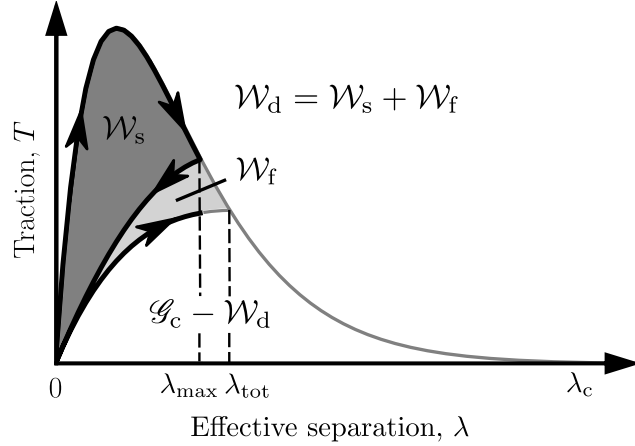


**Figure 4.9:** Cyclic cohesive zone model accounting for fatigue damage. The shaded areas below the traction–separation law indicate the dissipated energy rates during the damage process caused by quasi-static,  $\mathcal{W}_s$ , and fatigue,  $\mathcal{W}_f$ , loading.

Since the cyclic loading leads to an increase in the dissipated energy rate,  $\mathcal{W}_d$ , the total damage variable,  $D_{\text{tot}}$ , increases and the internal variable,  $d_{\text{tot}}$ , is related to the effective separation,  $\lambda_{\text{tot}}$ , as

$$d_{\text{tot}} = \lambda_{\text{tot}}^\beta \quad , \quad (4.33)$$

which is in accordance to Eq. (4.12). Due to the implicit nature of Eq. (4.32), the internal variable,  $d_{\text{tot}}$ , cannot be expressed explicitly and an iterative solution scheme is required. Newton’s method is, therefore, employed and the algorithm is described in Appendix B.

#### 4.2.4 Interface Closure – Nonlinear Penalty Contact

In the case of interface closure, penetration of the surfaces must be avoided. Therefore, a mechanical contact algorithm needs to be employed. An advanced version of the nonlinear penalty contact formulation utilized in [123] is formulated in the following. In the conventional penalty contact formulation the normal traction is a linear function of the normal separation,

$$T_3 = K_{\text{cont}} \Delta_3 \quad , \quad \text{for } \Delta_3 < 0 \quad , \quad (4.34)$$

where  $K_{\text{cont}}$  is the penalty contact stiffness. The choice of this contact stiffness can be a tedious task. Too high values may lead to convergence issues in the simulation, whereas too



low values may lead to unphysical large penetrations. A nonlinear penalty method offers more flexibility in the choice of  $K_{\text{cont}}$ . In the present work a sinusoidal stiffness–penetration relationship is formulated, as depicted in Fig. 4.10(a). For zero penetration ( $\Delta_3 = 0$ ) the penalty contact stiffness starts with an initial value,  $K_{\text{sc}}$ , and follows a sinusoidal slope until a final value,  $K_{\text{fc}}$ , at a penetration of  $(-\Delta_3^{\text{fc}})$ , is reached. Afterwards, the contact stiffness remains constant. The contact stiffness of the sinusoidal nonlinear penalty method can be expressed as

$$K_{\text{cont}} = \begin{cases} K_{\text{sc}} + \frac{K_{\text{fc}} - K_{\text{sc}}}{2} \left[ 1 - \cos \left( \frac{(-\Delta_3)\pi}{\Delta_3^{\text{fc}}} \right) \right] & \text{for } -\Delta_3^{\text{fc}} < \Delta_3 < 0 \\ K_{\text{fc}} & \text{for } \Delta_3 < -\Delta_3^{\text{fc}} \end{cases}, \quad (4.35)$$

and the pressure–penetration relation, Fig. 4.10(b), follows as

$$(-T_3) = \begin{cases} K_{\text{cont}}(-\Delta_3) & \text{for } \Delta_3 < 0 \\ 0 & \text{for } \Delta_3 \geq 0 \end{cases}. \quad (4.36)$$

In the case of complete interface failure frictionless contact is assumed and the shear tractions equal zero. For the undamaged interface in a contact state the shear tractions are described by the cohesive law Eq. (4.8).

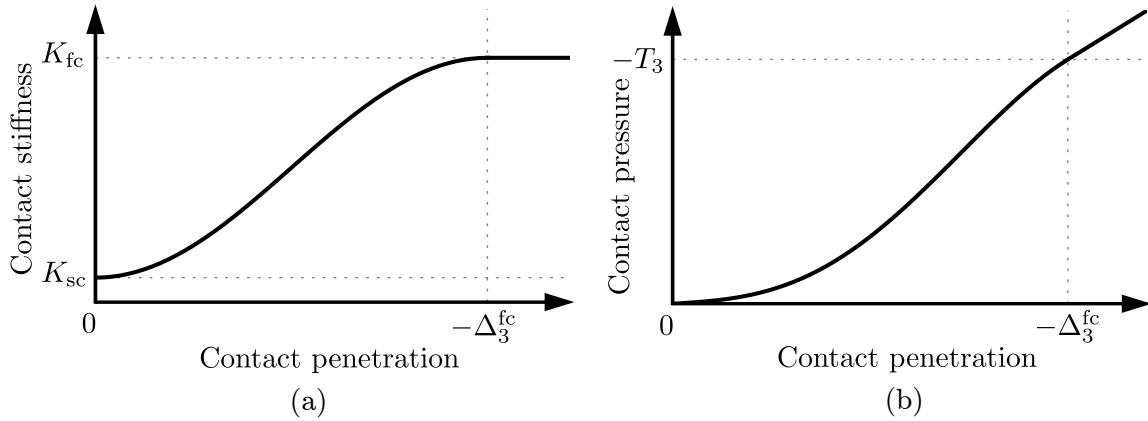


**Figure 4.10:** Nonlinear sinusoidal penalty contact formulation. (a) stiffness variation as a function of the contact penetration, (b) resulting traction–penetration relationship.

### 4.2.5 Thermo–Mechanical Extension

The CCZM is extended to account for thermo–mechanical loading conditions. The temperature dependence of cohesive laws has been investigated in [76, 227, 228]. There, the critical energy release rates and the damage onset tractions have been found to be temperature dependent. Therefore, the energy release rates,  $\mathcal{G}_{Mc}$ , and the damage onset tractions,  $T_{Mc}^o$  are modeled as temperature dependent in the present work. The shape of the cohesive law, described by the parameter  $\beta$ , is assumed to be temperature independent.

The modeling of the heat transfer across the interface follows the work of [125]. Herein, the cohesive zone’s thermal conductance is related to the mechanical damage variable. This way, the degradation of thermal and mechanical interface properties are controlled by one single damage variable.

The thermal flux in the bulk phase is obtained by Fourier’s equation and reads for isotropic materials

$$\mathbf{q} = -k\nabla\vartheta \quad , \quad (4.37)$$

where  $k$  is the thermal conductivity of the bulk material and  $\nabla\vartheta$  is the temperature gradient. The thermal flux across the interface,

$$q_+ = \mathbf{q} \cdot \mathbf{n}_+ \quad , \quad (4.38)$$

occurs only in the normal direction, where  $\mathbf{n}_+$  is the unit normal vector of the cohesive zone surface,  $(C_+)$ , as depicted in Fig. 4.11. The opposite interface surface is denoted by  $(C_-)$ . In the present work, heat generation due to damage or plasticity is neglected and the continuity condition of the normal thermal flux across the interface,

$$q_+ = -q_- \quad , \quad (4.39)$$

has to be fulfilled. Additionally, heat transfers by radiation or convection across the interface are neglected. Hence, the thermal flux across the interface is dependent only on the thermal conductance of the interface and the temperature jump between the cohesive

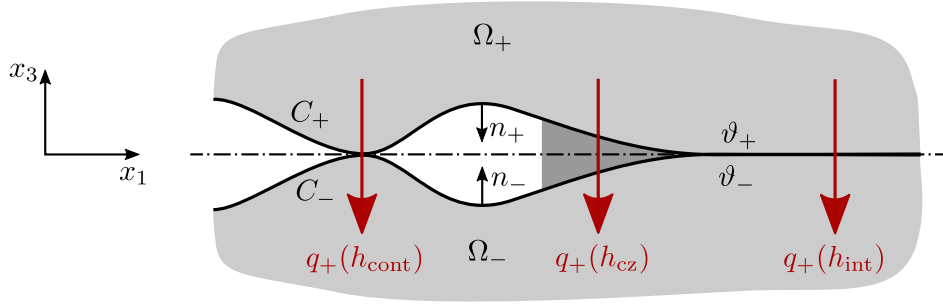


**Figure 4.11:** Schematic illustration of the thermal flux across the interface.  $q(h_{\text{int}})$  describes the thermal flux through the undamaged interface,  $q(h_{\text{cz}})$  through the partly damage interface (the cohesive zone), and  $q(h_{\text{cont}})$  through the damaged interface during contact.

surfaces,  $[[\vartheta]] = (\vartheta_+ - \vartheta_-)$ . Consequently, the thermal flux across the undamaged interface is obtained as

$$q_+(h_{\text{int}}) = h_{\text{int}}[[\vartheta]] \quad , \quad (4.40)$$

where  $h_{\text{int}}$  is the thermal conductance of the undamaged interface.

Following [93], the reduction of the thermal conductance of a damaged interface during opening is assumed to be proportional to the ratio of the damaged to the undamaged interface area. The ratio between the damaged and the undamaged interface area within the cohesive zone theory is described by the mechanical damage variable,  $D_{\text{tot}}$ . Hence, the thermal conductance of the damaged interface during interface opening is obtained as

$$h_{\text{cz}} = (1 - D_{\text{tot}})h_{\text{int}} \quad \text{for} \quad \Delta_3 \geq 0 \quad . \quad (4.41)$$

Hence,  $h_{\text{cz}} \in [0, h_{\text{int}}]$  is the thermal conductance of an interface point in the cohesive zone.

Upon interface closure heat transfer occurs through the cohesive zone and the delaminated interface due to surface contact. For this case ( $\Delta_3 < 0$ ) the thermal conductance can be obtained as [172]

$$h_{\text{cz}} = (1 - D_{\text{tot}})h_{\text{int}} + D_{\text{tot}}h_{\text{cont}} \quad \text{for} \quad \Delta_3 < 0 \quad , \quad (4.42)$$

where  $h_{\text{cont}}$  is the thermal conductance of the completely damaged interface during surface contact. In the present work  $h_{\text{cont}}$  is estimated from  $h_{\text{int}}$  as

$$h_{\text{cont}} = v h_{\text{int}} \frac{K_{\text{cont}} - K_{\text{sc}}}{K_{\text{fc}} - K_{\text{sc}}} . \quad (4.43)$$

This way,  $h_{\text{cont}} \in [0, v h_{\text{int}}]$  increases with increasing contact penetration described by the nonlinear penalty contact formulation, Eq. (4.35). Hence,  $h_{\text{cont}}$  starts at a value of zero for zero penetration and increases to a value described by  $v h_{\text{int}}$  for large penetrations greater than  $\Delta_3^{\text{fc}}$ . Herein,  $v$  is a scalar factor describing the difference between the thermal conductance of a perfectly bonded interface and that of a damaged interface during contact.

### 4.3 Implementation Aspects

The CCZM is implemented into the commercial software Ansys APDL v16.2 (ANSYS Inc., Canonsburg, PA, USA) employing the USERINTER user subroutine. The subroutine USERINTER allows for the definition of complex interactions between contacting surfaces, including interactions in the normal and shear directions in addition to coupled-field interactions [4]. Interface deformation as well as interface opening and closing are treated by the available contact elements, and only the constitutive interface behavior, as described in the previous section, has to be implemented. The implementation requires the use of the interface stiffness matrix,

$$\mathbf{K} = \begin{bmatrix} {}^{\text{m}}\mathbf{K} & {}^{\text{mt}}\mathbf{K} \\ {}^{\text{tm}}\mathbf{K} & {}^{\text{th}}\mathbf{K} \end{bmatrix} \quad (4.44)$$

where  ${}^{\text{m}}\mathbf{K}$  represents the mechanical submatrix;  ${}^{\text{mt}}\mathbf{K}$ ,  ${}^{\text{tm}}\mathbf{K}$  represent the mechanical–thermal and thermal–mechanical coupling terms, respectively; and  ${}^{\text{th}}\mathbf{K}$  represents the thermal submatrix. The entries of these four submatrices are derived in Appendix C.

The temperature dependent material properties are defined in table form. Ansys APDL v16.2 USERINTER provides a routine for the evaluation of these parameters. For temperature values in between the table values, a linear interpolation is utilized to obtain the parameters at the required temperatures.

The described constitutive interface model requires the determination of structural parameters during the simulation. These non-local evaluations have to be done for the cohesive zone length,  $l_{cz}$ , and the energy release rates  $\mathcal{G}_I$  and  $\mathcal{G}_{II}$ .

The length of the CZ has been defined as the part of the interface where the damage variable ranges between  $D_s \in (0, 1)$ . In the context of the FEM,  $l_{cz}$  is determined at the element level and is obtained from

$$l_{cz} = \sum_{e \in CZ} l_e \quad \text{for} \quad \{e \in CZ \mid 0.01 \leq D_s \leq 0.99\} \quad , \quad (4.45)$$

where  $l_e$  is the element length of an interface element,  $e$ , inside the cohesive zone, CZ. Hence, the damage state of all interface elements is checked and the length of all interface elements inside the CZ,  $D_s \in [0.01, 0.99]$ , is summed up. This evaluation works fine if there is only one CZ inside the model. If damage onset of the interface does not start at the model edges, but rather in the middle of the interface, as depicted in Fig. 4.12, the evaluation of  $l_{cz}$  needs more attention. In this case, the damaged interface in the middle of the model is treated as one CZ until the first interface element has completely failed ( $D_s > 0.99$ ). Afterwards, the CZ is split up into two CZs which are treated independently. This means that different rates of fatigue damage propagation,  $dD_f/dN$ , are computed for each of the CZs. Multiple delaminations and, consequently, multiple CZs can also arise inside the model. Each of these CZs needs to be separated from one another by either a completely undamaged interface ( $D_s < 0.01$ ) or a delamination ( $D_s > 0.99$ ), only then a proper identification of the different CZs inside the model is possible. The coalescence of CZs from multiple crack tips is not addressed in this work and further research is required

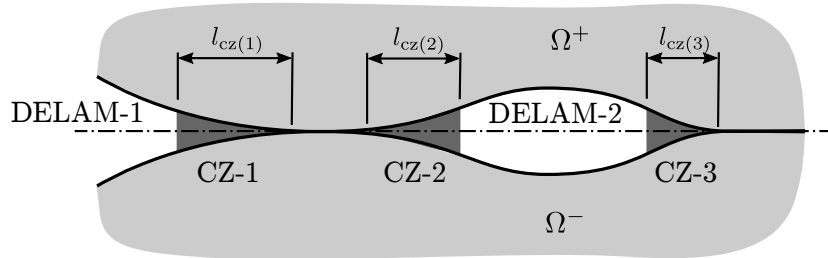


**Figure 4.12:** Illustration of two delaminations with three cohesive zones inside one model.

to develop a proper modeling strategy for this phenomenon. As a simple workaround, coalescing CZs are treated the same way as single CZs in this work.

The energy release rates  $\mathcal{G}_I$  and  $\mathcal{G}_{II}$  need to be computed for each of the identified CZs. The fracture criterion, Eq. (4.27), is evaluated for all CZs and the evaluation of  $\mathcal{G}_I$  and  $\mathcal{G}_{II}$  under the critical loading conditions may occur at different times  $t^{\max}$ . In the framework of the FEM, the energy release rates read

$$\mathcal{G}_I(t^{\text{BK}}) = \sum_{e \in \text{CZ}} \left[ \langle T_3^e \rangle \left| \frac{\partial \Delta_3}{\partial x_1} \right|_e l_e \right] = \sum_{e \in \text{CZ}} \left[ \langle T_3^e \rangle \left| \Delta_3^b - \Delta_3^a \right|_e \right] \quad (4.46)$$

$$\mathcal{G}_{II}(t^{\text{BK}}) = \sum_{e \in \text{CZ}} \left[ |T_1^e| \left| \frac{\partial \Delta_1}{\partial x_1} \right|_e l_e \right] = \sum_{e \in \text{CZ}} \left[ |T_1^e| \left( \Delta_1^b - \Delta_1^a \right)_e \right] , \quad (4.47)$$

where the derivatives,  $\partial \Delta_i / \partial x_1$ , are computed at the element level, as depicted in Fig. 4.13. The computation of the derivatives is done in a discrete way for cohesive elements with linear interpolation functions and expressed as [12]

$$\frac{\partial \Delta_i}{\partial x_1} = \frac{\Delta_i^b - \Delta_i^a}{l_e} , \quad (4.48)$$

where a and b denote the nodes of the element and  $l_e$  denotes the element length.

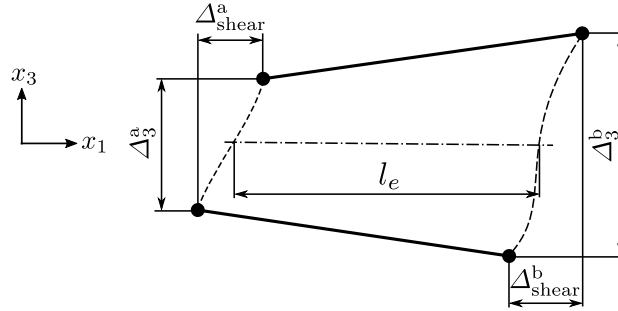


**Figure 4.13:** Deformed, linearly interpolated, interface element depicting the nodal displacements for the computation of the derivatives in the evaluation of the mode decomposed J–integral [12].

## 4.4 Cycle Jump Technique

A cycle-by-cycle analysis can get computationally expensive for high numbers of load cycles. The computation time is reduced by implementing a simple cycle jump technique. The cycle jump approach is limited to constant load amplitudes or slowly changing load amplitudes. The present strategy is focused on load spectra which can be represented by different load blocks of constant load amplitudes. Inside these load blocks, the cycle jump technique reduces the computational time but captures all the transient effects of alternating from higher to lower load amplitudes or vice versa. A review on different cycle jump techniques for CCZMs is provided in [11].

In the present model, a simple damage extrapolation technique is utilized. Eq. (4.30) is enhanced by the jump cycles and the total damage variable utilizing the cycle jump technique is obtained as

$${}^{(N^S+\Delta N)}D_{\text{tot}} \approx {}^{(N^S)}D_s + {}^{(N^S-1)}D_f + (\Delta N + 1) \left. \frac{dD_f}{dN} \right|_{(N^S)}, \quad (4.49)$$

where  $N^S$  is the last simulated load cycle for which the total damage variable has been evaluated.  $\Delta N$  is the increment, in cycles, for the cycle jump approach.  $dD_f/dN$  is the fatigue damage rate of the last simulated load cycle,  $N^S$ . The update procedure of the total damage variable during the cycle jump technique is depicted in Fig. 4.14. The distribution of the total damage variable in the cohesive zone is depicted at the end of the last simulated load cycle (before the cycle jump, Fig. 4.14(a)) and after the first equilibrium iteration of the subsequent load cycle (after the cycle jump, Fig. 4.14(b)). The static damage variable in the undamaged region in front of the cohesive zone is  $D_s = 0$ . Consequently, also the static damage rate,  $dD_s/dN = 0$ , and, therefore, cannot be considered in Eq. (4.49). However, the evolution of the static damage variable during the cycle jump is implicitly taken into account by the first equilibrium iteration after the cycle jump technique has been applied. A further limitation of the cycle jump technique is that fatigue damage is only accounted for inside the CZ, where damage onset has already been reached. As a result, the maximum delamination growth,  $\Delta a$ , during a cycle jump is limited by the length of the cohesive zone,  $l_{cz}$ . Hence, the number of cycles for the cycle jump needs to be limited since the static and

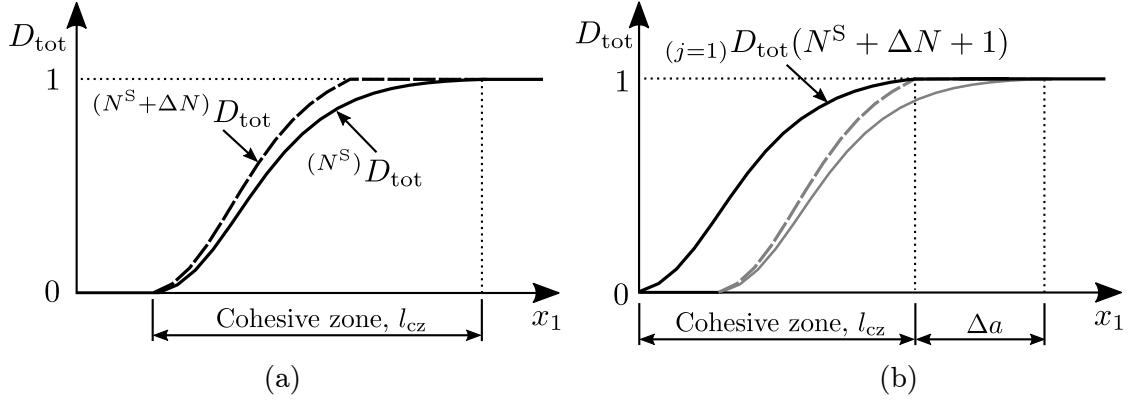


**Figure 4.14:** Illustration of the update procedure of the total damage variable during the cycle jump technique. (a) damage distribution in the cohesive zone at the end of the last simulated load cycle,  $D(N^S)$ , and the updated total damage variable after the cycle jump is applied,  $D(N^S + \Delta N)$ . (b) damage distribution after the first equilibrium iteration,  $j = 1$ , of the subsequent load cycle. The delamination growth is indicated by,  $\Delta a$ .

the fatigue damage rate in front of the CZ cannot be accounted for. Too large values for the cycle jump can lead to erroneous results. To keep this error within reasonable bounds, the maximum number of jump cycles is defined as

$$\Delta N_{\text{max}} = \frac{\Delta D_{\text{f}}^{\text{allow}}}{\max_{i \in \text{CZ}} \left\{ \left( \frac{dD_{\text{f}}}{dN} \right)_i \right\}}, \quad (4.50)$$

where  $\Delta D_{\text{f}}^{\text{allow}}$  is the maximum allowable damage increment prescribed for one cycle jump. The allowable damage increment is divided by the highest fatigue damage rate which occurred during the last simulated load cycle ( $N^S$ ). The highest fatigue damage rate is typically obtained at the crack tip. The index  $i$  denotes the integration points of the cohesive elements inside the CZ. If multiple CZs occur inside a model, the highest damage rate of all the CZs limits the possible number of load cycles for the cycle jump.



## 4.5 Demonstration of the Model

The mechanical constitutive interface model is demonstrated in this section. The thermal capabilities of the model are demonstrated in Chapter 5. First, the constitutive response of a single interface point during fatigue crack growth is discussed. Herein, the whole damage process from an initial perfect interface to complete interface failure is presented by simulating a Double–Cantilever–Beam (DCB) [8] test setup. Second, the mixed–mode behavior of the model is demonstrated at Mixed–Mode–Bending (MMB) [9] simulations under constant amplitude loading, resulting in a constant fatigue crack growth rate. Third, the variable amplitude loading behavior of the CCZM is exemplified on End–Notched–Flexure (ENF) [10] simulations. Herein, a constant displacement amplitude loading leads to a decrease of the reaction force amplitude caused by fatigue crack growth and, consequently, to a decelerated crack growth rate. The change in the loading conditions leads to a change of the cohesive zone length and the need for the non–local evaluation of this parameter is pointed out.

### 4.5.1 Traction–separation response

The constitutive response of the model is demonstrated on a structural problem undergoing subcritical crack growth. Therefore, a DCB setup as depicted in Fig. 4.15 is utilized. The DCB is employed to demonstrate the constitutive behavior of a single interface point during fatigue crack growth. In the FEM model the DCB is loaded by opposing, cyclic, bending moments to obtain a Mode I energy release rate that is independent of the crack length. This way, a constant fatigue crack growth rate is obtained [224]. The energy release rate,

$$\mathcal{G}_I = \frac{M_I}{bE_1I} \quad , \quad (4.51)$$

is related to the applied bending moments as [199]. Herein,  $b$  is the specimen’s width,  $E_1$  is the Young’s modulus in the longitudinal direction, and  $I = (bh^3)/12$  is the second momentum of area of the specimens arm. The specimen has a length of  $l = 100\text{mm}$  with two  $h = 1.55\text{mm}$  thick arms, a width of  $b = 25\text{mm}$ , and an initial crack length of  $a_0 = 35\text{mm}$ . The DCB specimen chosen for the demonstration purpose is made of a

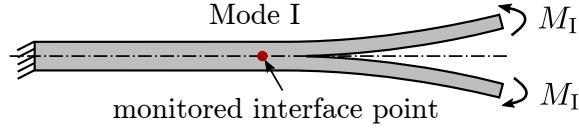


**Figure 4.15:** DCB specimen loaded by opposing, cyclic, bending moments to obtain a constant fatigue crack growth rate.

carbon/epoxy laminate. The material and interface parameters are taken from [12, 224] and summarized in Tab. 4.1. Three different magnitudes of the bending moments are applied corresponding to normalized energy release rates of  $\Delta\mathcal{G}/\mathcal{G}_c = [0.3, 0.5, 0.8]$  with an R-ratio of  $R = 0.1$ . The applied bending moments are provided in Tab. 4.2.

The specimen is analyzed by a plane strain FEM simulation utilizing continuum elements with quadratic interpolation functions. Two elements are used through the thickness,  $h$ , of each arm. In the region of fatigue crack propagation the quadratic shaped elements are refined to rectangular shaped elements, where one element side is reduced to an element aspect ratio of 6.2. The elements are coupled to Ansys APDL v16.2 contact and target elements, at the interface, employing the written USERINTER user subroutine. On the

**Table 4.1:** Elastic, interface, and fatigue properties for the symmetric uniaxial carbon–epoxy laminate [12]. The interface fatigue thresholds are taken from [224].

Elastic properties					
$E_1$	$E_2 = E_3$	$G_{12} = G_{13}$	$G_{23}$	$\nu_{12} = \nu_{13}$	$\nu_{23}$
120 GPa	10.5 GPa	5.3 GPa	3.5 GPa	0.3	0.51
Interface properties					
$\mathcal{G}_{Ic}$	$\mathcal{G}_{Ic}$	$T_I^o$	$T_{II}^o$	$\beta$	$\eta$
$0.260 \frac{\text{N}}{\text{mm}}$	$1.002 \frac{\text{N}}{\text{mm}}$	30 MPa	60 MPa	1.0	2.73
Fatigue properties					
$C_I$	$C_{II}$	$C_m$	$m_I$		
$3.08 \cdot 10^{-3} \frac{\text{mm}}{\text{cycle}}$	$1.49 \cdot 10^{-1} \frac{\text{mm}}{\text{cycle}}$	22 904 $\frac{\text{mm}}{\text{cycle}}$	5.4		
$m_{II}$	$m_m$	$\mathcal{G}_{Ith}$	$\mathcal{G}_{IIth}$		
4.5	4.94	$0.06 \frac{\text{N}}{\text{mm}}$	$0.10 \frac{\text{N}}{\text{mm}}$		

left end of the specimen the interface nodes are fixed against rigid body motion. The bending moments are applied on the opposite side of the specimen by force couples acting on the cantilever arms. The cycle jump technique is applied and an allowable damage increment of  $\Delta D_f^{\text{allow}} = 0.1$  is defined.

As indicated in Fig. 4.15 the traction–separation response of one fixed interface point is monitored. This way, the whole damage process experienced by this interface point is captured. At the beginning of the loading the interface point experiences only elastic deformation until the CZ propagates towards the monitored point. Once the CZ reaches the point, damage onset occurs and interface degradation starts. The damage progress is depicted by the traction–separation response of the interface point in Fig. 4.16. The whole degradation process is depicted ranging from local damage onset to local interface failure. Three different structural loading conditions are applied to illustrate the influence of the increasing interface opening caused by delamination growth on the local degradation process. The corresponding energy release rates,  $\mathcal{G}_I^{\text{max}}$ , of the applied bending moments are indicated by the grey areas below the quasi–static traction–separation response.

Beginning at the lowest load level,  $\Delta\mathcal{G}/\mathcal{G}_c = 0.3$ , the maximum separation at the material point is nearly constant during the whole degradation process. Therefore, the separation at damage onset and the separation shortly before delamination growth are roughly the same. Hence, there is only a negligible change in the damage predicted by quasi–static opening of the interface under this cyclic loading condition. Almost all of the energy dissipated

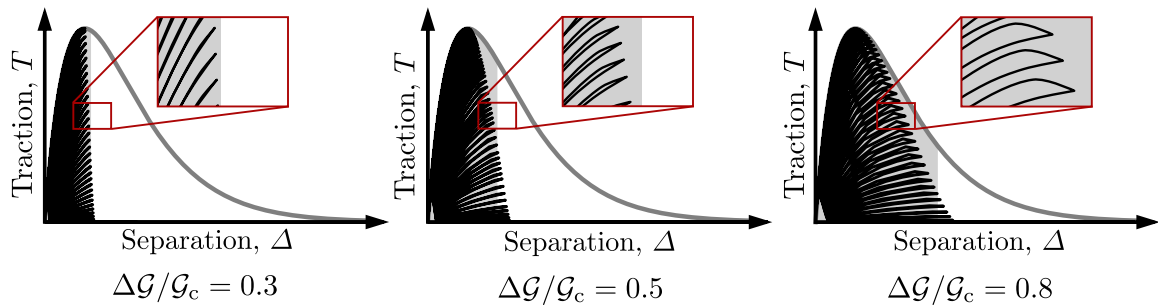


**Figure 4.16:** Traction–separation response of a fixed interface point experiencing fatigue delamination growth for three different loading conditions. The lightgrey areas indicate the applied energy release rates corresponding to the applied bending moments.

during the degradation process is caused by the fatigue damage rate. In contrast, for higher loading amplitudes the influence of the interface opening becomes more important. The opening of the interface from damage onset until delamination growth increases during subcritical crack growth. Consequently, also the quasi-static damage variable increases and contributes to a stiffness degradation. Hence, unloading occurs on a different path at decreased interface tractions. This behavior can be recognized by the small hysteresis loops in the sketched detail views for  $\Delta\mathcal{G}/\mathcal{G}_c = 0.5$  and  $\Delta\mathcal{G}/\mathcal{G}_c = 0.8$ .

#### 4.5.2 Constant Amplitude Loading

MMB tests are utilized to demonstrate the capabilities of the CCZM under mixed-mode, constant amplitude loading conditions. The geometry of the specimen, the test setup as well as the carbon/epoxy laminate's elastic, interface, and fatigue properties are taken from [12]. These properties and the specimen geometry are identical to the ones described in Section 4.5.1. Hence, the same FEM model is employed. Only, the loading conditions of the DCB model are changed to account for a cyclic loaded MMB simulation.

The MMB specimens, depicted in Fig. 4.17, are subjected to different loading patterns to account for pure Mode I, pure Mode II and Mixed-Mode loading,  $\phi = [0, 1, 0.5]$ . Various simulations with different load amplitudes are conducted. The bending moments for pure Mode I and pure Mode II simulations are chosen in such a way that the normalized energy release rates result in  $\Delta\mathcal{G}/\mathcal{G}_c = [0.3, 0.5, 0.8, 0.9, 0.95]$  with an R-ratio of  $R = 0.1$ . The Mode I bending moments are defined in Eq. (4.51), whereas the Mode II bending moments are obtained from [199]

$$\mathcal{G}_{\text{II}} = \frac{3M_{\text{II}}^2}{4bE_1I} \quad . \quad (4.52)$$

Herein, is  $E_1$  the Young's modulus in longitudinal direction, defined in Tab. 4.1, and  $I$  is the second moment of area. Mixed-mode loading simulations are conducted at the following load levels  $\Delta\mathcal{G}/\mathcal{G}_c = [0.3, 0.4, 0.6, 0.8, 0.9, 0.95]$  considering the same R-ratio as before. The mixed-mode bending moments for  $\phi = 0.5$  are given as [199]

$$M_1 = \frac{3}{4} \left(1 + \frac{\sqrt{3}}{2}\right)^2 bE_1I\mathcal{G}_1 \quad , \quad M_2 = M_1 \frac{1 - \frac{\sqrt{3}}{2}}{1 + \frac{\sqrt{3}}{2}} \quad . \quad (4.53)$$

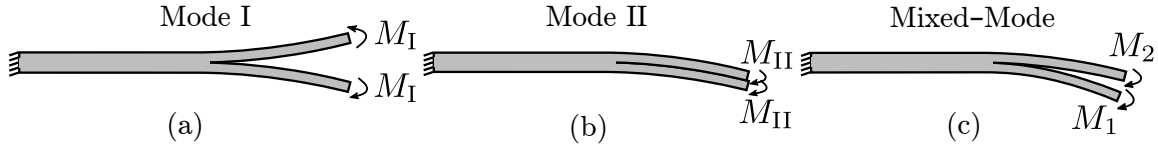


**Figure 4.17:** Loading pattern for (a) Mode I, (b) Mode II, and (c) Mixed-Mode ( $\phi = 0.5$ ) fatigue delamination growth.

The bending moments for the conducted simulations are summarized in Tab. 4.2. The moment loading of a MMB test ensures a constant energy release rate during fatigue crack propagation. The crack propagation rate during the tests (and simulations) remains, therefore, constant and simplifies the evaluation of the crack propagation rate. The cycle jump technique is employed and an allowable damage increment of  $\Delta D_f^{\text{allow}} = 0.05$  is utilized for Eq. (4.50). The simulations are stopped after the fatigue delamination has grown for a predefined length. For simulations greater than  $\Delta \mathcal{G}/\mathcal{G}_c = 0.5$  a fatigue crack length of 10 mm is chosen. Below this ratio the simulations are stopped after a crack length of 1 mm is reached. The crack length is divided by the number of load cycles obtained from the simulations resulting in the average crack propagation rate, depicted in Fig. 4.18. The numerical results are compared to the experimental data from [7]. Additionally, the Paris' laws obtained from the experimental data and utilized as input for the simulations are de-

**Table 4.2:** Bending moments applied in the MMB simulations obtained from beam theory-based solutions.

$\frac{\Delta \mathcal{G}}{\mathcal{G}_c}$	$M_I$	$M_{II}$	$M_1(\phi = 0.5)$	$M_2(\phi = 0.5)$
–	Nm	Nm	Nm	Nm
0.3	53.895	122.169	116.127	8.338
0.4	62.232	141.069	134.091	9.627
0.5	69.578	157.720	149.919	10.764
0.6	76.218	172.773	164.228	11.791
0.7	82.325	186.616	177.386	12.736
0.8	88.009	199.501	189.634	13.615
0.85	90.718	205.641	195.470	14.034
0.9	93.348	211.603	201.137	14.441
0.95	95.906	217.402	206.649	14.837

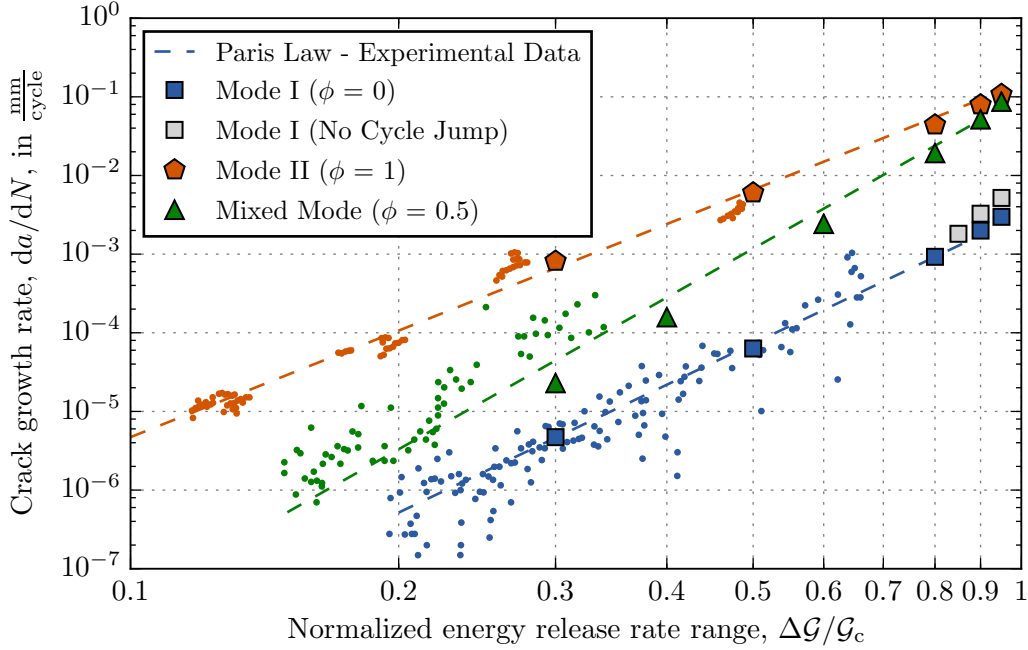


**Figure 4.18:** Comparison between the simulated crack propagation rates of the specimens with Mode I, Mode II, and Mixed-Mode loading patterns to the experimental data [7].

depicted as well. The numerical results fit closely to the Paris' laws for Mode I and Mode II. For mixed-mode loading the crack propagation rates are somewhat underestimated for high numbers of load cycles, probably caused by the cycle jump technique, but show again good agreement for smaller numbers of load cycles. Since the model is focused on the LCF regime the discrepancy between the simulation results and the Paris law in the mixed-mode loading case for high numbers of load cycles is not addressed in the present work. In the LCF case the application of the cycle jump technique leads to slightly lower fatigue crack propagation rates. This behavior is depicted for the Mode I case under  $\Delta\mathcal{G}/\mathcal{G}_c = [0.85, 0.9, 0.95]$  loading conditions, where simulations with and without the cycle jump technique are conducted. For higher numbers of load cycles, simulations without the cycle jump technique become computationally unfeasible.

### 4.5.3 Variable amplitude loading

Mode II fatigue simulations utilizing the ENF test setup, as depicted in Fig. 4.19(a), are employed to demonstrate the variable amplitude loading capabilities of the CCZM. The cyclic loading is applied by a constant displacement amplitude,  $\delta_{II}$ , which result in a decreasing reaction force amplitude,  $P_{II}$ , during fatigue delamination propagation. This way, a variable loading behavior at the cohesive zone is obtained. In addition to the demonstration of the variable amplitude loading capabilities of the CCZM the advantage of the non-local evaluation of the CZ length is demonstrated in this section. The initial response of Mode II delamination tests is influenced by the preparation of the initial delamination inside the specimen. Typically two types of specimen preparations are distinguished, (i) precracked specimens, where an initial delamination due to either Mode I or Mode II monotonic loading is introduced into the specimen, and (ii) non-precracked specimens, where, typically, a Teflon insert between the plies is utilized as an initial delamination. These differences in the specimen preparation influence the critical energy release rate,  $\mathcal{G}_{IIc}$ , for quasi-static tests [181], and the fatigue crack growth rate,  $da/dN$ , at the beginning of fatigue tests [171]. The latter work concludes that the accelerated  $da/dN$  of precracked specimens compared to non-precracked specimens at the beginning of fatigue tests is caused by an "area of uncoalesced microcracks ahead of the delamination front". Within the nomenclature of the present work, this "area" is equivalent to the cohesive zone. Non-precracked specimens do not have an initial cohesive zone and the perfect interface needs to be damaged by the applied cyclic loading conditions before cyclic delamination occurs. Hence, the initial crack growth rate is slower compared to the precracked specimens, where an initial cohesive zone (a pre-damaged interface) already exists. As soon as both specimen reach the same CZ length, steady-state subcritical crack growth is reached and the same fatigue crack propagation rate is obtained. The developed CCZM is applied to numerically demonstrate these phenomenons.

The ENF specimen has a length of  $l = 100\text{mm}$  with two  $h = 1.5\text{mm}$  thick arms, a width of  $b = 25\text{mm}$ , and the non-precracked specimens an initial crack length of  $a_0 = 35\text{mm}$ . The same carbon/epoxy laminate as in the previous chapter is utilized and the material and interface parameter are summarized in Tab. 4.1. The same FEM modeling strategy

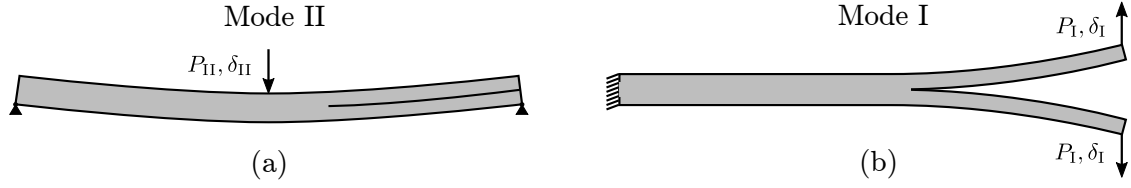


**Figure 4.19:** Schematic representation of an (a) End-Notched-Flexure (ENF) test, and (b) displacement loaded Double-Cantilever-Beam (DCB) test.

as in Section 4.5.1 is utilized and the boundary conditions are modified to account for the ENF test setup as depicted in Fig. 4.19(a). Interface closure is modeled by contact and target elements employing the CCZM with the following set of penalty contact parameters,  $\Delta_3^{\text{fc}} = 0.01\text{mm}$ ,  $K_{\text{sc}} = 10^6 \text{ N/mm}^3$  and  $K_{\text{fc}} = 10^8 \text{ N/mm}^3$ . Nine simulations with the displacement amplitudes  $\delta_{\text{II}} = [1.6\text{mm}, 2.0\text{mm}, 2.5\text{mm}]$  are conducted for specimens with (i) no precrack, (ii) a Mode I precrack, and (iii) a Mode II precrack. For simulations including a precracked specimen DCB (Mode I) or ENF (Mode II) quasi-static simulations are conducted before the fatigue ENF simulation is started. This way, a delamination and a certain CZ length is introduced into the simulated specimen. The length of the delamination and the introduced cohesive zone should lead to a comparable structural response of the precracked specimen compared to the non-precracked specimen at the beginning of the fatigue simulation. To achieve this the experimentally utilized procedure for the evaluation of the crack length is of importance and, therefore, summarized in the following.

In Mode II fatigue delamination experiments utilizing the ENF test, the specimen's compliance is often employed to describe the crack advance during the fatigue loading. If the specimen is purely elastic there is a direct relation between the length of the crack,  $a$ , and the specimen's compliance,  $\mathcal{C} = \delta_{\text{II}}/P_{\text{II}}$ . The Experimental Compliance Method (ECM) [192] is one way to calibrate this procedure. This method requires the measurement of the specimen's compliance at different initial crack lengths. Typically, the specimen is longer than the support distance of the test setup and the specimen with a certain initial crack length is simply moved side wards to obtain the specimen's compliance at different crack lengths. These measurements are then utilized in a linear least squares regression analysis to obtain the following relation,

$$\mathcal{C} = \mathcal{C}_0 + ma^3 \quad , \quad (4.54)$$



where  $\mathcal{C}_0$  and  $m$  are fitting parameters. This procedure is numerically reproduced for three different crack sizes, without an initial cohesive zone, and the fitting parameters are identified as depicted in Fig. 4.20. The ECM can, additionally, be utilized to obtain the energy release rate during fatigue testing as,

$$\mathcal{G}_{\text{II}}(N) = \frac{3 (P_{\text{II}}^{\text{max}}(N))^2 m (a(N))^2}{2b} \quad , \quad (4.55)$$

where  $P_{\text{II}}^{\text{max}}(N)$  is the maximum reaction force during a load cycle,  $N$ .

To numerically produce a precracked specimen quasi-static DCB and ENF simulations for Mode I and Mode II, respectively, are carried out. The DCB simulations utilize displacement boundary conditions at the end of the loading arms as depicted in, Fig. 4.19(b). The quasi-static ENF simulation utilizes the boundary condition setup depicted in Fig. 4.19(a). Additionally, the quasi-static ENF simulation requires viscous regularization to overcome the snap-back behavior of the specimen shortly after crack initiation. An energy-dissipation ratio of  $1 \cdot 10^{-4}$  is utilized for the nonlinear stabilization. For the quasi-static simulations, specimens with an initial crack length of  $a_0 = 25\text{mm}$  are modeled. The specimens are monotonically loaded until a compliance,  $\mathcal{C}$ , is obtained which equals the compliance of the non-precracked specimens. The non-precracked specimens have an initial crack length

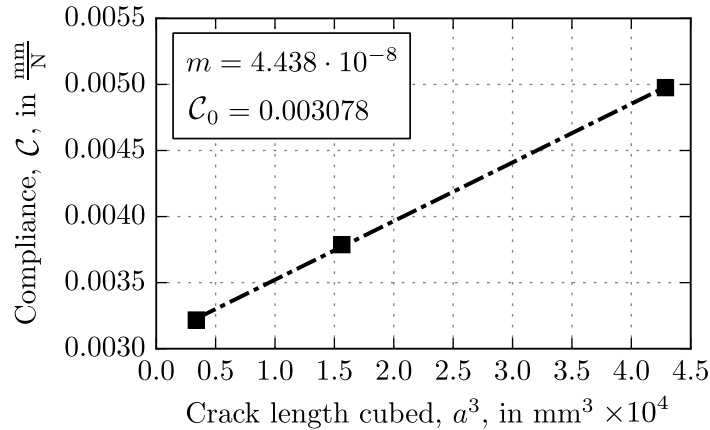


**Figure 4.20:** Compliance calibration of an ENF non-precracked test specimen with three different initial crack sizes, without a cohesive zone.

of  $a = 35\text{mm}$ , but do not contain a cohesive zone. The length of the cohesive zone in combination with the delamination length influences the specimen's compliance.

The loading amplitudes for the quasi-static simulations to reach a similar specimen's compliance need to be determined. Therefore, monotonically loaded DCB and ENF simulations with large loading amplitudes are conducted. The results of these quasi-static simulations are depicted in Fig. 4.21. In the first row the numerically obtained reaction force versus the applied displacement is depicted for the quasi-static DCB and ENF simulations. Additionally, the analytic results of the Corrected Beam Theory (CBT) [91] are included in the plot. In the second row the length of the delamination and the length of the CZ are depicted. For the DCB specimen stable crack growth occurs and a displacement amplitude of  $\delta_{\text{I}} = 1.4\text{mm}$  is identified to produce an initial crack length inside the precracked specimen which provides an ENF specimen's compliance similar to the non-precracked specimens. The identified displacement amplitude is indicated by the vertical dash-dotted line. In the ENF case unstable crack growth occurs and the delamination length increases rapidly after crack initiation. Hence, the obtained compliance is immediately below the searched for compliance and a smaller compliance value at  $\delta_{\text{II}} = 3.0\text{mm}$ , shortly after crack initiation, is accepted.

The identified loading amplitudes are utilized in the quasi-static simulation to produce precracked specimens prior to the fatigue analysis. The precracked specimens contain a delamination and a cohesive zone modeled by the CCZM. This simulation state is utilized for the subsequent fatigue analysis. The cycle jump technique is employed in the fatigue simulations and an allowable damage increment of  $\Delta D_{\text{f}}^{\text{allow}} = 5 \cdot 10^{-4}$  is utilized.

The results of the Mode II fatigue delamination simulation utilizing the ENF setup are summarized in the following. Simulations with non-precracked specimens are denoted as NON/FAT-II, whereas simulation with precracked specimens are denoted as PRE-I/FAT-II for Mode I precracks and PRE-II/FAT-II for Mode II precracks, respectively. The ECM is employed to calculate the fatigue crack growth rates which are depicted in Fig. 4.22. The obtained fatigue crack growth rates for the Mode I precrack and the non-precracked simulation are nearly identical. Initially a slightly lower  $da/dN$  is obtained from the numerical simulation as defined by the Paris law. In contrast, a much higher  $da/dN$  results from simulation with a Mode II precrack. After a transition phase, all of the simulations

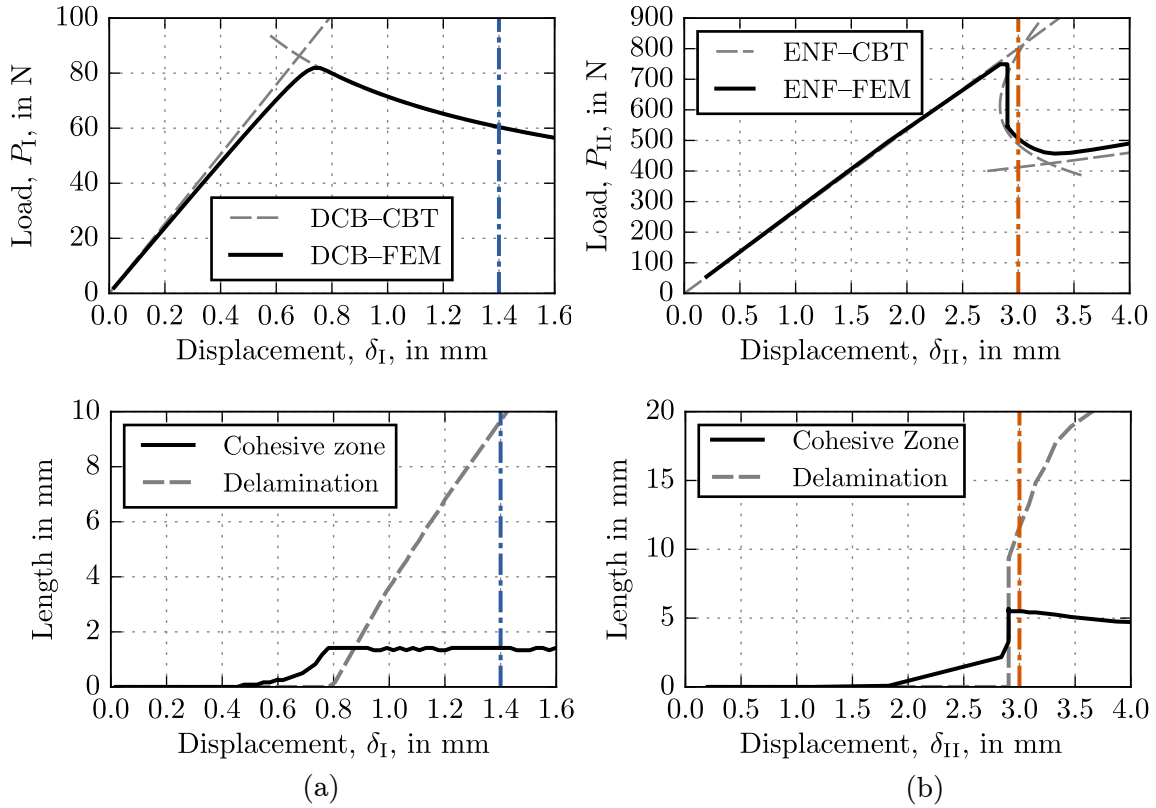


**Figure 4.21:** Quasi-static DCB (a) and ENF (b) simulations of the precracked specimens with an initial crack length of  $a_0 = 25\text{mm}$ . The simulations are carried out to obtain a comparable specimen compliance as the non-precracked specimens with an initial crack length of  $a_0 = 35\text{mm}$ . In the top row the load-displacement response of the specimens is depicted and compared to the Corrected-Beam-Theory (CBT). In the bottom row the introduced delamination and cohesive zone lengths are depicted. The required displacement load amplitude to obtain the searched for compliance is indicated by the vertical dash-dotted line.

result in the same  $da/dN$ . The predicted fatigue crack growth rate is close to the Paris law for the simulations with loading conditions above  $\Delta\mathcal{G}/\mathcal{G}_c = 0.4$ . For the simulations at  $\Delta\mathcal{G}/\mathcal{G}_c = 0.8$ , the crack growth rate is in well accordance to the Paris law at the beginning of fatigue crack propagation and drops slightly below the Paris law during the simulation of fatigue delamination growth. The simulations at  $\Delta\mathcal{G}/\mathcal{G}_c = 0.3$  provide predictions slightly above the Paris law.

The resulting length of the cohesive zone during the fatigue simulations is depicted in Fig. 4.23. For the non-precracked specimens no CZ exists at the beginning of the fatigue

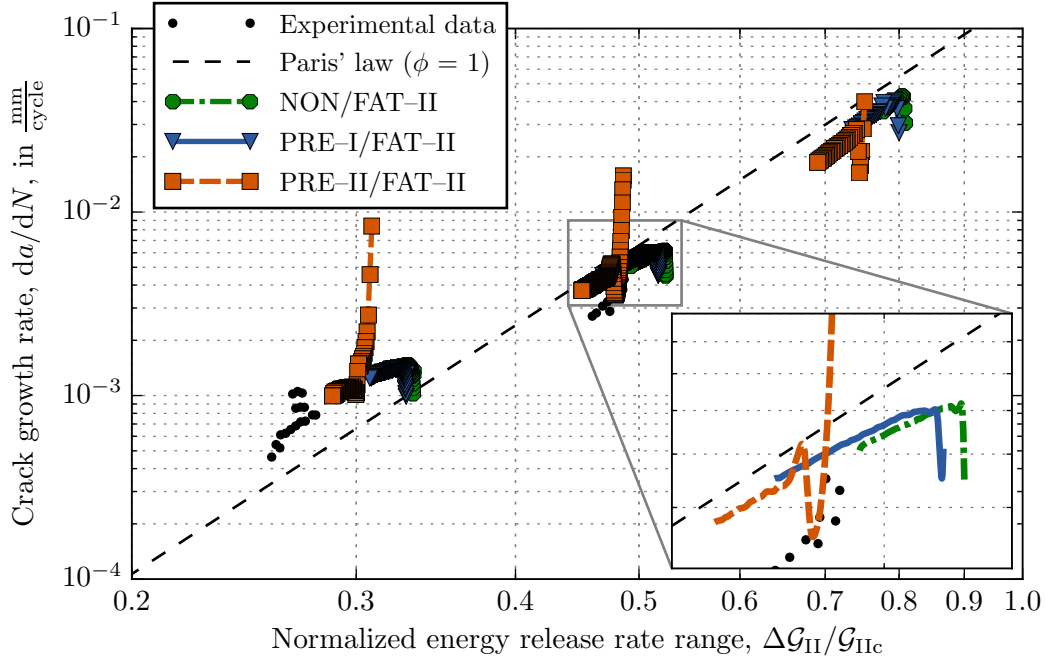


**Figure 4.22:** Fatigue crack growth rate of the Mode II fatigue simulations utilizing the ENF test. FEM simulations are conducted for non-precracked (NON/FAT-II) and Mode I (PRE-I/FAT-II) as well as Mode II (PRE-II/FAT-II) precracked specimens. The experimental data from [7] are additionally depicted.

Mode II loading. The first load cycle causes a certain CZ length, which increases with the simulation of the subsequent load cycles. The CZ reaches a certain maximum and starts to decrease again. For the precracked specimens a CZ exist at the beginning of the fatigue loading and is larger than the one predicted for the non-precracked specimen after the first load cycle. Continuous fatigue loading decreases the CZ length rapidly until a certain CZ length is reached. Afterwards, the CZ length decreases slower and follows the same slope for all specimens, with or without precrack. In the present work, this CZ length with constant slope is denoted as the CZ length required for steady-state subcritical crack growth. In a double-logarithmic plot this CZ lengths follows a linear slope,

$$l_{cz} = M_{cz} \left( \frac{\Delta \mathcal{G}}{\mathcal{G}_c} \right)^{n_{cz}} \quad (4.56)$$

where the parameters have been identified as  $M_{cz} = 2.8 \text{ mm}$  and  $n_{cz} = 2.0$ . Analytic expressions for the length of the cohesive zone are derived and reviewed in [89, 218, 225, 226].

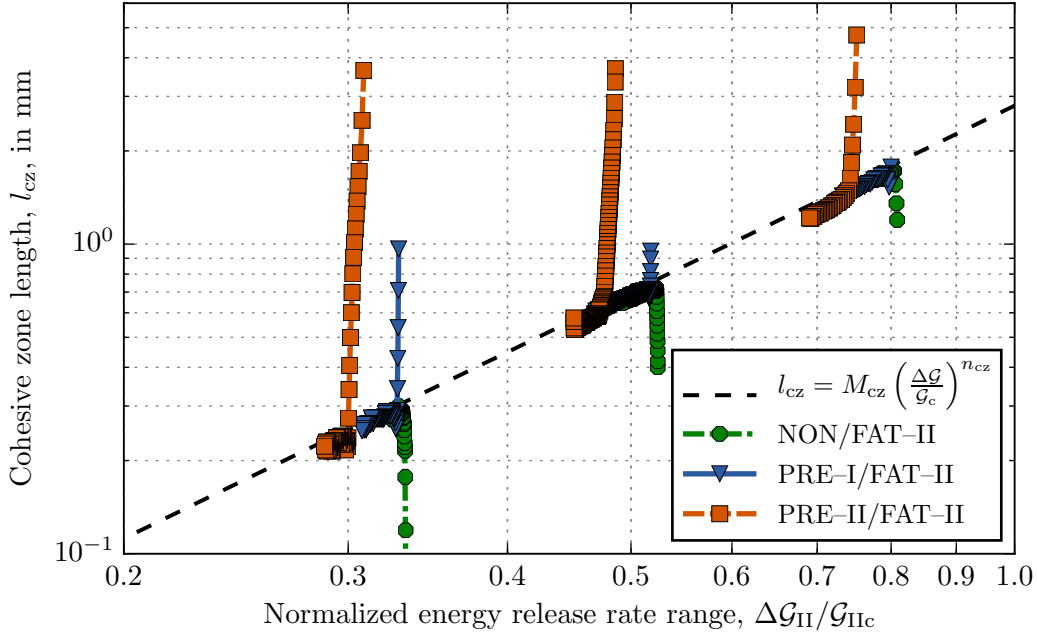


**Figure 4.23:** Length of the cohesive zone for non–precracked and precracked specimens under Mode II fatigue delamination propagation. The obtained cohesive zone length for steady–state subcritical crack growth follows a linear function inside a double logarithmic plot.

The length of the cohesive zone is dependent on the specimen geometry, the material, and the loading conditions. The derivation of an analytic expression for the cohesive zone length during subcritical crack growth is not carried out in the present work and further research is required on this topic.

For the simulations utilizing a Mode II precracked specimen followed by Mode II fatigue loading the introduced CZ increases the crack growth rate at the beginning of the fatigue loading. This behavior is expected since a predamaged zone in front of the crack tip (the cohesive zone) already exists and an accelerated propagation of a delamination through a predamaged interface compared to a propagation through a completely undamaged interface seems reasonable. For non–precracked specimens the CZ has to evolve at the beginning of the fatigue test and a decelerated fatigue crack growth rate is obtained, which supports the current understanding of the influence of the CZ on the fatigue crack propagation rate. Contrary, specimens with a Mode I precrack show a longer CZ as required for steady–state subcritical crack growth at the beginning of fatigue loading, but do not cause an accelerated

fatigue crack growth rate. This surprising behavior may be caused by the change of the mixed-mode ratio, but has not been addressed within the present work and further research on this topic is required. Nevertheless, the observation of these phenomena is enabled by the non-local evaluation of the CZ length during the simulation, which presents one of the advanced features of the formulated CCZM.

## 4.6 Summary

A thermo-mechanical cyclic cohesive zone model (CCZM) is developed focusing on the application of power semiconductor devices. The mechanical constitutive model is based on formulations developed for layered composite structures. These formulations seem to be the most advanced models currently available in terms of the considered loading conditions, easiness of the model calibration and the model predictive capabilities.

The mechanical constitutive behavior of the CCZM is based on an exponential traction-separation law developed for quasi-static loading conditions. In combination with the BK-Criterion allows this model for the analysis of mixed-mode loading conditions. The quasi-static formulation is extended by a Paris' law type formulation accounting for fatigue damage. The fatigue damage evolution law utilizes two structural parameters, i.e. the cohesive zone length and the mode ratio. Both parameters are evaluated by a non-local approach during the simulation. This way, the CCZM formulation relies only on physically interpretable interface parameters and parameter fitting is not required. The quasi-static and the fatigue damage rate are treated separately but are summed up to one total damage rate. The total damage variable is defined as the ratio between the dissipated energy rate during the damage process and the critical energy release rate. The thermal conductance of the interface is coupled with the total damage variable, resulting in an impeded thermal flux across the interface. This way, the mechanical and thermal interface deterioration is described by one single damage variable. Temperature dependent cohesive zone parameters are introduced and allow for the application of the CCZM in thermo-mechanical simulations.

The mechanical constitutive behavior of the CCZM is demonstrated by FEM simulations of well-established delamination tests from the field of layered composite materials. Constant

as well as variable amplitude loading conditions are considered and the obtained numerical results are in good agreement with the experimental data. The influence of the cohesive zone length on the fatigue crack propagation rate is shown. This model feature is enabled by the non-local evaluation of the cohesive zone length and allows for the simulation of varying loading conditions and their influence on the subsequent fatigue crack growth rate. The simulation of such load sequence effects has not been addressed extensively in the present work and further research is suggested in this area. The thermo-mechanical capabilities of the model will be exemplified in Chapter 5, where the CCZM is applied to a power semiconductor device.





## Chapter 5

# Application – DMOSFET

A DMOSFET power semiconductor is utilized to exemplify the developed fatigue damage modeling approaches. Two degradation mechanisms are assumed to occur during active power cycling, namely fatigue crack growth inside the ductile power metallization and cyclic interface delamination between the power metallization and the silicon chip. The damage mechanisms are simulated with the developed continuum damage mechanics approach for bulk fatigue damage modeling and the cyclic cohesive zone model for the modeling of cyclic delamination growth. A model reduction technique is employed and a simplified, generic DMOS cell model is generated. A coupled thermo–mechanical FEM analysis of repetitive overload pulses is conducted. The temperature field inside a DMOS cell during an electric overload pulse has been extracted from an electro–thermal simulation of the ”global” chip package [123]. Both damage modeling approaches are applied independently from each other and in combination for the stated DMOS cell problem. This way, the different damage mechanisms are studied both unaffected and influenced by each other and the obtained damage characteristics are compared.

### 5.1 Introduction

This chapter presents a numerical study on the material and interface deterioration of the power metallization inside a DMOSFET device during active power cycling with massive electric overload pulses. As discussed in Section 1.1, the numerical simulation of such a

problem is limited by several factors using the hard- and software available today. Simplifications strategies are applied to enable the analysis of an electro-thermo-mechanical problem, such as the operation of a power semiconductor device. The present work is narrowed down to the consideration of two different damage mechanisms in a thermo-mechanical analysis. Namely, the prediction of material degradation inside the ductile power metallization and the prediction of interface damage between the power metallization and the Si chip. Effects such as microstructural evolution, rate-dependent material properties, and environmental influences are not considered in the present work.

A submodel of a DMOSFET device is employed to reduce the model size. The modeling technique, based on [123], takes advantage of the thermal fields and external constraints experienced by a single DMOS cell as well as the cell's periodicity. This way, a single DMOS cell model is utilized to predict damage onset in the DMOSFET device. In the present work the same modeling technique is utilized to exemplify the developed continuum damage mechanics approaches presented in Chapters 3 and 4. Note that the modeling of localized damage progression in a "unit cell like" model does not represent the actual physical damage happening inside the chip package. The applied modeling technique is only valid as long as all DMOS cells are subjected to the same loading conditions and show the same constitutive response. Strictly speaking, this assumption is no longer valid as soon as damage localization starts in one of the DMOS cells. Damage modeling leads to a change of the constitutive response of the cell and affects the displacement field and loading conditions of the neighboring DMOS cells. Hence, a larger FEM model would be required for a proper analysis of damage progression inside an entire DMOSFET device subjected to overload conditions. The development of a numerical FEM embedding strategy of a damaged DMOS cell inside an array of undamaged DMOS cells resulting in a minimum model size is future work.

The aim of the present chapter, the demonstration of both damage modeling strategies on a DMOSFET device, is not affected by the modeling assumptions. A computationally efficient model of a simplified generic DMOS cell geometry is defined. The model consists of a bi-material compound of Cu and Si. The interface in-between is either modeled as perfectly bonded or by a cohesive law. The developed damage modeling approaches are applied for this structure. First, both approaches are applied independently, predicting either bulk

fatigue or interface degradation. Second, both approaches are applied in combination, resulting in a simultaneous damage progression in the bulk material and at the interface.

## 5.2 FEM–Model

The FEM modeling technique, developed in [123], for a DMOSFET device is summarized in the following. Assumptions in the modeling approach are discussed and modifications for the present work are pointed out. Ansys APDL v18.0 (ANSYS Inc., Canonsburg, PA, USA) is employed for the FEM simulations.

### 5.2.1 Geometry

The FEM simulations are carried out on a simplified, two–dimensional, generic DMOS cell model. In Fig. 5.1, a cross sectional view of a typical device used in automotive applications is sketched. On the left, the chip–package and the active Si chip area with periodically arranged DMOS cells is shown. The 2D–FEM model is depicted on the right–hand side of the figure. With respect to the considered damage behavior, two halves of the periodically arranged DMOS cells are modeled instead of one complete DMOS cell. A generic geometry and an extremely simplified metallization stack are assumed for the FEM model. Dimensions of the generic model are summarized in Table 5.1. The height of the two layers is chosen in such a way that the far–field stress and strain fields are not perturbed by the interface geometry. Linear interpolated, fully integrated, four noded, plane strain, isoparametric elements are used for discretization. An unstructured mesh is utilized, where the average element size is approximately  $w/30$ . The periodic arrangement of the DMOS cell is taken into account by the thermal and structural boundary conditions, discussed next.

**Table 5.1:** Dimensions of the generic DMOS cell model depicted in Fig. 5.1.

$a$	$b$	$c$	$d$	$h$	$w$	$r_1$	$r_2$
1.9 $\mu\text{m}$	3.8 $\mu\text{m}$	5.1 $\mu\text{m}$	3.2 $\mu\text{m}$	$\approx 30 \mu\text{m}$	12.8 $\mu\text{m}$	1.0 $\mu\text{m}$	1.0 $\mu\text{m}$



temperature field is required for the present work. The assumption of a spatial homogeneous temperature field made in [123] are based on a thermal transient analysis of the DMOS cell also carried out in [123]. Since a less resolved, but computational more efficient, model is utilized in the present work, the spatial temperature profile obtained in [123] cannot be applied directly to the present DMOS cell model. However, the same temporal temperature profile is employed, and the thermal boundary conditions are chosen in such a way that the spatial temperature field in the Cu layer is similar to the spatial temperature field obtained by the transient analysis in [123].

The spatial temperature field and the applied thermal boundary conditions are depicted in Fig. 5.2(b). Temperature boundary conditions are prescribed at the top nodes of the Cu layer, which follow the temporal temperature profile depicted in Fig. 5.2(a). The temperature difference between the bottom and the top of the Cu layer has been reported in [123] to range from  $\Delta T = 0\text{ K}$  to  $\Delta T = 35\text{ K}$  for the transient thermal simulation of an electric overload pulse. In the present work, a constant temperature difference between the top nodes and the bottom nodes of  $\Delta T \approx 10\text{ K}$  is chosen for simplicity. Since the heat produced by an electric overload pulse remains the same, even during material deterioration, heat flow boundary conditions are utilized at the bottom nodes of the Si layer. A temporal constant heat flow value is modeled and the magnitude is chosen in such a way that the desired temperature gradient in the Cu layer is obtained. A value of  $Q = 2.4\text{ W}$ , evenly distributed at the bottom nodes of the Si, is applied, resulting in the temperature difference of  $\Delta T \approx 10\text{ K}$  between the bottom and the top nodes of the Cu layer.

A single load cycle is simulated by three subsequent load steps utilizing quasi-static thermo-mechanical FEM analysis. The time points for the three load steps are depicted in Fig. 5.2(a). The last point in a load cycle is coincident with the first point of the subsequent load cycle. Since rate-independent material or interface parameters are chosen, a higher resolution of the load cycle is not necessary. Automatic adjustment of the load increment is utilized and the temperature on top of the Cu layer is linearly ramped between the load steps. The initial load increment of the second load step, which represents the rapid temperature increase, is set smaller than that of the first and third load steps of the load cycle. This way, the automatic adjustment of the load increment is sped up, resulting in a shorter computational time.

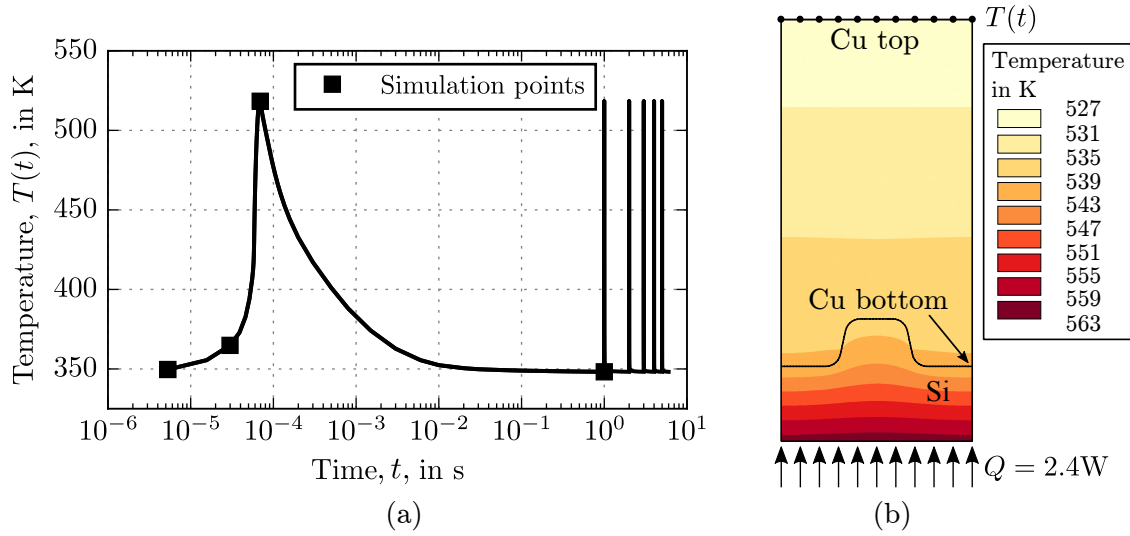


**Figure 5.2:** Thermal boundary conditions for the DMOS cell submodel. (a) temperature time profile of the first six load cycles applied to the top nodes of the Cu layer; (b) spatial temperature field obtained at the thermal peak load.

### 5.2.3 Mechanical Boundary Conditions

The mechanical boundary conditions aim to represent the kinematic constraint of a single DMOS cell apart from the edges of the DMOSFET. DMOS cells at the edge of the active DMOS area are considered to be significantly colder compared to the locations well inside the active DMOS area resulting in lower temperature swings and, consequently, in less damage accumulation. Hence, the applied modeling technique [123] focuses on the central part of the DMOSFET, where failure is expected to occur [163].

The extremely short heating phase during an overload power density pulse and the subsequent long pausing phase leads to acute localized heating inside the multilayer chip. Due to this loading characteristic (short heating—long cooling), only a thin layer of the active DMOS area gets rapidly heated while the rest of the chip package remains near the ambient temperature. The surrounding cold material prevents the hot region from expansion in lateral directions. On top of the Cu metallization, a small layer of mold compound is assumed, which does not constrain the heated region in the vertical direction. These

considerations, explained in detail in [123], lead to a lateral constraint and the following displacement boundary conditions:

$$u_1^{\text{left}} = u_1^{\text{right}} = u_2^{\text{bottom}} = 0 \quad , \quad (5.1)$$

which are depicted in Fig. 5.1. These boundary conditions provide a complete decoupling from the global model resulting in a substantial reduction of the model size. This significant reduction in the degrees of freedom is obtained by taking the cells periodicity into account. The main drawback of this modeling strategy is that the "unit cell like" submodel is only valid as long as the damage localization does not influence the far field stress, strain or temperature field. Hence, the damaged region inside the submodel has to be small compared to the geometry of the submodel. As soon as the damaged region affects the mechanical or thermal field on the model edges the obtained results are no longer representative for the DMOSFET device. In this case either a larger submodel is required or an advanced modeling technique needs to be employed. The development of such a submodeling technique is future work. In the present work, the inaccuracy obtained due to localized damage modeling inside the simplified submodel is accepted and should not affect the demonstration purpose of the current chapter.

#### 5.2.4 Material Properties

The initial material state is assumed to be stress-free. This is in contrast to the stress-state of real power semiconductor devices, where chip fabrication and packaging processes induce residual stresses into the multilayer chip structure, which may influence the fatigue life [152]. However, in the case of high plastic strain amplitudes, which occur during electric overload pulsing, the influence of residual stresses and strains has only a minor influence on the overall fatigue life. Hence, the assessment of the initial stress state is not addressed in the present work.

Further, the stress-free temperature for all materials is set equal to room temperature, 293 K. In an initial load step, the FEM model is heated up from this room temperature to the initial temperature of the thermal load cycle.

The elastic and temperature dependent thermal properties for the Si layer are provided in Table 5.2. The cubic elastic material properties are taken for a standard (100) silicon wafer, where the principal material axes are aligned with the crystal directions [100], [010], and [001] which, in turn, are aligned with the FEM model axes,  $x_1$ – $x_2$ – $x_3$ .

The Cu layer is modeled by the same constitutive model as employed in Chapter 3. In addition, the J2 plasticity model combined with the Chaboche nonlinear kinematic hardening model, Eq. (3.52), accounts for a temperature dependent yield stress,  $\sigma_Y$ . The temperature dependent  $\sigma_Y$  is taken from micro-tension tests conducted at variable temperatures, carried out in [237]. Based on that, the temperature dependence of the Chaboche plasticity parameters is estimated. The material data set for the Cu power metallization is summarized in Table 5.3.

The material fatigue and damage parameters required for the CDM approach are determined in Chapter 3 for a comparable polycrystalline Cu. There, the fatigue material data are estimated from literature data and the damage parameters are identified from the numerical simulation of cyclic microcantilever beam experiments. The obtained fatigue and damage parameters are listed in Table 3.3. Since, a user written material subroutine is

**Table 5.2:** Elastic and temperature dependent thermal properties of Silicon.

Elastic engineering moduli [101]		
$E_1 = E_2 = E_3$	$\nu_{12} = \nu_{23} = \nu_{31}$	$G_{12} = G_{23} = G_{31}$
130 GPa	0.28	79.6 GPa
Temperature dependent thermal properties		
Temperature K	CTE [174] $10^{-6} \text{ K}^{-1}$	$k$ [6] $\frac{\text{W}}{\text{mmK}}$
358	2.98	0.047
398	3.20	0.043
438	3.38	0.040
478	3.53	0.037
538	3.70	0.035



**Table 5.3:** Elastic, thermal, and temperature dependent plastic material properties of polycrystalline Copper with an average grain size of  $2.7\mu\text{m}$ . (The temperature variation of the Chaboche plasticity parameters is estimated.)

Thermo-elastic properties and thermal conductivity			
$E$	$\nu$	CTE [123]	$k$ [123]
100 GPa	0.35	$16.7 \cdot 10^{-6} \text{ K}^{-1}$	$0.385 \frac{\text{W}}{\text{mmK}}$
Temperature dependent plastic properties			
Temperature	$\sigma_Y$ [237]	$C_1$	$\gamma_1$
K	MPa	MPa	–
163	157	2000	9.0
293	142	1800	8.5
398	130	1600	8.0
473	107	1400	7.5
673	79	1200	7.0

required for orthotropic damage modeling, which is not available yet, the CDM approach is only exemplified for isotropic damage behavior, defined by  $\omega = 1$  in Eq. (3.21).

### 5.2.5 Interface Modeling and Properties

Two different approximation techniques are utilized for the interface modeling. First, the Cu–Si interface is modeled as perfectly bonded. This way, no interface opening, mechanical degradation, or thermal degradation occurs at the Cu–Si interface. Second, the developed CCZM is utilized to model cyclic delamination between the Cu–Si interface. Cohesive zone elements are introduced into the DMOS cell model and placed between the simplified Cu–Si material compound.

The evaluation of interface properties at the required length scale is a difficult task. To the author’s knowledge, the interface properties of material compounds utilized in a DMOSFET structure has not been reported in the literature and is a field of ongoing research [100, 205]. Hence, a proper calibration of the CCZM parameters is not yet possible, and an assumed set of interface properties is taken for the demonstration purpose.

The developed CCZM model does not account for the damage nucleation process, and damage onset is assumed to be caused only by the opening of the interface surfaces. Hence, the estimated CCZM parameter set is defined in such a way that damage onset at the interface occurs already within the first load cycle. The assumed parameter set is based on the following considerations.

During an electric overload pulse the traction state at a damaged interface inside the DMOS cell model represents a 2D mixed-mode crack propagation problem. Therefore, traction-separation laws for Mode I and Mode II, respectively, are defined. The elastic properties of the interface are estimated from an assumed thin layer of 500 nm consisting of a Cu-Si material compound around the interface. The Young's modulus perpendicular to the interface can be approximated by the inverse rule of mixture which results, for an equal volume fraction of both materials, in a Young's modulus of  $E_{\text{int}} = 120$  GPa. This approximated Young's modulus is divided by the assumed thickness of the material compound resulting in a cohesive stiffness of  $K = 240 \cdot 10^6$  N/mm<sup>3</sup>. The  $\beta$ -parameter of the cohesive laws is chosen to represent this cohesive stiffness. The interface onset tractions are chosen to be smaller than the yield stress of the Cu layer at room temperature. Additionally, the critical energy release rate for Mode II is chosen to be higher than for Mode I. These assumptions lead to the estimated traction-separation laws depicted in Fig. 5.3, and are defined for a temperature of 293 K. Temperature dependent cohesive law parameters are defined, and a second set of cohesive law parameters is defined at a temperature of 673 K. For this data set the temperature dependent interface properties, the critical energy release rates and the interface onset traction's, are assumed to be half the magnitude of the interface properties at 293 K. This way, a temperature increase leads to a weakening of the interface behavior. Interface properties inside this temperature range are linearly interpolated.

For simplicity, the fatigue interface properties are assumed to be temperature independent. The fatigue properties are chosen in such a way that interface delamination and fatigue damage progression in the bulk Cu occur after roughly the same number of load cycles and propagate at almost the same rate. This way, the interaction of the different damage mechanisms in the combined simulation becomes visible and supports the demonstration purpose of the current chapter. The mixed-mode Paris law parameters are defined to represent a linear interpolation between the fatigue properties of Mode I and Mode II.

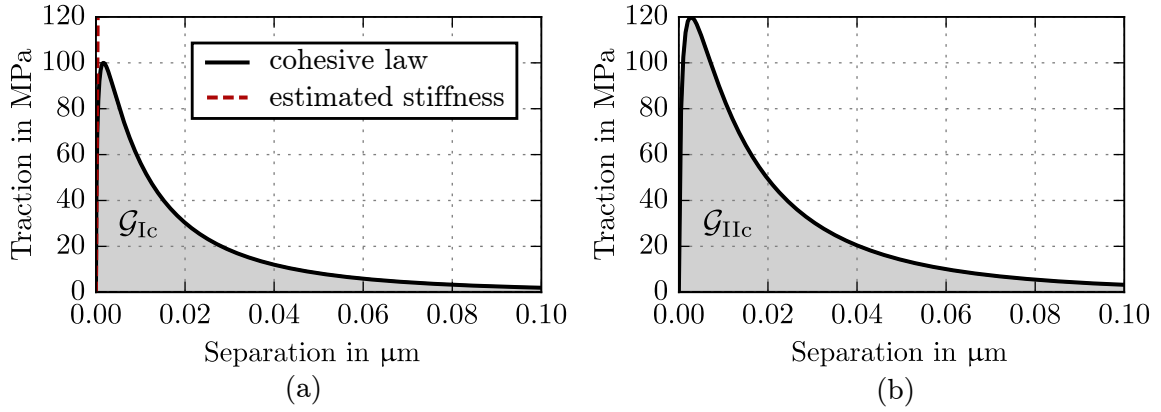


**Figure 5.3:** Estimated traction–separation laws for the Cu–Si interface. (a) Mode I cohesive law, (b) Mode II cohesive law.

No fatigue thresholds are considered and the corresponding values are set to zero. The estimated interface parameter set is listed in Table 5.4.

The thermal conductance of the interface is chosen in such a way that the temperature jump across the undamaged interface is less than  $[[\theta]] < 0.5$  K. This way, only a small thermal perturbation is introduced. The thermal conductance is determined through preliminary numerical studies and a value of  $h_{cz} = 1000$  W/mm<sup>2</sup> is picked for the DMOS cell model. The parameter  $v$  describing the thermal conductance at maximum interface penetration is

**Table 5.4:** Estimated parameter set for the CCZM describing the Cu–Si interface

Temperature dependent interface properties						
Temp. K	$\mathcal{G}_{Ic}$ $\frac{N}{mm}$	$\mathcal{G}_{IIc}$ $\frac{N}{mm}$	$T_I^o$ MPa	$T_{II}^o$ MPa	$\beta$ –	$\eta$ –
293	0.0020	0.0030	100	120	0.35	2.0
673	0.0010	0.0015	50	60	0.35	2.0
Fatigue properties						
$C_I$	$C_{II}$	$C_m$	$m_I$			
$5.0 \cdot 10^{-14} \frac{mm}{cycle}$	$1.0 \cdot 10^{-12} \frac{mm}{cycle}$	$1.0 \frac{mm}{cycle}$	5.0			
$m_{II}$	$m_m$	$\mathcal{G}_{Ith}$	$\mathcal{G}_{IIth}$			
3.0	0.0	$0.0 \frac{N}{mm}$	$0.0 \frac{N}{mm}$			

simple set to unity,  $\nu = 1$ . This way, the thermal conductance of a delamination during interface closing ranges between zero and the thermal conductance of the intact interface for a very high contact pressure at a penetration of  $\Delta_3^{\text{fc}} = 0.1 \mu\text{m}$ . The sinusoidal penalty stiffness parameters are chosen as  $K_{\text{sc}} = 10^8 \text{ N/mm}^3$  and  $K_{\text{fc}} = 10^9 \text{ N/mm}^3$ .

### 5.2.6 Cycle Jump Parameters and Other Model Features

The cycle jump parameters for the FEM models are explained in the following. In the case of a perfectly bonded interface, only the CDM approach is applied and the initial number of cycles overshooting the damage onset criterion is defined as  $\Delta N_{\text{os}} = 100$  in Eq. (3.44). The maximum and minimum damage tolerances for the adaptive damage extrapolation technique in Eq. (3.46) are chosen as  $\Delta D_{\text{max}} = 0.8$  and  $\Delta D_{\text{min}} = 0.4$ , respectively. The maximum number of jump cycles is limited by  $N_{\text{max}} = 500$  and the minimum number is set to  $N_{\text{min}} = 1$ .

In the case of cyclic delamination without considering bulk fatigue damage, only the CCZM approach is applied. The allowable damage increment for calculating the number of jump cycles is set to  $\Delta D_{\text{f}}^{\text{allow}} = 0.1$  in Eq. (4.50). The maximum and minimum number of jump cycles are limited by the same values as in the CDM approach.

In the case of the combined simulation where bulk fatigue damage and interface delamination are considered simultaneously, the same cycle jump parameters as in the independent simulations are chosen. Only the number of cycles overshooting the damage onset criterion in bulk fatigue differs and is set to  $\Delta N_{\text{os}} = 1$ . The cycle jump techniques of both approaches are formulated in such a way that an exchange of the predicted number of jump cycles is possible. This way, the minimum number predicted by one of the damage modeling approaches is utilized, and the damage extrapolation technique of the other approach adjusted in accordance to the minimum cycle jump number.

Additionally, viscous regularization is necessary in the simultaneous modeling case. The degradation of bulk elements directly at the interface can lead to convergence difficulties. Therefore, an energy–dissipation ratio of  $1 \cdot 10^{-6}$  is utilized for nonlinear stabilization. This way, the total amount of artificial energy dissipated during the simulation is around 0.5% of the total strain energy and should not affect the accuracy of the results.

## 5.3 Simulation Results and Discussion

Three different damage modeling cases of the single DMOS cell model are demonstrated. First, the DMOS cell model is computed with a perfectly bonded interface and only the CDM approach is applied, resulting in a prediction of fatigue damage inside the Cu layer. Second, the DMOS cell is simulated only with the CCZM approach, resulting in cyclic delamination growth at the interface. Herein, no fatigue damage inside the bulk Cu is considered, but the constitutive response of the interface is modeled by the CCZM. Third, both damage modeling approaches are applied simultaneously, resulting in material deterioration inside the bulk Cu and cyclic delamination growth at the interface. The predicted damage characteristics, caused by massive overload conditions, are discussed and compared to each other.

### 5.3.1 CDM – Fatigue Damage in Bulk

This subsection presents the application of the CDM approach for fatigue damage modeling in bulk materials on the Cu power metallization of a single DMOS cell. The Cu–Si interface is modeled as perfectly bonded. Consequently, no damage occurs between the Cu layer and the Si chip. The damage onset criterion and the damage variable are depicted in Fig. 5.4 for the ductile power metallization. Three different load cycles during the degradation process are chosen and the corresponding contour plots are depicted. Element averaged values are utilized for the contour plots. For the damage onset criterion, this technique works fine. For the damage evolution plots, however, the depicted element values can be underestimated due to the averaging process. The thickness of the region representing complete material failure is mostly simulated by a single finite element only. Elements surrounding the completely failed element usually show a much lower damage variable, leading to an averaged damage value below  $D = 1$ . Nevertheless, complete material failure occurs in the simulations and the elements representing material failure are explicitly depicted in the temperature plots below.

In the simulation applying the CDM approach only, the first damage onset is predicted after  $N = 9429$  electric overload pulses. The symmetric structure and loading of the DMOS cell leads to two locations equally prone for damage onset as depicted in Fig. 5.4.

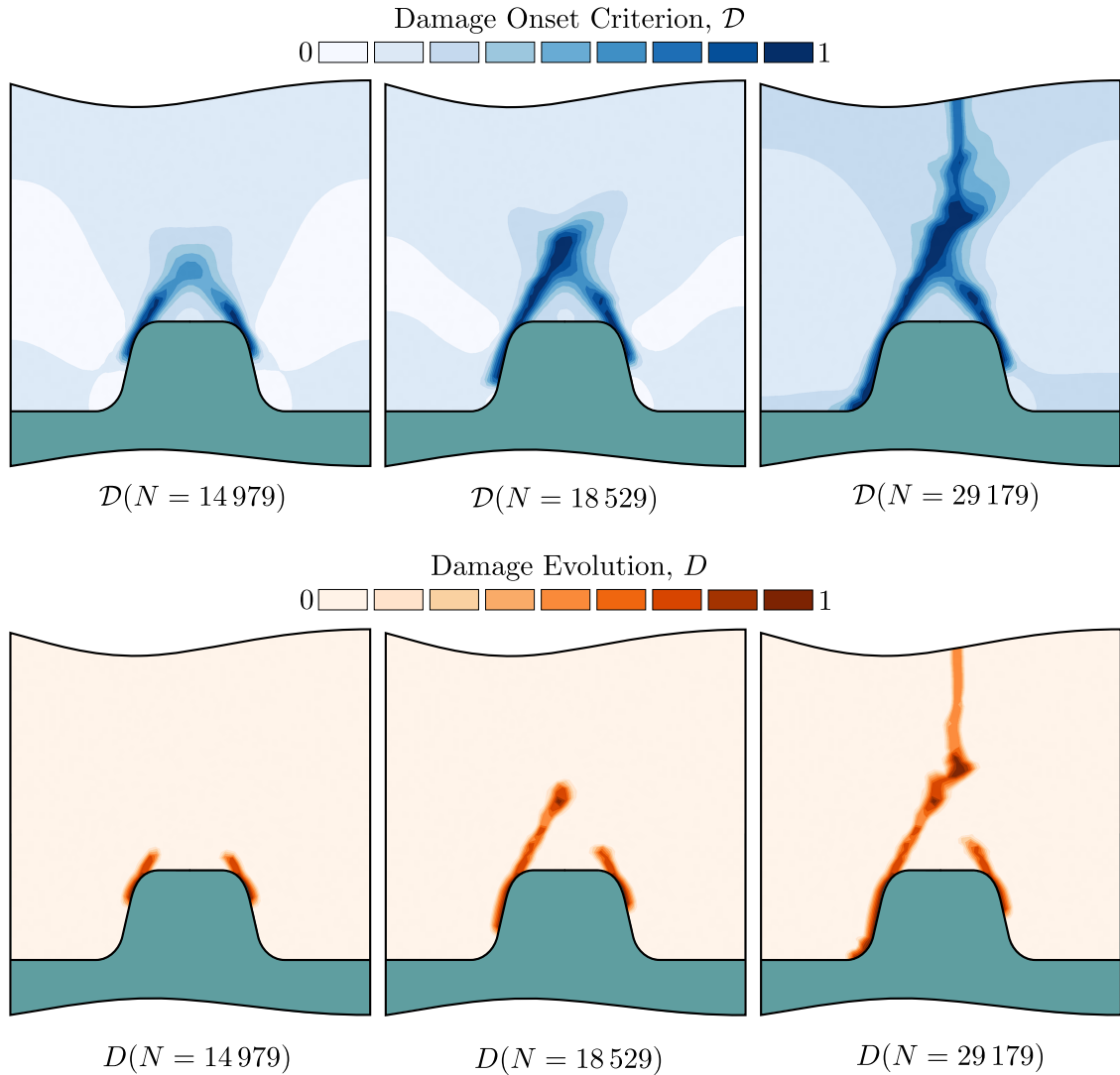


**Figure 5.4:** Damage characteristics of the generic DMOS cell model with a perfectly bonded interface, applying the CDM approach only. Contour plots of the damage onset criterion,  $\mathcal{D}$ , (top) and the damage variable,  $D$ , (bottom) are depicted for three different numbers of applied load cycles,  $N$ .

Damage evolution starts, and until  $N \approx 15\,000$  load cycles, the spatial damage evolution of both damage onset points is almost identical. Afterwards, the spatial evolution of the right-hand side damaged region slows down and further damage progression only occurs on the left-hand side. The geometry, boundary, and loading conditions of the problem are perfectly symmetric. Hence, also the obtained damage characteristics is symmetric at the beginning. The unstructured mesh is chosen to obtain slight numerical differences

between the left-hand side and the right-hand side of the model. This way, one of the damaged regions can become dominant. A different unstructured mesh may result in a mirrored prediction of the dominant damaged region. In a real component, initial flaws and defects inside the material may cause a similar macroscopic effect. At  $N = 18\,529$  load cycles, the left-hand side damaged region reaches the symmetry plane of the model and starts to change its propagation direction. Subsequently, the damaged region propagates vertically until the upper model edge is reached at  $N = 44\,929$  load cycles. The displayed edge of the Cu layer is reached by the damaged region after  $N = 29\,179$  load cycles. During vertical damage progression, the predicted critical plane orientation of the Fatemi–Socie critical plane method is oriented at  $45^\circ$  to the model axes. Since isotropic damage modeling is employed, this critical plane orientation is not utilized for the modeling of the elasto–plastic response of the damaged material. Hence, the application of the orthotropic damage modeling strategy may result in a slightly different path of the damaged region.

The spatial temperature field in the Si layer and the Cu power metallization are depicted in Fig. 5.5. The contour plots correspond to the same load cycle numbers as depicted in Fig. 5.4. The finite elements experiencing complete material failure, i.e.  $D = 1$ , are indicated in the contour plots. During an electric overload pulse, the DMOS cell is rapidly heated and slowly cooled down. The displayed temperature values are taken at the peak temperature of the temporal temperature profile depicted in Fig. 5.2(a). For the undamaged DMOS cell, a symmetric spatial temperature field is obtained, where a small temperature increase below the Si hump is visible. With continuing damage progression, the heat flow through the damaged region is impeded and an unsymmetric temperature field arises. Additionally, a slight increase in the temperature values below the Si hump, caused by material deterioration, becomes visible.

The thermal flux through the damaged model at a load cycle number of  $N = 29\,179$  is depicted in Fig. 5.6. Since a constant heat flow is applied at the bottom of the FEM model, the thermal flux during one load cycle across the single DMOS cell remains constant. Material degradation is modeled between two load cycles. The thermal conductance is degraded and the heat flow through the damaged region is impeded. In the subsequent equilibrium iteration of the FEM analyses, the heat flow is locally impeded and adjusted to circumvent the damaged regions, as depicted in detail on the right-hand side of Fig. 5.6.

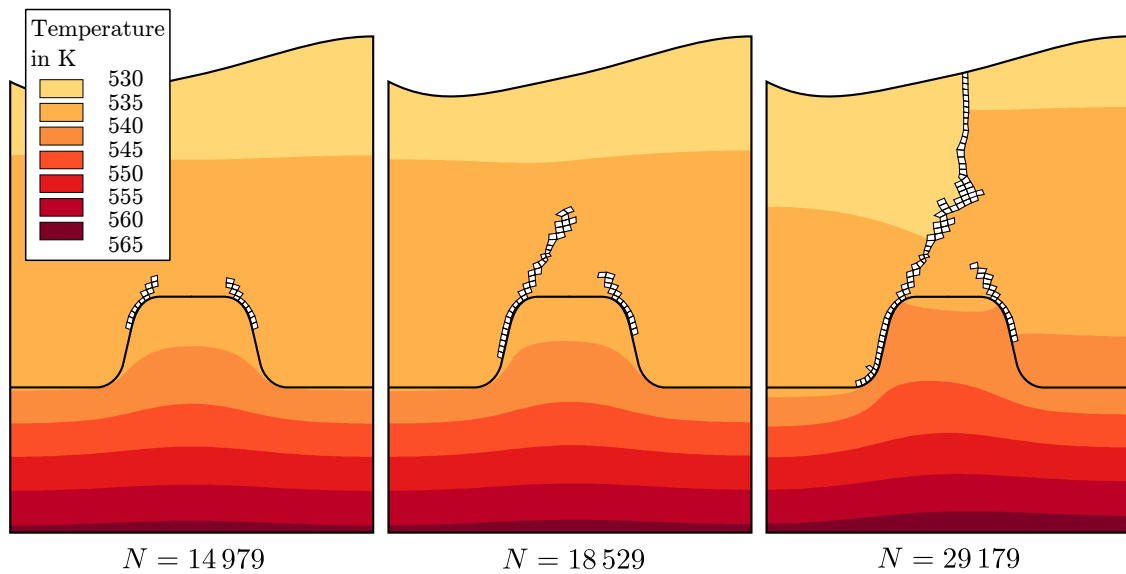


**Figure 5.5:** Temperature field of the generic DMOS cell model during bulk fatigue damage evolution. A perfectly bonded interface is assumed and only material deterioration in the bulk Cu leads to an impeded heat flow through the DMOS cell model. The impeded heat flow affects the temperature field and results in slightly increased temperatures.

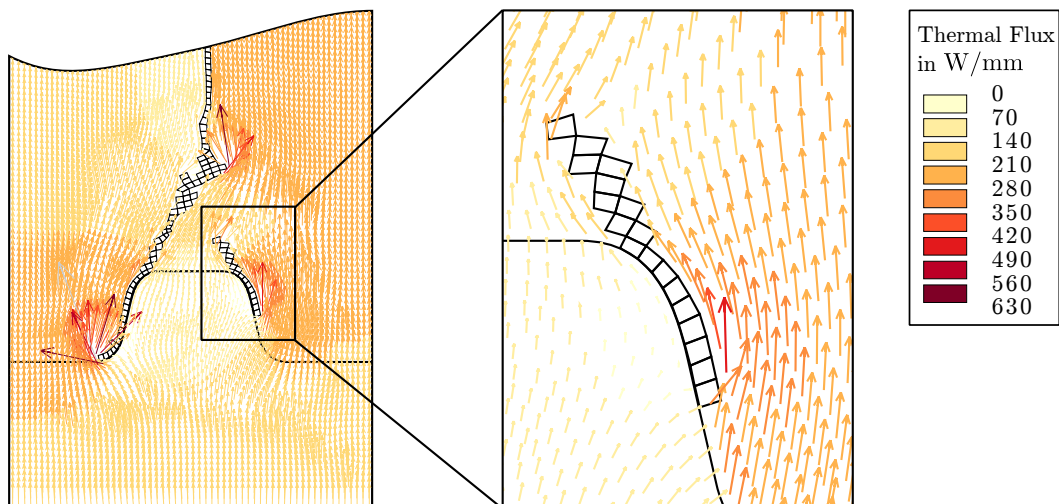


**Figure 5.6:** Vector plot of the thermal flux across the damaged DMOS cell model computed by the CDM only simulation for a load cycle number of  $N = 29179$ . A detailed view of the heat flow around the right-hand damaged regions is provided.



Next, the same FEM model and modeling strategy is utilized, but an initial void is introduced at the top of the Cu power metallization. The initial void is modeled by manually setting the damage state of a single element to  $D = 1$ , which represents a completely damaged material. This way, the first damage onset does not occur at the interface of the Cu–Si compound; instead, damage onset occurs at the modeled void after  $N = 8\,686$  load cycles and propagates vertically towards the Cu–Si interface. At the interface damage onset occurs after  $N = 9\,436$  load cycles, which corresponds to nearly the same load cycle number as in the previous simulation. Damage onset at the interface is again symmetric at the beginning of the simulation until the left-hand side damaged region becomes dominant. Afterwards, the dominant damaged region follows quite the same path as in the simulation without an initial void at the top of the Cu layer. The damage paths are depicted in Fig. 5.7. The left-hand side damaged region emerging from the interface changes its direction into a vertical slope at  $N = 21\,411$  load cycles, which is slightly later than in the simulation without an initial void. Afterwards, both damaged regions evolve in vertical direction. At  $N = 25\,061$  load cycles, the damage onset criterion predicts a mutual influence between the two propagating damaged regions. After  $N = 26\,311$  load cycles, both damaged regions start to change their propagation directions. At  $N = 27\,398$  load cycles, the damaged regions coalesce into one single region of material failure which traverses the Cu power metallization. The elements representing material failure are depicted in the third contour plot of Fig. 5.7. Additionally, the temperature profile at the peak temperature is depicted for this damage state. Note that the area of the maximum temperature, 565 K, is noticeable larger than in the simulation without an initial void at the top of the Cu layer. This is mainly caused by the additional direction change of the region of material failure triggered by the initial void.

The rates of spatial advance of the damaged regions for the two models, with and without a void at the top of the Cu layer, are depicted in Fig. 5.8. Herein, the number of elements in a damage state ( $D > 0$ ) is plotted against the number of load cycles,  $N$ . Damage onset occurs in both simulations roughly before  $N = 10\,000$  load cycles. Afterwards, a progressive increase in the number of elements in the damaged state is obtained. For the case without a void at the top of the Cu layer, the rate of spatial advance slows down after  $N \approx 15\,000$  load cycles, corresponding to the point at which the right-hand side damaged region is arrested.

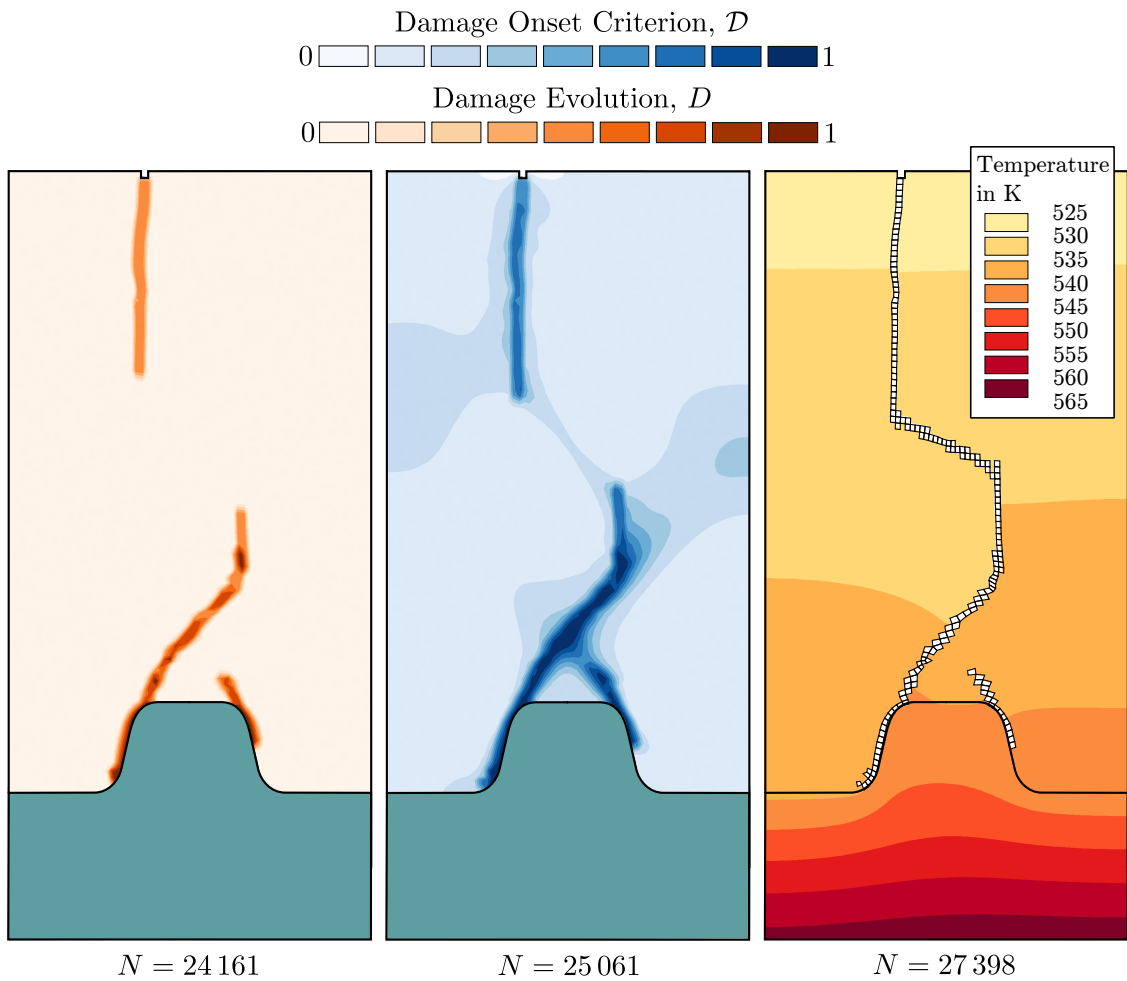


**Figure 5.7:** Damage characteristics of the generic DMOS cell model with an initial void at the top surface of the Cu power metallization. At a load cycle number of  $N = 24\ 161$  the damage variable is depicted, representing the damage state of the Cu layer. For  $N = 25\ 061$  load cycles the damage onset criterion is depicted indicating the mutual influence of both damaged regions. At  $N = 27\ 398$  load cycles the temperature profile is depicted and the elements representing material failure are indicated.

Subsequently, the direction change of the left-hand side damaged region occurs, and, after  $N \approx 22\ 000$  load cycles, only vertical damage progression at an almost constant rate is obtained. In contrast, the simulation with an initial void at the top of the Cu layer shows a much steeper slope, caused by two propagating damaged regions. At around  $N \approx 26\ 000$  load cycles, the two damaged regions coalesce at a very high rate. Consequently, the coalescence of both damaged region occurs rapidly over a very low number of load cycles.

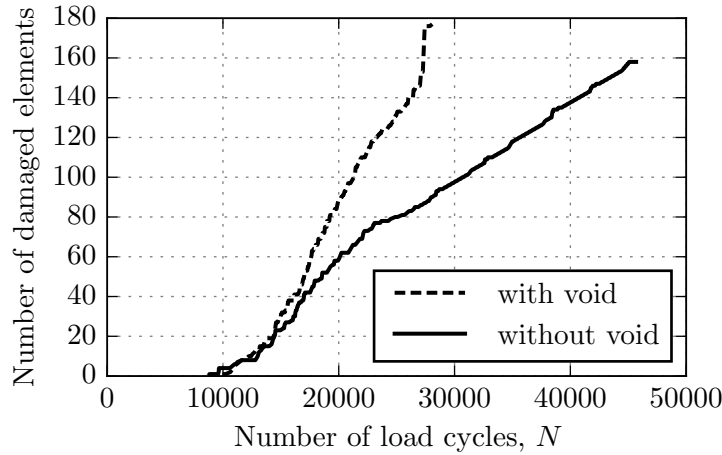


**Figure 5.8:** Rates of the spatial advance of the damaged region for the CDM only models with and without an initial void at the top of the Cu layer.

### 5.3.2 CCZM – Cyclic Delamination at the Interface

In this subsection, the CCZM is demonstrated at the single DMOS cell model. Therefore, the interface between the Cu–Si compound is discretized by cohesive elements and the estimated interface parameter set is employed. The bulk Cu of the power metallization is assumed to remain undamaged throughout the simulation. The same loading conditions as in the bulk fatigue damage models are utilized. The degrading interface behavior is depicted in Fig. 5.9 for three different time points. After the first stabilized cycle is found, a maximum damage variable inside the interface of  $D = 0.02$  is obtained. As in the bulk fatigue case, damage onset is predicted symmetrically at the left–hand side and right–hand side edges of the Si hump. Afterwards, the two cohesive zones start to evolve. At  $N = 6\,313$  load cycles, a damage variable of  $D = 0.55$  is reached inside the right–hand side cohesive zone, which becomes the dominant one for the following load cycles. The first occurrence of a complete delamination is detected after  $N = 8\,821$  load cycles. The single cohesive zone is split up into two cohesive zones and the obtained delamination propagates in both directions. This region is mostly dominated by Mode I delamination growth caused by the applied boundary conditions. After  $N = 9\,484$  load cycles, a fully developed delamination on the left–hand side of the Si hump also emerges and propagates. Near the radii of the Si hump, the delamination propagation slows down. After  $N = 15\,035$  load cycles, nearly the

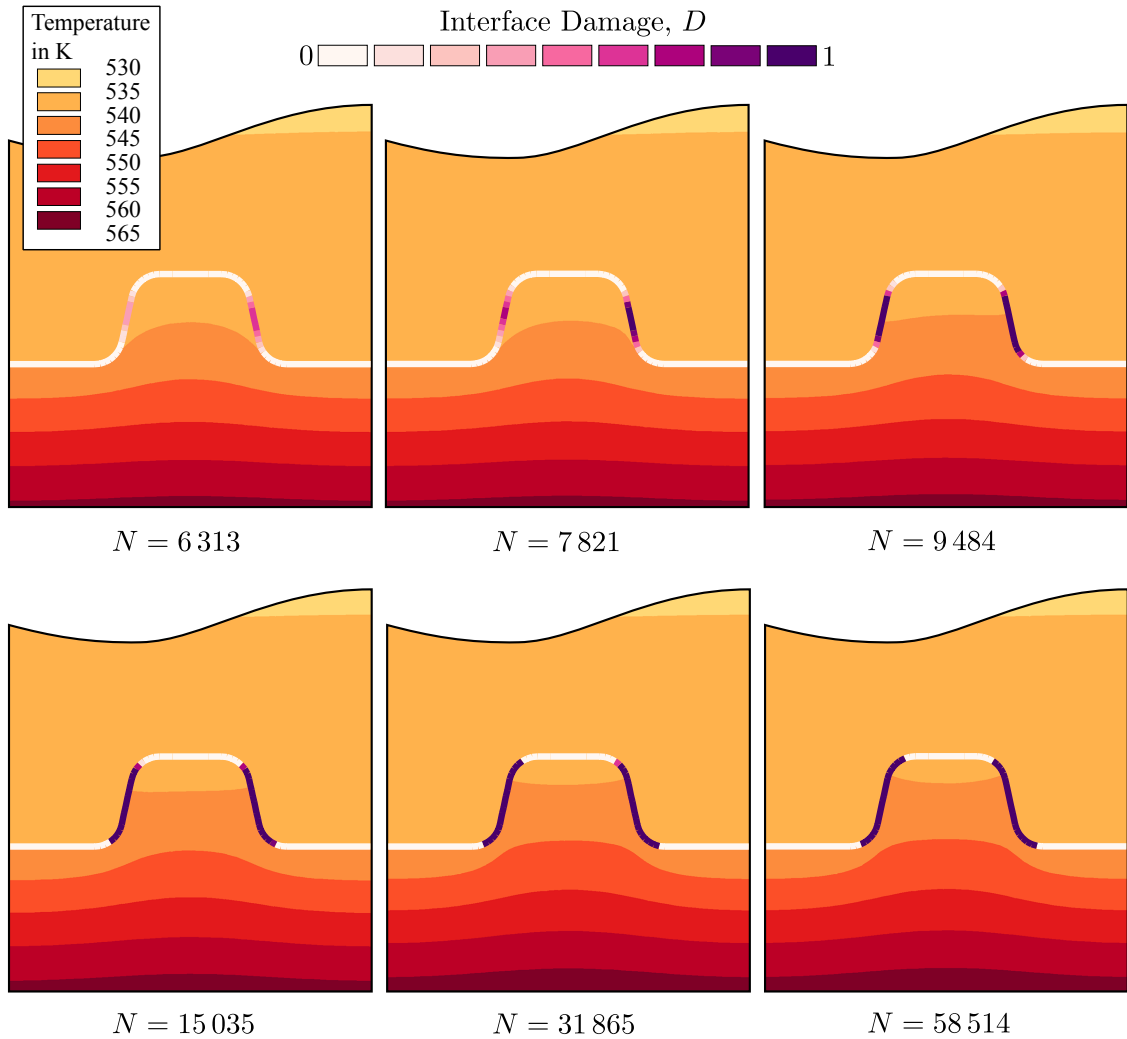


**Figure 5.9:** Damage characteristics and temperature profile of the generic DMOS cell model employing only the CCZM approach. The damage state of the interface is indicated by the interface damage variable,  $D$ . Three different damage states are depicted and identified by the number of applied load cycles,  $N$ .

whole vertical edges of the Si hump are delaminated. Subsequently, the delaminations keep propagating at a very low rate. At  $N = 58514$  load cycles are reached the two delaminations are arrested since all four cohesive zones are vanished in the simulation.

In addition to the damage state of the interface, the temperature profile at the peak temperature is depicted in Fig. 5.9. Similar characteristics as in the bulk fatigue damage case are found. The increasing damage state of the interface, obtained at the vertical edges of the Si hump, leads to an impeded heat flow through this region of the interface. Consequently,

the temperatures below the damaged interface are slightly higher than in the undamaged case.

The thermal flux across the interface is depicted in Fig. 5.10 for a load cycle number of  $N = 7821$ . For easier comparison, the intervals of the contour colors are chosen the same way as in Fig. 5.6. In the undamaged case, the thermal conductance is chosen to represent an almost perfect thermal interface. During damage progression, the thermal conductance is degraded, which results in a deterioration of the heat flow through the interface. In the case of a delaminated and open interface, the heat transfer across the interface is completely impeded. This case is depicted in the detailed view on the right hand side of Fig. 5.10. Similar to the bulk fatigue case, the thermal flux circumvents the open delamination.

In Fig. 5.11, the overall cohesive zone length and the length of the total delamination inside the single DMOS cell model are depicted. No distinction is made between the left- and right-hand side delaminations or cohesive zones. The total cohesive zone length after the first stabilized cycle is approximately  $2\ \mu\text{m}$ . Afterwards, the cohesive zone length increases until the first delamination emerges. Subsequently, the cohesive zone length drops and the delamination length rises, indicating a fast delamination growth. The cohesive zone length

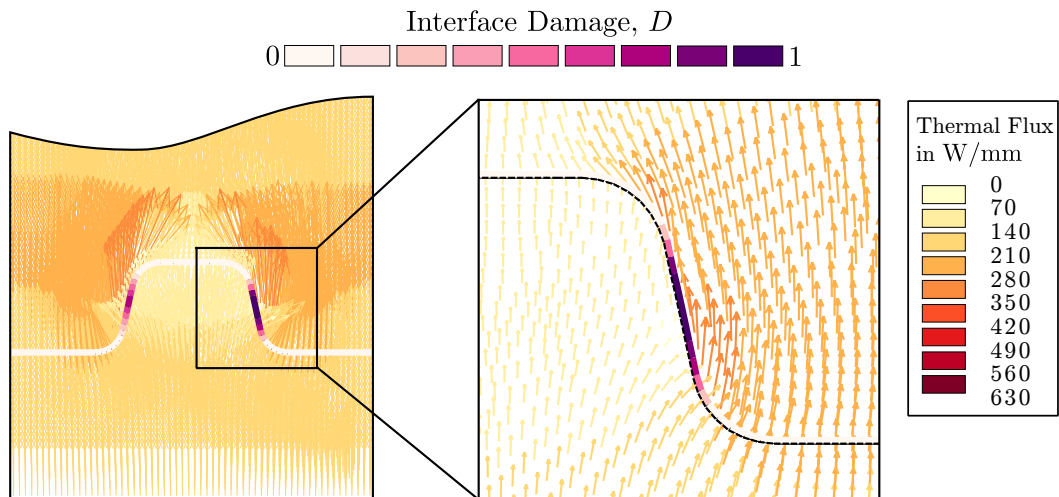


**Figure 5.10:** Vector plot of the thermal flux across the damaged interface computed by the CCZM only simulation for a load cycle number of  $N = 7821$ . A detailed view of the heat flow around the completely damaged and open interface is provided on the right-hand side of the figure.

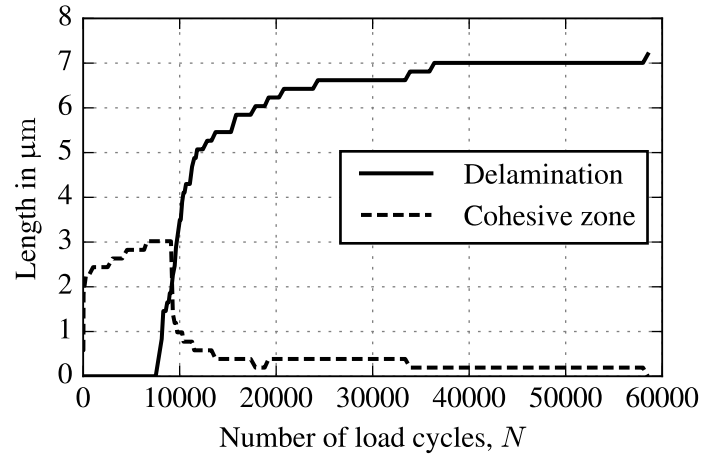


**Figure 5.11:** Evolution of the overall cohesive zone length and the total delamination length within the interface of the single DMOS cell model.

drops to approximately  $0.5 \mu\text{m}$  and keeps constant until  $N \approx 33\,000$  load cycles. At the same time, the delamination propagation slows down, but remains active until a delamination length of about  $7 \mu\text{m}$  is reached. After  $N \approx 33\,000$  load cycles, the cohesive zone length decreases again and remains at this level. For the region of very slow delamination propagation, which occurs after  $N \approx 15\,000$  load cycles, the cohesive zones vanish and only a few interface elements are within a damage state ( $0 < D < 1$ ). This can lead to inaccurate predictions of the fatigue propagation rates and may influence the estimated lifetime. For a sufficient analysis of this region, a refined mesh should be utilized. This inaccuracy is accepted in the present work since the change of the delamination state after  $N \approx 15\,000$  load cycles only has a negligible influence on the structural behavior of the DMOS cell model.

### 5.3.3 CDM & CCZM – Coupled Fatigue Damage Evolution

In this final subsection both modeling approaches are simultaneously applied to one single DMOS cell model subjected to electric overload pulsing. The model setup is the same as in the previous cases. The CDM approach is utilized to model bulk fatigue damage in the Cu power metallization. No initial void is modeled in the metallization. The CCZM approach is employed to model cyclic delamination at the Cu–Si interface.

The damage variable of the bulk fatigue CDM approach,  $D_b$ , and the interface damage variable of the CCZM approach,  $D_{cz}$ , are depicted in Fig. 5.12. First damage onset occurs at the interface, where a cohesive zone is established within the first load cycle. Damage onset in the Cu power metallization follows after  $N = 5\,586$  load cycles. Hence, damage onset in the bulk material occurs earlier in this simulation, considering the interface, than in the simulation neglecting the interface. In contrast to the simulation with the perfectly bonded Cu–Si interface, the CCZM model introduces a finite stiffness between the modeled Cu layer and Si layer, which results in a changed stress and strain state. These changes influence the damage behavior of the Cu metallization around the interface and result in the earlier damage onset. The damage state in the cohesive zone evolves since the first load cycle and results in a delamination after  $N = 7\,628$  load cycles. Afterwards, delamination propagation and damage evolution in the bulk Cu occur simultaneously. Around  $N = 9\,536$  load cycles, the right–hand side damaged region in the bulk Cu becomes dominant. The change of the dominant damaged region from the left–hand side in the CDM only approach to the right–hand side in the combined simulation is influenced by the evolution of the interface delamination and the unstructured mesh. For interface damage, the right–hand side delamination is again the dominant one, as in the CCZM only approach. Damage evolution of the left–hand side region in the bulk Cu stops and the dominant damaged region follows a similar, but mirrored path as in the simulation neglecting the interface. Delamination again occurs on both vertical edges of the Si hump and follows a similar propagation characteristic as in the simulation of the CCZM only approach. Compared to the simulation employing only the CDM approach, damage onset occurs earlier and the evolution of the damaged region is slightly faster. The evolving damaged region reaches the

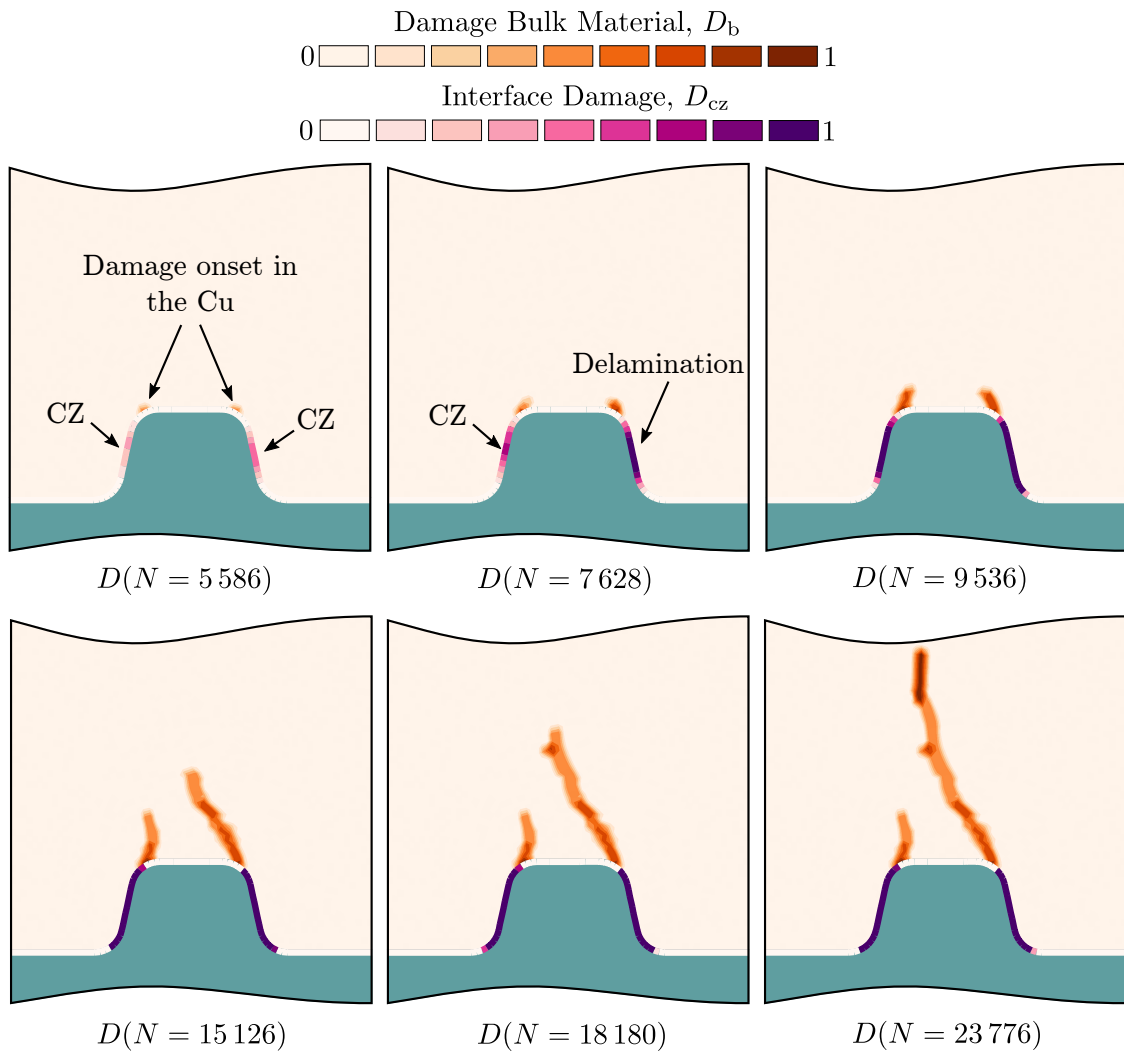


**Figure 5.12:** Damage characteristics of the generic DMOS cell model predicted by simultaneous application of the CDM & CCZM approaches. Contour plots of the bulk damage variable,  $D_b$  and the interface damage variable,  $D_{cz}$ , are depicted for six different damage states, identified by the number of applied load cycles,  $N$ .

displayed edge of the model at  $N = 23776$  load cycles, whereas the CDM only simulation needed  $N = 29179$  load cycles for the same spatial advance.

Finally, the spatial temperature fields for the simulation simultaneously applying the CDM and CCZM approach are depicted in Fig. 5.13. The elements representing material failure are indicated and the interface damage variable is displayed. The overall behavior of the temperature profile follows the same characteristics as those observed in the uncoupled sim-



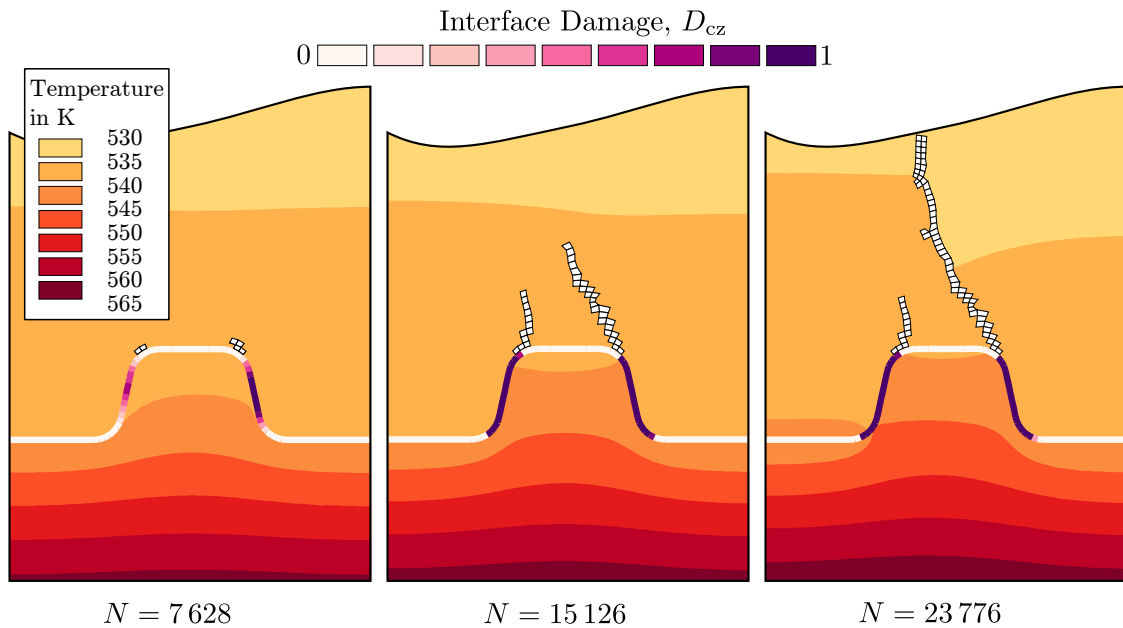


**Figure 5.13:** Temperature profile of the generic DMOS cell model during bulk fatigue damage evolution and cyclic delamination growth predicted by the coupled CDM & CCZM simulation.

ulations. Dependent on the damage state, a symmetric or unsymmetric temperature profile with slightly increased temperature values compared to the undamaged case is obtained.

## 5.4 Summary

The developed approaches based on continuum damage mechanics for fatigue damage modeling in bulk and for cyclic delamination growth are exemplified on a generic DMOS cell structure during massive electric overload pulsing. Thermo-mechanical FEM simulations are utilized to predict damage onset and damage progression inside the Cu power metalization and at the interface between the Si and Cu material compound.

Three different damage modeling strategies are applied and the obtained damage characteristics discussed and compared to each other. First, bulk fatigue damage and interface fatigue damage are simulated independently from each other. This way, the developed approaches are not affected by the progressive damage evolution of the other approach. Each damage model provides a lifetime estimation and the spatial damage evolution is depicted

for different numbers of electric overload pulses. Second, both approaches are simultaneously applied in a single FEM simulation resulting in an earlier damage onset and slightly accelerated damage progression inside the Cu power metallization. The applicability of the approaches in a combined simulation is, therefore, shown, but their interactive capabilities have not been addressed in detail in the present work and further research is required on this topic.

The progressing damage either in the bulk material or at the interface impedes the local thermal flux in the vertical direction, resulting in a slight increase of the temperatures below the damaged regions. In all simulations, the damage characteristics of either the bulk fatigue damaged region or the interface delaminations follows a path almost parallel to the heat flux through the model. Hence, the global heat flux through the submodel is only marginally affected by the obtained regions of material and interface failure for the current model geometry, the assumed material and interface parameter, the applied overload pulses, and the utilized modeling strategy. The application of orthotropic damage evolution modeling may influence the obtained damage path in the Cu power metallization and a slightly different damage characteristic may be obtained in this case.

In addition to the demonstration of the approaches, a second simulation utilizing only the bulk fatigue approach is conducted with an initial void at the top of the Cu layer. Damage onset inside the Cu layer first occur at this manually introduced void and a subsequent progressing damaged region is obtained. In addition, damage onset at the interface is predicted in the simulations and a second propagating region of material failure is obtained. After a certain amount of independent progression of the two damaged regions, a mutual influence between the propagating regions is detected by the bulk fatigue approach and the damaged regions coalesce to one single region of material failure across the Cu power metallization.

A substantial model size reduction is gained by the applied "unit cell like" modeling strategy. This modeling technique is, strictly speaking, only valid for the undamaged state up until damage localization is reached inside the model. Afterwards, the response of the damaged cell changes and effects the displacement field and loading conditions of the neighboring cells. Hence, for valid model results, the region of material failure should not affect the far-field stress and strain field of the submodel. This is only valid for a very small and localized

region of material failure inside the model. Therefore, a larger FEM model is required to model the actual damage response inside a DMOSFET device. An embedded modeling technique would provide a possible strategy to circumvent the limitations of the current submodel by keeping the computational time within reasonable bounds. Nevertheless, the developed progressive damage models are successfully applied to a power semiconductor device and their applicability to these kind of problems is, therefore, shown.



## Chapter 6

# Conclusion

Various failure mechanisms can be found in power semiconductor devices, which may lead to malfunctions or even destruction of the devices. Empirical lifetime models have been developed to assess the lifetime of such devices. A main drawback of these models is that they do not consider the actual physical damage mechanisms inside the power semiconductor devices. Hence, changes in the loading conditions may trigger different failure mechanisms and predictions by the empirical lifetime models may be compromised. Advances made in numerical simulation techniques allow for the development of physical lifetime models capable of predicting the actual physical damage mechanisms inside a power semiconductor. Numerical simulation techniques have been already successfully applied to a variety of different failure mechanisms, but few studies have been carried out on the numerical assessment of fatigue damage inside the ductile metallization of power semiconductors. Fatigue damage in the metallization may lead to hot-spot formation, which, in turn, may lead to local melt-up and possible device failure. The detection of such weak spots inside the metallization is of major interest in the development of modern power semiconductor devices. Physical lifetime models will help to identify and eliminate designs with locations prone for material failure prior to manufacturing of the first prototype devices. The present work is focused on the development of fatigue damage modeling strategies by means of advanced methods within the framework of the Finite Element Method. The developed fatigue damage modeling techniques aim to predict material degradation inside the power metallization and potential cyclic interface delamination between the metallization and the silicon chip.

The analysis of fatigue damage inside a power semiconductor device can be described as a thermo-mechanical fatigue problem. In the present work, the problem is narrowed down to the prediction of material and interface deterioration caused by mechanical stresses and strains. The stress and strain states within a power semiconductor are induced by temperature swings, caused by cyclic electric (overload) pulses, and by the differences in the coefficients of thermal expansion of the multilayer stacks. Effects such as microstructural evolution, creep fatigue interactions, environmental influences, and rate-dependent material properties are not considered in the present work.

A continuum damage mechanics based approach is developed to predict fatigue damage inside the bulk material of the metallization layer. The formulated approach utilizes a phenomenological, multiaxial fatigue criterion for the prediction of damage onset and a damage evolution law based on the strain energy density for the prediction of damage progression. The multiaxial fatigue criterion allows for the consideration of complex loading conditions and predicts locations prone to microcrack nucleation as well as the orientation of the emerging microcracks. The strain energy based damage evolution law allows for the consideration of thermo-mechanical loading conditions and describes the degradation rate of the material caused by microcrack accumulation and growth. The effect of damage on the thermal conductivity of the material is included in the model. The implementation of the local continuum damage mechanics formulation into the Finite Element Method enables the simulation of the whole damage process which ranges from damage onset to spatial damage progression. The spatial advance of a damaged region leads to a change in the mechanical and thermal structural response of the simulated problem. Fatigue material properties are required for the simulation. A calibration procedure for the fatigue damage modeling approach is exemplified on cyclic bending experiments of microcantilever beams. The test setup is numerically modeled and the required fatigue properties are gathered by comparison of the numerical results with the experimental data reported in the literature. The obtained parameter set is then utilized for the prediction of damage onset and progression in a simplified submodel of a power semiconductor device assuming isotropic damage behavior. The theoretical framework for orthotropic damage modeling is derived in the present work, but only the isotropic damage modeling is implemented entirely. To exploit the full potential

of the orthotropic damage modeling approach, a user written material subroutine, which is not available yet, is required.

A thermo–mechanical cyclic cohesive zone model is developed to predict cyclic delamination between the power metallization and the silicon chip. The cohesive zone concept is a highly versatile modeling technique for delaminations or cracks for which the crack path is *a priori* known. The most advanced cyclic cohesive zone formulations are found inside the research field of composite materials. Hence, the techniques employed there are further developed in the present work and applied to the field of microelectronics. The formulated model is purely based on physically interpretable interface parameters. This model feature is made possible by linking the damage mechanics concept of the cohesive zone model to the fracture mechanics crack propagation law, i.e. the Paris law. This way, tedious model calibration is circumvented and experimentally identified interface properties can be directly used for the model calibration. Two structural parameters are required for the integration of the fatigue damage evolution law, i.e. the cohesive zone length and the mix mode ratio. Both properties are evaluated by a non–local approach during the simulation. This way, no approximations or estimations of these parameters are required. Additionally, the non–local evaluation of the cohesive zone length allows for the simulation of transient effects in the fatigue crack growth rate, which may be obtained by overload pulses or variable amplitude loading conditions. The mechanical response of the modeling technique is exemplified on well–established delamination tests for composite materials. The obtained numerical results show good agreement with the available experimental data. The cyclic cohesive zone model is extended to account for thermo–mechanical loading conditions and a deterioration of the thermal flux across a damaged interface. The effect on the thermal flux is obtained by linking the thermal conductance with the mechanical damage variable. The experimental measurement of the interface properties inside a power semiconductor device is a complex task and a field of ongoing research. Hence, the required data are not available yet and an estimation of the cohesive zone parameters is conducted in the present work. This way, the cyclic cohesive zone model can be exemplified on a submodel of a power semiconductor device. The fatigue formulation of the current model is limited to two–dimensional problems, whereas the quasi–static formulation is already implemented for three–dimensional problems.

The bulk fatigue and the cyclic delamination approach are exemplified independently and in combination on a simplified generic submodel of a DMOSFET device. Various simulations accounting for damage onset and damage progression are conducted. The obtained damage characteristics, the spatial damage evolution with respect to the number of load cycles, and the influence of the damaged region on the thermal field are discussed. The applicability of both damage modeling approaches in a combined simulation is shown. The damage characteristics obtained from the independent and the combined simulation are slightly different, indicating an interaction between the two approaches. The employed submodeling technique allows for a significant reduction in the model size, but application of this technique to numerical analyses including damage progression should be handled with care. The proper assessment of damage localization inside the submodel requires the development of enhanced modeling techniques.

The presented fatigue damage modeling strategies provide a step forward towards physical lifetime models for power semiconductor devices based on numerical simulation techniques. One of the next steps towards numerical analyses with predictive capabilities is the proper determination of material and interface parameters. As exemplified on the microcantilever beams, the developed numerical models can be utilized to extract usable fatigue properties of the involved materials from available experimental test data. Similar procedures can be thought of for the identification of interface properties inside the compounds. In addition to a proper material and interface parameter set, an electro–thermo–mechanical analysis employing the developed damage models will be required to reach predictive capabilities. The deterioration of the electric properties can be obtained in analogy to the degradation of the thermal properties, as formulated in the present work. A multiphysics analysis supplemented with proper material and interface parameters in combination with an advanced embedding modeling strategy will allow for the prediction of fatigue damage inside and at the interface of the power metallization; this, in turn, will help to improve the robustness of future power semiconductor devices.



## Appendix A

# CDM – Effective Material Properties

Following [160], the elastic compliance tensor of the damaged material, Eq. (3.31),

$$\mathbb{S}(\mathbf{D}) = \mathbb{M}^T(\mathbf{D}) : \mathbb{S}_0 : \mathbb{M}(\mathbf{D}) \quad , \quad (\text{A.1})$$

is obtained from the compliance tensor of an isotropic material in the undamaged state,  $\mathbb{S}_0$ , and the fourth order damage effect tensor,

$$(\mathbb{M}(\mathbf{D}))^{-1} = \frac{1}{2} (\underline{\Phi} \otimes \underline{\Phi} + \overline{\Phi} \otimes \overline{\Phi}) \quad , \quad (\text{A.2})$$

$$\underline{\Phi} = (\mathbf{I} - \mathbf{D})^{1/2} \quad , \quad (\text{A.3})$$

which can be written in index notation as,

$$(M)_{ijkl}^{-1} = \frac{1}{2} (\Phi_{ik}\Phi_{jl} + \Phi_{il}\Phi_{jk}) \quad . \quad (\text{A.4})$$

By substituting Eq. (3.31) into the elastic constitutive behavior of the damaged material, Eq. (3.30), the elastic strain is given as

$$\boldsymbol{\varepsilon}^e = \mathbb{S}(\mathbf{D}) : \boldsymbol{\sigma} \quad , \quad (\text{A.5})$$

where  $\boldsymbol{\sigma}$  denotes the stress tensor.

It is convenient to express the tensors in the form of matrices and to execute tensor operations in terms of matrix calculus. Therefore, the Voigt notation with the component ordering as employed in Ansys APDL v 16.2 is utilized and given as

$$[\sigma_p] \equiv \begin{bmatrix} \sigma_{11} \\ \sigma_{22} \\ \sigma_{33} \\ \sigma_{12} \\ \sigma_{23} \\ \sigma_{31} \end{bmatrix}, \quad [\varepsilon_p] \equiv \begin{bmatrix} \varepsilon_{11} \\ \varepsilon_{22} \\ \varepsilon_{33} \\ \gamma_{12} \\ \gamma_{23} \\ \gamma_{31} \end{bmatrix} = \begin{bmatrix} \varepsilon_{11} \\ \varepsilon_{22} \\ \varepsilon_{33} \\ 2\varepsilon_{12} \\ 2\varepsilon_{23} \\ 2\varepsilon_{31} \end{bmatrix} \quad \text{for } p = \{1 \dots 6\} . \quad (\text{A.6})$$

The elastic constitutive equation of a damaged material and its compliance tensor in matrix form are expressed in Voigt notation as [160]

$$[\varepsilon_p^e] = [S_{pq}(\mathbf{D})][\sigma_q] \quad , \quad \text{and} \quad (\text{A.7})$$

$$[S_{pq}(\mathbf{D})] = [M_{rp}(\mathbf{D})]^T [S_{rs}^0] [M_{sq}(\mathbf{D})] \quad , \quad (\text{A.8})$$

respectively, where  $[S_{rs}^0]$  is the elastic compliance matrix of an undamaged isotropic material. The matrix representation of the damage effect tensor in the basis  $(\xi)$  takes the following form,

$$^{(\xi)}[M_{pq}(\mathbf{D})] = \begin{bmatrix} \Phi_1 & 0 & 0 & 0 & 0 & 0 \\ 0 & \Phi_2 & 0 & 0 & 0 & 0 \\ 0 & 0 & \Phi_3 & 0 & 0 & 0 \\ 0 & 0 & 0 & (\Phi_1\Phi_2)^{\frac{1}{2}} & 0 & 0 \\ 0 & 0 & 0 & 0 & (\Phi_2\Phi_3)^{\frac{1}{2}} & 0 \\ 0 & 0 & 0 & 0 & 0 & (\Phi_3\Phi_1)^{\frac{1}{2}} \end{bmatrix}, \quad (\text{A.9})$$

where  $\Phi_i = (1 - D_i)^{-1}$  for  $i = 1, 2, 3$ .

Consequently, the elastic compliance matrix of a damaged material in the same basis results in

$${}^{(\xi)}[S_{pq}(\mathbf{D})] = \begin{bmatrix} \frac{1}{\tilde{E}_1} & -\frac{\tilde{\nu}_{21}}{\tilde{E}_2} & -\frac{\tilde{\nu}_{31}}{\tilde{E}_3} & 0 & 0 & 0 \\ -\frac{\tilde{\nu}_{12}}{\tilde{E}_1} & \frac{1}{\tilde{E}_2} & -\frac{\tilde{\nu}_{32}}{\tilde{E}_3} & 0 & 0 & 0 \\ -\frac{\tilde{\nu}_{13}}{\tilde{E}_1} & -\frac{\tilde{\nu}_{23}}{\tilde{E}_2} & \frac{1}{\tilde{E}_3} & 0 & 0 & 0 \\ 0 & 0 & 0 & \frac{1}{\tilde{G}_{12}} & 0 & 0 \\ 0 & 0 & 0 & 0 & \frac{1}{\tilde{G}_{23}} & 0 \\ 0 & 0 & 0 & 0 & 0 & \frac{1}{\tilde{G}_{31}} \end{bmatrix}, \quad (\text{A.10})$$

where  $\tilde{E}_i$ ,  $\tilde{G}_{ij}$ , and  $\tilde{\nu}_{ij}$  denote the damaged Young's modulus in  $i$ -direction, the damaged shear modulus in the  $i$ - $j$  plane, and the damaged Poisson's ratios, respectively. These parameters are obtained from the following relations:

$$\frac{1}{\tilde{E}_i} = \frac{1}{E} \Phi_i^2, \quad \frac{1}{\tilde{G}_{ij}} = \frac{1}{G} \Phi_i \Phi_j, \quad \frac{\tilde{\nu}_{ij}}{\tilde{E}_i} = \frac{\nu}{E} \Phi_i \Phi_j, \quad (\text{A.11})$$

with  $\Phi_i = (1 - D_i)^{-1}$  for  $i, j = 1, 2, 3$ ,

where  $E$ ,  $G$ , and  $\nu$  denote the Young's modulus, the shear modulus, and the Poisson's ratio of a undamaged isotropic material, respectively.

The plastic constitutive behavior, Eqs. (3.36 to 3.41) of the damaged material is modeled by adapting the initial J2 yield condition to a decreasing orthotropic Hill yield condition. The positive semi-definite tensor characterizing the yield conditions of orthotropic materials, Eq. (3.40), is represented as

$${}^{(\xi)}[H_{pq}(\mathbf{D})] = \begin{bmatrix} \tilde{G} + \tilde{H} & -\tilde{H} & -\tilde{G} & 0 & 0 & 0 \\ & \tilde{H} + \tilde{F} & -\tilde{F} & 0 & 0 & 0 \\ & & \tilde{F} + \tilde{G} & 0 & 0 & 0 \\ & & & 2\tilde{N} & 0 & 0 \\ \text{sym.} & & & & 2\tilde{L} & 0 \\ & & & & & 2\tilde{M} \end{bmatrix}, \quad (\text{A.12})$$

where  $\tilde{F}$ ,  $\tilde{G}$ ,  $\tilde{H}$ ,  $\tilde{L}$ ,  $\tilde{M}$ , and  $\tilde{N}$  are the parameters characterizing the plastic orthotropy of the damaged material, and are called anisotropy parameters. In the case of isotropy (e.g. the undamaged material) these parameters have the values

$$\tilde{F} = \tilde{G} = \tilde{H} = 1 \quad , \quad \tilde{L} = \tilde{M} = \tilde{N} = 3 \quad . \quad (\text{A.13})$$

The anisotropy parameters are obtained in Ansys APDL v16.2 as,

$$\begin{aligned} \tilde{F} &= \frac{1}{2} \left\langle \frac{1}{\tilde{R}_{22}^2} + \frac{1}{\tilde{R}_{33}^2} - \frac{1}{\tilde{R}_{11}^2} \right\rangle & \tilde{L} &= \frac{3}{2} \left( \frac{1}{\tilde{R}_{23}^2} \right) \\ \tilde{G} &= \frac{1}{2} \left\langle \frac{1}{\tilde{R}_{33}^2} + \frac{1}{\tilde{R}_{11}^2} - \frac{1}{\tilde{R}_{22}^2} \right\rangle & \tilde{M} &= \frac{3}{2} \left( \frac{1}{\tilde{R}_{13}^2} \right) \quad , \\ \tilde{H} &= \frac{1}{2} \left\langle \frac{1}{\tilde{R}_{11}^2} + \frac{1}{\tilde{R}_{22}^2} - \frac{1}{\tilde{R}_{33}^2} \right\rangle & \tilde{N} &= \frac{3}{2} \left( \frac{1}{\tilde{R}_{12}^2} \right) \end{aligned} \quad (\text{A.14})$$

where so-called directional yield stress ratios,  $R_{ij}$ , are utilized as user input. In the present work, the Macaulay brackets are introduced to avoid negative anisotropy parameters. In terms of the presented elasto-plastic-damage model the damaged ratios,  $\tilde{R}_{ij}$ , are only dependent on the damage variables, since an isotropic material behavior combined with a J2 plasticity is assumed for the pristine material. The damaged parameters for orthotropic plasticity during damage development are, therefore, given as,

$$\begin{aligned} \tilde{R}_{11} &= \frac{1}{\Phi_1} & \tilde{R}_{12} &= \left( \frac{1}{\Phi_1 \Phi_2} \right)^{\frac{1}{2}} \\ \tilde{R}_{22} &= \frac{1}{\Phi_2} & \tilde{R}_{23} &= \left( \frac{1}{\Phi_2 \Phi_3} \right)^{\frac{1}{2}} \quad . \\ \tilde{R}_{33} &= \frac{1}{\Phi_3} & \tilde{R}_{31} &= \left( \frac{1}{\Phi_3 \Phi_1} \right)^{\frac{1}{2}} \end{aligned} \quad (\text{A.15})$$

The matrices above have been presented in the basis  $(\xi)$  which is aligned with the principal axes of the material system. These matrices can be rotated into an arbitrary coordinate system  $(x)$  as follows. In Voigt notation two rotation matrices  ${}^{(x,\xi)}[R_{pq}^\varepsilon]$  and  ${}^{(x,\xi)}[R_{pq}^\sigma]$  are necessary to transform the strains and stresses from a coordinate system  $(x)$  into a rotated coordinate system  $(\xi)$  as [47],

$${}^{(\xi)}[\varepsilon_p] = {}^{(x,\xi)}[R_{pq}^\varepsilon]{}^{(x)}[\varepsilon_q] \quad , \quad (\text{A.16})$$

$${}^{(\xi)}[\sigma_p] = {}^{(x,\xi)}[R_{pq}^\sigma]{}^{(x)}[\sigma_q] \quad , \quad (\text{A.17})$$

where the matrices follow the relations,

$${}^{(\xi,x)}[R_{pq}^\varepsilon] = {}^{(x,\xi)}[R_{pq}^\varepsilon]^{-1} = {}^{(x,\xi)}[R_{pq}^\sigma]^\text{T} \quad , \quad (\text{A.18})$$

$${}^{(\xi,x)}[R_{pq}^\sigma] = {}^{(x,\xi)}[R_{pq}^\sigma]^{-1} = {}^{(x,\xi)}[R_{pq}^\varepsilon]^\text{T} \quad . \quad (\text{A.19})$$

Consequently, the elasticity matrix and the compliance matrix follow as

$${}^{(x)}[C_{pq}(\mathbf{D})] = {}^{(x,\xi)}[R_{rp}^\varepsilon]^\text{T} {}^{(\xi)}[C_{rs}^0] {}^{(x,\xi)}[R_{sq}^\varepsilon] \quad , \quad (\text{A.20})$$

$${}^{(x)}[S_{pq}(\mathbf{D})] = {}^{(x,\xi)}[R_{rp}^\sigma]^\text{T} {}^{(\xi)}[S_{rs}^0] {}^{(x,\xi)}[R_{sq}^\sigma] \quad , \quad (\text{A.21})$$

respectively, where  $[C_{rs}^0]$  is the isotropic elasticity matrix for the undamaged material. The rotation matrices for a second order tensor in Voigt Notation, employing the component ordering as Ansys APDL v16.2 are given as [47]

$${}^{(x,\xi)}[R_{pq}^\sigma] = \begin{bmatrix} q_{11}^2 & q_{12}^2 & q_{13}^2 & 2q_{11}q_{12} & 2q_{12}q_{13} & 2q_{11}q_{13} \\ q_{21}^2 & q_{22}^2 & q_{23}^2 & 2q_{21}q_{22} & 2q_{22}q_{23} & 2q_{21}q_{23} \\ q_{31}^2 & q_{32}^2 & q_{33}^2 & 2q_{31}q_{32} & 2q_{32}q_{33} & 2q_{31}q_{33} \\ q_{21}q_{11} & q_{22}q_{12} & q_{13}q_{23} & (q_{11}q_{22} + q_{12}q_{21}) & (q_{13}q_{22} + q_{12}q_{23}) & (q_{13}q_{21} + q_{11}q_{23}) \\ q_{31}q_{21} & q_{32}q_{22} & q_{33}q_{23} & (q_{31}q_{22} + q_{32}q_{21}) & (q_{33}q_{22} + q_{32}q_{23}) & (q_{33}q_{21} + q_{31}q_{23}) \\ q_{31}q_{11} & q_{32}q_{12} & q_{33}q_{13} & (q_{31}q_{12} + q_{32}q_{11}) & (q_{33}q_{12} + q_{32}q_{13}) & (q_{33}q_{11} + q_{31}q_{13}) \end{bmatrix} \quad (\text{A.22})$$

$$({}^{x,\xi})[R_{pq}^\varepsilon] = \begin{bmatrix} q_{11}^2 & q_{12}^2 & q_{13}^2 & q_{11}q_{12} & q_{12}q_{13} & q_{11}q_{13} \\ q_{21}^2 & q_{22}^2 & q_{23}^2 & q_{21}q_{22} & q_{22}q_{23} & q_{21}q_{23} \\ q_{31}^2 & q_{32}^2 & q_{33}^2 & q_{31}q_{32} & q_{32}q_{33} & q_{31}q_{33} \\ 2q_{21}q_{11} & 2q_{22}q_{12} & 2q_{13}q_{23} & (q_{11}q_{22} + q_{12}q_{21}) & (q_{13}q_{22} + q_{12}q_{23}) & (q_{13}q_{21} + q_{11}q_{23}) \\ 2q_{31}q_{21} & 2q_{32}q_{22} & 2q_{33}q_{23} & (q_{31}q_{22} + q_{32}q_{21}) & (q_{33}q_{22} + q_{32}q_{23}) & (q_{33}q_{21} + q_{31}q_{23}) \\ 2q_{31}q_{11} & 2q_{32}q_{12} & 2q_{33}q_{13} & (q_{31}q_{12} + q_{32}q_{11}) & (q_{33}q_{12} + q_{32}q_{13}) & (q_{33}q_{11} + q_{31}q_{13}) \end{bmatrix}, \tag{A.23}$$

where  $q_{ij}$  are the entries of the rotation matrix  $[Q_{pq}]$ .

## Appendix B

### CCZM – Integrals

The integration of the exponential traction–separation law of the Cyclic Cohesive Zone Model (CCZM) is summarized in the following. The integration requires the utilization of the Euler gamma function,

$$\Gamma(z) = \int_0^{\infty} t^{z-1} e^{-t} dt \quad , \quad (\text{B.1})$$

where  $z$  is a complex number with positive real part. The lower incomplete gamma function is defined as

$$\gamma(z, x) = \int_0^x t^{z-1} e^{-t} dt \quad , \quad (\text{B.2})$$

and the regularized lower incomplete gamma function is provided by

$$P(z, x) = \frac{\gamma(z, x)}{\Gamma(z)} \quad . \quad (\text{B.3})$$

The range of the specific work, Eq. (4.21), is computed by

$$\Delta w = \int_{\lambda_{\min}}^{\lambda_{\max}} T(\lambda) d\lambda = \mathcal{G}_c \left[ P\left(\frac{2}{\beta}, \frac{\lambda_{\max}^{\beta}}{\beta}\right) - P\left(\frac{2}{\beta}, \frac{\lambda_{\min}^{\beta}}{\beta}\right) \right] \quad , \quad (\text{B.4})$$

which uses the regularized lower incomplete gamma function. This function is not intrinsic in the utilized Intel Fortran Compiler (IFORT 16.0.0 20150815). Therefore, ASA032 FORTRAN90 library [37], based on [27], has been employed for the computation.

Similarly, the static damage variable, Eq. (4.15), is computed as

$$D_s(\lambda_{\max}) = \frac{1}{\mathcal{G}_c} \left[ \int_0^{\lambda_{\max}} T(\lambda) \, d\lambda - \int_0^{\lambda_{\max}} T(\lambda, d_s) \, d\lambda \right] = \quad (\text{B.5})$$

$$= P \left( \frac{2}{\beta}, \frac{\lambda_{\max}^\beta}{\beta} \right) - \lambda_{\max}^2 \exp \left( \frac{1 - \lambda_{\max}^\beta}{\beta} \right) P \left( \frac{2}{\beta}, \frac{1}{\beta} \right) \quad , \quad (\text{B.6})$$

and the total damage variable, Eq. (4.32), follows as

$$D_{\text{tot}}(d_{\text{tot}}) = \frac{1}{\mathcal{G}_c} \left[ \int_0^{\lambda_{\text{tot}}} T(\lambda) \, d\lambda - \int_0^{\lambda_{\text{tot}}} T(\lambda, d_{\text{tot}}) \, d\lambda \right] = \quad (\text{B.7})$$

$$= P \left( \frac{2}{\beta}, \frac{d_{\text{tot}}}{\beta} \right) - d_{\text{tot}}^{\frac{2}{\beta}} \exp \left( \frac{1 - d_{\text{tot}}}{\beta} \right) P \left( \frac{2}{\beta}, \frac{1}{\beta} \right) \quad . \quad (\text{B.8})$$

The internal variable,  $d_{\text{tot}}$ , is iteratively computed by Newton's method,

$${}_{(j+1)}d_{\text{tot}} = {}_{(j)}d_{\text{tot}} - \frac{f({}_{(j)}d_{\text{tot}})}{f'({}_{(j)}d_{\text{tot}})} \quad \text{with} \quad {}_{(j=0)}d = {}^n d_{\text{tot}} \quad . \quad (\text{B.9})$$

Herein,  ${}^n d_{\text{tot}}$  denotes the internal variable from the last converged increment in the FEM analysis. The scheme is stopped at the iteration,  $(j)$ , where the stopping condition  $|f({}_{(j)}d_{\text{tot}})| \leq 1 \cdot 10^{-2}$  is fulfilled. The function  $f(d_{\text{tot}})$  and its derivative,  $f'(d_{\text{tot}})$ , are provided as

$$f(d_{\text{tot}}) = P \left( \frac{2}{\beta}, \frac{d_{\text{tot}}}{\beta} \right) - d_{\text{tot}}^{\frac{2}{\beta}} \exp \left( \frac{1 - d_{\text{tot}}}{\beta} \right) P \left( \frac{2}{\beta}, \frac{1}{\beta} \right) - D_{\text{tot}}(d_{\text{tot}}) \quad , \quad (\text{B.10})$$

$$f'(d_{\text{tot}}) = \frac{d_{\text{tot}}^{\frac{2-\beta}{\beta}} \exp \left( -\frac{d_{\text{tot}}}{\beta} \right)}{\beta^{\frac{2}{\beta}} \Gamma \left( \frac{2}{\beta} \right)} + \frac{d_{\text{tot}}^{\frac{2}{\beta}} - 2d_{\text{tot}}^{\frac{2-\beta}{\beta}}}{\beta} \exp \left( \frac{1 - d_{\text{tot}}}{\beta} \right) P \left( \frac{2}{\beta}, \frac{1}{\beta} \right) \quad . \quad (\text{B.11})$$



## Appendix C

# CCZM – Interface Stiffness Matrix

The derivatives of the interface stiffness matrix required by the Newton–Raphson algorithm, in the framework of the FEM [22], are presented in the following. The derivatives are employed by Ansys APDL v16.2 and v18.0 USERINTER user subroutine.

The traction–separation law of the Cyclic Cohesive Zone Model (CCZM), Eq. (4.8), can be written as [82]

$$\begin{bmatrix} \bar{T}_1 \\ \bar{T}_2 \\ \bar{T}_3 \end{bmatrix} = \begin{bmatrix} \bar{\Delta}_1 \Theta_1 \\ \bar{\Delta}_2 \Theta_2 \\ \langle \bar{\Delta}_3 \rangle \Theta_3 \end{bmatrix}, \quad (\text{C.1})$$

where the exponential terms are summarized within,

$$\Theta_1 = \frac{\mathcal{S}}{\nu} \exp\left(\frac{2 - \lambda^\beta/d - d}{\beta}\right), \quad \Theta_2 = \Theta_1, \quad \text{and} \quad \Theta_3 = \nu\Theta_1 = \nu\Theta_2. \quad (\text{C.2})$$

The interface stiffness matrix for the thermo–mechanical CCZM is given as

$$\mathbf{K} = \begin{bmatrix} {}^m\mathbf{K} & {}^{mt}\mathbf{K} \\ {}^{tm}\mathbf{K} & {}^{th}\mathbf{K} \end{bmatrix} = \begin{bmatrix} \frac{\partial T_1}{\partial \Delta_1} & \frac{\partial T_1}{\partial \Delta_2} & \frac{\partial T_1}{\partial \Delta_3} & \frac{\partial T_1}{\partial \vartheta_+} & \frac{\partial T_1}{\partial \vartheta_-} \\ \frac{\partial T_2}{\partial \Delta_1} & \frac{\partial T_2}{\partial \Delta_2} & \frac{\partial T_2}{\partial \Delta_3} & \frac{\partial T_2}{\partial \vartheta_+} & \frac{\partial T_2}{\partial \vartheta_-} \\ \frac{\partial T_3}{\partial \Delta_1} & \frac{\partial T_3}{\partial \Delta_2} & \frac{\partial T_3}{\partial \Delta_3} & \frac{\partial T_3}{\partial \vartheta_+} & \frac{\partial T_3}{\partial \vartheta_-} \\ \frac{\partial q_+}{\partial \Delta_1} & \frac{\partial q_+}{\partial \Delta_2} & \frac{\partial q_+}{\partial \Delta_3} & \frac{\partial q_+}{\partial \vartheta_+} & \frac{\partial q_+}{\partial \vartheta_-} \\ \frac{\partial q_-}{\partial \Delta_1} & \frac{\partial q_-}{\partial \Delta_2} & \frac{\partial q_-}{\partial \Delta_3} & \frac{\partial q_-}{\partial \vartheta_+} & \frac{\partial q_-}{\partial \vartheta_-} \end{bmatrix}, \quad (\text{C.3})$$

which consists of the four submatrices  ${}^m\mathbf{K}$ ,  ${}^{mt}\mathbf{K}$ ,  ${}^{tm}\mathbf{K}$ , and  ${}^{th}\mathbf{K}$ , provided in the following.

### Mechanical – Submatrix, ${}^m\mathbf{K}$

For interface opening ( $\Delta_3 \geq 0$ ) the components of the mechanical submatrix read

$${}^m\mathbf{K} = {}^mK_{ij} = \frac{\partial T_i}{\partial \Delta_j} = \frac{T_i^o}{\Delta_j^o} \left[ \delta_{ij} - \frac{\bar{\Delta}_i \bar{\Delta}_j}{\tilde{w} \lambda^{2-\beta}} + \frac{\bar{\Delta}_i \Delta_j^o}{S \chi_i} \frac{\partial \mathcal{S}}{\partial \Delta_j} \right] \Theta_i \quad , \quad (\text{C.4})$$

where  $\chi_1 = \chi_2 = 1$  and  $\chi_3 = \nu$ , for  $i = \{1, 2, 3\}$  and  $j = \{1, 2, 3\}$ . The Kronecker delta is given by  $\delta_{ij}$  and  $\tilde{w}$ , defined as

$$\tilde{w} = \begin{cases} 1 & \text{if } d_{\text{tot}} = \lambda^\beta \\ d_{\text{tot}} & \text{if } d_{\text{tot}} > \lambda^\beta \end{cases} \quad . \quad (\text{C.5})$$

The derivatives of  $\mathcal{S}$  are obtained from

$$\frac{\partial \mathcal{S}}{\partial \Delta_j} = \eta(\nu - 1) B^{\eta-1} \frac{\partial B}{\partial u_j} \quad , \quad (\text{C.6})$$

and the derivatives of the mode mixity,  $B$ , are derived numerically as

$$\frac{\partial B}{\partial u_1} = 2\Delta_1 \left( \frac{T_1^o \psi}{\mathcal{G}_{\text{Ic}}} \right)^2 \left\langle \frac{T_3^o \psi \Delta_3}{\mathcal{G}_{\text{Ic}}} \right\rangle^2 \Lambda^{-2} \quad (\text{C.7})$$

$$\frac{\partial B}{\partial u_2} = 2\Delta_2 \left( \frac{T_2^o \psi}{\mathcal{G}_{\text{Ic}}} \right)^2 \left\langle \frac{T_3^o \psi \Delta_3}{\mathcal{G}_{\text{Ic}}} \right\rangle^2 \Lambda^{-2} \quad (\text{C.8})$$

$$\frac{\partial B}{\partial u_3} = 2 \langle \Delta_3 \rangle \left( \frac{T_3^o \psi}{\mathcal{G}_{\text{Ic}}} \right)^2 \left[ \left\langle \frac{T_3^o \psi \Delta_3}{\mathcal{G}_{\text{Ic}}} \right\rangle^2 \Lambda^{-2} - \Lambda^{-1} \right] \quad , \quad (\text{C.9})$$

where

$$\Lambda = \left[ \left( \frac{T_1^o \psi \Delta_1}{\mathcal{G}_{\text{Ic}}} \right)^2 + \left( \frac{T_2^o \psi \Delta_2}{\mathcal{G}_{\text{Ic}}} \right)^2 + \left\langle \frac{T_3^o \psi \Delta_3}{\mathcal{G}_{\text{Ic}}} \right\rangle^2 \right] \quad , \quad (\text{C.10})$$

and  $\langle \bullet \rangle$  denotes the Macaulay brackets, Eq. (2.9).

For interface closure ( $\Delta_3 < 0$ ) the components which differ from the above stated ones read

$$\frac{\partial T_1}{\partial \Delta_3} = \frac{\partial T_2}{\partial \Delta_3} = \frac{\partial T_3}{\partial \Delta_1} = \frac{\partial T_3}{\partial \Delta_2} = 0 \quad (\text{C.11})$$

$$\frac{\partial T_3}{\partial \Delta_3} = K_{\text{cont}} \quad . \quad (\text{C.12})$$

### Mechanical–Thermal coupling, ${}^{\text{mt}}\mathbf{K}$

The components of the mechanical–thermal coupling submatrix are independent of the opening or closure state of the interface, and are obtained as

$${}^{\text{mt}}\mathbf{K} = {}^{\text{mt}}K_{kl} = \frac{\partial T_k}{\partial \vartheta_l} = \frac{\partial T_k^{\circ}}{\partial \vartheta_l} \bar{\Delta}_k \Theta_k + T_k^{\circ} \frac{\partial \bar{\Delta}_k}{\partial \vartheta_l} \Theta_k + T_k^{\circ} \bar{\Delta}_k \frac{\partial \Theta_k}{\partial \vartheta_l} \quad , \quad (\text{C.13})$$

where  $k = \{1, 2, 3\}$  and  $l = \{+, -\}$ . The cohesive law is defined by the temperature dependent interface properties  $\mathcal{G}_{\text{Ic}}$ ,  $\mathcal{G}_{\text{IIc}}$ ,  $T_3^{\circ} = T_1^{\circ}$ , and  $T_1^{\circ} = T_2^{\circ} = T_{\text{II}}^{\circ}$ . The remaining parameters are assumed to be temperature independent. The changes of the temperature dependent interface properties are computed as

$$\frac{\partial T_k^{\circ}}{\partial \vartheta_+} \approx \frac{\partial T_k^{\circ}}{\partial \vartheta_-} \approx \frac{\partial T_k^{\circ}}{\partial \vartheta_{\text{cz}}} = \frac{n+1 T_k^{\circ} - n T_k^{\circ}}{n+1 \vartheta_{\text{cz}} - n \vartheta_{\text{cz}}} \quad (\text{C.14})$$

$$\frac{\partial \mathcal{G}_{\text{Ic}}}{\partial \vartheta_+} \approx \frac{\partial \mathcal{G}_{\text{Ic}}}{\partial \vartheta_-} \approx \frac{\partial \mathcal{G}_{\text{Ic}}}{\partial \vartheta_{\text{cz}}} = \frac{n+1 \mathcal{G}_{\text{Ic}}^{\circ} - n \mathcal{G}_{\text{Ic}}^{\circ}}{n+1 \vartheta_{\text{cz}} - n \vartheta_{\text{cz}}} \quad (\text{C.15})$$

$$\frac{\partial \mathcal{G}_{\text{IIc}}}{\partial \vartheta_+} \approx \frac{\partial \mathcal{G}_{\text{IIc}}}{\partial \vartheta_-} \approx \frac{\partial \mathcal{G}_{\text{IIc}}}{\partial \vartheta_{\text{cz}}} = \frac{n+1 \mathcal{G}_{\text{IIc}}^{\circ} - n \mathcal{G}_{\text{IIc}}^{\circ}}{n+1 \vartheta_{\text{cz}} - n \vartheta_{\text{cz}}} \quad , \quad (\text{C.16})$$

where  $n + 1$  and  $n$  identify the current and the previous iteration, respectively. The temperature change is approximated by the average temperature change of the cohesive zone  $\vartheta_{\text{cz}} = (\vartheta_+ + \vartheta_-)/2$ . Hence, the derivatives  $\frac{\partial T_k}{\partial \vartheta_+}$  and  $\frac{\partial T_k}{\partial \vartheta_-}$  are equal. Therefore, only the derivatives with respect to  $\vartheta_+$  are presented in the following. The remaining components of Eq. (C.13) are given as

$$\frac{\partial \bar{\Delta}_1}{\partial \vartheta_+} = \left[ \frac{1}{\mathcal{G}_{\text{IIc}}} \frac{\partial T_1^{\circ}}{\partial \vartheta_+} - \frac{T_1^{\circ}}{\mathcal{G}_{\text{IIc}}^2} \frac{\partial \mathcal{G}_{\text{IIc}}}{\partial \vartheta_+} \right] \psi \Delta_1 \quad (\text{C.17})$$

$$\frac{\partial \bar{\Delta}_2}{\partial \vartheta_+} = \left[ \frac{1}{\mathcal{G}_{\text{IIc}}} \frac{\partial T_2^{\circ}}{\partial \vartheta_+} - \frac{T_2^{\circ}}{\mathcal{G}_{\text{IIc}}^2} \frac{\partial \mathcal{G}_{\text{IIc}}}{\partial \vartheta_+} \right] \psi \Delta_2 \quad (\text{C.18})$$

$$\frac{\partial \bar{\Delta}_3}{\partial \vartheta_+} = \left[ \frac{1}{\mathcal{G}_{\text{Ic}}} \frac{\partial T_3^{\circ}}{\partial \vartheta_+} - \frac{T_3^{\circ}}{\mathcal{G}_{\text{Ic}}^2} \frac{\partial \mathcal{G}_{\text{Ic}}}{\partial \vartheta_+} \right] \psi \langle \Delta_3 \rangle \quad (\text{C.19})$$

$$\frac{\partial \vartheta_+}{\partial \vartheta_+} = \frac{\partial \vartheta_-}{\partial \vartheta_+} = \left[ \frac{1}{\nu} \frac{\partial \mathcal{S}}{\partial \vartheta_+} - \frac{\mathcal{S}}{\nu^2} \frac{\partial \nu}{\partial \vartheta_+} \right] \exp \left( \frac{2 - \lambda^{\beta}/d - d}{\beta} \right) \quad (\text{C.20})$$

$$\frac{\partial \Theta_3}{\partial \vartheta_+} = \frac{\partial \mathcal{S}}{\partial \vartheta_+} \exp \left( \frac{2 - \lambda^{\beta}/d - d}{\beta} \right) \quad , \quad (\text{C.21})$$

where the derivative of  $\mathcal{S}$  can be obtained from

$$\frac{\partial \mathcal{S}}{\partial \vartheta_+} = \frac{\partial \nu}{\partial \vartheta_+} B^\eta + (\nu - 1) \eta B^{\eta-1} \frac{\partial B}{\partial \vartheta_+} \quad (\text{C.22})$$

$$\frac{\partial \nu}{\partial \vartheta_+} = \frac{1}{\mathcal{G}_{\text{Ic}}} \frac{\partial \mathcal{G}_{\text{IIc}}}{\partial \vartheta_+} - \frac{\mathcal{G}_{\text{IIc}}}{\mathcal{G}_{\text{Ic}}^2} \frac{\partial \mathcal{G}_{\text{Ic}}}{\partial \vartheta_+} \quad (\text{C.23})$$

$$\frac{\partial B}{\partial \vartheta_+} \approx \frac{{}^{n+1}B - {}^nB}{{}^{n+1}\vartheta_{\text{cz}} - {}^n\vartheta_{\text{cz}}} \quad (\text{C.24})$$

Herein, the derivative of the mode mixity,  $B$ , is approximated by a finite difference scheme.

### Thermal–Mechanical coupling, ${}^{\text{tm}}\mathbf{K}$

Upon interface opening ( $\Delta_3 \geq 0$ ) the components of the thermal–mechanical coupling submatrix are provided as

$${}^{\text{tm}}\mathbf{K} = {}^{\text{tm}}K_{lk} = \frac{\partial q_1}{\partial \Delta_k} = -\frac{\partial q_2}{\partial \Delta_k} = -h_{\text{int}}[\vartheta] \frac{\partial D_{\text{tot}}}{\partial \Delta_k} \quad , \quad (\text{C.25})$$

where the derivative of the total damage variable can be written as

$$\frac{\partial D_{\text{tot}}}{\partial \Delta_k} = \frac{\partial D_{\text{tot}}}{\partial d_{\text{tot}}} \frac{\partial d_{\text{tot}}}{\partial \Delta_k} \quad . \quad (\text{C.26})$$

The derivative of the energy based damage variable,  $D_{\text{tot}}$ , with respect to the internal variable,  $d_{\text{tot}}$ , is identical to Eq. (B.11) and given as

$$\begin{aligned} \frac{\partial D_{\text{tot}}}{\partial d_{\text{tot}}} = \frac{1}{\Gamma\left(\frac{2}{\beta}\right)} & \left[ \frac{d_{\text{tot}}^{\frac{2}{\beta}}}{\beta} \exp\left(\frac{1-d_{\text{tot}}}{\beta}\right) \gamma\left(\frac{2}{\beta}, \frac{1}{\beta}\right) + \frac{d_{\text{tot}}^{\frac{2-\beta}{\beta}}}{\beta^{\frac{2}{\beta}}} \exp\left(-\frac{d_{\text{tot}}}{\beta}\right) \right. \\ & \left. - \frac{2d_{\text{tot}}^{\frac{2-\beta}{\beta}}}{\beta} \exp\left(\frac{1-d_{\text{tot}}}{\beta}\right) \gamma\left(\frac{2}{\beta}, \frac{1}{\beta}\right) \right] \quad . \quad (\text{C.27}) \end{aligned}$$

Herein, the derivatives of  $d_{\text{tot}}$  with respect to the interface separations,  $\Delta_k$ , are approximated by a finite difference scheme as

$$\frac{\partial d_{\text{tot}}}{\partial \Delta_k} \approx \frac{{}^{n+1}d_{\text{tot}} - {}^nd_{\text{tot}}}{{}^{n+1}\Delta_k - {}^n\Delta_k} \quad . \quad (\text{C.28})$$

Upon interface closure ( $\Delta < 0$ ) the components change to

$$\frac{\partial q_+}{\partial \Delta_k} = (h_c - h_{\text{int}}) \llbracket \vartheta \rrbracket \frac{\partial D_{\text{tot}}}{\partial \Delta_k} \quad \text{for } k = 1, 2 \quad (\text{C.29})$$

$$\frac{\partial q_+}{\partial \Delta_3} = \begin{cases} D_{\text{tot}} \llbracket \vartheta \rrbracket \frac{\partial h_c}{\partial \Delta_3} & \text{for } (-\Delta_3) < \Delta_{\text{fc}} \\ 0 & \text{for } (-\Delta_3) \geq \Delta_{\text{fc}} \end{cases}, \quad (\text{C.30})$$

where the derivative of the thermal conductance with respect to the contact penetration,  $\Delta_3$ , for the nonlinear penalty method is given as

$$\frac{\partial h_c}{\partial \Delta_3} = \frac{v h_{\text{int}} \pi}{\Delta_3^{\text{fc}}} \frac{\pi}{2} \sin\left(\frac{(-\Delta_3)\pi}{\Delta_3^{\text{fc}}}\right). \quad (\text{C.31})$$

### Thermal-Submatrix, ${}^{\text{th}}\mathbf{K}$

The entries of the thermal submatrix for interface opening ( $\Delta_3 \geq 0$ ),

$${}^{\text{th}}\mathbf{K} = {}^{\text{th}}K_{mn} = \frac{\partial q_m}{\partial \vartheta_n} \quad \text{for } m = 1, 2 \quad \text{and} \quad n = 1, 2, \quad (\text{C.32})$$

are obtained from

$$\frac{\partial q_+}{\partial \vartheta_+} = h_{\text{int}} \left( 1 - D_{\text{tot}} - \llbracket \vartheta \rrbracket \frac{\partial D_{\text{tot}}}{\partial \vartheta_+} \right), \quad (\text{C.33})$$

where the state of the damage variable is temperature independent,

$$\frac{\partial D_{\text{tot}}}{\partial \vartheta_+} = 0. \quad (\text{C.34})$$

Hence, the first derivative simplifies to

$$\frac{\partial q_+}{\partial \vartheta_+} = h_{\text{int}} (1 - D_{\text{tot}}), \quad (\text{C.35})$$

and the components of the thermal submatrix follow the relations

$$\frac{\partial q_+}{\partial \vartheta_+} = -\frac{\partial q_+}{\partial \vartheta_-} = -\frac{\partial q_-}{\partial \vartheta_+} = \frac{\partial q_-}{\partial \vartheta_-}. \quad (\text{C.36})$$

For interface closure ( $\Delta_3 < 0$ ) the first derivative of the thermal submatrix reads

$$\frac{\partial q_+}{\partial \vartheta_+} = h_{\text{int}} (1 - D_{\text{tot}}) + h_c D_{\text{tot}} \quad , \quad (\text{C.37})$$

and the remaining derivatives are obtained from Eq. (C.36).

## Appendix D

# CDM – Routine

In this appendix some comments with respect to the CDM approach are provided. In the next subsection the APDL implementation of the CDM approach is shortly sketched and the main features are summarized. Afterwards, the input parameters for the CDM approach and the output parameters are listed.

### Sketch of the Implementation

The main APDL script calls various APDL macros, which can be categorized into macros for the computation of the stabilized cycle, for the evaluation of the damage onset criterion, for the calculation of the damage variable, and for the modeling of damage degradation. The macro for the damage onset criterion executes a Python script, `CriPl`, which computes the fatigue damage indicator for the current stabilized load cycle and calculates the contribution to the damage onset criterion. The accumulation of the damage onset criterion is realized via the `cp_dict.pkl` file, which contains the state variables required for the damage onset criterion of the previous stabilized load cycle. Once the damage accumulation is finished the file `cp_dict.pkl` is overwritten with the updated state variables. The variables required for the `CriPl` computation are provided by the file `vars.py`. This file is automatically written by an APDL macro. Hence, all input variables are defined inside the APDL main script and no additional definitions are necessary. In a combined simulation with the CCZM approach the possible load cycle number for the cycle jump,  $\Delta N_{CCZM}$ , is also defined in `vars.py`

and considered for the damage accumulation. Material degradation during the simulation is realized by changing the material cards in a separate load step. The external loading conditions for this load step are kept constant. After the material degradation is executed the next stabilized cycle is searched for and the whole simulation procedure is repeated. The computation of the FS-criterion is computationally demanding and the usage of an IPython cluster enabling parallel computing is suggested. All other computations are carried out directly in APDL.

## Input variables

The input variables for the CDM approach are defined in the main APDL script, which executes the simulation. The required parameters are grouped and listed in the following.

### Damage Onset Model

FIPname	'FSmod'	FS-criterion, Eq. (2.12)
	'SWTmod'	SWT-criterion, Eq. (2.13)
sig_yield	$\sigma_Y$	yield stress in the FS-criterion
k_fatsoc	$\kappa$	material property in the FS-criterion
int_ini	$\gamma'_f$	LCF coefficient for the FS-criterion
	$\sigma'_f \varepsilon'_f$	LCF coefficient for the SWT-criterion
exp_ini	$c_\gamma$	LCF exponent for the FS-criterion
	$b + c$	LCF exponent for the SWT-criterion

### Damage Evolution Model

dammodel	'isotropic'	isotropic damage modeling
	'ortho_energy'	orthotropic damage modeling
malpha	$\alpha$	modified strain energy parameter, Eq. (3.15)
int_evo	$\varkappa_1$	material parameter in the damage evolution law, Eq. (3.17)
exp_evo	$\varkappa_2$	material parameter in the damage evolution law, Eq. (3.17)



## Stabilized Load Cycle

<code>cycstabEV</code>	<code>'ELEM'</code>	accept stabilized cycle based on Eq. (3.42)
	<code>'MODEL'</code>	accept stabilized cycle based on Eq. (3.43)
<code>DISS_ENG</code>	$\delta W_{i,i-1}^{\text{th}}$	threshold value for Eq. (3.42)
	$\delta W_{i,i-1}^{\text{th}}$	threshold value for Eq. (3.43)
<code>maxcycinstab</code>	$N_{\text{stab}}$	max. number of load cycles to obtain a stabilized load cycle; if the criterion <code>cycstabEV</code> is not reached the cycle $N_{\text{stab}}$ is taken as stabilized load cycle.

## Cycle Jump Parameter

<code>deltaDmaxtol</code>	$\Delta D_{\text{max}}$	max. damage tolerance for cycle jump
<code>deltaDmintol</code>	$\Delta D_{\text{min}}$	min. damage tolerance for cycle jump
<code>maxN</code>	$N_{\text{max}}$	maximum number of jump cycles
<code>minN</code>	$N_{\text{min}}$	minimum number of jump cycles
<code>deltaN</code>	$\Delta N_{\text{os}}$	cycles overshooting the onset criterion

## Output variables

For each stabilized load cycle multiple output files are stored. The state variables can be found in the parameter files `*.parm`. The `CriP1` output can be found in the `*.dat` files. Information about the damage state of individual elements is provided in the output files `*.out`. Additionally, some load cycle numbers, the state of the stopping criterion, and the accepted dissipated energy values for the stabilized load cycle are summarized in this files. For the post processing of the results, APDL scripts as well as Python scripts are required. A short summary of the main parameters in the different files is provided in the following.

**Parameter files – \*.parm**

FIP	$\mathcal{P}^{\text{FS}} / \mathcal{P}^{\text{SWT}}$	fatigue indicator parameter
INItot	$\mathcal{D}^{\mathcal{O}}$	damage onset criterion
damtot	$D$	damage evolution variable

**CriPl files – \*.dat**

nx	$\xi_1 \cdot e_1$	$x_1$ -component of $\xi_1$
ny	$\xi_1 \cdot e_2$	$x_2$ -component of $\xi_1$
nz	$\xi_1 \cdot e_3$	$x_3$ -component of $\xi_1$
sig_nmax	$\sigma_n^{\text{max}}$	max. normal stress acting on the critical plane, $\Xi_c$
sigeps_a	$\mathcal{P}^{\text{FS}} / \mathcal{P}^{\text{SWT}}$	fatigue indicator parameter
DamTotFIP	$\mathcal{D}^{\mathcal{O}}$	damage onset criterion

**Output files – \*.out**

Cycstab	$^S N$	number of the stabilized load cycle for which the output is written for
Cyctot	$N_{\text{tot}}$	total number of load cycles including the cycle jumps
CycleJump	$\Delta N_{\text{CDM}}$	number of load cycles for the next cycle jump
EmaxRelDiss	$\delta w_{i,i-1}$	max. dissipated strain energy density between two LCs
SumRelDiss	$\delta W_{i,i-1}$	dissipated strain energy between two LCs

## Appendix E

# CCZM – USERINTER

In this appendix some comments are provided with respect to the usage of the `USERINTER` subroutine. In the next subsection the required user defined functions are discussed and their usage is briefly sketched. Afterwards, the input parameters `uprop` and the output state variables `usvr` are discussed.

### Usage of `USERINTER`

The application of `userinter.F` requires the following user programmed functions:

<code>user01.F</code>	...	set up the global variables and cycle jump parameters
<code>user02.F</code>	...	evaluate the number of load cycles for the cycle jump
<code>user03.F</code>	...	flag to set/unset fatigue interface degradation and adapt cycle jump number to CDM approach
<code>userou.F</code>	...	store user supplied element output in nmisc record

All five Fortran source code files need to be called and compiled with `/UPF` at the beginning of the APDL script. The `userou.F` subroutine needs to be activated with the `USRCAL` command. User-defined command names need to be assigned to the three user-defined functions by the `/UCMD` command, enabling the usage of the functions. In the following user-defined command names are suggested and the required input and output parameters

are listed. Input parameters are marked by parentheses ( ) and output parameters are marked by brackets [ ]:

```

user01.F ... fini, (Nmin), (Nmax), (ΔDfallow)
user02.F ... fev1, [ΔNCCZM], [( $\frac{\Delta G}{G_c}$ )max], [( $\frac{da}{dN}$ )max], [( $\frac{dD_f}{dN}$ )max], (lcz), (φ(tmax)), (1)
user03.F ... fset, [FLAG=0], (ΔNCDM), [Ntot], (ΔNstab)
user03.F ... fset, [FLAG=1], [Dtotmax], [ΔDtotmax]

```

Before the solution step is entered **fini** is called and the global variables and cycle jump parameter are defined. Then the solution process is started and the first load cycle is simulated. In a linear–elastic analysis **fev1** is called after the first load cycle. In a elasto–plastic analyses the simulation of the load cycle is repeated until a stabilized cycle,  $^S N$ , is found and **fev1** is called afterwards.

In a simulation utilizing the CCZM approach only, the first four output parameters of **fev1** are just for information. In a combined analysis with the CDM approach  $\Delta N_{CCZM}$  is required as input parameter for the Python script, **CriP1**, which computes the CDM damage onset criterion. This information exchange is necessary since the maximum number of jump cycles for the CDM approach is limited by  $\Delta N_{CCZM}$  from the CCZM approach. The latter three parameters of **fev1** are input parameters. The required structural properties,  $l_{cz}$ , and  $\phi(t^{\max})$ , are computed in the APDL script, executing the simulation. The last input value, (1), is a required integer value and is implemented for future use. If only one cohesive zone occurs during the simulation, the two structural properties are exchanged between APDL and **USERINTER** via **fev1**. If multiple cohesive zones occur during the simulation, the exchange of the structural properties is realized by the file **nonlocal.out**.

In a combined simulation the **CriP1** computation is executed and the maximum number of jump cycles of both approaches  $\Delta N_{CDM} \leq \Delta N_{CCZM}$  is obtained. If only the CCZM approach is utilized a large value for  $\Delta N_{CDM}$  needs to be defined. This way,  $\Delta N_{CCZM}$  is not affected by  $\Delta N_{CDM}$ . Subsequently, **fset** is called and the fatigue interface degradation carried out in a single load step. The external loading conditions are kept constant for this degradation step. The input parameter  $\Delta N_{stab}$  describes the number of load cycles simulated until a stabilized load cycle has been accepted. The output parameter  $N_{tot}$  is the total number of load cycles including the cycle jumps.

After the degradation load step `fset` is called again and the fatigue degradation flag is unset, [FLAG=0]. Two output parameters are provided by `fset` when unsetting the degradation flag. The maximum damage variable  $D_{\text{tot}}^{\text{max}}$  of an integration point inside the cohesive zone (completely damaged interface points are not considered here), and the maximum damage increment,  $[\Delta D_{\text{tot}}^{\text{max}}]$ , obtained after the cycle jump. This value should be close to or smaller as the defined allowable damage increment,  $(\Delta D_{\text{f}}^{\text{allow}})$ . After unsetting the degradation flag, the next load cycle is computed and the listed procedure repeated until the stopping criterion is reached.

## Input of USERINTER

The input of USERINTER is defined via the user-defined material properties, `uprop(i)`, per temperature:

<code>uprop(1)</code>	$\mathcal{G}_{\text{Ic}}$	mode I critical energy release rate
<code>uprop(2)</code>	$\mathcal{G}_{\text{IIc}}$	mode II critical energy release rate
<code>uprop(3)</code>	$T_{\text{I}}^{\circ}$	mode I cohesive strength
<code>uprop(4)</code>	$T_{\text{II}}^{\circ}$	mode II cohesive strength
<code>uprop(5)</code>	$\eta$	BK-exponent
<code>uprop(6)</code>	$\beta$	shape parameter of the cohesive law
<code>uprop(7)</code>	$D_{\text{cut}}$	damage cut off value (typically 0.99)
<code>uprop(8)</code>	2	integer value
<code>uprop(9)</code>	–	reserved for future use
<code>uprop(10)</code>	$C_{\text{I}}$	mode I Paris law coefficient
<code>uprop(11)</code>	$C_{\text{II}}$	mode II Paris law coefficient
<code>uprop(12)</code>	$C_{\text{m}}$	mixed-mode Paris law coefficient
<code>uprop(13)</code>	$m_{\text{I}}$	mode I Paris law exponent
<code>uprop(14)</code>	$m_{\text{II}}$	mode II Paris law exponent
<code>uprop(15)</code>	$m_{\text{m}}$	mixed-mode Paris law coefficient
<code>uprop(16)</code>	$\mathcal{G}_{\text{Ith}}$	mode I threshold value
<code>uprop(17)</code>	$\mathcal{G}_{\text{IIth}}$	mode II threshold value
<code>uprop(18)</code>	–	reserved for future use
<code>uprop(19)</code>	$\Delta_3^{\text{fc}}$	interface penetration for $K_{\text{fc}}$ (pos. value)
<code>uprop(20)</code>	$K_{\text{sc}}$	initial penalty contact stiffness
<code>uprop(21)</code>	$K_{\text{fc}}$	final penalty contact stiffness

uprop(22)	$h_{\text{int}}$	thermal conductance of the undamaged interface
uprop(23)	$v h_{\text{int}}$	max. therm. conductance of the damaged interface during contact

## Output of USERINTER

The output of the USERINTER subroutine, the updated additional state variables, `usvr[i]`, are accessible from the NMISC records. The user defined output variables are appended to the element standard output variables. The maximum number of the standard output variables is obtained by `maxnmisc = etyiqr(ETYPE,-110)`, where `ETYPE` is the element type number. The `usvr[i]` is accessed by `NMISC[maxnmisc+i]` in the `/POST1` or `/POST26` post processors.

<code>usvr[1]</code>	$\Delta_1$	interface shear separation in $x_1$
<code>usvr[2]</code>	$\Delta_2$	interface shear separation in $x_2$
<code>usvr[3]</code>	–	reserved for future use
<code>usvr[4]</code>	$d_{\text{tot}}$	total internal status variable
<code>usvr[5]</code>	$d_s$	static internal status variable
<code>usvr[6]</code>	$d_{\text{tot}} - d_s$	internal status variable associated to fatigue
<code>usvr[7]</code>	$\lambda_{\text{max}}$	maximum effective separation during load cycle
<code>usvr[8]</code>	$\lambda_{\text{min}}$	minimum effective separation during load cycle
<code>usvr[9]</code>	$D_{\text{tot}}$	total damage variable
<code>usvr[10]</code>	$\frac{\Delta \mathcal{G}}{\mathcal{G}_c}$	fraction between the energy release rate range and the critical energy release rate
<code>usvr[11]</code>	$\frac{da}{dN}$	fatigue crack growth rate
<code>usvr[12]</code>	$\Delta_3$	interface normal separation/penetration in $x_3$
<code>usvr[13]</code>	–	reserved for future use
<code>usvr[14]</code>	$l_{cz}$	length of the cohesive zone
<code>usvr[15]</code>	$\phi(t^{\text{max}})$	mix mode ratio
<code>usvr[16]</code>	$\mathcal{S}$	parameter of the BK-criterion
<code>usvr[17]</code>	$w(\lambda_{\text{max}})$	specific work at $\lambda_{\text{max}}$
<code>usvr[18]</code>	$C(\phi(t^{\text{max}}))$	mixed-mode Paris law coefficient
<code>usvr[19]</code>	$m(\phi(t^{\text{max}}))$	mixed-mode Paris law exponent
<code>usvr[20]</code>	$\mathcal{G}_{\text{th}}(\phi(t^{\text{max}}))$	mixed-mode threshold value
<code>usvr[21]</code>	$T^\circ(\lambda_{\text{max}})$	mixed-mode onset traction at $\lambda_{\text{max}}$

usvr [22]	$\Delta^o(\lambda_{\max})$	mixed-mode onset separation at $\lambda_{\max}$
usvr [23]	$\mathcal{G}_c(\lambda_{\max})$	mixed-mode critical energy release rate $\lambda_{\max}$
usvr [24]	$B$	mode mixity
usvr [25]	$\vartheta_{cz}$	average cohesive zone temperature
usvr [26]	$T_I^o(\vartheta_{cz})$	mode I temperature dependent onset traction
usvr [27]	$T_{II}^o(\vartheta_{cz})$	mode II temperature dependent onset traction
usvr [28]	$\mathcal{G}_{Ic}(\vartheta_{cz})$	mode I temperature dependent critical energy release rate
usvr [29]	$\mathcal{G}_{IIc}(\vartheta_{cz})$	mode II temperature dependent critical energy release rate
usvr [30]	$h_{cz}(\Delta_3, D_{\text{tot}})$	thermal conductance
usvr [31]	$T_1$	shear traction in $x_1$
usvr [32]	$T_2$	shear traction in $x_2$
usvr [33]	$T_3$	traction in $x_3$
usvr [34]	$q_+$	normal component of the thermal flux out of the interface $C_+$
usvr [35]	$\vartheta_+$	temperature of $C_+$
usvr [36]	$\vartheta_-$	temperature of $C_-$





# Bibliography

- [1] H. Altenbach. *Kontinuumsmechanik: Einführung in die materialunabhängigen und materialabhängigen Gleichungen*. Springer-Verlag, Berlin, Heidelberg, 2015.
- [2] S. Amiable, S. Chapuliot, A. Constantinescu, and A. Fissolo. A comparison of life-time prediction methods for a thermal fatigue experiment. *International Journal of Fatigue*, 28(7):692–706, 2006.
- [3] A. Amiri-Rad, M. Mashayekhi, and F. P. van der Meer. Cohesive zone and level set method for simulation of high cycle fatigue delamination in composite materials. 160: 61–69.
- [4] *ANSYS Mechanical APDL Documentation v16.2*. ANSYS, Inc., Canonsburg, PA, USA, 2015.
- [5] F. Armero and S. Oller. A general framework for continuum damage models. I. Infinitesimal plastic damage models in stress space. *International Journal of Solids and Structures*, 37(48):7409–7436, 2000.
- [6] M. Asheghi, K. Kurabayashi, R. Kasnavi, and K. E. Goodson. Thermal conduction in doped single-crystal silicon films. *Journal of Applied Physics*, 91(8):5079–5088, 2002.
- [7] L. Asp, A. Sjögren, and E. S. Greenhalgh. Delamination growth and thresholds in a carbon/epoxy composite under fatigue loading. *Journal of Composites, Technology and Research*, 23(2):55–68, 2001.

- [8] ASTM D5528–13. Standard test method for mode I interlaminar fracture toughness of unidirectional fiber-reinforced polymer matrix composites. Standard, ASTM International, 2013.
- [9] ASTM D6671/D6671M–13. Standard test method for mixed mode I–mode II interlaminar fracture toughness of unidirectional fiber reinforced polymer matrix composites. Standard, ASTM International, 2013.
- [10] ASTM D7905/D7905M–14. Standard test method for determination of the mode II interlaminar fracture toughness of unidirectional fiber-reinforced polymer matrix composites. Standard, ASTM International, 2014.
- [11] B. L. V. Bak, C. Sarrado, A. Turon, and J. Costa. Delamination under fatigue loads in composite laminates: a review on the observed phenomenology and computational methods. *Applied Mechanics Reviews*, 66(6):060803–1 – 060803–24, 2014.
- [12] B. L. V. Bak, A. Turon, E. Lindgaard, and E. Lund. A simulation method for high-cycle fatigue-driven delamination using a cohesive zone model. *International Journal for Numerical Methods in Engineering*, 106(3):163–191, 2016.
- [13] B. L. V. Bak, A. Turon, E. Lindgaard, and E. Lund. A benchmark study of simulation methods for high-cycle fatigue-driven delamination based on cohesive zone models. *Composite Structures*, 164:198 – 206, 2017.
- [14] B. J. Baliga. *Fundamentals of Power Semiconductor Devices*. Springer, Boston, MA, 2008.
- [15] J. A. Bannantine and D. F. Socie. A variable amplitude multiaxial fatigue life prediction method. In *Third International Conference on Biaxial/Multiaxial Fatigue, Stuttgart*, 1989.
- [16] G. Barenblatt. The mathematical theory of equilibrium cracks in brittle fracture. *Advances in Applied Mechanics*, 7:55–129, 1962.
- [17] J. Barés, L. Gélébart, J. Rupil, and L. Vincent. A joined finite element based method to simulate 3D crack network initiation and propagation in mechanical and thermal fatigue. *International Journal of Fatigue*, 44:279–291, 2012.

- [18] O. H. Basquin. The exponential law of endurance tests. *American Society of Testing Materials*, 10:625–630, 1910.
- [19] R. Bayerer, T. Herrmann, T. Licht, J. Lutz, and M. Feller. Model for power cycling lifetime of IGBT modules – various factors influencing lifetime. In *5th International Conference on Integrated Power Electronics Systems (CIPS), Nuremberg*, pages 1–6, 2008.
- [20] Z. P. Bažant and M. Jirásek. Nonlocal integral formulations of plasticity and damage: survey of progress. *Journal of Engineering Mechanics*, 128(11):1119–1149, 2002.
- [21] T. Behrens. Novel copper metallization on silicon carbide electronic devices enabling increased packaging lifetime and higher junction-temperatures. In *15th European Conference on Power Electronics and Applications (EPE), Lille*, pages 1–10, 2013.
- [22] T. Belytschko, W. K. Liu, B. Moran, and K. Elkhodary. *Nonlinear finite elements for continua and structures*. John Wiley & Sons, 2nd edition, 2013.
- [23] L. Benabou, Z. Sun, and P. Dahoo. A thermo–mechanical cohesive zone model for solder joint lifetime prediction. *International Journal of Fatigue*, 49:18–30, 2013.
- [24] L. Benabou, Z. Sun, P. Pougnet, and P. R. Dahoo. Continuum damage approach for fatigue life prediction of viscoplastic solder joints. *Journal of Mechanics*, 31(5): 525–531, 2015.
- [25] M. Benzeggagh and M. Kenane. Measurement of mixed–mode delamination fracture toughness of unidirectional glass/epoxy composites with mixed–mode bending apparatus. *Composites Science and Technology*, 56(4):439–449, 1996.
- [26] A. Bernasconi and I. Papadopoulos. Efficiency of algorithms for shear stress amplitude calculation in critical plane class fatigue criteria. *Computational Materials Science*, 34(4):355–368, 2005.
- [27] G. Bhattacharjee. Algorithm AS 32: The incomplete gamma integral. *Journal of the Royal Statistical Society. Series C (Applied Statistics)*, 19(3):285–287, 1970.
- [28] B. Bhattacharya and B. Ellingwood. Continuum damage mechanics analysis of fatigue crack initiation. *International Journal of Fatigue*, 20(9):631–639, 1998.

- [29] S. Bigl, S. Wurster, M. J. Cordill, and D. Kiener. Advanced characterisation of thermo-mechanical fatigue mechanisms of different copper film systems for wafer metallizations. *Thin Solid Films*, 612:153–164, 2016.
- [30] N. Blanco, E. K. Gamstedt, L. E. Asp, and J. Costa. Mixed-mode delamination growth in carbon-fibre composite laminates under cyclic loading. *International Journal of Solids and Structures*, 41(15):4219–4235, 2004.
- [31] B. K. Bose. Global warming: Energy, environmental pollution, and the impact of power electronics. *IEEE Industrial Electronics Magazine*, 4(1):6–17, 2010.
- [32] B. K. Bose. Global energy scenario and impact of power electronics in 21st century. *IEEE Transactions on Industrial Electronics*, 60(7):2638–2651, 2013.
- [33] J. Bouvard, J. Chaboche, F. Feyel, and F. Gallerneau. A cohesive zone model for fatigue and creep-fatigue crack growth in single crystal superalloys. *International Journal of Fatigue*, 31:868–879, 2009.
- [34] M. Brincker, P. Kristensen, K. Pedersen, and V. Popok. Mechanisms of metallization degradation in high power diodes. *Microelectronics Reliability*, 64:489–493, 2016.
- [35] M. W. Brown and K. J. Miller. A theory for fatigue failure under multiaxial stress-strain conditions. *Proceedings of the Institution of Mechanical Engineers*, 187(1):745–755, 1973.
- [36] F. M. Burdekin and D. E. W. Stone. The crack opening displacement approach to fracture mechanics in yielding materials. *The Journal of Strain Analysis for Engineering Design*, 1(2):145–153, 1966.
- [37] J. Burkardt. ASA032 the incomplete gamma function. [http://people.sc.fsu.edu/~jburkardt/f\\_src/asa032/asa032.html](http://people.sc.fsu.edu/~jburkardt/f_src/asa032/asa032.html). Accessed: 2017-08-29.
- [38] C. Busca, R. Teodorescu, F. Blaabjerg, S. Munk-Nielsen, L. Helle, T. Abeyasekera, and P. Rodriguez. An overview of the reliability prediction related aspects of high power IGBTs in wind power applications. *Microelectronics Reliability*, 51(9):1903–1907, 2011.

- [39] A. Carpinteri, R. Brighenti, E. Macha, and A. Spagnoli. Expected principal stress directions under multiaxial random loading. Part II: numerical simulation and experimental assessment through the weight function method. *International Journal of Fatigue*, 21(1):89–96, 1999.
- [40] A. Carpinteri, E. Macha, R. Brighenti, and A. Spagnoli. Expected principal stress directions under multiaxial random loading. Part I: theoretical aspects of the weight function method. *International Journal of Fatigue*, 21(1):83–88, 1999.
- [41] A. Carpinteri, M. Kurek, T. Łagoda, and S. Vantadori. Estimation of fatigue life under multiaxial loading by varying the critical plane orientation. *International Journal of Fatigue*, 100:512–520, 2017.
- [42] J.-L. Chaboche. Cumulative damage. In C. Bathias and A. Pineau, editors, *Fatigue of Materials and Structures*, pages 47–110. John Wiley & Sons, Inc., 2013.
- [43] J.-L. Chaboche. Sur l'utilisation des variables d'état interne pour la description du comportement viscoplastique et de la rupture par endommagement. In *Proc. Problemes non-linéaires de mécanique, Symposium franco-polonais, Cracow (Poland)*, pages 137–159, 1977.
- [44] J.-L. Chaboche. Constitutive equations for cyclic plasticity and cyclic viscoplasticity. *International Journal of Plasticity*, 5(3):247–302, 1989.
- [45] J.-L. Chaboche. On some modifications of kinematic hardening to improve the description of ratchetting effects. *International Journal of Plasticity*, 7(7):661–678, 1991.
- [46] J.-L. Chaboche. A review of some plasticity and viscoplasticity constitutive theories. *International Journal of Plasticity*, 24(10):1642–1693, 2008.
- [47] E. W. Chaves. *Notes on continuum mechanics*. Springer Science & Business Media, 2013.
- [48] Y. Chen, Y. Jin, and R. Kang. Coupling damage and reliability modeling for creep and fatigue of solder joint. *Microelectronics Reliability*, 75:233–238, 2017.

- [49] U.-M. Choi, F. Blaabjerg, and K.-B. Lee. Study and handling methods of power igt module failures in power electronic converter systems. *IEEE Transactions on Power Electronics*, 30(5):2517–2533, 2015.
- [50] U.-M. Choi, F. Blaabjerg, and S. Jorgensen. Power cycling test methods for reliability assessment of power device modules in respect to temperature stress. *IEEE Transactions on Power Electronics*, PP(99):1–1, 2017.
- [51] C. Chow and J. Wang. An anisotropic theory of continuum damage mechanics for ductile fracture. *Engineering Fracture Mechanics*, 27(5):547–558, 1987.
- [52] M. Ciappa. Selected failure mechanisms of modern power modules. *Microelectronics Reliability*, 42(4-5):653–667, 2002.
- [53] L. F. Coffin. A study of the effects of cyclic thermal stresses on a ductile metal. *Transactions of the American Society of Mechanical Engineers*, 76:931–950, 1954.
- [54] J. P. Cordebois and F. Sidoroff. Damage induced elastic anisotropy. In J. P. Boehler, editor, *Mechanical Behavior of Anisotropic Solids/Comportment Mécanique des Solides Anisotropes*, pages 761–774. Springer, Dordrecht, 1982.
- [55] P. Cova, N. Delmonte, and D. Chiozzi. Numerical analysis and experimental tests for solder joints power cycling optimization. *Microelectronics Reliability*, 55(9):2036–2040, 2015.
- [56] R. Darveaux. Effect of simulation methodology on solder joint crack growth correlation and fatigue life prediction. *Journal of Electronic Packaging*, 124:147–154, 2002.
- [57] *ABAQUS Analysis User’s Guide. V6(2016)*. Dassault Systemes Simulia Corp., Providence, RI, USA, 2016.
- [58] S. de Filippis. *Modeling, simulation and validation of the electro-thermal interaction in power MOSFETs*. PhD thesis, Università degli Studi di Napoli Federico II, 2013.
- [59] S. de Filippis, V. Košel, D. Dibra, S. Decker, H. Koeck, and A. Irace. ANSYS based 3D electro-thermal simulations for the evaluation of power MOSFETs robustness. *Microelectronics Reliability*, 51:1954–1958, 2011.

- [60] S. de Filippis, R. Illing, M. Nelhiebel, S. Decker, H. Kock, and A. Irace. Validated electro-thermal simulations of two different power mosfet technologies and implications on their robustness. In *25th International Symposium on Power Semiconductor Devices and ICs (ISPSD), Kanazawa*, pages 325–328, 2013.
- [61] D. Dibra, M. Stecher, S. Decker, A. Lindemann, J. Lutz, and C. Kadow. On the origin of thermal runaway in a trench power mosfet. *IEEE Transactions on Electron Devices*, 58:3477–3484, 2011.
- [62] N. E. Dowling and J. A. Begley. Fatigue crack growth during gross plasticity and the J-integral. In *Mechanics of crack growth*, STP590. ASTM International, 1976.
- [63] J. Dufailly and J. Lemaitre. Modeling very low cycle fatigue. *International Journal of Damage Mechanics*, 4(2):153–170, 1995.
- [64] D. Dugdale. Yielding of steel sheets containing slits. *Journal of the Mechanics and Physics of Solids*, 8(2):100–104, 1960.
- [65] C. Durand, M. Klingler, D. Coutellier, H. Naceur, A. Grams, and O. Wittler. Fracture mechanics in new designed power module under thermo–mechanical loads. In *MATEC Web of Conferences*, volume 12, page 04015. EDP Sciences, 2014.
- [66] C. Durand, M. Klingler, D. Coutellier, and H. Naceur. Study of fatigue failure in Al–chip–metallization during power cycling. *Engineering Fracture Mechanics*, 138:127–145, 2015.
- [67] C. Durand, M. Klingler, M. Bigerelle, and D. Coutellier. Solder fatigue failures in a new designed power module under power cycling. *Microelectronics Reliability*, 66:122–133, 2016.
- [68] C. Durand, M. Klingler, D. Coutellier, and H. Naceur. Power cycling reliability of power module: A survey. *IEEE Transactions on Device and Materials Reliability*, 16(1):80–97, 2016.
- [69] S. Dusmez, S. H. Ali, M. Heydarzadeh, A. S. Kamath, H. Duran, and B. Akin. Aging precursor identification and lifetime estimation for thermally aged discrete package

- silicon power switches. *IEEE Transactions on Industry Applications*, 53(1):251–260, 2017.
- [70] S. Eiser. *An extension to Nitsche-type mortaring for non-conforming finite elements*. PhD thesis, Vienna University of Technology, 2016.
- [71] A. Escolán, J. M. Bielsa, B. Hernández-Gascón, M. A. Jiménez, J. López, and R. Allende. Thermo-mechanical fatigue approach to predict tooling life in high temperature metal forming processes. *International Journal of Material Forming*, 10(4):535–545, 2017.
- [72] A. Fatemi and N. Shamsaei. Multiaxial fatigue: An overview and some approximation models for life estimation. *International Journal of Fatigue*, 33(8):948–958, 2011.
- [73] A. Fatemi and D. F. Socie. A critical plane approach to multiaxial fatigue damage including out of phase loading. *Fatigue and Fracture of Engineering Materials and Structures*, 11:149–165, 1988.
- [74] A. Fatemi and L. Yang. Cumulative fatigue damage and life prediction theories: a survey of the state of the art for homogeneous materials. *International Journal of Fatigue*, 20(1):9–34, 1998.
- [75] C. E. Feltner and J. D. Morrow. Microplastic strain hysteresis energy as a criterion for fatigue fracture. *Journal of Basic Engineering*, 83:15–22, 1961.
- [76] R. Fernandes, M. de Moura, and R. Moreira. Effect of temperature on pure modes I and II fracture behavior of composite bonded joints. *Composites Part B: Engineering*, 96:35–44, 2016.
- [77] A. Fissolo, S. Amiable, O. Ancelet, F. Mermaz, J. Stelmaszyk, A. Constantinescu, C. Robertson, L. Vincent, V. Maillot, and F. Bouchet. Crack initiation under thermal fatigue: An overview of CEA experience. Part I: Thermal fatigue appears to be more damaging than uniaxial isothermal fatigue. *International Journal of Fatigue*, 31(3): 587–600, 2009.
- [78] A. Fissolo, C. Gourdin, O. Ancelet, S. Amiable, A. Demassieux, S. Chapuliot, N. Haddar, F. Mermaz, J. Stelmaszyk, A. Constantinescu, L. Vincent, and V. Maillot. Crack



- initiation under thermal fatigue: An overview of CEA experience: Part II of II: Application of various criteria to biaxial thermal fatigue tests and a first proposal to improve the estimation of the thermal fatigue damage. *International Journal of Fatigue*, 31(7):1196–1210, 2009.
- [79] T. Gocmez, A. Awarke, and S. Pischinger. A new low cycle fatigue criterion for isothermal and out-of-phase thermomechanical loading. *International Journal of Fatigue*, 32(4):769–779, 2010.
- [80] L. R. GopiReddy, L. M. Tolbert, and B. Ozpineci. Power cycle testing of power switches: A literature survey. *IEEE Transactions on Power Electronics*, 30(5):2465–2473, 2015.
- [81] L. R. GopiReddy, L. M. Tolbert, B. Ozpineci, and J. O. Pinto. Rainflow algorithm-based lifetime estimation of power semiconductors in utility applications. *IEEE Transactions on Industry Applications*, 51(4):3368–3375, 2015.
- [82] V. K. Goyal. *Analytical modeling of the mechanics of nucleation and growth of cracks*. PhD thesis, Virginia Polytechnic Institute and State University, 2002.
- [83] V. K. Goyal and E. R. Johnson. Cohesive–decohesive interfacial constitutive law for the analyses of fatigue crack initiation and growth. In *44th AIAA/ASME/ASCE/AHS/ASC Structures, Structural Dynamics, and Materials Conference Norfolk, Virginia*, volume 1678. American Institute of Aeronautics and Astronautics, 2003.
- [84] V. K. Goyal, E. R. Johnson, and C. G. Dávila. Irreversible constitutive law for modeling the delamination process using interfacial surface discontinuities. *Composite Structures*, 65:289 – 305, 2004.
- [85] D. Gross and T. Seelig. *Bruchmechanik: mit einer Einführung in die Mikromechanik*. Springer, Berlin, Heidelberg, 2016.
- [86] H. Grover. An observation concerning the cycle ratio in cumulative damage. In *Symposium on fatigue of aircraft structures*, STP274. ASTM International, 1960.

- [87] G. Halford and S. Manson. Life prediction of thermal–mechanical fatigue using strain-range partitioning. In *Thermal fatigue of materials and components*, STP612. ASTM International, 1976.
- [88] S. R. Hallett and P. W. Harper. Modelling delamination with cohesive interface elements, Chapter 2. In P. P. Camanho and S. R. Hallett, editors, *Numerical Modelling of Failure in Advanced Composite Materials*, pages 55–72. Woodhead Publishing, 2015.
- [89] P. W. Harper and S. R. Hallett. Cohesive zone length in numerical simulations of composite delamination. *Engineering Fracture Mechanics*, 75(16):4774–4792, 2008.
- [90] P. W. Harper and S. R. Hallett. A fatigue degradation law for cohesive interface elements – Development and application to composite materials. *International Journal of Fatigue*, 32:1774–1787, 2010.
- [91] S. Hashemi, A. Kinloch, and J. Williams. The analysis of interlaminar fracture in uniaxial fibre–polymer composites. In *Proceedings of the Royal Society of London A: Mathematical, Physical and Engineering Sciences*, volume 427, pages 173–199. The Royal Society, 1990.
- [92] A. Hattiangadi and T. Siegmund. A thermomechanical cohesive zone model for bridged delamination cracks. *Journal of the Mechanics and Physics of Solids*, 52(3):533–566, 2004.
- [93] A. Hattiangadi and T. Siegmund. A numerical study on interface crack growth under heat flux loading. *International Journal of Solids and Structures*, 42:6335–6355, 2005.
- [94] M. Held, P. Jacob, G. Nicoletti, P. Scacco, and M.-H. Poech. Fast power cycling test of IGBT modules in traction application. In *Proceedings of Second International Conference on Power Electronics and Drive Systems*, volume 1, pages 425–430. IEEE, 1997.
- [95] M. Held, P. Jacob, G. Nicoletti, P. Scacco And, and M.-H. Poech. Fast power cycling test for insulated gate bipolar transistor modules in traction application. *International Journal of Electronics*, 86(10):1193–1204, 1999.

- [96] C. Herold, J. Franke, R. Bhojani, A. Schleicher, and J. Lutz. Requirements in power cycling for precise lifetime estimation. *Microelectronics Reliability*, 58:82–89, 2016.
- [97] N. Heuck, K. Guth, M. Thoben, A. Mueller, N. Oeschler, L. Boewer, R. Speckels, S. Krasel, and A. Ciliox. Aging of new interconnect–technologies of power–modules during power–cycling. In *8th International Conference on Integrated Power Electronics Systems (CIPS), Nuremberg*, pages 1–6, 2014.
- [98] R. Hill. *The mathematical theory of plasticity*, volume 11. Oxford university press, 1998.
- [99] A. Hillerborg, M. Mod er, and P. E. Petersson. Analysis of crack formation and crack growth in concrete by means of fracture mechanics and finite elements. *Cement and Concrete Research*, 6(6):773–781, 1976.
- [100] J. P. M. Hoefnagels, M. Kolluri, J. A. W. van Dommelen, and M. G. D. Geers. *An in-situ experimental–numerical approach for interface delamination characterization*, pages 569–576. Springer, New York, 2011.
- [101] M. A. Hopcroft, W. D. Nix, and T. W. Kenny. What is the Young’s modulus of silicon? *Journal of Microelectromechanical Systems*, 19(2):229–238, 2010.
- [102] R. Hormozi. *Experimental and numerical simulations of Type 316 stainless steel failure under LCF/TMF loading conditions*. PhD thesis, Imperial College London, 2014.
- [103] H. Huang and P. A. Mawby. A lifetime estimation technique for voltage source inverters. *IEEE Transactions on Power Electronics*, 28(8):4113–4119, 2013.
- [104] O. Huber, J. Nickel, and G. Kuhn. On the decomposition of the J-integral for 3D crack problems. *International Journal of Fracture*, 64(4):339–348, 1993.
- [105] T. Hung, S. Chiang, C. Huang, C. Lee, and K. Chiang. Thermal–mechanical behavior of the bonding wire for a power module subjected to the power cycling test. *Microelectronics Reliability*, 51(9):1819–1823, 2011.
- [106] J. Hutchinson. Plastic stress and strain fields at a crack tip. *Journal of the Mechanics and Physics of Solids*, 16(5):337–342, 1968.

- [107] J. Hutchinson. Singular behaviour at the end of a tensile crack in a hardening material. *Journal of the Mechanics and Physics of Solids*, 16(1):13–31, 1968.
- [108] T. Islam, J. Zechner, M. Bernardoni, M. Nelhiebel, and R. Pippan. A novel setup for wafer curvature measurement at very high heating rates. *Review of Scientific Instruments*, 88(2):024709, 2017.
- [109] S. Jimenez and R. Duddu. On the parametric sensitivity of cohesive zone models for high-cycle fatigue delamination of composites. *International Journal of Solids and Structures*, 82:111–124, 2016.
- [110] J. Jung, B. C. Do, and Q. D. Yang. Augmented finite-element method for arbitrary cracking and crack interaction in solids under thermo-mechanical loadings. *Philosophical Transactions of the Royal Society of London A: Mathematical, Physical and Engineering Sciences*, 374(2071), 2016.
- [111] L. M. Kachanov. *Introduction to continuum damage mechanics*. Springer Netherlands, 1986.
- [112] M. Kachanov. Elastic solids with many cracks: a simple method of analysis. *International Journal of Solids and Structures*, 23(1):23–43, 1987.
- [113] M. Kaltenbacher. *Numerical simulation of mechatronic sensors and actuators*. Springer, Berlin, Heidelberg, 2007.
- [114] W. Kanert. Reliability of semiconductor devices – The need for simulation. In *12th International Conference on Thermal, Mechanical Multi-Physics Simulation and Experiments in Microelectronics and Microsystems, Linz*, pages 1–5, 2011.
- [115] W. Kanert. Active cycling reliability of power devices: Expectations and limitations. *Microelectronics Reliability*, 52(9):2336–2341, 2012.
- [116] G. Kang. Ratchetting: Recent progresses in phenomenon observation, constitutive modeling and application. *International Journal of Fatigue*, 30(8):1448–1472, 2008.
- [117] A. Kapoor. A re-evaluation of the life to rupture of ductile metals by cyclic plastic strain. *Fatigue & Fracture of Engineering Materials and Structures*, 17(2):201–219, 1994.

- [118] A. Karolczuk and E. Macha. A review of critical plane orientations in multiaxial fatigue failure criteria of metallic materials. *International Journal of Fracture*, 134(3):267, 2005.
- [119] L. F. Kawashita and S. R. Hallett. A crack tip tracking algorithm for cohesive interface element analysis of fatigue delamination propagation in composite materials. *International Journal of Solids and Structures*, 49(21):2898–2913, 2012.
- [120] B. Khong, M. Legros, P. Dupuy, C. Levade, and G. Vanderschaeve. Alterations induced in the structure of intelligent power devices by extreme electro–thermal fatigue. *Physica Status Solidi (c)*, 4(8):2997–3001, 2007.
- [121] H. Köck. *Experimental and numerical study on heat transfer problems in microelectronic devices*. PhD thesis, University of Klagenfurt, 2012.
- [122] V. Košel. *Thermo–Mechanical Analysis of Smart Power Switches under Dynamic Thermal Stress Conditions*. PhD thesis, Slovak University of Technology, Bratislava, 2009.
- [123] G. Kravchenko. *Numerical simulations of fatigue crack problems in semiconductor devices subjected to thermomechanical loading*. PhD thesis, Vienna University of Technology, 2014.
- [124] G. Kravchenko, B. Karunamurthy, M. Nelhiebel, and H. E. Pettermann. Finite element analysis of fatigue cracks formation in power metallisation of a semiconductor device subjected to active cycling. In *14th International Conference on Thermal, Mechanical and Multi–Physics Simulation and Experiments in Microelectronics and Microsystems (EuroSimE)*, Wroclaw, pages 1–6, 2013.
- [125] G. Kravchenko, B. Karunamurthy, and H. E. Pettermann. FEM study of fatigue crack growth in a power semiconductor chip subjected to transient thermal loading. *Procedia Materials Science*, 3:63–70, 2014.
- [126] M. Kuna. *Numerische Beanspruchungsanalyse von Rissen – Finite Elemente in der Bruchmechanik*. Vieweg+Teubner Verlag, Wiesbaden, 2nd edition, 2010.

- [127] M. Kuna. *Finite elements in fracture mechanics: Theory—Numerics—Applications*. Springer, Dordrecht, 2013.
- [128] B. Landry and G. LaPlante. Modeling delamination growth in composites under fatigue loadings of varying amplitudes. *Composites Part B: Engineering*, 43(2):533–541, 2012.
- [129] C. S. Lau, C. Khor, D. Soares, J. Teixeira, and M. Abdullah. Thermo–mechanical challenges of reflowed lead–free solder joints in surface mount components: a review. *Soldering & Surface Mount Technology*, 28(2):41–62, 2016.
- [130] J. H. Lau, S. H. Pan, and C. Chang. A new thermal–fatigue life prediction model for wafer level chip scale package (WLCSP) solder joints. *Journal of Electronic Packaging*, 124(3):212, 2002.
- [131] L. R. LeBlanc and G. LaPlante. Experimental investigation and finite element modeling of mixed–mode delamination in a moisture–exposed carbon/epoxy composite. *Composites Part A: Applied Science and Manufacturing*, 81:202–213, 2016.
- [132] W. Lee, L. Nguyen, and G. Selvaduray. Solder joint fatigue models: review and applicability to chip scale packages. *Microelectronics Reliability*, 40(2):231–244, 2000.
- [133] J. Lemaitre. A continuous damage mechanics model for ductile fracture. *Journal of Engineering Materials and Technology*, 107(1):83–89, 1985.
- [134] J. Lemaitre. *A Course on Damage Mechanics*. Springer, Berlin, Heidelberg, 2nd edition, 1996.
- [135] J. Lemaitre and J.-L. Chaboche. Aspect phénoménologique de la rupture par endommagement. *Journal de mécanique appliqué*, 2(3):317–365, 1978.
- [136] J. Lemaitre and J.-L. Chaboche. *Mechanics of solid materials*. Cambridge university press, 1994.
- [137] J. Lemaitre and R. Desmorat. *Engineering Damage Mechanics*. Springer, 2005.
- [138] J. Lemaitre and I. Doghri. Damage 90: a post processor for crack initiation. *Computer Methods in Applied Mechanics and Engineering*, 115(3):197–232, 1994.

- [139] J. Lemaitre, J. Sermage, and R. Desmorat. A two scale damage concept applied to fatigue. *International Journal of Fracture*, 97(1):67–81, 1999.
- [140] C. Lim, K. Kim, and J. Seong. Ratcheting and fatigue behavior of a copper alloy under uniaxial cyclic loading with mean stress. *International Journal of Fatigue*, 31(3):501–507, 2009.
- [141] P. Lukáš and L. Kunz. Small cracks–nucleation, growth and implication to fatigue life. *International Journal of Fatigue*, 25(9):855–862, 2003.
- [142] J. Lutz, H. Schlangenotto, U. Scheuermann, and R. De Doncker. *Semiconductor Power Devices – Physics, Characteristics, Reliability*. Springer, Berlin, Heidelberg, 2011.
- [143] E. Macha. Simulation investigations of the position of fatigue fracture plane in materials with biaxial loads. *Materialwissenschaft und Werkstofftechnik*, 20(4):132–136, 1989.
- [144] E. Macha and C. Sonsino. Energy criteria of multiaxial fatigue failure. *Fatigue and Fracture of Engineering Materials and Structures*, 22(12):1053–1070, 1999.
- [145] S. S. Manson. Behavior of materials under conditions of thermal stress. Technical Report 1170, National Advisory Committee for Aeronautics, USA, 1954.
- [146] S. S. Manson. Interfaces between fatigue, creep, and fracture. *International Journal of Fracture Mechanics*, 2(1):327–327, 1966.
- [147] S. S. Manson, J. C. Freche, and C. Ensign. Application of a double linear damage rule to cumulative fatigue. Technical Report NASA TN D-3839, National Aeronautics and Space Administration, USA, 1967.
- [148] Z. Marciniak, D. Rozumek, and E. Macha. Verification of fatigue critical plane position according to variance and damage accumulation methods under multiaxial loading. *International Journal of Fatigue*, 58:84–93, 2014.
- [149] D. Martineau, T. Mazeaud, M. Legros, P. Dupuy, C. Levade, and G. Vanderschaeve. Characterization of ageing failures on power MOSFET devices by electron and ion microscopies. *Microelectronics Reliability*, 49(9):1330–1333, 2009.

- [150] D. Martineau, T. Mazeaud, M. Legros, P. Dupuy, and C. Levade. Characterization of alterations on power MOSFET devices under extreme electro-thermal fatigue. *Microelectronics Reliability*, 50(9):1768–1772, 2010.
- [151] D. Martineau, C. Levade, M. Legros, P. Dupuy, and T. Mazeaud. Universal mechanisms of Al metallization ageing in power MOSFET devices. *Microelectronics Reliability*, 54(11):2432–2439, 2014.
- [152] R. McClung. A literature survey on the stability and significance of residual stresses during fatigue. *Fatigue & Fracture of Engineering Materials & Structures*, 30(3):173–205, 2007.
- [153] D. McDowell and F. Dunne. Microstructure-sensitive computational modeling of fatigue crack formation. *International Journal of Fatigue*, 32:1521–1542, 2010.
- [154] M. A. Meggiolaro, J. T. P. de Castro, and H. Wu. Non-linear incremental fatigue damage calculation for multiaxial non-proportional histories. *International Journal of Fatigue*, 100:502–511, 2017.
- [155] H. D. Merchant, M. G. Minor, and Y. L. Liu. Mechanical fatigue of thin copper foil. *Journal of Electronic Materials*, 28(9):998–1007, 1999.
- [156] M. A. Miner. Cumulative damage in fatigue. *Journal of Applied Mechanics*, 12:159–164, 1945.
- [157] M. Mirsayar. Mixed mode fracture analysis using extended maximum tangential strain criterion. *Materials & Design*, 86:941–947, 2015.
- [158] F. Moroni and A. Pirondi. A procedure for the simulation of fatigue crack growth in adhesively bonded joints based on a cohesive zone model and various mixed-mode propagation criteria. *Engineering Fracture Mechanics*, 89:129–138, 2012.
- [159] J. Morrow. Fatigue properties in metals, Section 3.2. In J. A. Graham, editor, *Fatigue Design Handbook, Advances in Engineering*, volume 4, pages 21–29. Society of Automotive Engineers, Incorporated, Warrendale, 1968.
- [160] S. Murakami. *Continuum damage mechanics – A continuum mechanics approach to the analysis of damage and fracture*, volume 185. Springer, Dordrecht, 2012.



- [161] Y. Murakami and K. Miller. What is fatigue damage? a view point from the observation of low cycle fatigue process. *International Journal of Fatigue*, 27(8):991–1005, 2005.
- [162] J. Muñoz, U. Galvanetto, and P. Robinson. On the numerical simulation of fatigue driven delamination with interface elements. *International Journal of Fatigue*, 28(10):1136–1146, 2006.
- [163] M. Nelhiebel, R. Illing, C. Schreiber, S. Woehlert, S. Lanzerstorfer, M. Ladurner, C. Kadow, S. Decker, D. Dibra, H. Unterwalcher, M. Rogalli, W. Robl, T. Herzig, M. Poschgan, M. Inselsbacher, M. Glavanovics, and S. Fraisse. A reliable technology concept for active power cycling to extreme temperatures. *Microelectronics Reliability*, 51:1927–1932, 2011.
- [164] M. Nelhiebel, R. Illing, T. Detzel, S. Wöhlert, B. Auer, S. Lanzerstorfer, M. Rogalli, W. Robl, S. Decker, J. Fugger, and M. Ladurner. Effective and reliable heat management for power devices exposed to cyclic short overload pulses. *Microelectronics Reliability*, 53:1745–1749, 2013.
- [165] R. Neu and H. Sehitoglu. Thermomechanical fatigue, oxidation, and creep: Part I. damage mechanisms. *Metallurgical Transactions A*, 20(9):1755–1767, 1989.
- [166] R. Neu and H. Sehitoglu. Thermomechanical fatigue, oxidation, and creep: Part II. life prediction. *Metallurgical Transactions A*, 20(9):1769–1783, 1989.
- [167] J. C. Newman. A crack-closure model for predicting fatigue crack growth under aircraft spectrum loading. In *Methods and models for predicting fatigue crack growth under random loading*, STP748. ASTM International, 1981.
- [168] J. C. Newman. The merging of fatigue and fracture mechanics concepts: a historical perspective. *Progress in Aerospace Sciences*, 34(5-6):347–390, 1998.
- [169] O. Nguyen, E. Repetto, M. Ortiz, and R. Radovitzky. A cohesive model of fatigue crack growth. *International Journal of Fracture*, 110(4):351–369, 2001.
- [170] K. C. Norris and A. H. Landzberg. Reliability of controlled collapse interconnections. *IBM Journal of Research and Development*, 13(3):266–271, 1969.

- [171] T. K. O'Brien, W. M. Johnston, and G. J. Toland. Mode II interlaminar fracture toughness and fatigue characterization of a graphite epoxy composite material. Technical Report NASA/TM-2010-216838, National Aeronautics and Space Administration, USA, 2010.
- [172] I. Özdemir, W. A. M. Brekelmans, and M. G. D. Geers. A thermo-mechanical cohesive zone model. *Computational Mechanics*, 46(5):735–745, 2010.
- [173] H. Oh, B. Han, P. McCluskey, C. Han, and B. D. Youn. Physics-of-failure, condition monitoring, and prognostics of insulated gate bipolar transistor modules: A review. *IEEE Transactions on Power Electronics*, 30(5):2413–2426, 2015.
- [174] Y. Okada and Y. Tokumaru. Precise determination of lattice parameter and thermal expansion coefficient of silicon between 300 and 1500 K. *Journal of Applied Physics*, 56(2):314–320, 1984.
- [175] A. Palmgren. Die Lebensdauer von Kugellagern. *Zeitschrift des Vereins Deutscher Ingenieure*, 68(14):339–341, 1924.
- [176] I. V. Papadopoulos, P. Davoli, C. Gorla, M. Filippini, and A. Bernasconi. A comparative study of multiaxial high-cycle fatigue criteria for metals. *International Journal of Fatigue*, 19(3):219–235, 1997.
- [177] P. C. Paris and F. Erdogan. A critical analysis of crack propagation laws. *Journal of Basic Engineering*, 85(4):528–533, 1963.
- [178] J. Park and D. Nelson. Evaluation of an energy-based approach and a critical plane approach for predicting constant amplitude multiaxial fatigue life. *International Journal of Fatigue*, 22(1):23–39, 2000.
- [179] R. H. J. Peerlings, W. A. M. Brekelmans, R. de Borst, and M. G. D. Geers. Gradient-enhanced damage modelling of high-cycle fatigue. *International Journal for Numerical Methods in Engineering*, 49(12):1547–1569, 2000.
- [180] T. Péliisset. *Degradation analysis of thin die-attach layer under cyclic thermal load in microelectronics packaging*. PhD thesis, Montanuniversität Leoben, 2015.

- [181] C. L. Perez and B. D. Davidson. Evaluation of precracking methods for the end-notched flexure test. *American Institute of Aeronautics and Astronautics (AIAA) journal*, 45(11):2603–2611, 2007.
- [182] F. Pérez and B. E. Granger. IPython: A system for interactive scientific computing. *Computing in Science and Engineering*, 9(3):21–29, 2007.
- [183] G. Petrucci. A critical assessment of methods for the determination of the shear stress amplitude in multiaxial fatigue criteria belonging to critical plane class. *International Journal of Fatigue*, 74:119–131, 2015.
- [184] M. Pfost, C. Boianceanu, H. Lohmeyer, and M. Stecher. Electrothermal simulation of self-heating in DMOS transistors up to thermal runaway. *IEEE Transactions on Electron Devices*, 60(2):699–707, 2013.
- [185] B. Philippi, K. Matoy, J. Zechner, C. Kirchlechner, and G. Dehm. Microcantilever fracture testing of intermetallic Cu<sub>3</sub>Sn in lead-free solder interconnects. *Journal of Electronic Materials*, 3(46):1607–1611, 2017.
- [186] S. Pietranico, S. Lefebvre, S. Pommier, M. B. Bouaroudj, and S. Bontemps. A study of the effect of degradation of the aluminium metallization layer in the case of power semiconductor devices. *Microelectronics Reliability*, 51(9):1824–1829, 2011.
- [187] A. Pineau, D. L. McDowell, E. P. Busso, and S. D. Antolovich. Failure of metals II: Fatigue. *Acta Materialia*, 107:484–507, 2016.
- [188] A. Pironi and N. Bonora. Modeling ductile damage under fully reversed cycling. *Computational Materials Science*, 26:129–141, 2003.
- [189] L. P. Pook. *Metal Fatigue – What It Is, Why It Matters*, volume 145. Springer, Dordrecht, 2007.
- [190] N. Post, S. Case, and J. Lesko. Modeling the variable amplitude fatigue of composite materials: A review and evaluation of the state of the art for spectrum loading. *International Journal of Fatigue*, 30(12):2064–2086, 2008.

- [191] Y. N. Rabotnov. Creep rupture. In M. Hetényi and W. G. Vincenti, editors, *Proceedings of applied mechanics conference, Stanford University*, pages 342–349. Springer, Berlin, Heidelberg, 1969.
- [192] J. Renart, J. Vicens, S. Budhe, A. Rodríguez-Bellido, J. Comas, J. Mayugo, and J. Costa. An automated methodology for mode II delamination tests under fatigue loading based on the real time monitoring of the specimen’s compliance. *International Journal of Fatigue*, 82(3):634–642, 2016.
- [193] J. R. Rice. A path independent integral and approximate analysis of strain concentration by notches and cracks. *Journal of Applied Mechanics*, 35:379–386, 1968.
- [194] J. R. Rice and G. F. Rosengren. Plane strain deformation near a crack tip in a power-law hardening material. *Journal of the Mechanics and Physics of Solids*, 16(1):1–12, 1968.
- [195] S. Ridout and C. Bailey. Review of methods to predict solder joint reliability under thermo-mechanical cycling. *Fatigue & Fracture of Engineering Materials & Structures*, 30(5):400–412, 2007.
- [196] M. Riedler, H. Leitner, B. Prillhofer, G. Winter, and W. Eichlseder. Lifetime simulation of thermo-mechanically loaded components. *Meccanica*, 42(1):47–59, 2007.
- [197] R. H. Rigby and M. H. Aliabadi. Decomposition of the mixed-mode J-integral—revisited. *International Journal of Solids and Structures*, 35(17):2073–2099, 1998.
- [198] J. W. Ringsberg. Life prediction of rolling contact fatigue crack initiation. *International Journal of Fatigue*, 23(7):575–586, 2001.
- [199] P. Robinson, U. Galvanetto, D. Tumino, G. Bellucci, and D. Violeau. Numerical simulation of fatigue-driven delamination using interface elements. *International Journal for Numerical Methods in Engineering*, 63(13):1824–1848, 2005.
- [200] K. Roe and T. Siegmund. An irreversible cohesive zone model for interface fatigue crack growth simulation. *Engineering Fracture Mechanics*, 70(2):209–232, 2003.
- [201] M. L. Roessle and A. Fatemi. Strain-controlled fatigue properties of steels and some simple approximations. *International Journal of Fatigue*, 22(6):495–511, 2000.

- [202] S. Roth and M. Kuna. Prediction of size-dependent fatigue failure modes by means of a cyclic cohesive zone model. *International Journal of Fatigue*, 100(1):58–67, 2017.
- [203] R. Ruffilli, M. Berkani, P. Dupuy, S. Lefebvre, Y. Weber, and M. Legros. In-depth investigation of metallization aging in power MOSFETs. *Microelectronics Reliability*, 55(9):1966–1970, 2015.
- [204] S. Russo, R. Letor, O. Viscuso, L. Torrisi, and G. Vitali. Fast thermal fatigue on top metal layer of power devices. *Microelectronics Reliability*, 42(9):1617–1622, 2002.
- [205] A. P. Ruybalid, J. P. M. Hoefnagels, O. van der Sluis, and M. G. D. Geers. Comparison of the identification performance of conventional FEM updating and integrated DIC. *International Journal for Numerical Methods in Engineering*, 106(4):298–320, 2016.
- [206] M. D. Sangid. The physics of fatigue crack initiation. *International Journal of Fatigue*, 57:58–72, 2013.
- [207] C. Sarrado, A. Turon, J. Renart, and I. Urresti. Assessment of energy dissipation during mixed-mode delamination growth using cohesive zone models. *Composites Part A: Applied Science and Manufacturing*, 43(11):2128–2136, 2012.
- [208] U. Scheuermann and U. Hecht. Power cycling lifetime of advanced power modules for different temperature swings. In *Proceedings of the 45th International Power Electronics Conference (PCIM), Nürnberg*, pages 59–64, 2002.
- [209] O. Schilling, M. Schäfer, K. Mainka, M. Thoben, and F. Sauerland. Power cycling testing and FE modelling focussed on Al wire bond fatigue in high power IGBT modules. *Microelectronics Reliability*, 52(9):2347–2352, 2012.
- [210] R. Schmidt, R. Werner, J. Casady, B. Hull, and A. Barkley. Power cycle testing of sintered SiC-MOSFETs. In *Proceedings of the International Exhibition and Conference for Power Electronics, Intelligent Motion, Renewable Energy and Energy Management (PCIM Europe), Nuremberg*, pages 1–8. VDE, 2017.
- [211] W. Schmitt, R. Mohrmann, H. Riedel, A. Dietsche, and A. Fischersworing-Bunk. Modelling of the fatigue life of automobile exhaust components. In *Proceedings of*

- the 8th International Fatigue Congress Fatigue 2002, Warley*, pages 781–788. EMAS Publishing, 2002.
- [212] M. Schöllmann, H. A. Richard, G. Kullmer, and M. Fulland. A new criterion for the prediction of crack development in multiaxially loaded structures. *International Journal of Fracture*, 117(2):129–141, 2002.
- [213] N. Shamma. Present problems of power module packaging technology. *Microelectronics Reliability*, 43(4):519–527, 2003.
- [214] R. Sleik, M. Glavanovics, S. Einspieler, A. Muetze, and K. Krischan. Modular test system architecture for device, circuit and system level reliability testing. In *Applied Power Electronics Conference and Exposition (APEC)*, pages 759–765. IEEE, 2016.
- [215] K. N. Smith, P. Watson, and T. H. Topper. A stress–strain function for the fatigue of metals. *Journal of Materials*, 5(4):767–778, 1970.
- [216] D. F. Socie. Multiaxial fatigue damage criteria, Section 6.8. In J. Lemaitre, editor, *Handbook of Materials Behavior Models*, pages 453–456. Academic Press, Burlington, 2001.
- [217] D. F. Socie. Multiaxial fatigue damage models. *Journal of Engineering Materials and Technology*, 109(4):293–298, 1987.
- [218] A. Soto, E. González, P. Maimí, A. Turon, J. Sainz de Aja, and F. de la Escalera. Cohesive zone length of orthotropic materials undergoing delamination. *Engineering Fracture Mechanics*, 159:174–188, 2016.
- [219] P. Steinhorst, T. Poller, and J. Lutz. Approach of a physically based lifetime model for solder layers in power modules. *Microelectronics Reliability*, 53(9):1199–1202, 2013.
- [220] S. Suresh. *Fatigue of materials*. Cambridge University Press, 2nd edition, 1998.
- [221] L. Susmel, R. Tovo, and D. F. Socie. Estimating the orientation of stage I crack paths through the direction of maximum variance of the resolved shear stress. *International Journal of Fatigue*, 58:94–101, 2014.

- [222] S. Tabibian, E. Charkaluk, A. Constantinescu, F. Szmytka, and A. Oudin. TMF-LCF life assessment of a lost foam casting A319 aluminum alloy. *International Journal of Fatigue*, 53:75–81, 2013.
- [223] A. Turon, P. P. Camanho, J. Costa, and C. G. D’ávila. A damage model for the simulation of delamination in advanced composites under variable-mode loading. *Mechanics of Materials*, 38(11):1072–1089, 2006.
- [224] A. Turon, J. Costa, P. P. Camanho, and C. G. Dávila. Simulation of delamination in composites under high-cycle fatigue. *Composites Part A: Applied Science and Manufacturing*, 38(11):2270–2282, 2007.
- [225] A. Turon, J. Costa, P. P. Camanho, and P. Maimí. Analytical and numerical investigation of the length of the cohesive zone in delaminated composite materials, Chapter 4. In P. P. Camanho, C. G. Dávila, S. T. Pinho, and J. J. C. Remmers, editors, *Mechanical Response of Composites*, pages 77–97. Springer, Dordrecht, 2008.
- [226] A. Turon, B. L. V. Bak, E. Lindgaard, C. Sarrado, and E. Lund. Interface elements for fatigue-driven delaminations in advanced composite materials, Chapter 3. In P. P. Camanho and S. R. Hallett, editors, *Numerical Modelling of Failure in Advanced Composite Materials*, pages 73–91. Woodhead Publishing, 2015.
- [227] T. Walander, A. Biel, and U. Stigh. An evaluation of the temperature dependence of cohesive properties for two structural epoxy adhesives. In *19th European Conference on Fracture, Kazan*, 2012.
- [228] T. Walander, A. Biel, and U. Stigh. Temperature dependence of cohesive laws for an epoxy adhesive in mode I and mode II loading. *International Journal of Fracture*, 183(2):203–221, 2013.
- [229] C. Wang and X. Xu. Cohesive element analysis of fatigue delamination propagation in composite materials with improved crack tip tracking algorithm. *Composite Structures*, 134:176–184, 2015.
- [230] H. Wang, M. Liserre, F. Blaabjerg, P. de Place Rikken, J. B. Jacobsen, T. Kvisgaard, and J. Landkildehus. Transitioning to physics-of-failure as a reliability driver in power

- electronics. *IEEE Journal of Emerging and Selected Topics in Power Electronics*, 2(1):97–114, 2014.
- [231] Y. Wang and L. Susmel. The modified Manson–Coffin curve method to estimate fatigue lifetime under complex constant and variable amplitude multiaxial fatigue loading. *International Journal of Fatigue*, 83(2):135–149, 2016.
- [232] Y. Wang, N. Z. Faruq, and L. Susmel. Evaluation of different techniques in estimating orientation of crack initiation planes and fatigue lifetime under complex multiaxial loading paths. *International Journal of Fatigue*, 100:521–529, 2017.
- [233] A. A. Wells. Unstable crack propagation in metals – cleavage and fast fracture. In *Symposium on Crack Propagation, Cranfield*, volume 1, pages 210–230, 1961.
- [234] E. Wilfried, W. Gerhard, M. Robert, and R. Martin. Comparison of energy–based and damage–related fatigue life models for aluminium components under TMF loading. In P. Z. Ahmad, editor, *Recent Trends in Processing and Degradation of Aluminium Alloys*. InTech, 2011.
- [235] A. Wimmer, A. Leitner, T. Detzel, W. Robl, W. Heinz, R. Pippan, and G. Dehm. Damage evolution during cyclic tension–tension loading of micron–sized Cu lines. *Acta Materialia*, 67:297–307, 2014.
- [236] A. Wimmer, W. Heinz, T. Detzel, W. Robl, M. Nellessen, C. Kirchlechner, and G. Dehm. Cyclic bending experiments on free–standing Cu micron lines observed by electron backscatter diffraction. *Acta Materialia*, 83:460–469, 2015.
- [237] A. Wimmer, W. Heinz, A. Leitner, T. Detzel, W. Robl, C. Kirchlechner, and G. Dehm. Micro–tension study of miniaturized Cu lines at variable temperatures. *Acta Materialia*, 92:243–254, 2015.
- [238] E. H. Wong, W. D. van Driel, A. Dasgupta, and M. Pecht. Creep fatigue models of solder joints: A critical review. *Microelectronics Reliability*, 59:1–12, 2016.
- [239] S. C. Wu, Z. W. Xu, C. Yu, O. L. Kafka, and W. K. Liu. A physically short fatigue crack growth approach based on low cycle fatigue properties. *International Journal of Fatigue*, 103:185–195, 2017.



- [240] T. Wu and P. Wriggers. Multiscale diffusion–thermal–mechanical cohesive zone model for concrete. *Computational Mechanics*, 55(5):999–1016, 2015.
- [241] B. Yang, S. Mall, and K. Ravi-Chandar. A cohesive zone model for fatigue crack growth in quasibrittle materials. *International Journal of Solids and Structures*, 38(22):3927–3944, 2001.
- [242] Q. Yang, D. Shim, and S. Spearing. A cohesive zone model for low cycle fatigue life prediction of solder joints. *Microelectronic Engineering*, 75(1):85–95, 2004.
- [243] W. Zhuang and N. S. Swansson. Thermo–mechanical fatigue life prediction: a critical review. Technical Report DSTO–TR–0609, Aeronautical and Maritime Research Laboratory, Melbourne, 1998.
- [244] O. C. Zienkiewicz, R. L. Taylor, and J. Z. Zhu. *The Finite Element Method: Its Basis and Fundamentals*. Butterworth–Heinemann, Oxford, 7th edition, 2013.
- [245] O. C. Zienkiewicz, R. L. Taylor, and D. Fox. *The Finite Element Method for Solid and Structural Mechanics*. Butterworth–Heinemann, Oxford, 7th edition, 2014.



# Martin SPRINGER

## Curriculum Vitae



---

### Personal Data

<b>Address</b>	Im Winkl 17, 3743 Röschitz, Austria	<b>Email</b>	springer@ilsb.tuwien.ac.at
<b>Date of Birth</b>	August 10 <sup>th</sup> , 1989	<b>Phone</b>	+43 664 1576404
<b>Military Service</b>	July 2008 – January 2009	<b>Nationality</b>	Austria

---

### Education and Training

- Oct. 2014–present **Doctoral program in Engineering Sciences (Mechanical Engineering)**  
*Vienna University of Technology, Austria*
- PhD Thesis: *Modeling and Simulation of Fatigue Damage in Power Semiconductors*
- Sept. 2016–Dec. 2016 **Research Stay**  
*AMADE, University of Girona, Spain*
- Development of a numerical model for the prediction of fatigue interface damage
- Apr. 2013–Sept. 2014 **Master program Mechanical Engineering**  
*Vienna University of Technology, Austria*
- Specialization in automation engineering, mechatronic systems, continuum mechanics of solids, and the nonlinear Finite Element Method
  - Thesis: *Nichtlineare FE Simulationen der Schädigungsmechanismen sowie der Resttragfähigkeit von schlagbenaspruchten Kohlenstofffaser-Epoxydharz-Verbunden*
  - Passed with distinction
- Oct. 2009–Apr. 2013 **Bachelor program Mechanical Engineering**  
*Vienna University of Technology, Austria*
- Specialization in lightweight design, fracture mechanics, and numerical methods
  - Thesis: *Singuläre isoparametrische Elemente mit variabler Ordnung der Singularität*
- Sept. 2003–Jun. 2008 **Technical College for Mechanical Engineering**  
*HTL Hollabrunn, Austria*
- Fundamentals of mechanical engineering focused on environmental technologies
  - Passed with distinction

---

### Work experience

- Nov. 2014–present **Project Assistant**  
*Institute of Lightweight Design and Structural Biomechanics (ILSB), Vienna University of Technology (TU Wien), Austria*
- Numerical modeling of fatigue damage in power semiconductors
  - Cooperation with KAI GmbH, Villach and Infineon Technologies Austria AG
  - Supervision of master's and bachelor's theses
- Jan. 2009–Oct. 2014 **Design Engineer**  
*Wagner Biro Austria Stage Systems AG, Vienna*
- Design and development of stage machinery for theatres and opera houses
  - Concept design, regulatory approval, and detailed design with CAD
  - Drive unit specifications and static calculations for load-bearing structures

---

## Languages

**German** Native  
**English** Fluent

*Mother Tongue*  
*Daily practice, all work performed in English, CEFR C1*

---

## IT Skills

**Numerics** ANSYS APDL, ABAQUS, HyperWorks, MATLAB, Mathcad, RSTAB  
**Programming** Python, Fortran (basics)  
**CAD** AutoCad Mechanical, Catia, Autodesk Inventor, Creo (ProEngineer)  
**Design** Inkscape, Gimp, Illustrator, Photoshop, InDesign  
**Office** MS Office, L<sup>A</sup>T<sub>E</sub>X, LibreOffice  
**OS** Linux, Windows

---

## Community Involvement

**FF-Röschitz** member of the executive board of the local, volunteer fire department

---

## Publications, Conference Contributions, and Talks

2017

---

M. Springer, A. Turon, and H. E. Pettermann. “A Cyclic Cohesive Zone Model for Variable Amplitude Loading and Mixed-Mode Behavior”. In: *Proceedings of 6th ECCOMAS Thematic Conference on the Mechanical Response of Composites (COMPOSITES 2017)*, Eindhoven. IEEE, pp. 48–59.

2016

---

M. Springer, M. Nelhiebel, and H. E. Pettermann. “Combined simulation of fatigue crack nucleation and propagation based on a damage indicator”. In: *Fracture and Structural Integrity* 38. Proceedings of 11th International Conference on Multiaxial Fatigue & Fracture (ICMFF11), Sevilla, pp. 155–161.

2016

---

M. Springer, M. Nelhiebel, and H.E. Pettermann. “Fatigue crack growth modeling in the metallization of power semiconductors under cyclic thermo-mechanical loading”. In: *17th International Conference on Thermal, Mechanical and Multi-Physics Simulation and Experiments in Microelectronics and Microsystems (EuroSimE)*, Montpellier. IEEE, pp. 1–5.

2016

---

M. Springer and H. E. Pettermann. *Fatigue Damage Modeling of Power Semiconductor Devices*. Invited talk at the AMADE Group of the University of Girona, Spain.

2015

---

M. Springer, M. Schwab, and H. E. Pettermann. *Simulation of ply damage and delamination in multilayer composites to predict the residual compressive strength after impact loading*. Conference talk at 4th International Conference on Computational Modeling of Fracture and Failure (CFRAC 2015), Cachan.

---

## References

**Dr. Heinz E. Pettermann**  
Associate Professor  
ILSB, Technische Universität Wien  
Vienna, Austria  
pettermann@ilsb.tuwien.ac.at

**Dr. Albert Turon Travesa**  
Associate Professor  
AMADE, University of Girona  
Catalonia, Spain  
albert.turon@udg.edu

**Dipl.-Ing. Josef Fugger**  
Director R&D  
KAI Kompetenzzentrum Automobil-  
und Industrieelektronik GmbH  
Villach, Austria  
josef.fugger@infineon.com

**Ing. Erich Raser**  
Head of Project- & Operations  
Management  
Waagner Biro Austria Stage  
Systems AG, Vienna  
erich.raser@waagner-biro.com